CTS and CZTS for solar cells made by pulsed laser deposition and pulsed electron deposition

Ettlinger, Rebecca Bolt; Schou, Jørgen; Jepsen, Peter Uhd

Publication date:
2016

Document Version
Publisher's PDF, also known as Version of record

CTS and CZTS for solar cells by pulsed laser deposition and pulsed electron deposition

Rebecca Bolt Ettlinger

November 14, 2016

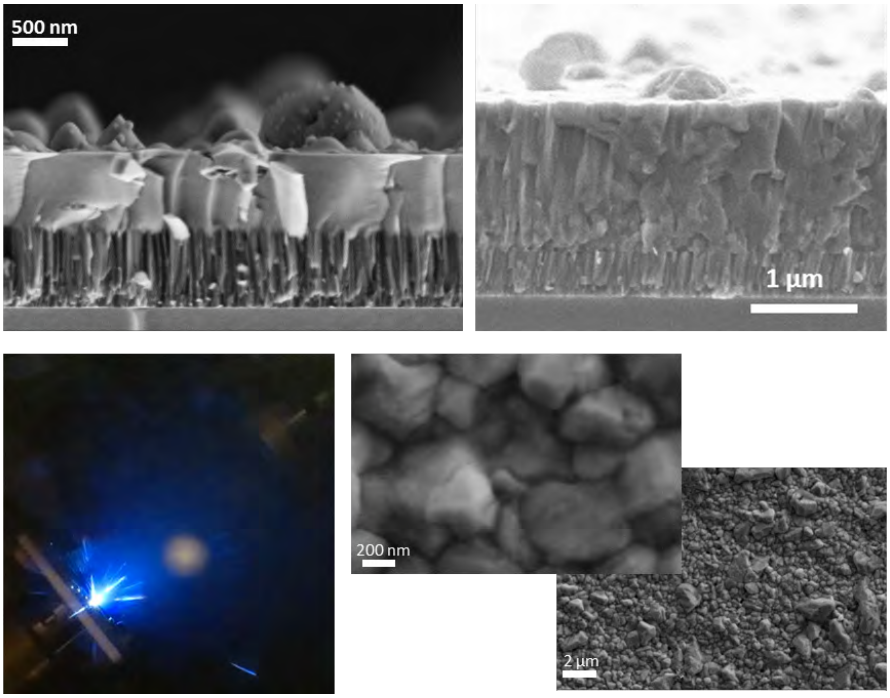

PhD thesis
Supervisor: Jørgen Schou
Co-supervisor: Peter Uhd Jepsen
DTU FOTONIK, Technical University of Denmark

Contents

Contents i

List of Figures v

List of Tables vii

Abstract ix

Dansk opsummering xi

List of publications xv

Acknowledgments xvii

Technical terms and abbreviations xix

1 Introduction 1
- 1.1 Why chalcogenide solar cells? . . . 1
- 1.2 State-of-the-art CZTS and CTS solar cells . . . 4
  - 1.2.1 The architecture of a CZTS solar cell . . . 5
- 1.3 Solar cells in a broader context . . . 7
  - 1.3.1 Life cycle analysis of CZTS solar cells . . . 9
- 1.4 The deposition techniques used in this work . . . 10
- 1.5 Research aims . . . 11
  - 1.5.1 Milestones achieved . . . 12
- 1.6 Structure of the thesis . . . 13

2 CZTS and CTS solar cells 15
- 2.1 Semiconductors and solar cells . . . 15
- 2.2 CZTS: material properties and solar cell processing . . . 20
  - 2.2.1 Composition dependence of defects and secondary phases . 21

2.2.2 CZTS thin film formation . . . 24
2.2.3 SnS loss . . . 25
2.3 Secondary Phases of CZTS . . . 26
2.3.1 Copper tin sulfide . . . 26
2.3.2 Solar cells of CTS . . . 28
2.3.3 ZnS material properties . . . 28
2.3.4 Copper sulfides . . . 29
2.3.5 Tin sulfides . . . 30
2.4 Summary: CZTS and CTS solar cells . . . 31

3 Background: PLD and PED **33**
3.1 Ablation and thin film formation . . . 33
3.1.1 Energy absorption in the target . . . 35
3.1.2 Plume and plasma generation . . . 37
3.1.3 Plume expansion geometry . . . 38
3.1.4 Energy and time scale of plume expansion . . . 39
3.1.5 Film formation . . . 41
3.2 Conditions for stoichiometric transfer . . . 42
3.2.1 Non-stoichiometric CTS growth; where did the SnS go? . . . 44
3.3 Droplet generation . . . 46
3.4 Impact of deposition conditions . . . 52
3.5 Pulsed electron deposition . . . 54
3.5.1 Initiation of ablation in PED . . . 55
3.5.2 Plasma generation and expansion - PED versus PLD . . . 57
3.6 Summary: Advantages and drawbacks of PED and PLD . . . 58

4 PLD of chalcogenides in the literature **59**
4.1 PLD of CZTS . . . 59
4.2 PLD of CIGS and CdTe . . . 62
4.2.1 PLD of CIGSe . . . 62
4.2.2 PLD of CdTe for solar cells and photodetectors . . . 63
4.2.3 Lessons from PLD of CIGS and CdTe . . . 64
4.3 PLD of ZnS . . . 65
4.3.1 Literature on PLD of ZnS . . . 65
4.4 Other chalcogenides . . . 67
4.5 Summary of the lessons from literature on PLD of chalcogenides . . . 68

5 Materials and Methods **69**
5.1 Pulsed laser deposition . . . 69
5.1.1 PLD: 355 nm setup . . . 70
5.1.2 PLD: 248 nm setup . . . 71
5.1.3 Heating the films . . . 73

5.2 Pulsed electron deposition . . . 74
5.2.1 Optical Emission Spectroscopy . . . 74
5.3 Annealing . . . 75
5.4 Targets and substrates . . . 78
5.4.1 Targets . . . 78
5.4.2 Substrates . . . 79
5.5 Solar cell fabrication . . . 80
5.6 Characterization . . . 80
5.6.1 Deposition rate measurement . . . 80
5.6.2 Transmission and reflection measurements . . . 81
5.6.3 Scanning Electron Microscopy (SEM) . . . 82
5.6.4 Energy Dispersive X-ray Spectroscopy (EDX) . . . 82
5.6.5 X-ray diffraction . . . 85
5.6.6 Raman spectroscopy . . . 86
5.7 Photoluminescence and solar cell characterization . . . 87

6 Pulsed laser deposition of metals and ZnS 89
6.1 Background . . . 89
6.1.1 Literature on UV-PLD of elemental metals . . . 90
6.1.2 Quick recap on ZnS . . . 90
6.2 Methods . . . 91
6.3 Results and discussion: metal films . . . 91
6.3.1 Metal deposition rates . . . 93
6.3.2 Lessons from metal deposition . . . 96
6.4 Results and discussion: ZnS . . . 97
6.4.1 Deposition rate of ZnS versus metals . . . 97
6.4.2 ZnS film characteristics . . . 101
6.4.3 Crystalline film texture . . . 103
6.5 Summary . . . 104

7 Pulsed laser deposition of CTS 105
7.1 Background and aims for PLD of CTS . . . 106
7.2 Results and discussion: As-deposited films . . . 107
7.2.1 Deposition rate at different wavelengths . . . 107
7.2.2 Fluence effect on composition . . . 108
7.2.3 Fluence and laser wavelength effect on droplets . . . 110
7.2.4 CTS films deposited at 150-300 °C . . . 112
7.3 Results: Annealed CTS films . . . 118
7.3.1 Effect of different annealing conditions . . . 121
7.3.2 Example: Phase analysis in an improved annealed film . . . 123
7.3.3 Films for ellipsometry . . . 124

7.4 Results: Solar cells . . . 126
7.5 Summary . . . 129

8 PED and PLD of CZTS 131
8.1 PED versus PLD - background on other materials . . . 132
8.1.1 Methods for PED and PLD of CZTS . . . 133
8.2 Results and discussion: PED and PLD of CZTS . . . 134
8.2.1 Deposition rate and morphology of as-deposited films . . . 135
8.2.2 Composition of the as-deposited PLD films . . . 138
8.2.3 Composition of the as-deposited PED films . . . 142
8.2.4 Crystallinity of films deposited at 300 °C . . . 143
8.2.5 Lessons from a low-fluence PLD film . . . 147
8.2.6 Solar cells . . . 147
8.3 Summary and discussion . . . 150

9 Conclusion 153
9.1 Main results on CTS . . . 153
9.2 Main results on CZTS . . . 154
9.3 Observations on PLD and PED of chalcogenides . . . 155
9.4 Discussion . . . 156
9.4.1 On using a multi-phase chalcogenide target . . . 156
9.4.2 On CZTS by PED and PLD . . . 157
9.5 Perspectives . . . 158
9.5.1 Non-equilibrium methods for CZTS and CTS . . . 158
9.5.2 Epitaxial films of CZTS and CTS . . . 158
9.5.3 Single-step CZTS and CTS deposition . . . 158
9.5.4 CZTS as a future solar cell material . . . 159

A Article: Pulsed laser deposition of ZnS and CTS 161

B Article: CTS by pulsed laser deposition at 248 and 355 nm 169

C Conf. Proc.: Pulsed laser deposition of Cu-Sn-S 181

D In prep: PED versus PLD of CZTS 185

E Reference matrix for PLD of CZTS 215

F Reference matrix for PLD of ZnS 219

G Material constants 225

Bibliography 227

List of Figures

1.1 Price vs earth-abundance of selected elements 3
1.2 CZTS solar cell architecture 6
1.3 Renewables share of total primary energy supply 7
1.4 Photovoltaic market growth 8

2.1 Conceptual illustration of a p-n junction 17
2.2 Conceptual illustration of an illuminated p-n junction 18
2.3 Sphalerite, chalcopyrite, kesterite and stannite crystal structure 21
2.4 Pseudoternary phase diagram of CZTS 22
2.5 Point defect energy levels in CZTS 23
2.6 Crystal structure of Cu_2SnS_3 27

3.1 PLD setup and ablation plume 34
3.2 Comic-strip depiction of ablation process 38
3.3 Thickness gradient across a wide ZnS film 40
3.4 Timeline of a ns-PLD pulse 41
3.5 Film formation processes 42
3.6 Film deposited at right angles versus opposite the target 45
3.7 Map of droplet density on film surface 47
3.8 Droplets on SnS-rich CTS films with different spot size, constant energy 48
3.9 Close-ups of droplets of as-deposited CTS and SnS-rich CTS 50
3.10 Cross-sections of droplets on SnS-rich CTS 51
3.11 Morphology of films deposited at 7 Hz versus 45 Hz 54
3.12 Schematic representation of a PED setup 55

5.1 355 nm setup 70
5.2 Variation of spot size with laser energy 72
5.3 248 nm setup 72
5.4 PED setup 75
5.5 Annealing setup 76

5.6 Annealed samples . . . 77
5.7 EDX map of a CTS target . . . 78
5.8 X-ray diffractograms of CZTS targets . . . 79
5.9 Comparison of EDX quantification by different instruments . . . 83
5.10 Error in EDX due to surface roughness . . . 84

6.1 Metal, ZnS and CTS film images . . . 92
6.2 Ablated surfaces of metal targets . . . 93
6.3 Dektak profile examples . . . 94
6.4 Zn deposition rate . . . 95
6.5 All metals deposition rates . . . 95
6.6 ZnS versus metal deposition rates . . . 98
6.7 Reflectance and absorbance of ZnS target . . . 99
6.8 Reflectance of metal target surfaces . . . 100
6.9 ZnS target surface before and after ablation . . . 100
6.10 ZnS deposition rates at room temperature and 300 °C with the 248 nm laser . . . 101
6.11 Relatively high ZnS deposition rate at 248 nm versus 355 nm . . . 102

7.1 Deposition rate of CTS at room temperature versus 300 °C . . . 108
7.2 Droplets on SnS-rich CTS films at different fluence with constant spot size . . . 110
7.3 EDX maps showing Sn-rich and Cu-rich droplets . . . 111
7.4 SEM images of the CTS target surface before and after ablation. . . . 112
7.5 Composition at different deposition temperatures . . . 113
7.6 SnS-rich CTS films deposited at 150 °C and 300 °C . . . 114
7.7 XRD of CTS films as-deposited at 150 °C and300 °C . . . 115
7.8 XRD of SnS-rich CTS films as-deposited at 150 °C and300 °C . . . 117
7.9 Initial annealing results for SnS-rich CTS: SEM images . . . 118
7.10 Cross-sectional SEM of CTS solar cells . . . 119
7.11 Surface of SnS-rich CTS layers used for solar cells . . . 120
7.12 Annealing results: SEM showing mix of monoclinic and cubic CTS . . . 122
7.13 SEM images of an improved annealed CTS film . . . 123
7.14 Raman and XRD analysis of the improved annealed film . . . 125
7.15 100 nm monoclinic CTS film for ellipsometry . . . 126
7.16 JV and EQE curve for CTS solar cells . . . 128

8.1 Morphology of as-deposited room-temperature PED and PLD films . . . 136
8.2 Droplets versus fluence for as-deposited PED and PLD CZTS films . . . 137
8.3 Morphology of PED-deposited CZTS films made at 300 °C . . . 138
8.4 Morphology of CZTS films with different composition . . . 139
8.5 Composition of CZTS films made by PLD and PED at room temperature 140

8.6 Composition of CZTS by PLD: room temperature vs 300 °C 141
8.7 Raman spectroscopy of CZTS by PED and PLD at 255-325 °C 145
8.8 XRD of CZTS by PED and PLD at 255-300 °C 146
8.9 JV curve for a PED solar cell 148
8.10 PL measurements of PLD and PED-deposited CZTS 150

List of Tables

3.1 Composition of films deposited at right angles to the target compared to films deposited opposite the target 45

5.1 Parameters of the two lasers used in this study 69

7.1 Composition of SnS-rich CTS films at different fluences 109

8.1 Deposition parameters for PED and PLD 134

Abstract

This thesis concerns the deposition of thin films for solar cells using pulsed laser deposition (PLD) and pulsed electron deposition (PED). The aim was to deposit copper tin sulfide (CTS) and zinc sulfide (ZnS) by pulsed laser deposition to learn about these materials in relation to copper zinc tin sulfide (CZTS), a new material for solar cells. We were the first research group to deposit CTS by pulsed laser deposition and since this is a potential solar cell material in its own right we experimented with CTS solar cells in parallel with CZTS. Both CTS and CZTS contain only earth-abundant elements, which make them promising alternatives to the commercially successful solar cell material copper indium gallium diselenide (CIGS). Complementing our group's work on pulsed laser deposition of CZTS, we collaborated with IMEM-CNR in Parma, Italy, to deposit CZTS by pulsed electron deposition for the first time. We compared the results of CZTS deposition by PLD at DTU in Denmark to CZTS made by PED at IMEM-CNR, where CIGS solar cells have successfully been fabricated at very low processing temperatures.

The main results of this work were as follows:

- Monoclinic-phase CTS films were made by pulsed laser deposition followed by high temperature annealing. The films were used to understand the double bandgap that we and other groups observed in the material.

- The Cu-content of the CTS films varied depending on the laser fluence (the laser energy per pulse and per unit area). The material transfer from the multicomponent target to the film was generally not stoichiometric.

- The annealed CTS films could not be more than about 700 nm thick to avoid exfoliation and bubbles in the films. The CTS solar cells have therefore not yet been optimized and the maximum efficiency of our CTS solar cells was 0.3 % so far.

- The aim of using pulsed electron deposition was to make CZTS at a low processing temperature, avoiding the 570 °C annealing step used for our pulsed laser deposited solar cells. Preliminary solar cells had an efficiency

of 0.2 % with a 300 °C deposition step without annealing. Further process control is needed.

- With both pulsed laser deposition and pulsed electron deposition we found that the Cu-content of the films could be altered by changing the fluence (in PLD) or the voltage and pressure (in PED). SnS evaporated preferentially from the multicomponent target at low laser intensity and low pulsed electron beam voltage.

- Finally we compared two different lasers for deposition of CZTS and CTS: a 248 nm, 20 ns KrF excimer laser and a 355 nm, 6 ns Nd:YAG laser. While my colleague found that CZTS was best deposited with the 248 nm laser which has a high enough photon energy to exceed the band gap of the ZnS phase in the target, I found that it did not make a large difference which of the two lasers was used for the deposition of CTS. Due to the longer pulses leading to a lower laser intensity at a given fluence, the 248 nm laser afforded a somewhat wider fluence range for optimal Cu-content in the films.

- Droplets of up to micron size were found on the films of CZTS and CTS by both pulsed laser deposition and pulsed electron deposition. The number of droplets diminished when the fluence was reduced in PLD or when the accelerating voltage was reduced in PED. The change in laser wavelength from 355 nm to 248 nm in contrast had no impact on the number of droplets on the CTS films at a given fluence.

Dansk opsummering

Denne PhD-afhandling drejer sig om fremstilling af materialer til en ny type solceller: CZTS og CTS. CZTS står for kobber-zink-tinsulfid (Cu_2ZnSnS_4) mens CTS er kobbertinsulfid (Cu_2SnS_3). Bestanddelene kobber, zink, tin og svolvl er alle almindelige i jordens skorpe og er dermed velegnede til udvikling af en solcelleteknologi, som skal kunne udbredes vidt og bredt under omstillingen til vedvarende energi. CZTS minder om et andet solcellemateriale, kobber indium gallium selenid (CIGS), som er i kommerciel produktion, men som indeholder det sjældne og eftertragtede metal indium. På grund af svingende priser og stigende efterspørgsel på indium er der i løbet af de sidste ti-femten år kommet fokus på at finde et alternativt materiale. CZTS er dog endnu ikke lige så effektivt et solcellemateriale som CIGS: de bedste solceller af CIGS er over 20 % effektive mens de bedste CZTS solceller er knap 10 % effektive.

I mit arbejde har jeg benyttet en speciel teknologi, som min gruppe på DTU har mange års erfaring med, nemlig pulset laserdeponering. I denne metode bruger man en pulset laser med meget høj energi til at bestråle en pille af fast stof (et 'target'), som vaporiseres og danner en tynd film på en overflade inde i et vakuumkammer. På grund af den høje energi kan man danne krystalstukturer ved relativt lav temperatur og man har haft succes med metoden til at danne meget komplicerede materialer. Derfor kunne metoden også tænkes at være velegnet til CZTS og CTS.

Det viste sig, at det var svært at kontrollere sammensætningen af materialet med denne metode, da svolv og tinsulfid fordamper meget nemt. Vi har derfor arbejdet med forskellige strategier til at få den rette balance mellem elementerne i tyndfilmene. For eksempel kunne vi opnå den rette balance mellme kobber og tin ved at ændre laserenergien og/eller vinklen mellem den bestrålede pille og den fremvoksende film. Svovltab var dog et fortsat problem. Den bedste løsning til dato har været at bage filmene sammen med svovl efter deponeringen.

Nogle få andre grupper har arbejdet med samme teknik til CZTS før os, mens ingen andre har prøvet at lave CTS med denne teknik før. Vi har derfor kunnet komme med noget helt nyt. Efter vi fandt ud af, hvordan vi kunne styre laserdeponeringsprocessen, så vi fik det rigtige forhold mellem kobber og

tin i kobbertinsulfid, lykkedes det at bage filmene og fremstille kobbertinsulfid af høj kvalitet, som kunne blive karakteriseret optisk. Min kollega Andrea Crovetto fandt derefter sammen med nogle samarbejdspartnere ud af, at det såkaldt dobbelte båndgab, som vi så i materialet, kunne forklares teoretisk på grund af asymmetri i materialet, hvilket har bidraget til den grundlæggende viden om denne form af CTS, Cu_2SnS_3 i en monoklinisk krystalstruktur. At materialet har to båndgab betyder, at der er to energiniveauer, som kan optage lys, når man netop når op over de lave fotonenergier, hvor materialet er gennemsigtigt. Den teoretiske forklaring på fænomenet gør, at forskere nu kan føle sig mere sikre på, at de har lavet det rigtige materiale, når de ser to energiniveuaer i absorptionsspekret, fremfor at tro, at de er kommet til at lave to forskellige materialer, som er blandet sammen.

Vi har arbejdet med at fremstille både CZTS og CTS med to forskellige strategier: 1) via deponering af en tyndfilm med de rigtige bestanddele (kobber, tin, zink og svovl), som derefter bages sammen med svovl for at opnå den rigtige krystalstruktur til at indgå i en solcelle; 2) ved at deponere tyndfilmen direkte i den rigtige krystalstruktur. At deponere filmene direkte ved høj temperatur var i første omgang svært, fordi vi ikke havde lært, hvordan man kunne kontrollere svovltabet fra filmene. For at fremstille CTS-solceller benyttede vi derfor bagning af filmene, ligesom til de film, der blev benyttet til optisk karakterisering. Filmene til optisk karakterisering var i princippet samme materiale, som det, vi skulle bruge til solceller, men de var meget tynde, kun 100 nm, og behøvede heller ikke dække større samlede områder. Det viste sig, at når vi arbejdede med tykkere film til solceller (selve CTS-laget var stadig kun lidt over en mikrometer tykke), fik vi problemer med, at filmene løsnede sig fra underlaget, sandsynligvis fordi de udvidede sig, når de blev bagt. Vi har brugt meget tid på at optimere sammensætningen og tykkelsen (til under 700 nm) for at undgå, at CTS-lagene pillede af. Vores foreløbig bedste CTS-solceller udviste 0,3 % effektivitet, men disse var lavet af en meget tin-beriget film, som ovenikøbet havde huller fra fordampning af tinsulfid. Med vores forbedrede fremstillingsproces bør det i fremtiden være muligt at lave bedre solceller.

Strategi nummer 2, at deponere filmene direkte i den rigtige krystalstruktur uden at bage dem bagefter, arbejdede vi på i samarbejde med institutet IMEM-CNR i Parma i Italien. Her brugte vi en teknik, som er nært relateret til pulset laserdeponering, nemlig pulset elektrondeponering. I pulset elektrondeponering er den kraftige laser byttet ud med en kraftig elektronkanon, men ellers er princippet det samme. Da en elektronkanon er billigere end en pulset laser med høj energi, er pulset elektrondeponering en potentielt billigere metode end pulset laserdeponering - og måske en, som kan kommercialiseres. Dette gælder især, hvis man kan udnytte metodens potentiale til at fremstille de krystallinske solcellematerialer ved lav temperatur, således at de kan deponeres på sårbare

underlag såsom bøjeligt plast eller siliciumsolceller (sidstnævnte kunne være en mulighed til fremstilling af tandemsolceller med større effektivitet end de gængse siliciumsolceller, vi kan købe i dag).

Ved IMEM-CNR har man erfaring med at deponere effektive CIGS-solceller ved lav temperatur, og da meget af teknologien fra CIGS kan overføres til CZTS var det oplagt at forsøge at lære af deres erfaringer. Vi lavede derfor de første forsøg med at fremstille CZTS med deres metode. Igen viste det sig at være svært at kontrollere sammensætningen af materialet og vores bedste solcelle, som var 0,2 % effektiv, var kobberrig og svovlfattig. Det vil være en udfordring at balancere sammensætningen af alle fire komponenter i CZTS for at fremstille højkvalitetssolceller med CZTS, men det er ikke umuligt, da der er mange parametre at skrue på. Første skridt på vejen vil være at benytte en sammenpresset targetpille, som består af CZTS-pulver fremfor pulver af kobbersulfid, tinsulfid og zinksulfid.

Arbejdet var en del af CHALSOL-projektet, som er finansieret af Dansk Strategisk Forskningsråd i 2013-2016.

List of publications

Published journal articles

Ettlinger, R. B., Crovetto, A., Canulescu, S., Cazzaniga, A. C., Ravnkilde, L., Youngman, T. H., Schou, J. (2016). Formation of copper tin sulfide films by pulsed laser deposition at 248 and 355 nm. Applied Physics A, **122**(4), 1-10. DOI: 10.1007/s00339-016-9939-4

Crovetto, A., Chen, R., **Ettlinger, R. B.**, Cazzaniga, A. C., Schou, J., Persson, C., Hansen, O. (2016). *Dielectric function and double absorption onset of monoclinic Cu2SnS3: Origin of experimental features explained by first-principles calculations.* Solar Energy Materials & Solar Cells, **154**, 121-129. DOI: 10.1016/j.solmat.2016.04.028

Ettlinger, R. B., Cazzaniga, A. C., Canulescu, S., Pryds, N., Schou, J. (2015). *Pulsed laser deposition from ZnS and Cu2SnS3 multicomponent targets.* Applied Surface Science, **336**, 385-390. DOI: 10.1016/j.apsusc.2014.12.165

Crovetto, A., Cazzaniga, A. C., **Ettlinger, R. B.**, Schou, J., Hansen, O. (2015). *Optical properties and surface characterization of pulsed laser-deposited Cu2ZnSnS4 by spectroscopic ellipsometry.* Thin Solid Films, **582**, 203-207. DOI: 10.1016/j.tsf.2014.11.075

Cazzaniga, A. C., **Ettlinger, R. B.**, Canulescu, S., Schou, J., Pryds, N. (2014). *Nanosecond laser ablation and deposition of silver, copper, zinc and tin.* Applied Physics A, **117**, 89-92. DOI: 10.1007/s00339-013-8207-0

In preparation

Ettlinger, R. B., Pattini, F., Rampino, S., Bronzoni, M., Annoni, F., Crovetto, A., Bosco, E., Cazzaniga, A. C., Gilioli, E., Hansen, O., Schou, J., in prep. *Pulsed Electron vs. Pulsed Laser deposition for the growth of CZTS films*

Conference proceedings

Ettlinger, R. B., Crovetto, A., Bosco, E., Rasmussen, P., Hansen, O., Schou, J. 2014. *Pulsed laser deposition of Cu-Sn-S for thin film solar cells.* In proc: World Conference on Photovoltaic Energy Conversion 6 (WCPEC-6), Kyoto, Japan.

Cazzaniga, A. C., Crovetto, A., **Ettlinger, R. B.**, Canulescu, S., Hansen, O., Pryds, N., Schou, J. (2015). *ZnS top layer for enhancement of the crystallinity of CZTS absorber during the annealing.* In 2015 IEEE 42nd Photovoltaic Specialists Conference (PVSC). IEEE. DOI: 10.1109/PVSC.2015.7355905

Acknowledgments

Writing this acknowledgments section has made me very happy and grateful. So many people have been part of this PhD journey, helped me along the way, and have made all the difference in the last few years. Thank you so much!

Thank you to Jørgen, my main advisor, for your continued encouragement and for always setting aside time to discuss our project, whether the topic was the physics of PLD, a paper, a poster, or practical matters of the PhD. Thank you, Peter Uhd, my co-supervisor, for your patient physics explanations and support. And thank you, Stela, for your valuable advice on PLD, your input on papers and on this thesis, and your constant help with measurements and with getting things to work in the lab whenever we had trouble.

Thank you Andrea Cazzaniga, Sara Engberg and Andrea Crovetto for the great discussions and collaboration, it's been wonderful to work closely with all of you over the last three years and you have each helped me immensely. Besides, I would have never learned to make kombucha, tried cross fit, sung karaoke, or found out how amazing Kajak bar is without you all!

Thank you to all the guys in Parma who were so welcoming, generous and helpful during my stay at IMEM-CNR - especially Patto, Stefano, Matteo, and Edi. Also a big thank you to Fillippo, Marco, and Francesco for helping with CdS and XRD. I was really bowled over by the kindness and the positive atmosphere I experienced in your department.

For measurements and photos not made by myself, I've tried to acknowledge the photographer/measurement maker in the correct spots, but I've surely missed or misplaced some, so thank you emphatically once again. First of all I would like to acknowledge Andrea Crovetto, who has taken care of most of the steps related to solar cell fabrication from PLD-made CTS films from depositing the bottom Mo-layer to depositing all the layers on top of CTS. Andrea also carried out characterization from photoluminescence, IV-curve measurements, and EQE-measurements to ellipsometry and Raman spectroscopy. Thank you for always being helpful and full of inspiration! Thank you also to Stela for your help with Raman measurements and thank you to all the people who have helped with SEM and EDX measurements: Andrea Crovetto, Edoardo Bosco, Lasse Ravnkilde,

Tomas Youngman, Sara Engberg, Andrea Cazzaniga, and Li Han. Finally thank you to the people at the Department of Energy Conversion who trained us in SEM, EDX and XRD and helped whenever we needed it.

Thank you, Jørgen Stubager, for helping with the Dektak and all the odds and ends in the labs. Thank you, Søren Stentoft and Peter Jensen, for helping to make things work in the 355 nm PLD lab, and Yunzhong Chen and Simone Sanna for help in the 248 nm PLD lab. And thank you, Eugen Stamate, for making it possible to deposit the solar cell window layers and for your encouragement and advice.

Thank you my colleagues in the Fotonik department at Risø for making it nice to come all the way out north of Roskilde to work. I feel fortunate to have spent the last three years with you. A special thank you to Maria and Linda for always helping with practical matters great and small and for always being kind and positive.

Finally, a huge thank you to my mom, my sister and my friends. Mor og Abbe, tak for al støtten, altid, og for aftensmad og kage og kærlighed og ture ud til haven. Ayoe og Pernille, tusind tak for at I har været der for mig nu i over ti år med the, chokolade og gennemgange af livets små og store spørgsmål – og så kom I endda med til Italien! Ayoe, tak for din store støtte her til sidst med tabeller, korrekturlæsning og opmuntring. Thank you, Cat, for the coffees/teas, lunches and breakfasts, it's been so hyggeligt. Jesica, Sabrina, Ana, and Zeynep, thank you for all the hugs and encouragement, and Imke, Cristina and Judith, thank you for making me feel at home on my travels through Europe in the last few years.

Last but not least, thank you to my Mikoso, Andrés, who has been my constant support throughout the last three years and who is the best person I could imagine spending my life with.

Technical terms and abbreviations

absorber layer The layer in a solar cell where free charge carriers are generated by absorbtion of light. In a CZTS solar cell, this is the role of CZTS.

annealing Heat treatment of a material that causes its constituents to coalesce and form a crystalline structure.

AZO Aluminum-doped zinc oxide

buffer layer In a CZTS solar cell these are the CdS and i-ZnO layers. Their role is not completely clear and they may serve multiple functions, but they improve the overall efficiency. See Section 1.2.1.

CHALSOL "Chalcogenide solar cells of CZTS," the project that this work was part of, financed by the Danish Council for Strategic Research

co-evaporation A vacuum deposition technique, where materials are heated so that they evaporate and form a thin film on a substrate. The evaporation can be directed in a vacuum chamber where the evaporated particles do not collide very often, especially if one uses an evaporation source where the materials only escape in one direction.

CTS Copper tin sulfide, can refer either to Cu_2SnS_3 or to a copper tin sulfide compound of unknown stoichiometry as specified in the text.

CZTS Copper zinc tin sulfide, Cu_2ZnSnS_4

charge carriers The fundamental units of current. Electrical current arises from the movement of electrons in a particular direction. Charge carriers are electrons and electron vacancies (holes) and may be free (able to move and create a current) or bound (attracted to a particular area of the material).

doping Addition of a relatively small amount of impurity to a semiconductor to change the properties of the semiconductor

EDX Energy-dispersive X-ray spectroscopy. Used to determine material composition. See Section 5.6.4.

E_g Band gap energy, an important quantity for a semiconductor as it is the energy difference between the valence band and the conduction band. See Section 2.1.

EQE External quantum efficiency: The efficiency with which the solar cell converts light of different wavelengths into charge carriers that are collected by the contacts.

fluence Laser energy received by the target surface per unit area ($\mathrm{J\,cm^{-1}}$)

hole A type of charge carrier that is equivalent to an electron vacancy. A hole can move in a material as though it were an electron with negative mass and positive charge.

IMEM-CNR Istituto dei Materiali per l'Elettronica ed il Magnetismo - Consiglio Nazionale delle Richerche. The Institute for Materials for Electronics and Magnetism under the National Research Council of Italy

i-ZnO Intrinsic zinc oxide, i.e., undoped zinc oxide. Zinc Oxide is transparent to visible light while the main part of the window layer of CZTS solar cells is usually AZO, it apparently helps to deposit a thin layer of i-ZnO beneath it.

JV-curve (or IV curve) Current-voltage characterization curve for solar cells. See Section 2.1

J_{sc} Short-circuit current, characteristic of a solar cell. See Section 2.1

lattice site specific atom position within a crystal lattice

Mo/SLG Molybdenum-coated soda lime glass (usually used as the bottom layer of a CZTS solar cell with Mo forming the bottom contact).

PED Pulsed electron deposition

PL Photoluminescence

PLD Pulsed laser deposition

p-n junction Interface between a p-doped semiconductor and an n-doped semiconductor. See Section 2.1.

Raman spectroscopy Technique that identifies the characteristic phonon modes in a material and can help identify particular crystal structures. See Chapter 5.

RF sputtering Radio frequency sputtering: sputtering where an AC current is applied between the target and the substrate to reduce build-up of charge on an insulating target.

R_s Series resistance of a solar cell, must be low in an efficient solar cell

R_{sh} Shunt resistance of a solar cell, must be high in an efficient solar cell

secondary phase an unintended material that forms instead of, alongside or embedded within the primary material one is interested in, e.g., SnS forming alongside Cu_2SnS_3

SEM Scanning electron microscopy. See Chapter 5

SLG Soda lime glass

sputtering A deposition method that like in PLD takes place in a vacuum chamber where material from a solid target is transferred to a substrate. This happens by bombardment of the target by a plasma of Ar. The plasma is created by passing a strong current through the Ar in the chamber.

stoichiometric In this thesis, the term 'stoichiometric' is used to describe the desired composition of a material in terms of the ratios of the elemental constituents (e.g., Cu:Sn:S of 2:1:3 for stoichiometric Cu_2SnS_3 or Cu:Sn=2 for stoichiometric Cu_2ZnSnS_4).

stoichiometry The ratios of chemical components in a compound or a reaction.

V_{oc} Open circuit voltage, characteristic of a solar cell. See Section 2.1

XRD X-ray diffraction. See Chapter 5

Chapter 1

Introduction

The commercial thin film solar cells with the highest efficiency today are made of CdTe or CIGS: cadmium telluride or copper indium gallium diselenide. The former, CdTe, contains cadmium, which is toxic, and tellurium, which is a rare element in the crust of the Earth, while the latter, CIGS, also contains rare elements: indium, currently in high demand for mobile phone displays, and gallium and selenium, less rare but still not abundant enough for widespread global deployment of solar power generation at the terawatt scale.

CZTS and CTS are two alternative thin film solar cell absorber materials that contain only Earth-abundant elements: copper, zinc, tin and sulfur in CZTS (Cu_2ZnSnS_4); copper, tin and sulfur in CTS (Cu_2SnS_3). The aim of this thesis was to investigate whether the special technique we have available at the Technical University of Denmark, pulsed laser deposition, could help bring the development of these materials forward as part of the CHALSOL project (CHALcogenide SOLar cells of CZTS).

This introductory chapter will briefly explain the context for CZTS development in the solar cell market followed by a description of the state-of-the-art in CZTS and CTS solar cells and the broader perspectives for solar power and environmentally friendly materials in photovoltaics. Next, the methods of pulsed laser deposition and pulsed electron deposition are introduced. Finally this chapter will provide an overview of the aims and results of the work and the structure of the remainder of the thesis.

1.1 Why chalcogenide solar cells?

Chalcogens are the materials in column 16 of the periodic table, also known as group VI A: the elements O, S, Se and Te. Usually when researchers write about

chalcogenides, they mean compounds containing S, Se or Te, leaving oxides aside. That means that chalcogens include CIGS, CdTe and CZTS.

These materials are direct bandgap semiconductors, which means they are much more efficient absorbers of sunlight for the same material thickness than crystalline silicon, the most common solar cell material, which has an indirect bandgap. The amount of material needed to absorb most of the sunlight hitting a direct band-gap semiconductor is a tiny fraction of the amount needed for silicon. While crystalline silicon solar cells are not exactly thick - today they are only hundreds of µm thick - thin film solar cells need only about 1-2 µm of active material. At the same time CIGS, CdTe and CZTS are manufactured in different ways to traditional manufacture of silicon: they can be deposited directly onto the substrate, which may even be a cheap and/or somewhat bendy material, like steel or plastic. CIGS, CdTe and CZTS can also be made at far lower temperatures than conventional monocrystalline silicon, which when produced by the widely used Czochralski method requires a processing temperature of 1400 °C [1].

The majority of the world's solar panels today are made of crystalline Si, which have achieved over 26 % efficiency for monocrystalline Si [2] and more than 21 % for the cheaper polycrystalline variety [3]. CdTe and CIGS are already competitive with polycrystalline Si in efficiency [3] and CdTe is also competitive in price (see [4]), proving that there is a place for chalcogenide solar cells in the market. However, in a world aiming for zero-carbon energy sources, solar power needs to supply terawatts of peak electricity production capacity at the scale of 100s if not 1000s of TWh and on this scale the projected world production of Te or In will not be able to meet demand [5].

Earth-abundant minerals (i.e., CZTS rather than CIGS or CdTe) are important for thin film solar voltaics both in terms of price of the materials and in terms of the sheer amount of solar cells that can practically be deployed given the amount of each element that it will be possible to extract. The price in 2010 versus estimated abundance in the Earth's crust is shown for a number of elements in Figure 1.1. We see that the materials for CZTS are generally in greater supply and far cheaper than those for CdTe or CIGS solar cells. A third technology for thin film solar cells, amorphous Si, has no such problems with abundance but has struggled to deliver efficient solar cells, with about 10-12 % maximum.

Figure 1.1 does not include the additional technological risk factor of price volatility: According to the US Geological Survey's mineral database, the inflation-corrected price of In quadrupled from 2003 to 2005 as demand rose for LCDs, which contain In (and perhaps also from stockpiling as the prices rose) [9]. The prices since fell by half around 2009-2010, but the volatility of the price and the limits to the absolute availability of In (as well as Te in CdTe solar cells) were perhaps the most important reasons why so much research in the more earth-abundant CZTS absorber took off in the following years.

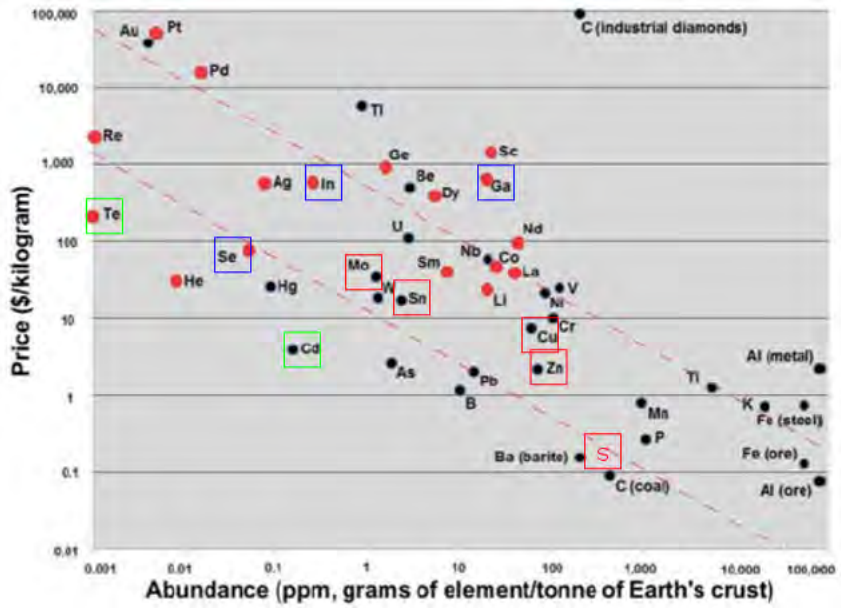

Figure 1.1: Price versus earth-abundance of selected elements as presented by Jaffe et al. [6] (Copyright 2011 by the American Physical Society). Red dots: Elements deemed critical for the United States energy supply by Jaffe et al. Boxes highlight the critical elements used for CZTS solar cells (red boxes), CIGS (blue boxes) and CdTe (green boxes). Note that both CIGS and CZTS solar cells require Mo and also often small amounts of Cd for the buffer layer. S was not included in the original map; its location has been estimated based on the 2011-2012 prices [7] and its earth abundance as reported by the US Geological Survey [8]. Si is off the scale with an abundance greater than Al as it is the second-most common element in the Earth's crust after oxygen. The price of photovoltaic-grade Si has decreased in the last few years and the spot price in November 2016 is about 15 USD/kg (seen, e.g., on pvinsights.com).

1.2 State-of-the-art CZTS and CTS solar cells

This year a record active area efficiency for CZTS solar cells of 9.4 % was published by researchers at Toyota Central R&D labs [10], surpassing a record of 8.8 % published by the same group last year [11] (an active area efficiency excludes the area of the solar cell shaded by non-transparent electrical contacts). These records were for pure sulfide CZTS solar cells, which have proven even more challenging to researchers than their selenide and sulfoselenide sister materials CZTSe and CZTSSe. Selenide CZTSe forms the same crystal structure as CZTS with slightly larger lattice parameters (about 5 % bigger) and with a lower bandgap. In CZTSSe only part of the sulfur in CZTS is substituted by Se. The bandgap is about 1 eV for CZTSe versus 1.5 eV for CZTS with the sulfoselenides having tunable bandgaps in between depending on the selenium content. The record efficiency for all three materials belongs to CZTSSe with 12.6 % efficiency [12], presented in 2014 by the same research group at IBM that also held the previous record for sulfide CZTS at 8.4 % [13].

The record CZTS solar cell efficiencies were achieved by vacuum techniques: the researchers at Toyota use sputter deposition to form the precursor layers followed by annealing in an H_2S/N_2 atmosphere [10], while at IBM, researchers used co-evaporation of the precursor layer followed by annealing with S on a hot plate [13, 14]. Surprisingly, the CZTSSe record solar cell was achieved by a solution-based method, even though solution processing is generally expected to allow less material control than vacuum techniques. The IBM researchers used a hydrazine-based solution, warning their readers at the start of their experimental section that hydrazine (N_2H_4) is highly toxic and flammable. Thus the CZTSSe record solar cell was achieved with a toxic solution while the CZTS record solar cell was achieved with annealing in toxic H_2S gas, leaving some challenges ahead for this environmentally friendly solar cell.

For CTS, which is one element simpler but structurally more complicated than CZTS, the record efficiency is 4.6 % achieved by university researchers in Japan [15]. Similar to the best CZTS solar cells, these films were made by vacuum processing, in this case with sequential evaporation of a stacked metallic precursor followed by annealing in a S/SnS atmosphere. Runners up in efficiency have also been made by Japanese groups using a variety of vacuum techniques: Kanai et al. [16] reached 4.3 % efficiency by co-evaporation of CTS followed by annealing with S, while Aihara et al. [17] reached 2.9 % efficiency a few years earlier using electron beam evaporation. Adding one more element to the mixture, germanium, to make CTGS ($Cu_2Sn_{1-x}Ge_xS_3$ solar cells, researchers at Toyota reached 6 % efficiency in 2013 also with a vacuum technique (co-sputtering of Cu-Sn layers followed by sulfurization in S and GeS_2 vapor) [18].

Research on CZTS solar cells started in earnest in the Katagiri group in the

late 1990s at Nagaoka University of Technology following the first CZTS solar cell developed by Ito and Nakazawa in 1988 [19]. Around 2006-2007 when CIS and CIGS technology was being commercialized, the Katagiri group reached 6-7 % conversion efficiency and CZTS research took off in other groups around the world. In 2013/2014, when we started our work, solar cell conference seminars on CIGS and CZTS attracted hundreds of people. Today perovskite research has captured some of the hype and CZTS research attention has leveled off for the time being.

1.2.1 The architecture of a CZTS solar cell

A conceptual CZTS solar cell is shown in Figure 1.2. The CZTS layer is known as the absorber layer as this is where the sunlight is absorbed. Most CZTS solar cells are made with the architecture (i.e., the types of layers) shown in this figure, although this is no natural law, and many other designs could be conceived of and some others have been tried. This architecture is borrowed from CIGS solar cells, which have been very successful and which have a similar structure to CZTS, although the energy bandgap of CZTS is not exactly the same as for CIGS, which may be causing some problems for advanced CZTS devices (the concept of bandgaps is introduced in Section 2.1). The architecture shown in Fig. 1.2 is the one used in our project as we were starting from scratch and needed to compare our CZTS layers to the status quo in our research field.

Apart from CZTS, the other layers seen in Figure 1.2 are the front and back electrical contacts, the *buffer layer*, the n-type window layer and the substrate (a substrate is the underlying layer that the solar cell is built on). The concepts of p- and n-type layers (labeled in the figure) will be explained in Section 2.1. For now we focus on which materials are involved.

Starting from the bottom, the substrate is **soda-lime glass**, which is important because the **Na** in soda lime glass diffuses into the CZTS layer when it is heat-treated and improves the efficiency of the solar cell. If soda lime glass is replaced by another material such as plastic or steel or if the heat treatment is not hot enough to induce Na diffusion, Na must be added to the CZTS layer in another way [20]. The next layer is the **Mo** back contact, a metal which is usually sputter-deposited onto the glass in two steps, the first to ensure good adhesion and the second to ensure low resistivity in order to improve current collection [21]. A $\mathbf{MoS_2}$ layer usually forms on top of the Mo layer during the heat treatment of the subsequent p-type CZTS absorber layer. The **CZTS** layer is deposited in a variety of ways (Section 2.2.2) and is usually annealed at 550 °C-570 °C afterwards to ensure good crystallinity. A buffer layer, usually **CdS**, is deposited next by chemical bath deposition. This layer provides the first of the n-layers of the solar cell so that the interface between the CdS layer and the CZTS layer

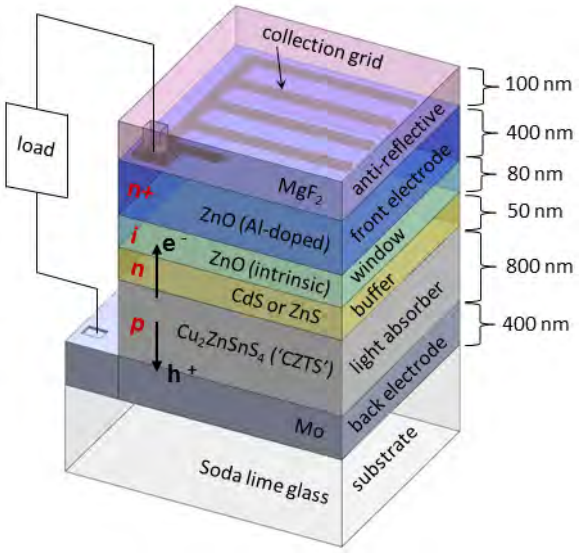

Figure 1.2: Conceptual CZTS solar cell architecture (illustration by A. Crovetto). The layers are described in the text. Briefly, Mo is the back contact and CZTS (or CIGS or CTS) is formed on top to absorb sunlight and generate charge carriers (free electrons). CdS and intrinsic ZnO form so-called buffer layers that help carry the electrons to the transparent conductive layer of Al-doped ZnO before they are swept away into the Al fingers that form the front contact. An antireflective MgF_2 layer may be used on top. e- stands for electrons and h+ stands for holes. Holes, n-layers, and p-layers will be introduced properly in Section 2.1.

forms the heart of the p-n junction that is the essence of a solar cell (Section 2.1. In addition, the CdS layer protects the CZTS layer from damage during the sputtering deposition of the subsequent layers. The next layer, a very thin region of **undoped ZnO** (intrinsic ZnO or i-ZnO), is also a buffer layer, which may improve the conductivity of the top n-layer, a transparent conducting oxide. This is often **AZO** (Al-doped ZnO) but may also be other materials such as ITO (indium tin oxide) or GZO (Ga-doped ZnO as used by the CZTS record holders, Tajima et al. [10]). Finally, in high-efficiency cells a $\mathbf{MgF_2}$ anti-reflective layer is sometimes applied and the full structure is topped off with thin, narrow metallic top electrodes, usually electron-beam evaporated **Al**. Since the top metallic contacts shade part of the solar cell, it is important that they take up as little room as possible. Because record solar cells are often very small (less than 0.5

cm^2 is routine), the top contacts can take up a relatively large amount of space, so record solar cell efficiencies are often reported for the active area of the solar cell only.

The best CTS solar cells described above also use the CIGS solar cell architecture, again because of a similar crystal structure and energy band levels, allowing researchers to focus on one innovation step at a time.

Apart from the CZTS layer itself, research on CZTS solar cells has also focused on the buffer layer, with some groups trying to find alternative buffer layers with similar or better band alignment such as In_2S_3 that would eliminate the toxic heavy metal Cd from these otherwise environmentally friendly solar cells [22].

1.3 Solar cells in a broader context

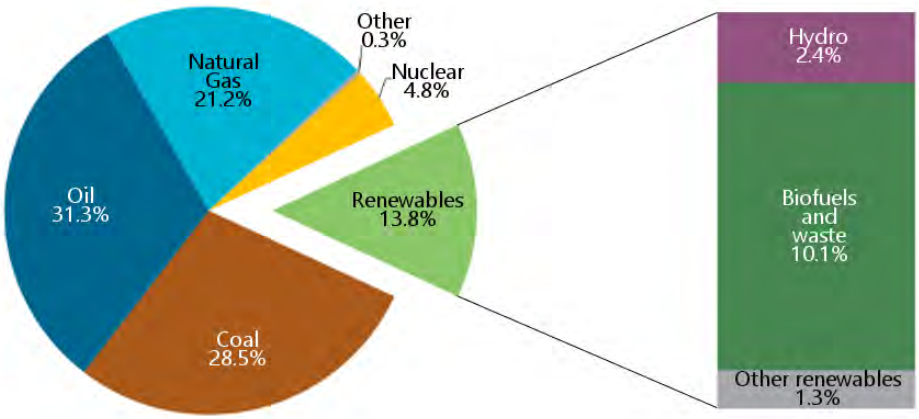

Figure 1.3: The amount of renewable energy as a fraction of total global primary energy supply in 2014 according to the IEA. "Other[1]" includes non-renewable waste, peat, oil shale and chemical heat while "Other renewables" includes solar, wind, geothermal, and tidal energy. Solar together with tidal energy makes up less than 1/3 of the 'other renewables'. Reprinted from IEA's Key Renewables Trends [23] ©OECD/IEA 2016 Except from: Renewables information, IEA statistics. Licence: `www.iea.org/t&c`.

A few graphs help put solar power into perspective. Figure 1.3 shows that renewable energy other than hydropower and biomass supplied less than 1.3 %

of the world's total primary energy in 2014. The IEA report that the figure comes from goes on to show that solar power together with tidal power makes up only 2.4 % of the total renewable energy supply - or about 0.34 % of the world's primary energy supply [23]. Here solar includes both solar photovoltaics (i.e., solar electricity generation) and solar thermal power such as solar water heaters. So there is a long way to go before the world is powered entirely by solar power - or even entirely by renewables.

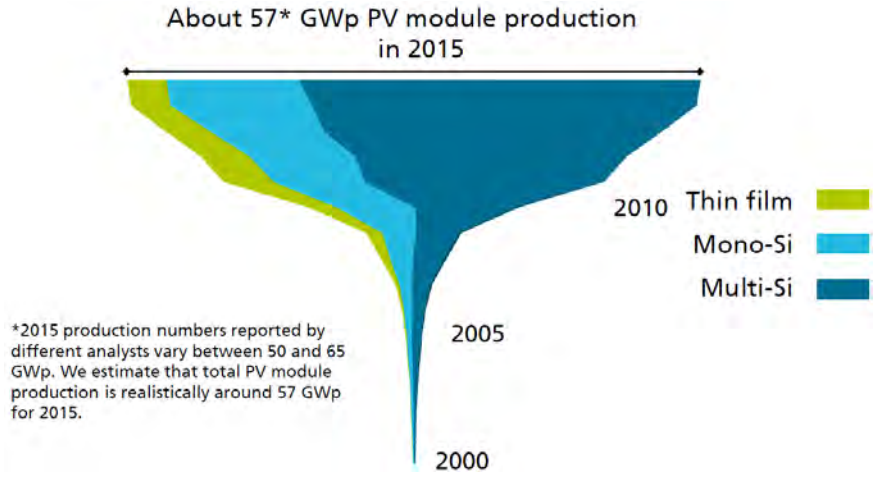

Figure 1.4: Global growth of photovoltaics since 2000 detailing the market share of thin film solar cells. GWp: Gigawatt peak production. Illustration from the Fraunhofer Institute for Solar Energy Systems Photovoltaics Report 2016, slide 18 [24].

Figure 1.3 shows the state of the world's power generation in 2014 and is already outdated because solar power installation is growing tremendously at the moment. The IEA states that all renewables have been growing at an average rate of 2.2 % per year between 1990 and 2014, slightly higher than the growth of the total energy supply at 1.9 % annually [23]. In recent years, the relative difference in the growth rate of renewables and traditional energy sources has probably widened. Certainly solar electricity is growing exponentially at the moment. Figure 1.4 shows the increasing deployment of solar photovoltaics divided among different types of solar cells, making it clear how silicon dominates the market. Of the thin film solar cell market, the share of CIGS technology is about 25 % and CdTe accounts for more than half [24].

1.3.1 Life cycle analysis of CZTS solar cells

The assertion that the CO_2-emissions from the production of a solar panel is so high that one might as well use fossil fuels is a myth. It takes energy and resources to make a solar panel, but the electricity generated by that solar panel results on average in less than a percent of the greenhouse gas emissions associated with an equivalent electricity production from fossil fuels [25, 26]. Also in terms of other pollutants and the question of land use, solar panels are more environmentally friendly than the fossil fuel alternatives. Fthenakis [25] argues that even CdTe solar panels emit orders of magnitude less Cd per GWh than coal. In terms of land use, Fthenakis and Kim have shown that Si-based solar power and coal mining are comparable in area requirement per GWh [26].

Nevertheless it is important to think about the lifecycle of a new material as part of its development. Do CIGS, CdTe and CZTS solar cells pollute more or less than Si panels? Can they be recycled? For CdTe solar panels a recycling pathway has been developed, though ensuring that all the panels will be collected for recycling at the end of their 20-30 year lifespan will be a challenge. For CIGS no recycling pathway has yet been developed, though one could probably be developed if In becomes valuable enough. Anctil and Fthenakis argue that the rareness of Te in CdTe and In in CIGS is an advantage from a life cycle perspective because these materials are valuable enough that recycling is economically feasible. With regard to CZTS, these authors suggest that the relatively low value and volume of materials in CZTS and CZTSSe may mean that these materials end up in landfill at the end of their life [27]. On the other hand, if it becomes possible to eliminate Cd from the CZTS solar cells, landfilling of these solar panels would be less of a problem than disposal of CdTe.

So far only a few studies have been published on the life cycle impacts of CZTS. Collier et al. looked at the greenhouse gas emissions, primary energy demand, ecotoxicity potential and freshwater use for the production of CZTS in comparison to CIGS, CdTe, and Zn_3P_2, another potential solar cell material [28]. Assuming that sputter deposition would be used in commercial CZTS production just as it is for CIGS, they predict a similar impact on energy use, greenhouse gas emissions and water use from the two materials, whereas the ecotoxicity potential of CIGS is far higher because of the Ga content (Ga can suppress the immune system and interfere with the uptake of iron, though its toxic and medical effects are not fully understood [29]).

Many different frameworks and methodologies have been developed for carrying out life cycle analyses. It is extremely important to define the limits of the system one examines, as there are any number of derived effects one may look at including:

- material extraction including land use, social impacts, and pollution

- material abundance and competing uses
- material and processing toxicity to humans and to the environment during manufacture and use
- energy requirement (measured in myriad ways and including any number of steps in the chain from material extraction to solar panel mounting)
- durability
- land use change and perhaps indirect land use change if for instance a solar cell farm displaces farmland that in turn displaces a forest
- job creation
- upfront investment requirement and total lifetime costs
- options for recycling / cradle-to-cradle

Addressing the worry that some of the raw materials may be wasted at the end of the CZTS solar panel lifetime, it is worthwhile to put the amounts into perspective. The Cu and Zn needed for CZTS solar cells to cover an area large enough to supply half of Denmark's annual electricity use is smaller than the amounts of Cu and Zn added every year to pig feed and mostly subsequently spread in manure on Danish fields. According to ing.dk, a Danish engineering news site, about 300 metric tons of Cu and 1300 metric tons of Zn are used to prevent diarrhoea in suckling pigs every year in Denmark [30]. For comparison, a quick back-of-the-envelope calculation says that assuming 10 % efficient future CZTS solar panels, one could deliver 15 TWh electricity with about 15 GW installed power, which would cover about 150 km^2 and use about 700 t CZTS. Of this about 1/3 by weight is Cu and 1/6 is Zn. (This order-of-magnitude estimate for CZTS does not take into account any need for power storage associated with such a large deployment of solar power. The annual Danish electricity consumption is about 33 TWh according to energinet.dk, the Danish power distribution company).

1.4 The deposition techniques used in this work

In this thesis, pulsed laser deposition (PLD) and pulsed electron deposition (PED) were used to deposit thin films of CTS and CZTS both for solar cells and for gaining a better understanding of the materials and the methods themselves. The two techniques will be discussed in detail in Chapter 3. Both are vacuum deposition methods in which thin films (nm to µm thickness) are grown from high-energy particles for various applications in solid state research. They have

two potentially important advantages for producing CZTS and related materials with a complicated composition:

- the species landing on the thin film have a high amount of kinetic energy, enabling them to form a crystalline lattice at a lower substrate temperature than would be the case under equilibrium conditions, e.g., by evaporation.
- under the right circumstances, the stoichiometry of a bulk target containing atoms of several elements can be preserved in the growing thin film.

The crucial importance of *the right circumstances* for stoichiometric transfer will be discussed further in Section 3.2. The premise of this project was that PLD could potentially have an advantage for fundamental material studies by enabling the deposition of high-quality crystalline films. Additionally, working with PLD and PED was exciting because of the possibility of exploring a one-step method for depositing CZTS which would not require a separate high-temperature annealing step ($> 500\,^{\circ}\mathrm{C}$).

The majority of the work in this thesis (on metals, ZnS, CTS and CZTS) was carried out by PLD at Risø campus in Denmark, while comparative work on CZTS by PED was carried out at IMEM-CNR in Parma, Italy.

1.5 Research aims

This thesis was part of the CHALSOL project at the Technical University of Denmark in collaboration with the Ernst-Ruska Centre in Jülich, Germany, the Nanyang Technological University's School of Materials Science and Engineering and the Danish company Solcell Aps. We were four PhD students working in parallel: Andrea Cazzaniga and myself working with pulsed laser deposition of CZTS and related materials, Sara Engberg synthesizing nanoparticles of CZTS in a solution-based process, and Andrea Crovetto, who worked with all the other layers of a CZTS solar cell and helped us all with characterization. Andrea Cazzaniga, Sara and I worked at the Department of Photonics Engineering in Risø near Roskilde, Denmark together with Jørgen Schou and Stela Canulescu, while Andrea Crovetto worked at the Department of Nanoscience in Lyngby with Ole Hansen as his main supervisor.

The original aims of my part of the project were

- To deposit single-phase copper tin sulfide (CTS) and zinc sulfide (ZnS) by pulsed laser deposition
- To learn about the properties of these materials in relation to pulsed laser deposition of copper zinc tin sulfide (CZTS)

- To evaluate whether THz spectroscopy could be used for secondary phase identification in CZTS
- To use THz spectroscopy to understand the charge carrier dynamics of CZTS

Along the way the goals gradually changed as we found that it was a challenge to make phase pure materials for THz spectroscopy - especially ZnS. We also decided that THz spectroscopy had too large a spot size to be able to finely pinpoint the location of secondary phases and within the first 1.5 years other research groups published results of THz spectroscopy probing the carrier dynamics of CZTS and CTS. Meanwhile we realized that CTS can be used as a solar cell material in its own right and decided to investigate this. We also met researchers from IMEM-CNR in Parma who were successfully making as-deposited low-temperature CIGS solar cells by a method very similar to our own, namely pulsed electron deposition. Gradually new goals were added to the project:

- To make solar cells from the CTS films we deposited
- To deposit CZTS by pulsed electron deposition and compare it to pulsed laser deposition
- To evaluate whether it will be possible to make as-deposited low-temperature CZTS solar cells by PED

1.5.1 Milestones achieved

The main results of this 3-year PhD project were:

- We deposited CTS by PLD for the first time
- We were able to make phase-pure monoclinic CTS thin films that were characterized with ellipsometry measurements by Andrea Crovetto. In collaboration with two theoretical researchers in Stockholm, Rongzhen Chen and Clas Persson, Andrea identified a possible physical origin of the double absorption onset of this material, which both we and other groups had detected.
- We compared PLD with a 248 nm and a 355 nm laser for CTS deposition and found that both could be tuned to give the right proportion of Cu to Sn in the films for solar cells
- We found that droplets in the films could be reduced by reducing the fluence but that they were not affected by which laser we used.

- We deposited CZTS by PED for the first time
- We found that PED of CZTS also did not result in stoichiometric material transfer but the composition could be tuned by altering the deposition voltage and pressure
- I deposited CZTS by PLD at 300 °C confirming some of Andrea Cazzaniga's work and the work of other groups
- We compared the deposition of CZTS by PED and PLD and CTS by PLD and found that in all cases SnS from the multicomponent targets was preferentially evaporated at low laser or electron beam intensity while the films became more Cu-rich at higher intensity.
- We made the first preliminary as-deposited low-temperature processed CZTS solar cells by PED.

1.6 Structure of the thesis

The rest of this thesis comprises 8 chapters. The first three are background chapters: Chapter 2 covers solar cells of CZTS and CTS as well as their secondary phases while Chapter 3 describes the physics of the PLD and PED techniques and Chapter 4 reviews the literature on PLD of CZTS and other chalcogenide materials. After this, four chapters describe the experimental work done in this thesis: Methods and materials are covered in Chapter 5 and the experimental results are described in Chapter 6 on PLD of metals and ZnS, Chapter 7 on PLD of CTS, and Chapter 8 on PLD and PED of CZTS. The results chapters are ordered chronologically and become more complex as the thesis work progressed. Finally Chapter 9 summarizes the results and provides conclusions and perspectives.

Chapter 2

CZTS and CTS solar cells

This chapter will introduce the basic principles of a solar cell followed by an introduction to CZTS solar cells and to the secondary phases found in CZTS with a special emphasis on CTS and ZnS, two materials that have been a focus in this study because they have proved challenging to distinguish from CZTS by X-ray diffraction (XRD) or Raman spectroscopy. As CTS can be used in solar cells, we review work on making CTS solar cells as well. Finally we will briefly look at other secondary phases associated with CZTS.

2.1 Semiconductors and solar cells

The following section is based on Green's book, "Solar cells - Operating Principles, Technology and System Applications" [31] as well as the online resource "pv-education.org" by Honsberg and Bowden [32].

Solar cells are made from semiconductors, which as the name implies are materials that are neither very good nor very bad electrical conductors. Whereas most metals can conduct electricity and most insulators such as plastics cannot, semiconductors conduct electricity when they receive the right amount of energy. They are defined by their *bandgap energy*: in the ground state, all the electrons are bound to atoms and no net current can move through the device, but when some of the electrons absorb enough energy and get excited to energy levels above the bandgap they are able to move freely and conduct electricity. In the ground state the most energetic electrons are found in the *valence band*, which is full. Above the valence band, there is a forbidden region of energy states that cannot be occupied by the electrons (the energy gap) until they reach the *conduction band*. If enough energy is added to the material, some electrons can pass into the conduction band. Then, because of the symmetry of the semiconductor crystalline structure, they can move from atom to atom in the material. If an electric

field is applied to the material, the electrons will tend to move in the direction opposite the field and a net current will be generated.

In order for a solar cell to generate electricity, it therefore needs to fulfill two conditions: 1) it must include a semiconductor with a bandgap energy that matches the energy of the photons in the solar spectrum such that the photons can excite carriers to the conduction band, and 2) it must be asymmetric so that an electric field arises that coerces the electrons to move in a particular direction, generating an electric current. This asymmetry is accomplished with a so-called p-n junction. In a p-n junction, two different semiconductor materials share a common interface. On the n-side, there are impurities called *donor atoms* that tend to release free electrons to the material, while on the p-side, *acceptor atoms* tend to capture an electron from neighboring atoms, creating a mobile electron vacancy or *hole*. The free electrons and the freely moving electron vacancies (holes) are collectively known as *charge carriers*. While most of us are familiar with the concept of electrical current associated with moving electrons, the concept of positive charge carriers, i.e., holes, can be a strange idea at first. It is very useful, however, and is taken for granted by materials scientists.

At the point where the p- and n-type materials meet, some free electrons will diffuse from the n-side to the p-side and some holes will diffuse from the p-side to the n-side. See Fig. 2.1. The carriers that cross the junction leave behind fixed donor and acceptor sites in the crystal lattice which have a charge. This means that the junction consists of a positively charged region next to a negatively charged region, which creates an electric field pointing from the n-side to the p-side. The electric field, which is always accompanied by a change in the electric potential (a drop in the voltage), moves the free carriers away from the charged region, creating a *depletion region*. On the p-side of the material, the depletion region has negative charge called *space charge*, while on the n-side there is positive space charge. A larger depletion region creates a larger built-in field, which is good for the solar cell efficiency. Ideally, the depletion region of a solar cell should be almost as wide as the absorber layer itself so that the charge carriers generated by the light will immediately be swept to the correct contact.

CZTS is intrinsically a p-type semiconductor because the type of defect in the crystal lattice that is most likely to occur (substitution of Cu on the sites where there should be Zn atoms) is acceptor-type. When it absorbs sunlight, extra electrons from the valence band are excited to the conduction band. The electrons are attracted to the positively charged region on the n-side of the junction and if a circuit is provided for them to move into, a net current can be generated, the *short circuit current,* J_{sc} (the current by definition is the movement of positive charges - holes - from a high potential to a lower potential, while the net electron movement is opposite to the direction of the current - so in a solar cell under illumination the electrons move to the n-side and the current moves to the p-side). This is

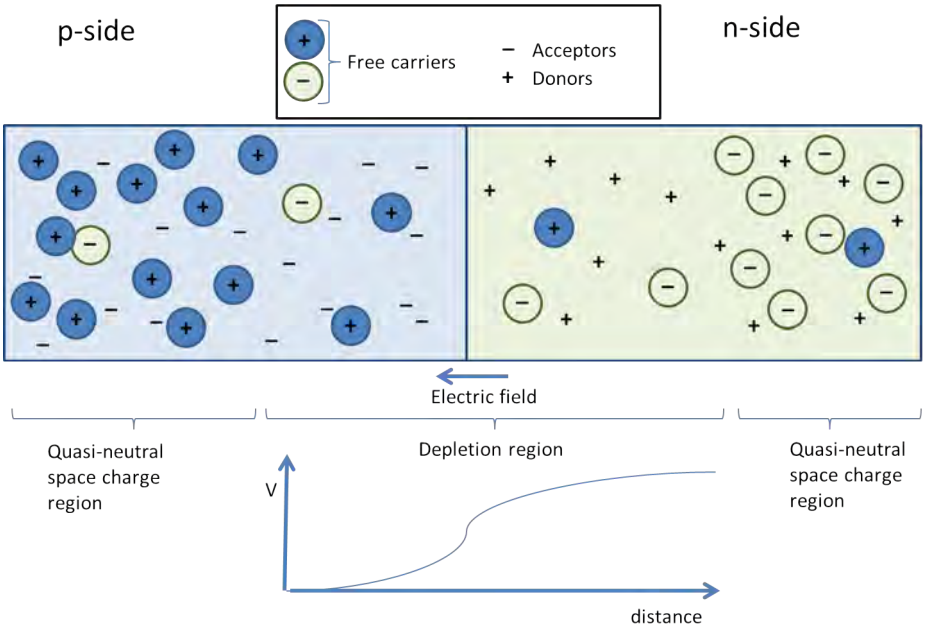

Figure 2.1: Conceptual illustration of a p-n junction showing the formation of a depletion region by diffusion of holes from the p-side and electrons from the n-side. The diffusion leaves excess bound charge on the donor and acceptor sites on each side, causing a net negative charge on the p-side from the acceptors and net positive charge on the n-side from the donors. This in turn creates an electric field and a voltage drop, which sweeps free charge carriers quickly out of the region. This is easier to visualize if one remembers that the amount of donors or acceptors far, far outnumber the number of minority carriers in each type of material (this is hard to draw).

illustrated in Figure 2.2a. If there is no circuit, a different equilibrium state will occur where excess electrons are constantly generated on the p-side (when using a p-type light absorbing layer), creating a voltage called the *open circuit voltage,* V_{oc}. This voltage is opposed to the original built-in voltage of the junction in the dark. See Figure 2.2b.

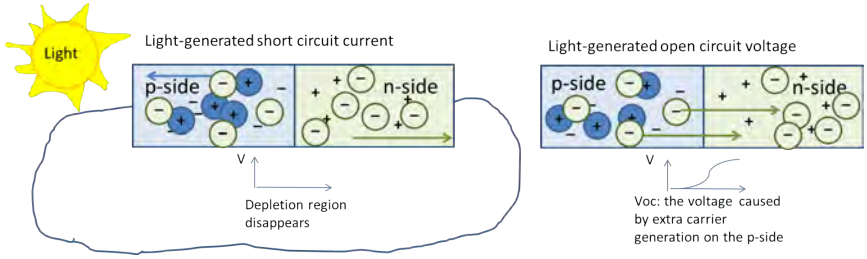

(a) Short-circuit current (b) Open circuit voltage

Figure 2.2: Conceptual illustration of the illuminated p-n junction. (a): a short-circuited solar cell where the electrons generated by the light absorbed in the p-layer move freely to the n-layer and around the circuit, generating a current. The potential drop is zero and the depletion region disappears. (b): a solar cell with no circuit connected. The continually generated charge carriers have nowhere to go and build up an open-circuit voltage.

One can probe the characteristics of the solar cell by applying positive and negative voltage to it (*forward* and *reverse* bias) to see how good it is at ensuring only one-way current flow (the diode characteristics). The forward bias opposes the built-in potential, helping current to flow through the junction, while the reverse bias increases the built-in potential. The characterization is done both under illumination and in the dark. Under illumination at zero voltage, the short-circuit current will be detected. The more reverse bias is applied, the less current will flow. Eventually the open-circuit voltage can be identified as the voltage that exactly stops the flow of current. The resulting curves of current versus applied voltage (*IV or JV-curves*) can be fitted by the diode equation (see Green's book [31]).

If the absorber material of the solar cell does not efficiently absorb sunlight, the amount of charge carriers generated will be low and the solar cell efficiency will also be low. But the opposite - a very high amount of excited charge carriers - is also not a good thing. This gives degeneracy: the empty states in the conduction band become filled and as a consequence the average carrier lifetime decreases because the likelihood of recombination of a conduction band electron with a hole in the valence band increases per carrier. The overall effect is that photons are wasted creating carriers that do not generate a net current.

The V_{oc} is directly related to the magnitude of the bandgap: a high bandgap energy gives a high potential energy to the charge carriers. The maximum amount of current that can be collected from the solar cell - the J_{sc} - depends on how many photons are available for absorption above the bandgap energy in the solar spectrum. Therefore the bandgap can neither be too high or too low. If it is too high, few photons have enough energy to generate free carriers. If it is too low, many carriers will be generated but they will have very little energy and the voltage will be low. The bandgap of CZTS of about 1.5 eV is close to the optimum bandgap for solar cells because it provides the best trade-off between a high voltage and a high current. The Shockley-Queisser limit allows one to formally calculate the potential solar cell efficiency of a material based only on its bandgap energy and the amount of photons in sunlight at different wavelengths. The potential efficiency of CZTS material is over 30 % based on the theoretical Shockley-Queisser limit without taking into account losses from reflection or shading of the solar cell by the electrical contacts [33].

Realizing the full potential for high voltage and high current for CZTS is another story - for that to happen the carriers need to be collected at the contacts successfully. This is a complicated matter where both the quality of the CZTS layer and all the other layers in the solar cell play important roles. As seen in Section 1.2.1, in real CZTS solar cells there is not just one n-layer, but rather three, which play different roles not all of which are well understood as discussed in the PhD thesis of my colleague A. Crovetto [21]. The rest of this chapter, however, will focus on the quality of the p-type absorber materials CZTS and CTS as well as several materials closely related to them, as this was the topic of my own work.

For a CZTS or CTS layer to result in an efficient solar cell, we would expect that large, defect-free, uniform crystal grains give the best solar cell efficiencies: whenever there are defects in the crystal structure, there can be fluctuations in the allowed energy states in the material, which can both reduce the effective bandgap (and V_{oc}) and trap the charge carriers, giving them a chance to recombine before they reach the contacts. *Secondary phases* (unintended crystal structures which have a different composition from the surrounding material) can have different effects depending on the resistivity and bandgap of the material. Some might block charge carriers because they have a very high bandgap energy, so the charge carriers usually do not have enough energy to make it to the conduction band, causing high series resistance in the cell. Other secondary phases may do the opposite: provide a shunt path allowing holes and electrons to recombine without generating any current in the external circuit.

2.2 CZTS: material properties and solar cell processing

CZTS, Cu_2ZnSnS_4, crystallizes in the kesterite and the stannite structures, which are both tetragonal forms, as well as the usually less favorable wurtzite (hexagonal) structure [34]. The kesterite and stannite states are very similar, differing only in the ordering of the Cu and Zn anions, as shown in Figure 2.3. The figure shows how similar the CZTS, CIGS, and ZnS structures are and also that the CIGS structure is somewhat simpler than CZTS and therefore perhaps more tolerant of differences in composition since the In and Ga atoms randomly share the same sites in the crystal lattice. In contrast, the CZTS kesterite and stannite structures allow no random lattice points. The kesterite structure has been predicted theoretically to be more thermodynamically stable than the stannite phase but the difference between the structures in potential energy is very small (about 3 meV/atom) [34]. Several groups have recently observed that the kesterite structure assumed in CZTS is actually disordered and forms a kind of intermediate structure between stannite and kesterite (still belonging to the same space group as kesterite) when enough thermal energy is present [35, 36, 34]. The change consists only in random exchanges in the lattice sites of Cu and Zn in some of the (001) planes, which happens easily partly because of the similar size of these atoms [37]. (The term '(001) planes' refers to the Miller indices of the crystal planes, which are introduced in many solid state physics texts).

Many authors have described the complicated phase diagram of CZTS and the numerous secondary phases that may form when one deviates from the ideal structure (see for example [37, 38, 39]). Two instructive variants of the pseudoternary phase diagram of CZTS are reproduced in Figure 2.4. We see that the stability region of CZTS is very narrow. In Zn-rich films, ZnS will form as a secondary phase, while in Cu-rich, Zn-poor films, Cu_2SnS_3 and Cu_xS will be expected and in the Sn-rich region, we will see SnS_y. Additionally, Olekseyuk et al. found the phase $Cu_2ZnSn_3S_8$ in Sn-rich, Cu-poor films in a fundamental materials study at $\approx 400\,^{\circ}C$ [40], but this phase has to our knowledge not been reported by others and Berg et al. question whether it occurs under normal annealing conditions [39]. It could be that excess Sn is instead lost through the evaporation of SnS as reported by Du et al. [38]. Note that the pseudoternary phase diagram assumes that the S cation content always balances the anion content to match CuS_2, ZnS, and SnS_2. Later in this study when we encounter Sn-rich CZTS, we find that it coexists with SnS or Sn_2S_3, meaning that S-loss must have occurred and we are no longer located in the ternary plane of the full quarternary CZTS phase diagram shown in Fig. 2.4.

Much research is still investigating what happens to the CZTS lattice and material properties when the stoichiometry is changed. There is no full agreement that the CZTS single-phase region is as narrow as that shown in Fig. 2.4.

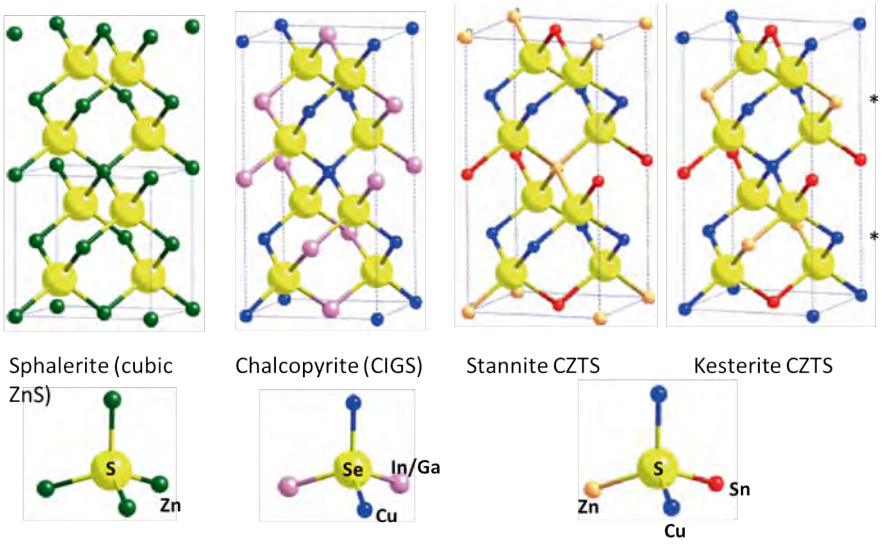

Figure 2.3: The crystal structure of sphalerite (cubic-phase ZnS), chalcopyrite (CIGS), and stannite and kesterite CZTS along with the basic structural motifs (bottom panel) that are repeated in each structure. The boxes indicate the size of a single unit cell. The stars to the right of the kesterite structure indicate the planes in which Cu and Zn are intermixed randomly in the disordered kesterite structure. Yellow: S/Se; Green, orange: Zn; blue: Cu; red: Sn. Illustration adapted from Schorr [34] with permission from the publisher.

2.2.1 Composition dependence of defects and secondary phases

The efficiency of CZTS solar cells has been highest for materials that are Cu-poor and Zn-rich relative to stoichiometric CZTS and CZTSe [19, 42] with an optimal Cu/(Zn+Sn) ratio of about 0.8-0.9 and a Zn/Sn ratio of about 1.2-1.3 [19, 37]. In the best solar cells, therefore, ZnS would be the expected secondary phase. Apparently CZTS has a very low tolerance to excess ZnS even though the lattice of the two are very similar. Just et al. recently showed that ZnS has a tendency to precipitate out when samples are Zn-rich by as little as 1 atomic percent, yielding a combination of CZTS and small amounts of ZnS [43]. However, Valle Rios et al. argue that it is possible to find single-phase CZTS in the Zn-rich region of the phase diagram [44]. The truth may lie somewhere in between: other authors have shown by atom probe tomography that ZnSe and CZTSe may be intermixed in nanoscale regions in Zn-rich CZTSe absorber layers

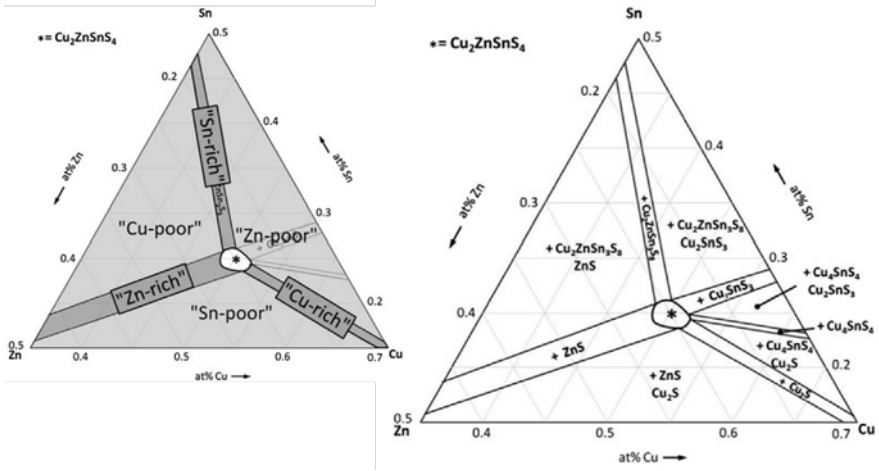

Figure 2.4: The pseudoternary phase diagram of CZTS as depicted by Scragg [41] based on data from Olekseyuk et al. [40], reprinted with permission from the publishers. The central starred region shows the composition range where single-phase kesterite CZTS is formed. The left image defines the terms Zn-rich, Zn-poor, etc., while the right image indicates which secondary phases are likely to form under a given composition.

[37]. The effect of the presence of ZnS or ZnSe in small quantities alongside CZTS is not yet well understood, but they are apparently not as detrimental as other secondary phases. It may be that small regions of ZnS just act as small insulating grains ("dark space") that the charge carriers need to pass around [13].

Why Zn-rich CZTS is best for solar cells is still an open question. Theoretical groups have examined which point defects are most likely to occur in CZTS based on their energy of formation and what their ionization energy is inside the bandgap [45]; see Figure 2.5. We can see that S-vacancies give defect levels right in the middle of the bandgap. Zn-interstitials and Sn-substitutions on Cu or Zn sites also give rise to disastrous mid band-gap levels, so intuitively it seems logical that a S-poor and/or Sn-rich state is detrimental. Chen et al. [45] calculate the energy of formation of the individual defects as well as simple defect clusters and show that under stoichiometric conditions, the compensating donor-accepter defects of $2Cu_{Zn}$ and Sn_{Zn} easily occur and are detrimental to the solar cell voltage (and efficiency) because they provide quite deep energy levels inside the bandgap, decreasing the width of the bandgap locally. These defects are suppressed when the cell is Cu-poor and Zn-rich. It is easy to imagine that on the other hand, the

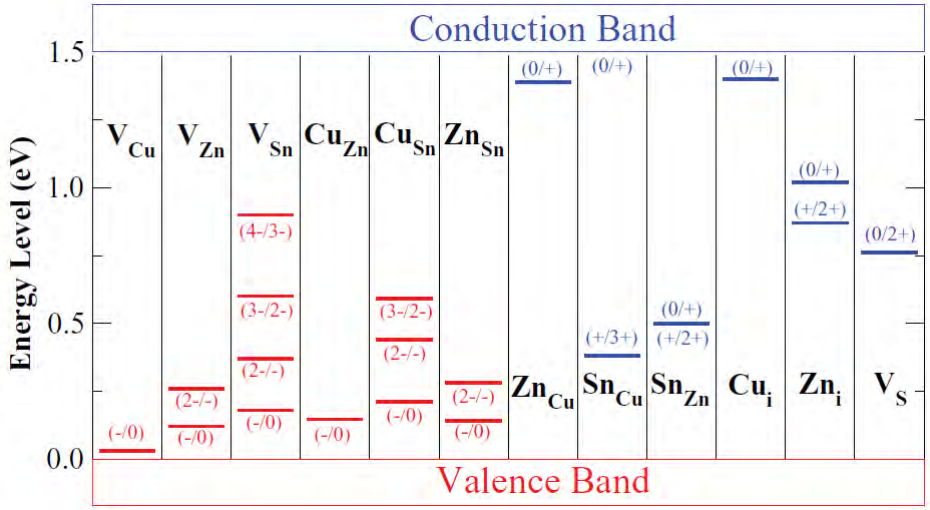

Figure 2.5: The energy levels calculated by density functional theory for the point defects that can occur in CZTS as shown by Chen et al. [45]. Red are accepter levels while blue are donor levels. The initial and final charge states of the lattice site are shown in the parentheses. Reprinted with permission from the publisher.

much shallower compensating defects of Cu vacancies and Zn-substitutions on Cu sites (V_{Cu} + Zn_{Cu}) would be the ones forming under Cu-poor, Zn-rich conditions. Such defects have also been shown experimentally in slightly off-stoichiometric CZTS [46, 34]. However, Chen et al. note that the energy of formation of the different defects could be very different when one moves into the regions where competing secondary phases form [45]. The jury is therefore still out on how the composition influences the solar cell parameters.

In the Cu-rich state, grain growth is better than under Cu-poor conditions [5]. This is part of the reason cited by the CZTS record-efficiency group, Tajima et al., for using a two-layer structure with a relatively Cu-rich (very near to stoichiometric) layer at the base [10]. However, as we saw above, Cu-rich conditions in absolute terms can lead to detrimental defects, and for Cu/Sn >1, Just et al. found that Cu_2S will precipitate out [43]. Groups that find copper sulfides in their films remove them with KCN etching [5] (that's potassium cyanide - needs to be treated with care!) and our group also sometimes used this technique.

2.2.2 CZTS thin film formation

As mentioned in Section 1.2, the deposition of the pure sulfide CZTS has been most successful using vacuum techniques for depositing a precursor (metallic or containing some sulfur) followed by a high-temperature annealing step. In fact as mentioned, the record efficiency was achieved by depositing two different CZTS layers, one on top of the other, with a high-temperature annealing step for both the first precursor layer (at 580 °C) and the second (at 500 °C) [10]. Following the deposition of the CdS buffer layer, these films were annealed at somewhat lower temperature a third time, cementing the idea that a *post-annealing* heat treatment can be helpful for solar cell efficiency, whether because it helps reduce disorder in the CZTS layer as suggested by Liu et al. [37] or because it increases intermixing of Cd into the CZTS surface as argued by Tajima et al. [10].

Apart from the record cell achievements by precursor sputtering [10] and co-evaporation [13], a host of other deposition techniques have been used to make CZTS, as detailed in reviews by Mitzi et al. [47] and Jiang and Yan [48]. The latter focuses exclusively on CZTS. Among the **vacuum techniques**, besides co-evaporation and co-sputtering deposition, several groups have used sequential evaporation of metallic or binary metal sulfide layers followed by CZTS formation during annealing, the original method pioneered by Katagiri's group [19]. Sputtering has also been employed both for co-sputtering deposition (for instance by the Katagiri group [19]), sequential sputtering of metal and binary layers as used by Tajima et al. [10] and reactive sputtering with a H_2S/Ar background as used at Uppsala University [49]. Pulsed laser deposition will be covered in detail later on (Section 4.1), as it has also been tried by a few other groups before us.

As for *non-vacuum techniques*, again numerous methods have been employed including nanoparticle synthesis (the subject of Sara Engberg's work in the CHALSOL project), electrodeposition, spray pyrolysis, spin coating, or printing of precursor inks or sol-gel mixtures followed by sintering, and more, as listed by Jiang and Yan [48]. One notable non-vacuum-based approach is the monograin CZTS synthesis carried out at Tallinn University, which is being commercialized by the Estonian-Austrian company Crystalsol [50]. By this method, micron-sized CZTS crystals are grown in a molten salt solution at very high temperature (1000 °C). The CZTS grains are subsequently embedded in an organic polymer matrix on a graphite contact with roll-to-roll technology, resulting in flexible and potentially very cheap CZTS solar cells.

2.2.2.1 Approaches to avoid high-temperature annealing

Several groups have tried to develop single-step processes, avoiding the high-temperature annealing step, though so far this has proved very challenging. For

example, Schubert et al. made CZTS by co-evaporation at 550 °C in a single step (no sulfurization step) and achieved an efficiency of 4.1 % [51]. In a somewhat more complicated process with the pure selenide CZTSe, Repins et al. [52] achieved a very impressive 9.1 % efficient solar cells using a three-stage co-evaporation process, eliminating the sulfurization step and using a maximum substrate temperature of just over 500 °C. Also using co-evaporation, Mise et al. [20] reached 5.2 % efficiency this year using a substrate temperature of 460 °C and so far represent the lowest-temperature succesful application of single-step deposition for CZTS absorber layer production. Others have worked with CZTS co-evaporation at lower temperature than 460 °C, but none have to my knowledge reported working solar cells [53, 54].

Single-step co-evaporation has so far been more successful than single-step sputtering deposition, even though sputtering deposition imparts a high amount of kinetic energy to the growing film, just like PLD and PED, allowing crystalline growth at relatively low substrate temperatures. Platzer-Björkman et al. [49] report that single-step reactive sputtering of CZTS so far has led to a maximum efficiency of 1.3 %. They write that "a one-stage deposition would require a very rapid cool-down or other measures to protect the surface from decomposition."

Overall the many steps in the record efficiency achievement shows that CZTS processing for solar cells requires great control. It is interesting to see in the cutting edge work by Tajima et al. [10, 11] that relatively small differences in the absorber layer treatment (single or double CZTS layer, different post-annealing temperatures) can lead to nearly 50 % changes in the efficiency. Informally, other accomplished CZTS and CZTSe research groups also discuss large variation between different solar cell production runs.

2.2.3 SnS loss

The topic of decomposition of the CZTS layer during processing deserves some extra attention: During annealing (or single-step reactive sputter deposition or co-evaporation), S and Sn are often lost from the films. This has been documented by several authors, including Weber et al. [55] as well as Redinger et al., who found that all the Sn in the film could disappear if one annealed the sample long enough in vacuum [56].

In some of my own CTS films, I saw a similar effect: loss of Sn from the films - with a relatively smaller loss in S percentage-wise, which at first seemed surprising: Sn may have a low melting point, but its boiling point is high and the vapor pressure low. How could it disappear? And why would there still be S in the films if all the Sn has vanished? Surely S would vaporize long before Sn? The answer is provided by both Weber et al. (for CZTS) [55] and Redinger et al. (for CZTSe) [56]: Sn disappears in the form of the very volatile compound

SnS (or SnSe for CZTSe), leaving behind ZnS and Cu_xS (or in the case of CTS annealing, just Cu_xS).

Scragg et al. [57] carefully examined the chemical equilibria between the metal-sulfide binaries, S_2(g) and the CZTS phase to explain these findings. They point out that when a gas-phase product is formed from the breakdown of CZTS, the evaporation of the volatile compound will drive the reaction towards formation of more of the volatile phase even if it is not particularly favorable in terms of potential energy. Therefore a counterpressure of SnS(g) as well as S(g) is needed to maintain an equilibrium where CZTS will form without significant degradation [58]. This finding helps explain why many groups have found rapid thermal annealing more successful than longer annealing times, as in most CZTS studies no SnS powder is used to provide an SnS (g) counterpressure.

2.3 Secondary Phases of CZTS

We have already seen above that many secondary phases impact the efficiency of CZTS solar cells. In the following we will introduce the secondary phase of CTS as a solar cell material in its own right, followed by an introduction to ZnS, Cu_xS, and SnS_y.

2.3.1 Copper tin sulfide

Copper tin sulfide, Cu_2SnS_3, or CTS for , is a secondary phase of CZTS that we focus on in this study because it is not easily detected by XRD: in its cubic phase, which may occur in the same temperature range as CZTS, the XRD peaks overlap with the main peaks of CZTS. A number of polymorphs of CTS have been proposed (all with the elemental composition Cu_2SnS_3) including a tetragonal, cubic, monoclinic, hexagonal, and triclinic phase. The hexagonal phase has only been reported in nanoparticles and apparently has metallic characteristics [59], but is not thermodynamically stable according to theoretical predictions [60]. In thin films, the tetragonal and cubic [61], triclinic [62], and monoclinic phases [63] have been reported (the listed references are not exhaustive).

Chen et al. [64] suggest that below 780 °C, CTS forms a tetragonal structure, while at higher temperature the cubic phase is found. Zhai et al. [60] explain that the monoclinic, cubic, and tetragonal phase are all closely related, differing only in the level of ordering of the Cu and Sn cations in the lattice. The cubic phase is the most disordered, while the tetragonal phase is partly ordered and the monoclinic phase is fully ordered; see Figure 2.6. While the figure suggests that the cations surrounding the S anions could be any combination of Cu and Sn, Zawadzki et al. [65] show that $S-CuSn_3$ and $S-Cu_4$ are highly unlikely at temperatures around 500 °C or lower. They also show that even the most

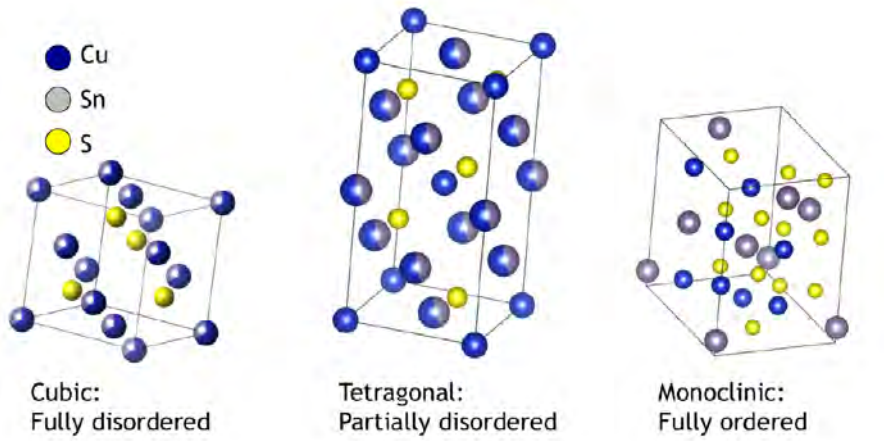

Figure 2.6: Crystal structure of Cu_2SnS_3. Left, the atomic arrangement of CTS in the monoclinic phase. Right, the fully disordered cubic phase. The possible structural motifs in CTS are also shown. Reprinted from the Supplemental Material of Baranowski, L. L., McLaughlin, K., Zawadzki, P., Lany, S. , Norman, A., Hempel, H., Eichberger, R., Unold, T., Toberer, E. S., and Zakutayev, A. Effects of Disorder on Carrier Transport in Cu2SnS3. Physics Review Applied **4**, 044017 (2015) with permission of the main author and the publisher. Copyright 2011 by the American Physical Society.

ordered phase, monoclinic CTS, will have some degree of disorder just due to random distribution of the $S-Cu_3Sn$ and $S_Cu_2Sn_2$ motifs that must be mixed throughout the structure, spelling trouble for solar cells made of monoclinic CTS as this will inevitably lead to potential fluctuations in the crystal.

The many potential crystal structures of CTS lead to several possible bandgaps. Most of the structures have reported bandgaps around 1 eV, while the tetragonal phase has a reported bandgap of 1.35 eV (see, e.g., [61, 17, 60]). The 1.35 eV bandgap is potentially more promising for solar cells and was used in a solar cell by Tiwari et al. [66], achieving ≈ 2 % efficiency with a different type of design to that used by most groups (they built a superstrate cell where the CZTS layer is deposited on top of the window layer rather than the other way around). Most other reported solar cells have closely mimicked CZTS solar cell architecture and processing, with annealing taking place at about 570 °C and resulting in the monoclinic CTS phase.

In addition to the various Cu_2SnS_3 polymorphs it is important to be aware that several other copper tin sulfides exist, including Cu_3SnS_4, Cu_4SnS_4, Cu_4SnS_6,

and $Cu_4Sn_7S_{16}$. Zawadzki et al. [67] describe a number of these materials and evaluate the potential of three of them as solar cell materials, concluding that Cu_2SnS_3 is the most promising despite a relatively narrow stable region in the SnS-Cu_2S phase diagram. They remark that Cu_3SnS_4 (kuramite) crystallizes in a similar tetragonal form to Cu_2SnS_3 and may be difficult to distinguish from it if one finds oneself in an SnS-poor region of the phase diagram of either CTS or CZTS.

2.3.2 Solar cells of CTS

As mentioned in Section 1.2, the current pure CTS record solar cell reached 4.6 % efficiency in 2015 [68], while a CTGS (Ge alloyed CTS) solar cell reached 6 % already in 2013 [18]. The first CTS solar cell of 0.11 % efficiency was made by Kuku and Fakolujo already in 1987 [69], but no more CTS solar cells were reported until CZTS research was well underway with papers on the properties of thin film CTS and its potential application to solar cells appearing from 2009/2010. A large amount of work on CTS has been done in Japan where the record cells have been produced. The rather small bandgap makes CTS a less than ideal absorber layer choice, but it could for example act as a potential bottom layer for a heterojunction solar cell [18].

Like CZTS, CTS is a p-type direct band-gap semiconductor, at least in the monoclinic phase, and some of the observations made on CZTS solar cell processing also apply to CTS: a Cu-poor composition yields a higher efficiency [17, 16] and Na-doping increases the efficiency [68] just as it does for CZTS [20]. Unlike CZTS, however, the grain growth is worse under Cu-rich conditions than Sn-rich conditions [16, 70].

The phase diagram of CTS is not yet fully mapped, although several groups have worked on it. Fiechter et al. [71] explored the phases formed under different ratios of Cu_2S to SnS_2 at a wide range of temperatures and show a single point of Cu_2SnS_3 stability, but did not investigate the range of solid state compositions near this point. Zawadzki et al. [67] calculated the phase space theoretically and Baranowski [70] explored the structures obtained under different compositions experimentally, showing a rather small stability region of Cu_2SnS_3 that requires not only a rather low concentration of Cu but also a low concentration of S.

2.3.3 ZnS material properties

ZnS forms two crystal polytypes: the cubic/zinc blende/sphalerite form also known as β-ZnS, which is more commonly found in nature, and the hexagonal/wurtzite form, α-ZnS, which is metastable below 1020 °C [72, 73]. For the physical properties of ZnS, see tables in Appendix G. The bandgap is high, about 3.5 eV for the zinc blende form and 3.8 eV in the wurtzite form, which means

that ZnS is transparent to both visible and infrared light in its dense form (it appears white in powdered form). The high bandgap energy means that when ZnS occurs in CZTS it blocks current transport, acting as an insulator. However, as noted above, small amounts of ZnS may be less detrimental than similar amounts of CTS or other low band-gap impurities, which reduce V_{oc} and therefore the efficiency [33].

ZnS is a very stable compound and ZnS films do not easily oxidize, staying reflective for years when stored in the laboratory as noted by Cox and Hass in 1959 [74] and confirmed in the present study. However, ZnS may decompose - and oxidize - when exposed to UV irradiation. Hass et al. describes oxidation under UV irradiation even in vacuum at 10^{-6} mbar because a monolayer of O always forms on the surface due to residual gas in the chamber. Other authors writing about CVD of ZnS note that subliming S from ZnS extremely quickly reacts with any stray molecules of water or hydrogen in the chamber, leading to non-stoichiometry even at very low vacuum pressure [75]. This problem should be smaller in PLD, where the molecules spend less time bouncing around the chamber before they reach the substrate.

ZnS has relatively high reflectivity in the far UV and very low reflectivity in the visible and infrared spectrum and has therefore been used in optical coatings since the 1950's [74]. Doped ZnS can be phosphorescent and has been widely used in cathode ray tubes and electroluminescent displays (e.g., in the screens of old fashioned TVs and oscilloscopes) [76, 77]. For example, Mn-doped ZnS (ZnS:Mn) emits orange-yellow cathodoluminescence, as has been shown in thin films produced by PLD [78, 79]. Cu-doped ZnS is used as a blue luminescent material [80]; other dopings lead to other colors [77]. For these reasons as well as its nonlinear optical properties, ZnS is widely used today in infrared optics as well as lasers, LEDs and electroluminescent displays among others [81, 82]. Nanoforms of ZnS have also been extensively researched in various forms, e.g., for use as quantum dot shells [73].

Due to its high bandgap and its good lattice match to CZTS, ZnS has been considered as a buffer layer instead of CdS in CZTS and CIGS solar cells [83, 84, 22, 85, 86]. The role of the bandgap is to help guide electrons to the n-side of the solar cell and not let them get back to the p-side to recombine with the holes. The bandgap of this layer is therefore crucial. Some authors, such as Barkhouse et al. [22], suggest that ZnS has too high a bandgap even compared to CZTS and suggest focusing on other materials such as In_2S_3 [87].

2.3.4 Copper sulfides

Copper sulfides are generally considered detrimental impurities when they occur in CZTS and it may therefore be surprising to learn that in the 1980's extensive

research was dedicated to Cu_2S solar cells and > 10 % was achieved for CdS/Cu_2S devices. Apparently development of this material for solar cells was abandoned when it became clear that Cu migrated through the device, making them unstable [88].

A quick overview of the different copper sulfides is provided here mainly based on information from Rao and Pisharody [89]:

Cu_2S has several phases depending on the temperature. Below 104 °C it is in a monoclinic form, then it passes through a hexagonal phase before reaching a cubic form (digenite) above 435 °C. The bandgap is about 1.2 eV [88].

$Cu_{2-x}S$ with $x \approx 0.2$-0.25 naturally exists as cubic digenite but can also be found, e.g., in an orthorhombic form synthetically (Cu_7S_4).

$Cu_{1.96}S$ is in orthorhombic djurleite form below 93 °C but passes into a mix of CuS and Cu_2S at higher temperatures. It can also make a tetragonal phase at high pressure.

CuS is a hexagonal, metallic phase (covellite) wherein S is both in the S_2^- and S^{-2} state. It decomposes above 507 °C into S_2(g) and $Cu_{2-x}S$ or Cu_2S.

CuS_2 can only be prepared under high pressure and is also metallic.

Cu_2S is most likely to occur in the CZTS phase diagram because the valence of Cu in Cu_2S is the same as in CZTS (Cu(I)).

2.3.5 Tin sulfides

SnS_2 with Sn in the (IV) valence state is the secondary phase that would be expected in CZTS unless there is lack of S. This material is an n-type semiconductor with a direct bandgap around 2.2-2.5 eV.

SnS is a semiconductor with a smaller bandgap than SnS_2 with various reported bandgap energy values from 1-1.2 eV indirect to 1.2-1.5 eV direct. It is being explored as a solar cell material with efficiencies so far similar to those achieved by CTS: 4.4 % maximum to date [90]. Usually SnS is found in the orthorhombic phase [91], though several other crystal phases have been reported under special circumstances.

Another Sn-S secondary phase is Sn_2S_3, an orthorhombic phase in which the valence states of Sn(II) and Sn(IV) are mixed.

2.4 Summary: Lessons on CZTS and CTS as well as the secondary phases from literature

This chapter has outlined the working principles of a solar cell and the characteristics of the CZTS and CTS layers for solar cells in current research. The most important observations in relation to the rest of the thesis include:

- Compositional and processing control is very important and difficult in CZTS solar cell fabrication
- The best CZTS solar cells have been Cu-poor and Zn-rich, perhaps because the most likely defects formed in the CZTS itself are not so harmful under these conditions, or perhaps because detrimental narrow band-gap secondary phases are less likely to form
- The single-phase region for CZTS in the phase diagram is most likely quite narrow with secondary phases precipitating out as soon as the composition deviates from Cu_2ZnSnS_4 (in the Zn-rich part of the phase diagram, we will find ZnS).
- SnS is easily lost from the films during annealing and this type of degradation must be prevented by using short annealing times and a compensating $SnS_{(g)}$ and $S_{(g)}$ pressure.
- CTS like CZTS is most efficient when it is Cu-poor
- CTS has an even more complex phase diagram than CZTS, apparently also with a very narrow stability region
- ZnS is a very stable secondary phase which acts as an insulator due to its high bandgap.
- Several of the possible secondary phases of CZTS are in themselves potential solar cell absorber layers including Cu_2SnS_3, SnS and CuS.

Chapter 3

Background: PLD and PED

As mentioned in the introduction, pulsed laser deposition (PLD) and pulsed electron deposition (PED) are both vacuum techniques with particles of high energy that enable non-equilibrium deposition of thin films. While PLD has been used widely in research and is also implemented in commercial production, PED is less widespread because it took longer to develop a stable electron source [92].

Many good introductions to PLD and PED explain the mechanism of ablation, so the following chapter will focus on concepts I have found helpful in relation to the present results. For a complete beginner in PLD, I would recommend the first pages of the tutorial by Ashfold et al. [93] as well as Schou's review from 2009 [94]. An overview of many applications and materials tackled by PLD is provided by Eason's book [95] while many helpful experimental observations are described by Lowndes [96] and Geohegan [97]. On the physical mechanisms behind PLD I found Willmott and Huber's treatment very useful [98], as well as Schou's book chapter on laser beam-solid interactions [99]. Harshavardhan and Strikovski provided a nice introduction to PED in 2005 [100] while Strikovski et al. present a more thorough comparison of the physics of PED and PLD [101].

3.1 Ablation and thin film formation

In both PED and PLD, thin film deposition takes place by ablation of the target material. 'Ablation' really just means removal of material, but in PLD and PED literature, it is often used in a more specific sense: as a process in which material is broken down to atomic constituents and ejected very rapidly as plasma. The word 'evaporation' in PLD literature instead evokes an equilibrium process, where the material may be in molecular form. This is further discussed below in Section 3.2.

Plasma, meanwhile, is 'a fully or partially ionized gas consisting of electrons and ions' [102].

> **What does 'non-equilibrium' mean?** Willmott and Huber defined it as follows (slightly rewritten) : Ensembles of species "are said to deviate from thermal equilibrium" when they "have energy distributions that cannot be described by the Maxwell-Boltzmann equation and therefore cannot be described by a single temperature." [98]

The transfer of energy from beam to target naturally differs from PLD to PED and also differs for different types of PLD (using nanosecond or femtosecond lasers). The following discussion will primarily focus on ns-PLD. A PLD setup is sketched in Figure 3.1a (the laser does not have to be in the UV, but in ns-PLD it often is, as explained further below). An immediately visible characteristic of PLD is the confined and primarily forward-directed ablation plume, in which excited atoms and ions emit radiation in the visible spectrum, which means the ablation is visible through the vacuum chamber viewports. For example, a Zn-plume looks blue and a Cu-plume looks green (Figure 3.1b).

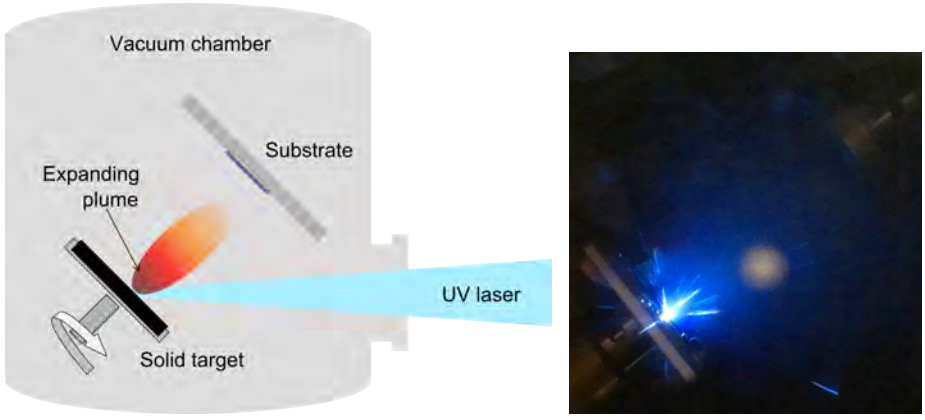

(a) (b)

Figure 3.1: PLD setup and ablation plume. (a)Schematic of PLD setup. (b) The ablation plume during PLD of zinc. The plume clearly contains large droplets (streaks) and is very wide due to a very small spot size ($\approx$ 2 mm) in our initial experiments on metals. See more on spot size in section 3.1.3 below.

3.1.1 Energy absorption in the target

When a laser pulse strikes the target material, energy is transferred from the incoming photons to the electrons in the material. In ns-PLD, this happens most efficiently if the material has a high absorption coefficient, explaining why much work with ns-PLD is done with UV lasers, which are generally more efficiently absorbed than longer-wavelength light. The energy absorption is exponential and can be expressed by the Lambert-Beer-Bourget law:

$$I = I_0 exp^{-\alpha(\lambda)d}[1 - R(\lambda)] \tag{3.1.1}$$

where I_0 is the incident laser intensity, $R(\lambda)$ is the wavelength-dependent reflectivity, $\alpha(\lambda)$ is the wavelength-dependent absorption coefficient, and d is the distance that the light has traveled into the material. Note that the laser is usually incident on the target at an angle of 45 °, which means that R can be substantial, especially for metallic or very smooth targets.

The excited electrons equilibrate with the core atoms (i.e., the energy is transferred to lattice vibrations), increasing the temperature of the target within picoseconds in ns-PLD [99]. The heating of the target leads to breakdown of the material within the region where the energy concentration is high enough, accompanied by an extremely quick rise in pressure and subsequent expulsion of material. The process is even faster in fs-PLD, where the laser pulse is so fast and intense that the material ejection may actually happen because so many free electrons are created under certain conditions that they can result in a Coulomb explosion [103, 104].

The volume of material that is ablated depends on both the absorption depth and the thermal diffusion length of the material: if the absorption depth is shallow, the heat will be absorbed close to the surface and if the thermal diffusion length is short, it will stay in the region where it was absorbed and cause efficient ablation. Therefore one would expect the ablation efficiency to be highest for materials with a high absorption coefficient and a low thermal diffusivity.

Normally, the thermal diffusion length l_{th} is defined as [105]:

$$l_{th} = 2(D\tau_L)^{\frac{1}{2}} \tag{3.1.2}$$

and describes the point where the temperature is reduced by 1/e compared to that of the external heat source of a laser pulse of length τ_L . D is the thermal diffusivity defined as:

$$D = \frac{\kappa}{\rho c_p} \tag{3.1.3}$$

where κ is the thermal conductivity, ρ is the density and $c_p(T)$ is the specific heat. These material parameters are all temperature dependent, which becomes important to remember in the extreme conditions caused by the laser irradiation.

The definition of D comes from solving the (equilibrium) heat diffusion equation of temperature T as a function of time t and distance $\mathbf{r}$ from a point source of heat Q:

$$\rho(T)c_p(T)\frac{\partial T(\mathbf{r},t)}{\partial t} - \nabla[\kappa(T)\nabla T(\mathbf{r},t)] = Q(\mathbf{r},t) \tag{3.1.4}$$

where Q is the heat source (power per unit volume) provided by the laser. Q can be approximated by $\partial I/\partial \mathbf{r}$ (or $\partial I/\partial z$ assuming 1-dimensional propagation of the light) as given by Equation 3.1.1. For further detail, see Bäuerle's treatment [105].

These equations assume that heat loss by radiation or convection is negligible, and that the material is uniform, totally neglecting the pressure gradient and phase changes occurring in the material. Since we are usually working under non-equilibrium conditions in PLD (see Box 3.1) and pressure gradients and phase changes are non-negligible, the equations break down, but they still provide a useful framework. For example, having measured D, Matthias et al. were able to show the importance of l_{th} in determining the melting and vaporization threshold in 14 ns, 248 nm laser ablation of Ni and Au: Ni with a smaller l_{th} was much easier to ablate and for both materials it was easier to ablate a thin film than a thicker one on a heat insulating substrate because the substrate helped increase the local heating. Mirroring this effect, Cranton et al. saw that the threshold fluence increased in thin films of ZnS (which is insulating) on a heat conducting substrate because the heat was transported away from the ZnS before it could be ablated using ns XeCl 308 nm laser pulses [106]. Note that these measurements were made very close to the ablation threshold.

In a treatment that is closer to the conditions used in this thesis, Fähler and Krebs modeled the irradiation of Fe by a 248 nm laser also taking into account only equilibrium heating and evaporation of the material, using Equation 3.1.4 with Q, the source term (absorbed laser power per volume), modified by absorption in the evaporated layer. In their model, the high-pressure gas region next to the target (the Knudsen layer) was treated exactly as the bulk material at room temperature in terms of density, absorption coefficient, and even reflectivity. A retraction of the surface due to evaporation was included in the model, ignoring any changes in density due to temperature change, and cooling of the surface by the heat of evaporation was subtracted from Q. That's all - no erosion of the target by the energetic plasma or other effects were included. Yet this very simple model led to reasonable estimates of the ablation rate as measured by the mass loss of the target [107].

By gravimetric measurements, Timm et al. estimate the ablation depth in three other bulk metals, Sn, Ti, and Al, which was only 5-50 nm, much much lower than the thermal diffusion length. They explained the low ablation rate by the low thermal diffusivity of the plasma, which contrasts to the treatment of

the nascent plasma as similar to the bulk by Fähler and Krebs. Another example where simple thermodynamic equilibrium modeling was unsatisfactory was in explaining Ni and Ag ablation by Svendsen et al., where the model predicts a higher deposition rate for Ag than Ni at 532 nm, but the experimental results showed the opposite [108]. In this case effects like diminishing reflectivity of Ni during the laser pulse or resputtering of Ag may have had a large effect.

Compared to metals, which were used as ablation model systems in the 1990's, in a dielectric the absorption length $1/\alpha$ is generally longer and the thermal conductivity often much smaller, meaning that absorption length and thermal diffusion length approach each other. Semiconductors have intermediate characteristics. Since these materials are compounds and their thermodynamic characteristics are less well known than for metals, they are even more difficult to model than the metals.

3.1.2 Plume and plasma generation

As the material affected by the laser pulse gains enough heat to melt and vaporize, increasing the local pressure and expanding, it begins to be ejected from the target. Since this happens on the ps timescale, in ns-PLD the ejected material continues to be irradiated by the laser beam, leading to further energy absorption and ionization of the plume, creating plasma. The absorption in the plume shields the target, such that the highest temperature of the target surface may be reached long before the laser pulse is over (this means that τ_L is not a very good parameter in Equation 3.1.2). Including this effect in their simple model of PLD of Fe, Fähler and Krebs predicted a higher surface temperature at 5 ns than at 10 ns or subsequent time steps even though the modeled pulse was 30 ns long [107].

The laser-target interaction and plume generation is shown schematically in Figure 3.2. The initial high-pressure material ejected from the target forms a Knudsen layer where the molecules or atoms ejected constantly collide - here the pressure can be up to 1 kbar [99]! The Knudsen layer is the non-equilibrium region "within a few mean free paths of the target surface" where the velocity distribution of the particles emitted from the surface changes from being all forward-directed and in equilibrium with the surface to having a new (lower) average forward-directed velocity with a distribution of velocities that are both forward and backward-directed due to the many collisions [109]. The subsequent absorption of laser light will then increase the velocity of the particles in all directions, causing some to further erode the target as they strike it while others recondense and most of the others speed off towards the substrate as described below.

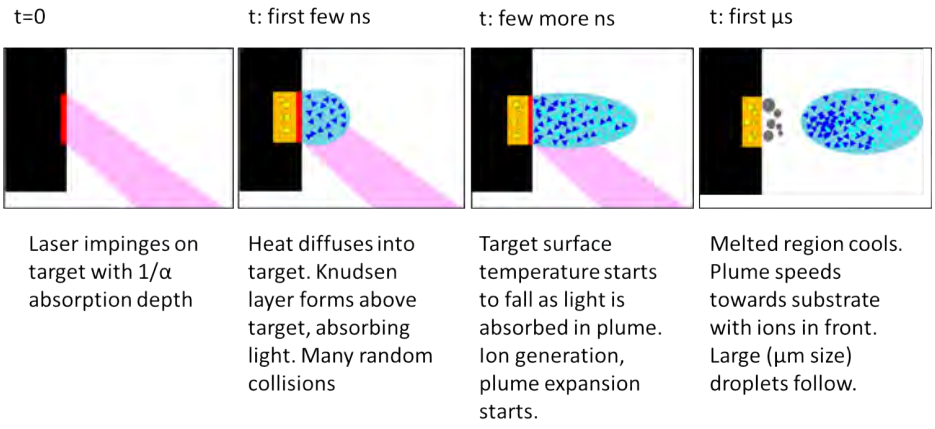

Figure 3.2: Comic-strip depiction of ablation process: Target interaction and plume generation in ns-PLD. Dark blue triangles represent atoms, light-blue triangles represent ions.

3.1.3 Plume expansion geometry

As the hot particles ejected from the target collide with each other and the target, they gain an average forward-directed velocity with an empirically determined angular distribution of $cos^n\theta$ where θ is the angle from the target surface normal and $n > 2$ depending on numerous factors including the spot size, the fluence, and the background pressure [98, 99]. In contrast, 'normal' evaporation is $cos\theta$-distributed from the heated surface area because of the relatively low number of collisions.

Modeling the many competing processes taking place during ns-PLD is extremely challenging: one has to take into account the target irradiation, target breakdown with associated pressure and temperature changes, material ejection, Knudsen layer dynamics, laser irradiation of the plume-in-formation, plasma formation, further plasma excitation by the laser, partial shielding of the target by the plasma, and finally plume expansion concurrent with decay of the plasma excitation. The non-equilibrium nature of some of the steps is especially vexing because it means that the modeled quantities are not well represented by an average, and the extremely high temperature and pressure that lead to a critical state of the matter is very difficult to describe accurately as well. Nonetheless, many authors have tried to capture PLD by modeling, both analytical and numerical (mostly the latter in the last 20 years).

One model that is important because it predicts the spread of the ejected

molecules is the Anisimov model of plume expansion [110]. After the laser pulse has passed and beyond the surface of the Knudsen layer, the expansion of the plasma plume can be modeled as an adiabatically expanding cloud of gas and Anisimov et al. solved the governing equations analytically [110]. The full expression for the plume shape is quite complicated, but they show that for a substrate placed far from the target relative to the dimensions of the laser spot on the target ($d_{target-substrate} >> r_{spot}$) the thickness of the deposited film $h(\theta)$ can be approximated by:

$$h(\theta) = \frac{Mk^2}{2\pi\rho d^2} * \frac{1}{(1 + k^2 tan^2\theta)^{3/2}} \tag{3.1.5}$$

where θ is the angle from the normal to the target, M is the total mass of ablated material, k describes the eccentricity of the ellipsoid of the plume expansion ($k = Z(t)/X(t)$ where $Z(t)$ and $X(t)$ describe the maximum extent of the ellipsoid in the directions vertically and laterally away from the point of expansion), ρ is the density of the growing film, and d is the target-substrate distance. This expression looks quite unwieldy but may easily be plotted and was shown by Anisimov et al. to be well approximated by $cos^n\theta$ for small θ. Several authors have shown that the Anisimov model provides a better fit than the simple $cos^n\theta$ approximation, as is for instance clear from Fig. 6 by Ojeda-G-P et al. [111].

The Anisimov model predicts that the larger the laser spot size, the more forward directed the plume, which can be intuitively understood because the lateral dimensions of the laser spot on the target are so much larger than the depth of the heated area or the thickness of the ejected material. This means that the outward pressure in the expanding gas layer is more forward directed than outwards directed. The smaller the spot, the larger the relative pressure towards the edges, and the more the plume spreads out. Figure 3.3 shows the thickness gradient that exists even for a relatively small spot (in this case ≈ 0.3 mm^2).

3.1.4 Energy and time scale of plume expansion

The ablated material from the target has a velocity on the order of 10 km/s corresponding to 10s of keV. The velocity of the light element ions can be as high as 40 km/s for 248 nm nanosecond PLD of graphite, while the atoms travel more slowly, on the order of 20 km/s for the same material [93]. The ions travel fastest because they are pulled ahead by the free electrons speeding ahead at the front of the plasma plume. However the spread of ion velocities is very large and the majority of the ions travel more slowly [101]. Large droplets ejected from the target are an order of magnitude slower yet, with a speed of only 0.2 km/s in the graphite experiment [93]. For heavier elements, maximum kinetic energies

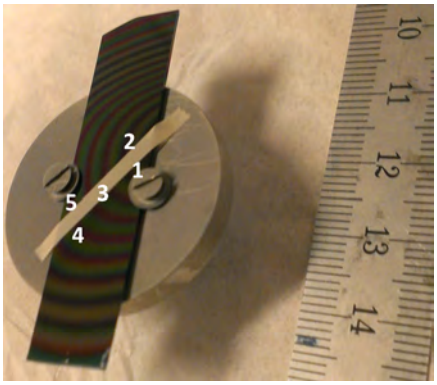

Point	Thickness (nm)
1	1790
2	1740
3	1590
4	1370
5	1380

Figure 3.3: Thickness gradient of ZnS as deposited on Si. The thickness was measured at the labeled points, illustrating the magnitude of the thickness gradient in a ZnS deposition with a ≈ 0.3 mm^2 spot, leading to a relatively low degree of forward peaking of the deposition on the substrate

of Ag ions of 150 eV (16 km/s) have been measured [112] or about 100 eV for Fe ions ($\approx$ 19 km/s) while Fe droplets traveled at only 20-150 m/s [107]. In a background gas, the ions and atoms are slowed down significantly, arriving later. For PED, which always takes place in a background gas, and which additionally has a slightly different material ejection mechanism, the range of ion energies is wider, with a lower average ion velocity but a longer tail of high-velocity ions[101].

In a background gas the expanding plume collides with the atoms or molecules of the gas (for example Ar, O_2 or N_2). The gas will be compressed in the direction of plume expansion, creating a shock front, as shown in detail, e.g., by [113]. Collisions with the gas cause the atoms and ions from the target to scatter, with light elements scattered more than heavy elements - see for example Chen et al. [114].

The time scale of PED and PLD is difficult to comprehend. The PED and PLD pulses used in these studies are approx. 5-100 ns long and the pulse repetition rates used were 5-45 Hz, which means that the time between pulses is immense compared to the length of the pulses themselves. To put the pulse-to-no-pulse ratio in perspective, 20 ns PLD pulses at a repetition rate of 10 Hz correspond to 1 s pulses repeated every 58 days! After the laser or electron pulse itself, the ablation plume continues expanding for several microseconds: With a target-substrate distance of 4 cm, ions traveling at 16 km/s will hit the target in 4 microseconds, while atoms might take 2-10 times as long and droplets 10 times as long again. On the scale of the imaginary 1 s pulse with a 58-day repetition

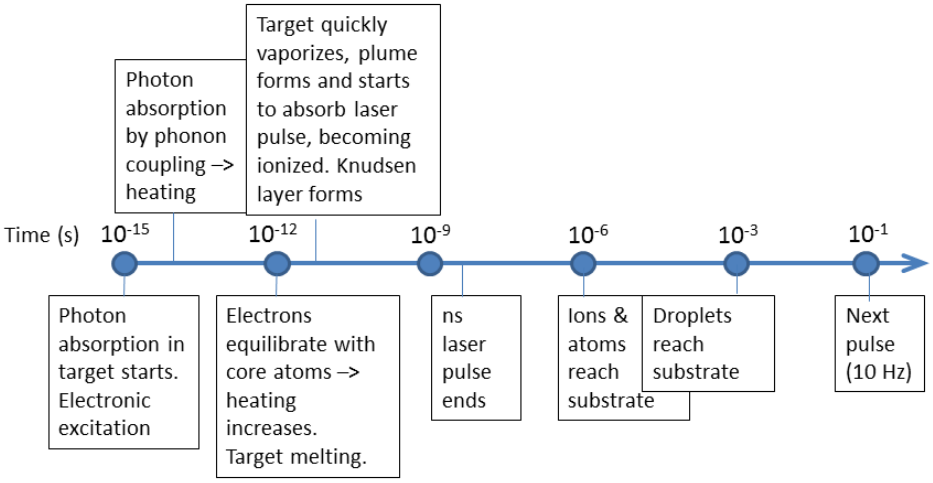

Figure 3.4: Timeline of a ns-PLD pulse (approximately logarithmic scale)

rate, the ions and atoms arrive from within several minutes up to half an hour after the pulse, while the droplets keep coming in for hours, still leaving plenty of time between pulses for the atoms to rearrange themselves on the substrate. See Figure 3.4.

3.1.5 Film formation

When the plume hits the substrate, it condenses. Each pulse typically delivers less than 0.1 nm, i.e., less than an atomic layer. In vacuum, with incoming ions and atoms with energies of several eV up to more than 100 eV, the incoming material energy is usually high enough to overcome the surface diffusivity barrier [98] and the atoms can form crystalline solids far below the equilibrium temperature. The energy of the incoming particles is also so high that particles can be resputtered (especially atoms with low atomic weight [94]) and both interstitial atoms and tensile stress can be induced [115] (compression in the direction normal to the surface gives tensile stress parallel to the surface). See Figure 3.5 In a background gas the species are slowed down, so these effects will be less pronounced, which can be an important advantage. However, this also reduces the surface mobility of the incoming atoms and therefore the ability of the material to crystallize at low temperatures.

Note that while the time between pulses is long compared to the amount of time that atoms impinge on the substrate, the time needed for complete diffusion

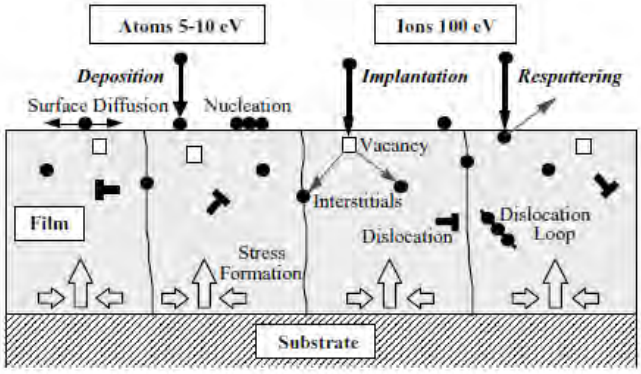

Figure 3.5: Figure by Krebs [116] showing various processes during film formation leading to film growth but also to stresses and defects in the growing film. Reprinted with permission of the publisher.

of atoms on the surface is similarly long. In a Monte Carlo model of the growth of $BaTiO_3$, Zhu et al. show that the surface roughness increases for 50 Hz deposition versus 1 Hz deposition [117]. Their model simply assumes a constant energy of the incoming atoms of 10 keV (quite high), a substrate temperature of 700 K and a constant deposition rate of 1 monolayer/s. They explain the increased roughness effect by the decreased diffusion time of the adatoms before the next pulse arrives.

3.2 Conditions for stoichiometric transfer

Paper after paper quotes stoichiometric transfer of the material composition from the bulk target to the growing film as the main advantage of PLD [115, 94, 118, 119, 96]. A newcomer to the field may not immediately notice the frequent qualifications that are added to this statement: "under optimal conditions" [98], "except for cases where non-ablative heating leads to dominant evaporation [94], "when the focused laser energy density ... and its spot size and shape are chosen properly" [96]. Even the enthusiastic Norton concedes: "While stoichiometric transfer of target composition is readily achieved for nearly every material, this does not ensure stoichiometric film growth at elevated temperature if any of the cation species possess high vapor pressures" [115].

These qualifications turn out to be key to the research in this thesis: The composition of the deposited film may be congruent to that of the target *under the right circumstances.* Indeed a great number of papers on PLD describe specific

instances of film deviation from the target stoichiometry (e.g., [120, 121, 122, 114, 123]).

An important observation on PLD was made in 1988 when Venkatesan and coauthors described how the material ejected by pulsed laser deposition consists of both an incongruently evaporated, $cos\,\theta$-distributed component and a congruent, forward-peaked component, with incongruent evaporation dominating at low fluence and congruent transfer at higher fluence [118]. While Venkatesan did not use the word 'ablated' to describe the congruent component, this word was subsequently adopted by the PLD community, as defined, for example, by Haglund, who calls laser ablation a sputtering process, where the material ejection is nonlinear with respect to the energy input and where a plasma ablation plume is formed. He notes that there is probably a continuum between what he terms laser 'desorption' (where material ejection is very low and linear with the energy input) and laser 'ablation' [124].

To obtain stoichiometric transfer, it is necessary to make sure that ablation dominates over evaporation. This balance can be viewed in terms of how fast the absorbing region of the target heats up versus how fast the heat is conducted away into the remaining target. Intuitively it makes sense that if a very large amount of heat is constrained within a very small region of the target, that heat will cause explosive vaporization much better than if the heat is 'spread out' either by being absorbed over a greater region or by being transported away by a high heat conductivity.

For depositions containing volatile components, numerous authors suggest the use of a background gas of the volatile species (often O_2 but in our case it would be the highly toxic H_2S) or a dual target with one target enriched in the volatile species (e.g., Zn or K) - see, for example, the suggestions of Norton [115], Lowndes [96], Frumar et al. [125] and Christen and Eres [126].

A second factor that strongly influences the composition of the growing film is the preferential scattering in the presence of a background gas mentioned above. Inside the plasma, all atoms are scattered so much that mass differences don't make much difference. Beyond the limit of the luminous plasma plume, however, a background gas will scatter light elements more than heavy elements [94, 120].

Third, as noted in Subsection 3.1.5 the atomic species may not all have the same sticking coefficient on the substrate, especially if the film is heated and the species have low vapor pressure. Also, light elements may be preferentially resputtered by incoming high-energy species.

In summary, non-stoichiometric film growth can be caused either by processes at the target, in the plume or at the growing film. Plume diagnostics can help distinguish which processes are taking place.

CZTS exemplifies the perfect storm of unlucky circumstances that make stoichiometric transfer difficult: S, Zn and Sn have all previously challenged PLD.

S is a volatile element and previous reports on PLD of S-containing compounds show that the films are frequently (though not always) poor in S [127, 128, 123], as further discussed in Chapter 4. Zn is also relatively volatile, and Norton specifically notes that Zn is known to give problems with film composition because the high vapor pressure in combination with a heated substrate gives a low sticking coefficient [115]. Finally, Krebs observed that among 30 metal alloys deposited by his group, a 50:50 Fe-Sn alloy was the exception to the rule of stoichiometric transfer at high fluence using a 248 nm KrF-laser, with highly Fe-rich films resulting [119], perhaps due to the relatively low cohesive energy of Sn relative to Fe and many other metals. Thus in hindsight it is easy to see that plenty of challenges might come up in deposition of CTS and CZTS by PLD as well as PED, where many of the same considerations are relevant.

3.2.1 Non-stoichiometric CTS growth; where did the SnS go?

When growing CTS films from a SnS-enriched target, we noticed that the composition of the films were highly Cu-rich compared to the desired composition. In order to find out where the SnS was going, we compared films grown facing the target and films grown nearly at right angles to the target. See Figure 3.6. The deposition rate at right angles to the target naturally was relatively low, so only a few films were grown thick enough for EDX quantification. Also see Table 3.1 which includes measurements of the average original target composition and the composition of powder scraped from the target after similar ablation to that used to make the films. The films were deposited at room temperature with the 355 nm laser. Note that due to the heavy droplet bombardment of both films, it is hard to measure the composition accurately; when making the comparison one must assume that there is a similar systematic error due to droplets in all the films. The error in the composition quantification of the multidomain target and the powder is even greater.

From Table 3.1 it is clear that the films deposited at a 90° angle to the target were far richer in S and Sn than the films facing the target. This demonstrates that the initial distribution of the elements in the plume was non-uniform: the S and Sn were scattered to higher angles while the Cu-expulsion was more forward-directed. This points to concurrent evaporation of SnS (with a nearly spherical $cos\,\theta$ distribution) and forward-directed ablation of the Cu-rich phases in the target. The high number of droplets on both types of films appears consistent with some kind of explosion where liquid droplets are hurled away in all directions from the laser spot.

Turning to the composition of the powders scraped from the ablated target, it appears that the lower the fluence, the higher the Cu-content remaining in the target was. This is consistent with the idea that SnS and S were evaporated

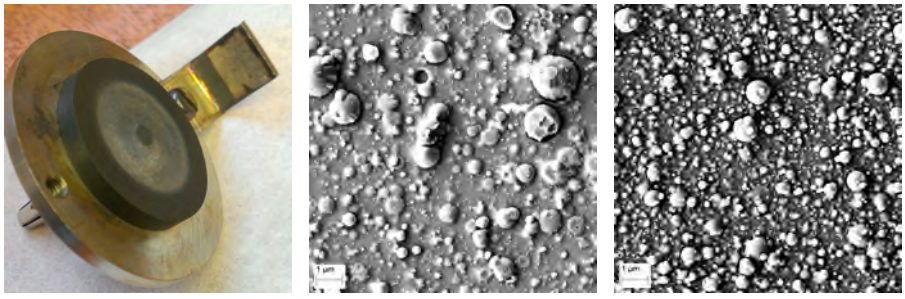

(a) (b) (c)

Figure 3.6: Deposition of a film at right angles to the target as well as one facing the target in the usual manner. (a) Target and substrate holder for (almost) 90° deposition. (b) Surface of film deposited opposite target (target-substrate distance 4.5 cm). (c) Surface of film deposited at nearly 90° from target. The spot size was 2.5 mm^2.

Table 3.1: Comparison of SnS-rich CTS films deposited facing the target or almost at right angles to the target (see text). Composition measured by 15 kV EDX in the Supra VP40 by Edoardo Bosco and Philip Rasmussen (films, powders) as well as Lasse Ravnkilde and Tomas Youngman (target). At least three measurements were averaged for each sample and the standard deviation of the measurements was about 1 % absolute.

Sample	Fluence J/cm^2	Spot size mm^2	Pulses #	Thickness µm	Cu %	Sn %	S %
Facing target	1.8	2.5	162000	> 6	25-29	29-30	42-44
90 °to target	1.8	2.5	162000	3	14	32	54
Facing target	5.1	0.9	81000	2	26-28	28-30	44-45
90 °to target	5.1	0.9	81000	1.1	12	34	53
Target	-	-	-	-	19	28	52
Powder	1.8	2.5	18000	-	25	29	46
Powder	2.3	2.0	18000	-	23	30	47
Powder	3.0	1.4	18000	-	20	30	50
Powder	5.1	0.9	18000	-	17.5	31	51.5

relatively easily, while ablating the Cu-rich phases in the target required more energy. The volatility of SnS was mentioned in Section 2.2.3.

Directly comparing the composition of the target to the films (or even the powders) is made difficult by systematic error due to the different roughness as well as the multicomponent nature of the target. The Sn- and Cu-rich domains seen in the target by EDX mapping meant that the EDX software's automatic inclusion of secondary fluorescence absorption and reemission was not correct. See section 5.6.4.

3.3 Droplet generation

Droplets of up to micron size are a regularly mentioned drawback of PLD and PED, especially if the films are to be used as deposited with no post treatments such as annealing or etching. Even with post-treatment, droplets can result in a rough surface, which is sometimes not an issue, but certainly poses a problem for solar cells, where a subsequent very thin buffer layer needs to be deposited on top of the film (the solar cell structure was shown in Figure 1.2). In this context it is interesting to note that in Fig. 3.6 we do not see a strong reduction in the droplet density at 90° compared to deposition on a target facing the substrate.

Examples of as-deposited CTS films are shown in Figure 3.7. A thickness gradient is clearly visible in Figure 3.7c, yet the amount of droplets in different areas of the film was not particularly different as seen in Fig. 3.7a. The composition was also similar across this sample size, with a slight change in the sample corner furthest away from the plume center, as seen in the table in Figure 3.7d, which demonstrates that composition measurements within about 1 cm of the plume center can be trusted for CTS films made even with a relatively large spot ($\approx 2.5\,\mathrm{mm}^2$). Inspection by low-resolution SEM (not shown) indicated that the surface morphology was similar in area F to areas A-E (Fig. 3.7c).

In principle, relatively low energy is needed for ejection of particulates compared to ablation since the fraction of energy that goes into fragmentation is small [125, 105]. Therefore, at least in metals, low fluence can lead to high droplet incidence when the target is rough: the energy is high enough to break structures on the target but not high enough to vaporize them fully [129]. In other words, inhomogeneity in the target surface increases droplet formation; this process is known as exfoliation [130]. However, other studies show a decrease in droplet density at low fluence [96] (this was also seen in our studies of CTS and CZTS as shown in Chapters 7 and 8).

Apart from target roughness, an important mechanisms leading to µm size droplets as mentioned by Lowndes [96] and Willmott and Huber [98] is subsurface boiling, leading to ejection of material above before it is vaporized. These authors also mention the recoil pressure from the Knudsen layer which is hard to

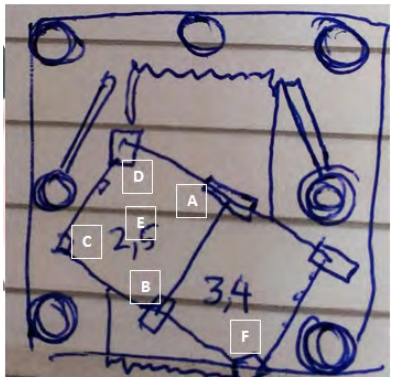

(a)

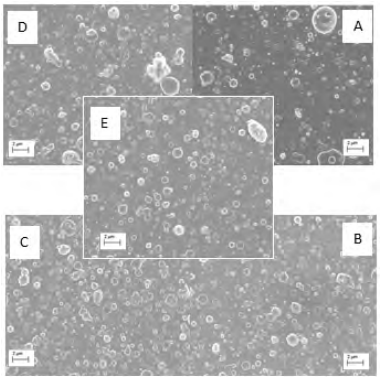

(b)

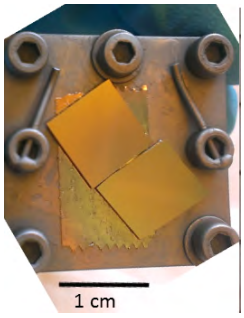

(c)

Spot	Thickness µm	Cu %	Sn %	S %
A	≈ 1.6	43	19	38
B	≈ 1.6	n.d.	n.d.	n.d.
C	n.d.	43	19	38
F	1.3	39	21	40

(d)

Figure 3.7: Mapping film uniformity. (a) Map of a CTS film with respect to the holder. The plume center was between points A and E. (b) SEM images of film surface at points A, B, C, D, E (approximately). (c) Photo of 100 nm thick CTS film as deposited by the 355 nm laser at room temperature on the substrate holder using a spot size of 2.5 mm^2. The different color of the film indicates the thickest/thinnest parts of the films due to interference. The plume center is located in a slightly different position than in (a). (d) Composition and thickness at different points. Composition measured by 15 kV EDX in the TM3000. The standard deviation of the measurements was about 1 % absolute. SEM images by Lasse Ravnkilde and Tomas Youngman.

distinguish from subsurface boiling experimentally. Both of these mechanisms are reduced when the absorption length of the laser is high compared to the thermal diffusion length, because there will be relatively less melted material compared to vaporized material.

Finally, an important mechanism causing droplets at very high laser fluence or very short pulses (i.e., fs PLD) is phase explosion: the heating of the target is so fast that the material passes the critical point and the temperature is too high for the liquid phase, but the pressure is too high for the gas phase, causing explosion of a gas and liquid mixture. This is likely the reason why material ejection in fs-PLD is often observed to be in the form of nanoparticles [104, 103].

Many strategies have been used to reduce the incidence of droplets on the films. The simplest is fast target spinning, intermediate to low fluence, and movement of the laser spot on the target in a raster pattern. As part of the work we tested what happened when we kept the laser energy per pulse constant and changed the spot size when depositing SnS-rich copper tin sulfide CTS films (i.e., the target was SnS-rich compared to the composition of stoichiometric Cu_2SnS_3). We found that there was little difference in the droplet area density for the three smaller spot sizes tested as shown in Figure 3.8, but the amount of droplets increased at very high fluences ($> 5\,\mathrm{J/cm^2}$). This could be due to increased target roughening with a smaller spot size.

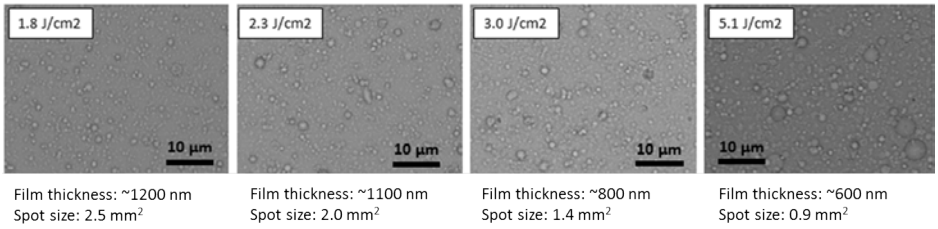

Figure 3.8: SEM images of SnS-rich CTS films made with a changing spot size and constant energy and number of pulses. The area density and size of the droplets is largest on the film made with the smallest spot size (0.9 $\mathrm{mm^2}$) and the highest fluence ($5.1\,\mathrm{J/cm^2}$) illustrating poorer coupling of energy into the target at this fluence.

As seen from the film thicknesses listed below the SEM images in Figure 3.8, the little experiment illustrated that using a small spot size was inefficient: the thickness of the films decreased, even though the number of pulses on the target was the same for each film. This reduction in deposition rate is most likely due to the wider plume expansion that would be expected when decreasing the spot size. However, it could also be influenced by an increased target roughening,

which also reduces the degree of forward direction of the plume, and a relatively higher shielding of the target by the nascent plume when the same amount of energy is coupled into a smaller area. The effect of changing the spot size on the deposition rate was investigated in detail by Ohnishi et al. [131], who found that for a given laser energy, there was a spot size that would give the highest deposition rate - it should neither be too large nor too small.

Another approach to reducing the amount of droplets is off-axis deposition, since the droplets are heavy and not significantly scattered by a background gas. Notice, however, that this will not always work, at least in vacuum: As noted, in our experiments with CTS with a 2.5 mm^2 spot size, there were still plenty of droplets at 90 °from the target (Figure 3.6), and droplets were also visibly ejected at large angles in a Zn-deposition with a much smaller spot size of ≈ 0.2 mm^2 as seen in Figure 3.1b. In such cases, one can even use a reversed substrate orientation, so that the deposition happens on the surface facing away from the target. More sophisticated methods include velocity filtering by a mechanical shutter synchronized with the laser repetition rate, allowing fast atoms and ions to pass, but blocking the slow droplets [129]. Both in PLD and PED it is also possible to apply a negative voltage between the target and the substrate, repelling the droplets, which have negative charge [132]. With a high enough voltage, one may even evaporate the droplets [125].

Finally, several authors suggest that reducing the laser wavelength reduces the amount of droplets on the films. This approach was attempted as part of this thesis, reducing the wavelength for CTS deposition from 355 to 248 nm, and the results of the study were published in an article in Applied Surface Science (Appendix B) as described in Chapter 7. As discussed in the article, at least two mechanisms may contribute to the reduction of droplets in films deposited with UV lasers compared to visible or infrared lasers: 1) the absorption depth is shorter, resulting in more efficient ablation [133], and 2) even when there is little difference in the absorption coefficient, as in 355 nm versus 248 nm PLD of YBCO, the droplets themselves may be fragmented by absorption of UV light at the end of the laser pulse as remarked by Koren et al. [134].

From our SEM images of CTS films it appears that sometimes a gas bubble bursts inside a droplet, leaving a round crater in the droplet. Also, droplets are often surrounded by a crown of smaller droplets or crystallites - maybe due to splashing and/or nucleation on the surface- or perhaps the large droplets attract smaller droplets electrostatically. See Fig. 3.9. Cross sectional images are shown in Fig. 3.10 illustrating how deeply the droplets are sometimes embedded in the film. It appears that some droplets look like cones sticking up from the surface while others are more round and low.

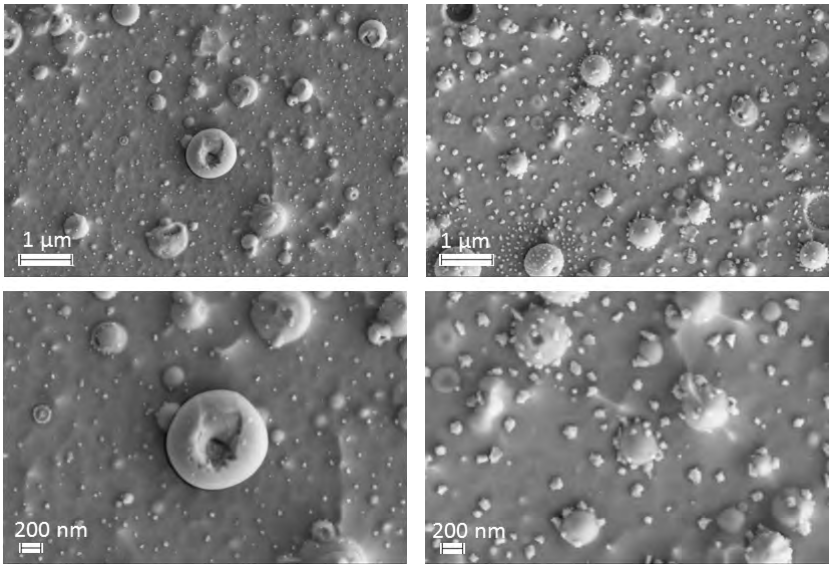

(a) Droplets on CTS (b) Droplets on SnS-rich CTS

Figure 3.9: Closeup SEM images of films deposited at room temperature with the 248 nm laser showing droplets on CTS (a) and SnS-rich CTS (b). In (a) we see that apparently a bubble has burst inside a droplet as it solidified. In (b) we see that although the main part of the film was amorphous and no crystallinity was detected by X-ray diffraction, apparently small crystals or crystal-like grains were able to form on the film surface. SEM images by L. Ravnkilde and T. Youngman.

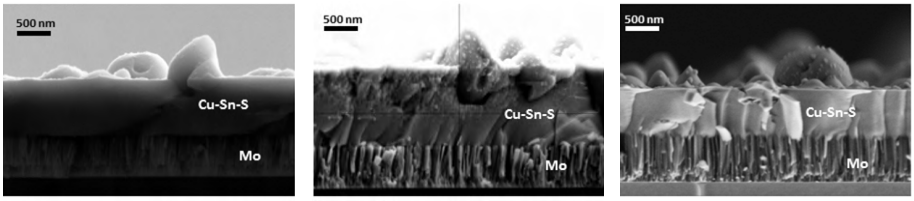

(a) (b) (c)

Figure 3.10: Cross-sections showing droplets penetrating deep into the growing film as well as the profile of different types of droplets - some apparently rounded, perhaps due to vapor boiling off after they landed on the substrate, others characteristically cone shaped. (a) and (b) depict SnS-rich CTS made with exactly the same recipe of $2.3\,\mathrm{J/cm^2}$ using the 355 nm laser. (c) shows a film made with the 248 nm laser at about $1.6\,\mathrm{J/cm^2}$; image (c) taken by L. Ravnkilde and T. Youngman.

3.4 Impact of deposition conditions

A large number of factors influence the quality of the films made in PLD including:

- laser wavelength and pulse duration
- target rotation (as fast as possible for uniform ablation)
- laser raster pattern and speed
- adjustment of the background pressure
- adjustment of the distance from target to substrate (especially in the presence of a background gas)
- angle of the substrate surface to the direction of plume expansion
- spot size
- density of the target
- repetition rate
- substrate temperature
- type of substrate (amorphous or crystalline, lattice (mis-)match with film, possible reaction with growing film)

Laser wavelength and pulse duration have a fundamental impact on the deposition as we will see in Chapter 7. The best wavelength is the one where the material absorbs the most, which is often in the UV. The pulse length directly influences the intensity and therefore also the ablation efficiency. Additionally, longer pulses may proportionally ablate the target less efficiently but heat the plume more, causing extra ionization as well as perhaps additional breakup of droplets as discussed above.

Some of the remaining factors have already been mentioned above, but will here be treated one by one:

First, fast target rotation and a large laser raster area usually reduce the number of droplets by reducing the ablation-induced roughening of the target. We saw above directly how changing the spot size can influence the number of droplets and the efficiency of the ablation (Fig. 3.8. Note that the spot size on the target may change appreciably if the laser beam spot is moved in such a way that it impinges on the target at a different distance from the focusing lens, as pointed out by my colleague Andrea Cazzaniga in his PhD thesis [135]. This may be avoided by steering the target rather than the laser beam or by ensuring that the laser is moved only in the plane where the size on the spot is constant.

Ujimoto et al. provide a detailed description of a target steering pattern that reduces target roughening and droplet surface density drastically for deposition of $BiFeO_3$ with an ArF excimer laser [136].

Adjustment of the background pressure and the distance from target to substrate can influence the energy and angular distribution of the species impinging on the substrate. The angle of the substrate surface relative to the direction of plume expansion is also important for both the amount of droplets and the stoichiometry of the growing film as noted above. Many studies are devoted to exploring these parameters; see, e.g., [96, 137, 111, 114, 138].

The importance of a dense target is stressed by both Lowndes and Norton as a method of reducing the number of droplets[96, 115]. Additionally, a single phase target may be important for controlling film stoichiometry. Lowndes comments on the experiments by Uchiki et al. [123] on non-uniform deposition of $AgGaS_2$ from an AgS-GaS target: "it is difficult to precisely control composition and quality of films deposited by ablation of an unreacted two-phase target" ([96] p. 541). This certainly corresponds to the experience that will be presented in this work. In principle a multiphase target should be ablated stoichiometrically if the laser energy is high enough to vaporize all elements within the spot. In practice, using a target with large differences in the volatility of the different phases turned out not to be so easy.

Although one would not expect repetition rate to play a major role as long as the time between pulses is much longer than the plume expansion time itself, we found experimentally that CZTS deposited at 45 Hz were different from films deposited at 7 Hz: the high repetition rate films were slightly more S-poor and Cu-rich and contained more droplets (Fig. 3.11) as will be discussed further in Chapter 8. This may be because the heat dissipation from the target is slow enough that parts of the target is still melted when the next laser pulse hits. Neither the laser raster pattern nor the target rotation rate were changed from 7 Hz to 45 Hz, so there may have been more local heating which was not fully dissipated between adjacent pulses. This could lead to splashing of a greater proportion of molten phase as well as SnS evaporation and Cu-enrichment of the films.

As for the type of substrate, Shen and Kwok demonstrated for a number of metal-chalcogenide binary phases that lattice matching with the substrate influences the orientation of the growing films [137]. On lattice-matched substrates, PLD can allow growth of epitaxial films, e.g., CZTS on GaP [139], CdTe on GaAs [140] and (somewhat lattice-mismatched) CIGS on Si [141].

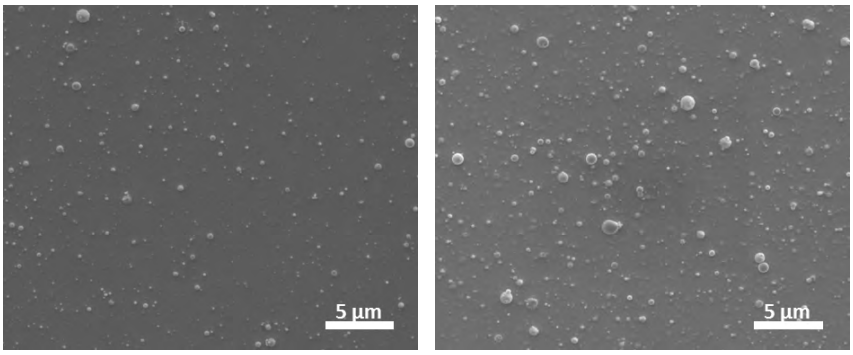

(a) 7 Hz (b) 45 Hz

Figure 3.11: Morphology of CZTS films deposited at room temperature with the 248 nm laser at 7 Hz versus 45 Hz. (a): 7 Hz. (b): 45 Hz. The 45 Hz film was on average a little bit more Cu-rich and S-poor according to EDX measurements. SEM imaging carried out together with S. Engberg.

What is epitaxial growth? According to Martin et al. [142], "Epitaxial growth refers to extended single-crystal film formation on top of a crystalline substrate... heteroepitaxy refers to the case where the film and substrate are different materials, but have similar structures [i.e., lattice parameters] that help guide the growth of the film. Typically f $<$ [10 %] is a requirement for epitaxy" (where f is the size of the lattice mismatch between the materials)

3.5 Pulsed electron deposition

PED was developed in its modern form a few years after PLD gained popularity in the late 1980's by Schultheiss and co-workers at Kernforschungszentrum, Karlsruhe. In the early 1990's they worked on the design of a "pseudospark" device originally invented in 1979 [143, 144] and in 1994 they demonstrated the more stable and efficient "channel spark" configuration in collaboration with the HTS lab at the International Centre for Theoretical Physics in Trieste [145]. The channel spark design is the most successful discharge method for PED [146] and by 2005 a device of this design was available commercially from Neocera, Inc. [92].

PED like PLD is capable of achieving stoichiometric ablation and low-temperature film crystallization because of the high-energy pulsed beam impinging on the target. Since PED requires only a reliable pulsed electron source rather than an expensive high-power pulsed laser, PED is potentially a cheaper technique. Nonetheless, so far only relatively few labs around the world work with PED, probably because reliable commercial PED guns have only been available for a short time. Like PLD, the technique has proved successful for the deposition of oxide layers. Here we will look at the physics of the process.

3.5.1 Initiation of ablation in PED

In pulsed electron deposition the ablation process is initiated as follows: an electrical trigger allows a capacitor to release a high voltage pulse (10-20 kV), which in turn initiates an electrical discharge inside a hollow cathode filled with low-pressure Ar gas. The hollow cathode is generally an alumina tube about 3 mm in inner diameter. The discharge takes the form of plasma which propagates rapidly down a dielectric tube, giving rise to ablation when it hits the solid target that acts as the anode. See Figure 3.12. Like in PLD, the ablation process takes place in a vacuum chamber, which is grounded.

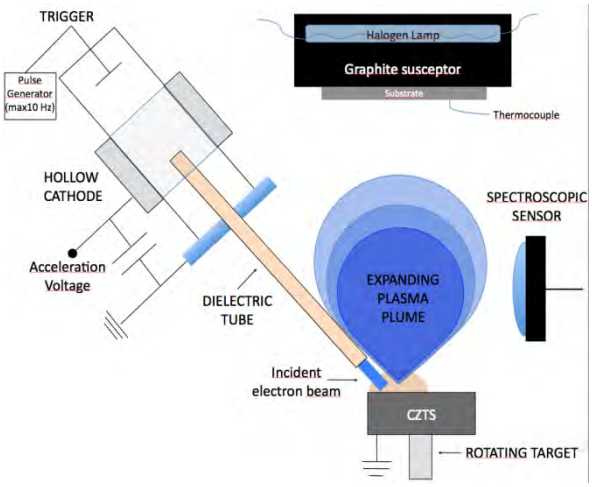

Figure 3.12: Schematic representation of the PED setup used in this work. Illustration by S. Rampino and F. Pattini.

The design of the pulsed electron discharge system used in this study (and in all recent PED work that I am aware of) is a channel spark discharge system. The channel spark system was first demonstrated in 1994 [145] after much work by

the same group on thin film deposition using the pseudospark discharge system [147, 144].

The irradiance in PED can be comparable to PLD, on the order of 10^8 W cm^{-2} [148]. The energy transfer from the electrons to the target atoms happens through collisions with the electrons in the target and is dependent on the density of the material as well as the ionization energy [149]. The main energy loss happens when a core electron is excited or even ejected from an atom and then loses energy again by thermal dissipation [150].

Strikovski and Harshavardhan describe the temperature rise at the surface in terms of a simple model similar to what we examined above for PLD: the target surface temperature change over time dT/dt is expressed as a function of the absorbed power per unit area, q (note that this is defined differently from Q, the power per unit volume used above), the specific heat, c_p, the density, ρ, and the distance over which the heat is absorbed and distributed by thermal diffusion during the electron pulse [151]:

$$\frac{dT}{dt} \approx \frac{q}{c_p \rho (l_{abs} + l_{th})} = \frac{J(U)U}{c_p S \rho (l_{abs} + l_{th})} \tag{3.5.1}$$

where $l_{abs} \propto U^2$ is the distance over which the electron energy is absorbed, l_{th} is the thermal diffusion length given by the heat diffusion equation (Equation 3.1.4), S is the beam spot area, U is the voltage, and $J(U)$ the voltage-dependent current per unit area impinging on the target. The power area density q=JU. The $l_{abs} \propto U^2$ approximation derives from the expression for the electron stopping power that they assume; several models exist which should lead to similar results according to the authors [151].

The expression provides a useful framework for thinking about PED because it shows that for large l_{th} (i.e., in metals), the surface heating rate of the target and therefore the ablation efficiency will be highest for high voltage and current. On the other hand for relatively low l_{th}, the electron absorption length will be important in determining the heating rate, and since it increases with increasing voltage, there will be a maximum rate of heating for some value of J(U)/U which is not necessarily equivalent to the highest possible voltage the setup can achieve [151]. Strikovski et al. advise that once one has found the best voltage it is helpful for achieving efficient ablation to increase the current by keeping the hollow cathode as close to the target as possible so that the beam is as confined as possible when it hits the target [101].

It is important to note that the electron pulses in PED are poly-energetic with the initial part of the pulse consisting of highly energetic electrons followed by a tail of lower energy ones [149, 152] in contrast to the single photon energy of the lasers used for PLD. This means that slow, low-energy electrons will always be present and can cause non-stoichiometric evaporation even while faster high-

energy electrons give rise to stoichiometric ablation as seen, e.g., by Pattini et al. [153].

While for a monoenergetic electron beam the maximum energy deposition (and therefore heating) occurs some distance beneath the material surface, Tricot et al. show that for a modeled polyenergetic beam hitting a ZnO target the maximum temperature is always at the surface [149]. This is important to avoid subsurface boiling and explosions of the target.

Using an imaginary single-phase CZTS target as an example for comparing PLD and PED conceptually, 99 % of the intensity of a 248 nm laser would be absorbed less than 100 nm into the material as calculated from the absorption coefficient [154], while the energy of 16 kV electrons will be deposited at depths of hundreds of nm (modeled by the program Casino [155] assuming a CZTS density of 4.56 g/cm3 [156]). Taking into account the polyenergetic beam in PED, the energy deposition will occur closer to the surface, but the maximum depth of the energy transfer to CZTS would still be expected to be deeper with a pulsed electron beam than with a 248 nm laser.

3.5.2 Plasma generation and expansion - PED versus PLD

While in PLD the nascent plume shields the target from further irradiation, the energy absorption from electrons does not change depending on whether the material is in the vapor or solid phase [101] and the absorption depth therefore continues to be relatively long even after the ablation plume forms, allowing the electrons to continue ablating the target. This helps explain why PED generally leads to a higher deposition rate than PLD.

The effect of the lower absorption means that more of the PED energy goes into removing material from the target and less into energizing the species in the plume. This matches what is seen experimentally: the plasma electron temperature in the early PED plume is lower than that in similar PLD experiments [150]. Nistor et al. [146] showed through ICCD imaging that the velocity distribution of the species ejected from the target in PED is broader than in PLD with the most energetic species moving just as fast as the ones in PLD but with a lower average energy. Similar findings of a very broad PED energy distribution in the plume with species both much more and much less energetic than in PLD was shown by ion probe measurements by Strikovski et al. [101]. The broader velocity distribution means that ablated species keep arriving on the substrate for a longer time in PED than in PLD.

Some species in the PED plume are still ionized, making it a true plasma (i.e., a partially or fully ionized gas) rather than 'just' a fast atom cloud: the electrons are able to ionize the atoms in the plume through collisions just as they may ionize atoms in the target. Tricot et al. showed by time-resolved OES spectroscopy that

though the main pulse in PED is around 100 ns (this pulse length is commonly reported in PED literature), low-energy, weakly focused electrons keep being emitted for hundreds more nanoseconds, ionizing the nascent plume [150].

3.6 Summary: Advantages and drawbacks of PED and PLD

The main advantages of PLD and PED include:

- the high energy of the adatoms landing on the film, enabling crystallization at low temperature
- the possibility of stoichiometric transfer under the right circumstances
- the flexibility of the method as there are many parameters that can be tuned in a given setup (laser fluence, electron voltage, background pressure, distance from target to substrate, density of the target, type of substrate, substrate heating, substrate orientation, different background gases, and more)
- good adhesion of the film to the substrate and the possibility of layer-by-layer epitaxial growth due to the pulsed nature of the process

Some important drawbacks include:

- the volatile components of the target may not always be congruently transferred to the growing film
- the many parameters can be challenging to navigate
- the uniformly deposited area is generally small (from about 2 cm in diameter in our setups up to about 10 cm in diameter in others)
- droplets can be ejected from some types of target material, making the deposited material rough, and requiring removal through modification of the deposition process
- defects and strain can occur in the deposited films due to the high energy of the incoming particles (especially if there is no background gas)

The physics of the nanosecond laser ablation process is complicated and the high-pressure, high-temperature physical constants of many materials are little known. Therefore no accurate models have been developed that can predict exactly what might happen when one decides to deposit a new material by this technique.

Chapter 4

PLD of chalcogenides in the literature

A number of research groups have studied PLD of CZTS and numerous more have studied other chalcogenides, particularly ZnS. This chapter will review the literature on PLD of CZTS followed by the literature on PLD of CIGS, CdTe, ZnS and other chalcogenides.

4.1 PLD of CZTS

PLD of CZTS has been carried out under a wide array of conditions including different lasers, target types, substrates, substrate temperatures, and background gases. The earliest study, by Sekiguchi et al., is from 2006 and describes epitaxial growth of CZTS on (100) GaP [139]. A subset of the studies describe making solar cells. In all of these, the films were annealed at high temperature following the deposition, including the 5.2 % efficiency solar cell made by my colleagues in the CHALSOL project [157].

In Section 2.2 we looked at the material characteristics of CZTS and the experience from other groups in general on how to make good solar cells. Here we will look at the experience of other groups making CZTS by PLD. We will start by looking at room temperature depositions of CZTS by PLD followed by higher temperature depositions. An overview of a number of results on PLD-deposition of CZTS and closely related targets, mainly at 248 nm, is shown in Appendix E. The main trends in the studies will be summarized below.

At room temperature, films deposited by PLD were amorphous with micron-sized droplets [158]. Large CZTS grains do not form unless the substrate temperature is raised [159]. Therefore CZTS films made at room temperature must be annealed, and this is the main focus of the articles that describe room tem-

perature deposition [160, 158, 161, 162, 163, 164]. The main lessons from these articles are:

- the amount of droplets is lower using a low fluence [158, 164]
- stoichiometric transfer is not assured using UV ns-PLD even at room temperature [160].

Regarding the stoichiometry, Moriya et al. [160] found S and Sn-rich, Cu-poor films relative to the target composition with a 248 nm laser. Che Sulaiman et al. [164] investigated the composition as a function of fluence and saw no particular trend, in contradiction to the strong trends in the composition that my colleague Andrea Cazzaniga observed when the fluence was increased [157], as will be discussed in Chapter 8. It may be that the trend was obscured by errors in the measurements due to different thicknesses at different fluences, as the authors kept the deposition time constant rather than increasing it at low fluence to compensate for the lower deposition rate, or it may be that the fluence they used was not low enough for there to be a major change. Their films were in the 300-600 nm thickness range, so their reported absolute values of the film composition cannot be trusted (see discussion on the impact of sample thickness in EDX measurements of CZTS and CTS, Section 5.6.4.

On the composition of the droplets (all groups that show SEM images of the as-deposited room temperature films or discuss their morphology observe droplets): one group observed that the droplets contained Cu-Sn-S [160, 158], while another group saw Cu_xS and SnS_y (or perhaps Cu_xS and Cu-Sn-S) [164]. In contrast, in a study in which CZTSe was deposited by a 1064 nm laser, the droplets were of the same composition as the target [165]. This is similar to the observations in PED of CIGSe.

In 248 nm PLD of CZTS at 300 °C, a lack of S has been observed a few times in the as-deposited films: Sekiguchi et al. measured a Cu-rich, S-poor composition of films on GaP substrates at 300 to 400 °C by EMPA (electron micro-probe analysis) [139], and Sun et al. measured a Cu-rich, Zn- and S-poor composition by EDX on 1.2 µm thick films deposited on Mo/SLG at 300 to 450 °C [159]. Other groups that found S-deficiency at 300 °C measured thinner films with EDX, so their quantification may be more uncertain [161, 166]. One of these groups varied the fluence at 300 °C while keeping the film thickness constant, which should make it possible to compare the composition measurements among each other, but they found no trend in composition versus fluence [166].

The CZTS films deposited at a substrate temperature above room temperature (e.g., 200-500 °C) were crystalline and often had a strong XRD peak corresponding to the CZTS (112) planes, indicating a preferential growth direction [139, 159]. Some of the studies report secondary phases: Cu_xS [159] and Sn_2S_3

[167] or non-specified secondary phases [168]. Even the authors that report no other secondary phases and use Raman to complement the XRD studies cannot rule out the presence of ZnS as they do not use UV-Raman [161]. Higher temperature generally led to larger grains, but not always to the best film quality overall in terms of, e.g., bandgap close to that predicted for CZTS or in terms of pinholes and roughness of the films [159, 161].

Two other high-temperature studies report the composition of thick deposited films: One group found S-rich films compared to the targets, surprisingly at as high a temperature as 450 °C using a fluence of 2 J/cm^2 with a laser very similar to our 248 nm laser [169] - this fluence would result in Cu-rich, S-poor films in our setup. The final group found decidedly Cu-rich films at fluences of 0.5-0.8 J/cm^2 with a 266 nm frequency quadrupled Nd:YAG laser and an extremely long deposition time of 5 hours (!) at 500 °C in vacuum [168]. In contrast to the multiphase target used in our study, this group used a polycrystalline CZTS target which truly consisted of CZTS crystals (stannite or kesterite phase). This diligent study attests that a single-phase target is not enough to ensure stoichiometric transfer from target to substrate in PLD of CZTS at least for a prolonged deposition at high temperature. It would have been interesting to see the composition of room temperature-deposited films from the same target.

Altogether, the experience of other groups in making as-deposited films at elevated temperature hinted that there might be problems with Cu-rich, S-poor films, but because of the many free parameters (fluence, temperature, deposition time, nature of the target, etc.), it is difficult to say if it might be possible to overcome this problem or not.

Finally, several studies shown in Appendix E use quite a different PLD-approach to obtain CZTS: One group deposited CZTO (Cu_2ZnSnO_x) with a 248 nm laser at room temperature and subsequently annealed it to obtain CZTS; this group held the record PLD CZTS solar cell efficiency with 4.94 % efficiency [170] until the results of Cazzaniga & Crovetto [157]. Another group used a CZT target with a 248 nm laser, performing depositions at room temperature up to 150 °C; this group struggled with a very low depositon rate and thin films that were non-continuous after annealing [167]. A third group used a completely different approach of ablating a Cu and a Zn/Sn target in a H_2S background gas followed by N_2 annealing.

A number of other studies are not included in the table for example if the data or the experimental description was incomplete in relation to the as-deposited PLD films.

4.2 PLD of other chalcogenide solar cell materials: CIGS and CdTe

PLD has been used not only to deposit CZTS but also to deposit CIGS and CdTe. Compaan provided an overview of the early use of laser processing and laser deposition for solar cells in 1995: lasers were used to induce surface modifications in amorphous silicon solar cells, for scribing of silicon solar cells (this means dividing the surface layer up into cells and preparing for the deposition of bus bar layers), and of course for deposition of solar cell materials. Although he did not believe that PLD could be used for large-scale deposition of solar cells for commercial use, he saw PLD as a useful technique for experimenting with doping and graded composition of, e.g., CdTe [171].

4.2.1 PLD of CIGSe

In the following we will use the term CIGSe to distinguish selenide CIGS (the commercial and 22.6 % record efficiency variety) from pure sulfide CIGS and sulfo-selenide CIGS, which are also being researched but have been less efficient so far. Most work on PLD of CIGS has been with selenides.

Already in the early 1990's, Schock's group in Stuttgart experimented with PLD of CISe2 and obtained > 8 % efficient solar cells, compared with a record efficiency at the time of > 15 % for the pure indium absorber layer [172]. They obtained Se-poor films as-deposited at 520 to 580 °C from slightly In-rich polycrystalline targets by a 266-nm, 6-ns Nd:YAG frequency-quadrupled laser, and they compensated the Se-deficiency simply by evaporating Se from a boat near the substrate inside the deposition chamber [173]. The films they produced were single-phase and the main problems cited in the articles were droplets on the film surface as well as an In-poor surface layer.

Several other groups have worked with PLD of CIGSe or CISe. For example, Gremenok et al. focused on the deposition of single-phase stoichiometric CIGSe films on glass substrates by millisecond-pulsed 1064 nm laser irradiation at 320 °C-380 °C in order to investigate the bandgap as a function of composition [174, 175]. Yoshida et al. also claim no problems with stoichiometric transfer of CISe using an XeCl excimer laser at 308 nm at as high a substrate temperature as 550 °C [176]. In contrast, e.g., Tverjanovich et al., Leppävuori et al. and Jo et al. report Se-poor films at high fluence and temperatures from room temperature to > 300 °C using 308 nm XeCl lasers (the two first) or a 248 nm KrF laser (the last) [177, 178, 179]. Levoska et al. found that the Se-content depended on temperature (as might be expected) with a slight Se-loss relative to the target in CISe above 150 °C and in CIGSe above 350 °C.

In the last few years, groups in Taiwan have been working on fs- and ns-

PLD of CIGSe with the stated aim of developing a low-temperature deposition technique for use on flexible substrates. Shih-Chen Chen et al. find that fs-PLD of CIGSe results in films made up essentially of nanoparticles, which they deem more promising than ns-PLD, plagued by droplets and Cu_xSe phases on the surface. However, no solar cells are presented to prove that the films work as intended and an Se-poor composition is found for all the films [180]. Chia-Chuan Chen et al. have further explored fs-PLD of CIGS at 300 °C, but have multiple issues that need to be resolved including droplets and Se-deficiency in the films in order to create low-temperature as-deposited solar cells [181]. Like the groups making CZTS solar cells from PLD films, this group has experimented with annealing [182].

Other groups have continued working with laser irradiation of CIGS not to manufacture the absorber layer but to scribe the cells [183], but to my knowledge no groups have achieved higher efficiency with as-deposited CIGSe or CISe than the early work by Dittrich et al. in Stuttgart [172].

Overall it is clear that stoichiometry can be an issue not only in deposition of CZTS but also in CIGSe, as many of the groups surveyed here apparently experienced Se-loss during the deposition whether using UV ns-lasers or fs-lasers. The ones who did not have this problem (or who perhaps found ways to overcome it) were generally using fused silica or glass substrates and apparently did not go on to make solar cells.

4.2.2 PLD of CdTe for solar cells and photodetectors

Compaan et al. were able to make > 10 % efficient CdTe solar cells using films deposited by PLD (or what they called laser physical vapor deposition, LPVD) already in the early 1990's [184]. They used PLD to explore incorporation of ZnSe and ZnTe in the films, and had slight issues with preferential encorporation of Te over Se.

In other early CdTe experiments by PLD, Bhattacharya and Bose deposited CdTe on Si using a ruby laser and found slightly Te rich cubic phase films [185]. Ismail et al. demonstrated good photoresponse for similar heterojunctions made by PLD at 200 °C much later, in 2007 [186]. A very recent article used PLD to deposit a CdS/CdSe stack on a SnO2 transparent conducting oxide window layer for a superstrate CdTe solar cell [187]. The aim was to widen the transmission region of the solar cell top layers above a CdTe absorber layer deposited by closed-space sublimation and the PLD layers succeeded in increasing the performance of their solar cells, though they are far from the world record efficiencies [187]. Other groups have used PLD to make both the CdS and the CdTe layer of thin CdTe/CdS solar cells with the aim of reducing the material use (mainly of the rare Te) while increasing the material quality. These groups achieved 5-6.7 %

efficiency (one group after annealing with $CdCl_2$, a treatment often used in CdTe solar cell processing) [188, 189]. Li et al. explored the temperature and pressure required to obtain good-quality CdS and CdTe and found that above 200 °C the deposition rates of both materials dropped in vacuum, perhaps due to a lower sticking coefficient, but that CdTe could be made to stick up to 500 °C by applying a background Ar pressure [189].

A few other articles on PLD of CdTe within the last decade are exploratory in nature, concluding vaguely that the method holds promise but that further optimization of e.g. grain growth is needed for high-quality devices. CdTe films deposited by PLD (either by 355 nm or 1064 nm irradiation) on glass and transparent conductive oxides are in some cases porous [190, 191]. In the 355 nm laser study, which was done on heated substrates in vacuum, Ghosh et al. found Te enrichment of all the films [191].

Overall, PLD has apparently been a useful tool for exploring the growth of CdTe and related layers for solar cells. While most groups do not focus on stoichiometry issues, a few authors report Te-enrichment of the films. CdTe used for solar cells (and CdTe grown on Si) is cubic-phase, but PLD depositions also sometimes produce the wurtzite phase (possibly mixed with the cubic phase) [191, 192], as also demonstrated by Shen and Kwok already in 1994 [137]. Which phase is obtained may in general be influenced by the amount of metallic versus non-metallic component present; Tairov and Tsvetkov noted that the hexagonal phase may preferentially form for both CdTe and ZnS during co-evaporation with an excess of the metallic component, while the cubic phase is formed under non-metal excess [193]. However, this does not match the observation of Ghosh et al. of hexagonal phase under Te excess, which may occur due to the non-equilibrium nature of PLD.

4.2.3 Lessons from PLD of CIGS and CdTe

Compared to the number of groups working with CIGS and CdTe solar cells, relatively few use PLD. Schock's and Compaan's groups who pioneered the use of PLD for these materials have continued to do research on CIGS and CdTe extensively, but have stopped publishing papers using PLD as the deposition method. Clearly other methods were deemed more suitable for continuing research. Compaan writes that the experience gained from experimenting on CdTe by PLD could be transferred to RF-magnetron sputtering, a method he continued to pursue for nearly two more decades [194]. In the case of CIGS, research by PLD continues but appears plagued by difficulties in obtaining the correct crystalline quality for solar cells. In general, for the high-quality materials needed for solar cells, these chalcogenide materials seem to pose a challenge, be it due to stoichiometric deviation from the ideal or other defects introduced by the high-energy

ablated particles arriving at the film.

4.3 PLD of ZnS

The most important other chalcogenide treated in this thesis were CTS and ZnS. CTS has only been deposited by PLD by one other group, whose first article came out after our first work had been published. This will be briefly reviewed in Section 7.1. Here we focus on PLD of ZnS, which has been extensively investigated. Some general results can be learned from Shen and Kwok [137] who deposited ZnS with a 193 nm ArF excimer laser ($\tau = 15$ ns) along with a number of other binary chalcogenides, namely ZnSe, CdS, CdSe, and CdTe, which all crystallize in both a cubic and a hexagonal form. They make the following observations that are useful for the present thesis:

- the films could form crystals from 100 °C but had the highest quality at 300 °C
- above 400 °C the films lose some of the chalcogen component (measured by EDX)
- the authors use a laser repetition rate of 10 Hz, explaining that a higher repetition rate leads to defects because it does not give enough time for the atoms landing on the film to diffuse to the correct lattice sites.

Many other groups have used PLD to deposit ZnS and on the whole it appears to be quite a well behaved material for PLD, as noted by my colleague Andrea Cazzaniga in his PhD thesis [135]. The films are generally smooth and although some authors report problems with lack of S, it does not appear to be a large problem.

4.3.1 Literature on PLD of ZnS

Because of the many applications of ZnS, a large body of work has been published on ZnS thin film deposition. Since the 1990's numerous groups have used PLD to make ZnS, some focusing on making doped cubic-phase ZnS for various luminescent properties, others aiming to use PLD as a route to wurtzite-phase ZnS. Wurtzite ZnS is the less thermodynamically favorable phase but has stronger nonlinear properties than sphalerite ZnS, and PLD's ability to yield non-equilibrium phases has been exploited to grow wurtzite ZnS on sapphire [81, 195].

A matrix detailing the many PLD studies of ZnS is shown in Appendix F. This format provides a much easier overview of the many studies than the text summary below.

Substrate crystal orientation and temperature as well as background pressure all influence the growing ZnS films in PLD. Several authors report deteriorating quality of cubic ZnS films above approx. 400 °C [196, 137]. On the other hand, wurtzite ZnS depositions were most successful at 400-600 °C [81, 195, 197]). These authors all report decomposition of the films at higher temperatures.

Cubic epitaxial ZnS has been grown on GaAs (with some lattice mismatch in the bottom 150 nm of the films) [196] and on Si, where the epitaxy was best below 500 nm film thickness, with a mixture of cubic phase orientations occurring at higher thickness [76]. In the cubic films, a high background pressure was apparently best for obtaining high-quality films [196, 198]. On glass, the crystalline phase was not as clear as on structured substrates [78, 199]. This was also the case in PED of ZnS on soda lime glass [83]. However, Yano et al. and Shen and Kwok found predominantly cubic-phase ZnS on glass at substrate temperatures of 300-400 °C.

Overall, the best cubic-phase films were found around 300-400 °C. The crystalline phase of the film is strongly influenced by which substrate it is growing on and most authors were also specifically looking for this effect. Thus to get cubic-phase films it is best to use a lattice matched cubic substrate.

In nanoparticle ZnS and in films on unstructured substrates or formed at low temperatures, the phases may be mixed as the hexagonal and wurtzite polytypes differ only in the stacking orientation in one dimension, so the energy of transformation from one form to the other is very small [200]. Stoichiometry could also play a role in determining the most energetically favorable phase; as mentioned above in the discussion on PLD of CdTe in Section 4.2.2, this is the case in co-evaporation [193].

As for the stoichiometry of the as-deposited films, some authors found that the films were sometimes S-poor compared to the target (e.g., Karner et al. [79] in a background gas with the stoichiometry depending on the distance between substrate and target). McLaughlin et al. found that the S content depended on the fluence in films made with a 248 nm laser: films made at 2.5 and 5 J/cm^2 were S-rich (most at the lowest fluence) while a film made at 20 J/cm^2 was S-poor [78]. It is not clear if the observation of slightly S-poor films relates to the temperature, other than the fact that above about 550 °C the films lose S and degrade [195].

An interesting investigation of non-stoichiometric transfer of Cr-doped ZnS was carried out recently [201] which showed that the inclusion of metallic Cr in a ZnS matrix did not result in complete ablation of both metal and ZnS, but that Cr was left behind in the target. The explanation presented by the authors was that Cr existed as small distinct regions in the target which were highly reflective to the 248 nm laser and which had a high thermal diffusivity, quickly dissipating the heat that they did absorb. With increasing fluence, they found an increase

in the amount of Cr in the films, which could have a variety of causes. While this situation is not exactly like the one we had with the multicomponent CZTS targets discussed in Chapter 8, the same kinds of mechanisms may play a role.

A similar observation on increasing dopant incorporation with increasing fluence was made in an investigation of Cu-doped ZnS, where the non-equilibrium nature of PLD to create an otherwise thermodynamically unlikely mixing of Cu in ZnS. The aim - which was apparently achieved successfully - was to create a p-type transparent conductive film [195].

4.4 Other chalcogenides

Two other important chalcogenide families treated in this thesis are Cu_xS and SnS_y, two materials with very different properties introduced in Section 2.3.4 and Section 2.3.5 respectively. The literature on PLD of these phases is sparse. UV and visible ns-PLD of SnS and SnS_2 has been used to create nanostructures: nanosheets of SnS were made with 248 nm laser irradiation at a substrate temperature of 350 °C) [202] while nanoparticles were made by 532 nm irradiation of a 150 °C SnS_2 target) [203].

In contrast to the fluffy SnS_y nanostructures, Cu_2S by PLD seems to form flat sheets: PLD of Cu_2S has been reported recently by authors proposing to exploit the thermoelectric properties of the materials [204] or to use it in a switchable memory unit [205], and these films are apparently low in droplets, like ZnS films. Neither of these fairly exploratory studies on Cu_2S complain of problems with stoichiometry or unwanted phases. In the deposition of SnS_2 for nanoparticle production, the authors observed multilayers of SnS and SnS_2 with different degrees of sulfur deficiency giving rise to different nanoparticle shapes.

Numerous other chalcogenides have been deposited by PLD - far too numerous to be comprehensively surveyed here. Some of the recent hot research topics include 2D layers of MoS_2, $MoSe_2$, WS_2, and WeS_2 [206].

In the interest of finding out if S-deficiency is always an issue in ns-PLD of sulfur-containing chalcogenides, we will examine a few other materials briefly:

- As_2S_3: stoichiometry depends on fluence with S deficient films at 1.9-3.8 J/cm2 and As-deficient films at very high fluence using a KrF-laser [127].

- Ga-La-S films deposited with 532 nm laser irradiation were S-deficient relative to the target [207]

- $AgGaS_2$ films were strongly non-stoichiometric as-deposited by 308 nm ns-PLD at high temperatures (560-620 C) from a multicomponent target: they were both Ag and S-poor and a separate Ag-phase formed at up to 600 C.

Frumar et al. extensively review PLD of chalcogenides in 2006 [125] and list other examples of more complicated sulfides, many of them produced by a Jülich-St. Petersburg collaboration around 1999-2001, where off-axis deposition was used to explore a number of different chalcogenide sensor materials using 248 nm ns-PLD. This group demonstrated stoichiometric transfer of Ag-As-S films from target to substrate at room temperature in a N_2 background gas [208]. Other, more complicated materials were not always quite as well behaved: Ag-Cd-As-I-S was slightly S-rich and very Cd-rich, Ag-Tl-As-I-S was nearly stoichiometric in S but rich in As, and Ag-As-I-S was S-poor and Ag-rich. All of these depositions were apparently carried out at the same fluence, so adjusting the fluence might have changed the stoichiometry [209]. For these films, however, the exact stoichiometry was not the main concern, rather the focus was the applicability of the films as sensors. No reason is offered for the off-axis geometry, but it makes it hard to compare these results to our on-axis configuration.

Overall it appears that while ZnS and Cu_2S are fairly well-behaved chalcogenides where big issues in stoichiometry may be avoided, many other chalcogenides are much more difficult to deposit.

In relation to the experiments carried out in this thesis, the result that the stoichiometry of As-S films depended on the incident fluence [127] is interesting: this is similar to what we saw for CTS and CZTS. Other highly relevant results include the observation that Cu-incorporation in heavily Cu-doped ZnS increases with fluence, and the same is true for lighter Co-doping [195, 201].

4.5 Summary of the lessons from literature on PLD of chalcogenides

Several challenges are clear from the literature on PLD of CZTS and other chalcogenides. The stoichiometry can clearly be a challenge, and many groups report S- or Se- deficiency in the films. Some groups were able to overcome these difficulties and make high-quality films of e.g. CIGSe. However, no solar cells made from as-deposited CZTS films have been reported since the 1990's and no solar cells made from as-deposited CZTS have been reported whatsoever. Droplets could be another challenge for materials that need to provide good electrical contacts between adjacent layers. Droplets are prominent features on room-temperature deposited CZTS and are also seen in CZTS and CIGSe deposited at higher temperatures, but apparently tend to decrease with substrate temperature, perhaps due to reaction with the surrounding film (REFS). Overall we saw that PLD for solar cells has been used in many exploratory studies but has yet to yield very high quality solar cells, especially as deposited. This may be due to both droplets and stoichiometry issues and could also have to do with material defects at the microscale introduced by the high-energy particle bombardment during PLD.

Chapter 5

Materials and Methods

This chapter describes the deposition and characterization techniques used in this study with emphasis on information that would be useful from a practical standpoint for a beginner in materials science and for reproducing the results of this thesis. The deposition methods will be described first followed by the targets and substrates, the fabrication of complete solar cells and finally the characterization.

5.1 Pulsed laser deposition

PLD was done with a 355 nm Nd:YAG laser and a 248 nm KrF laser. Important parameters of the two setups were compared in one of our articles that discusses the differences between CTS deposited by the 248 and the 355 nm lasers (Appendix B [210]). Below, a few additional parameters are added to the comparison (Table 5.1).

Table 5.1: Parameters of the two lasers used in this study

laser type	Nd:YAG	KrF
wavelength (nm)	355	248
pulse length (ns at FWHM)	5-7	20
spot shape	oval	rectangle
intensity profile	Central part of a Gaussian beam (cut by aperture)	top hat

5.1.1 PLD: 355 nm setup

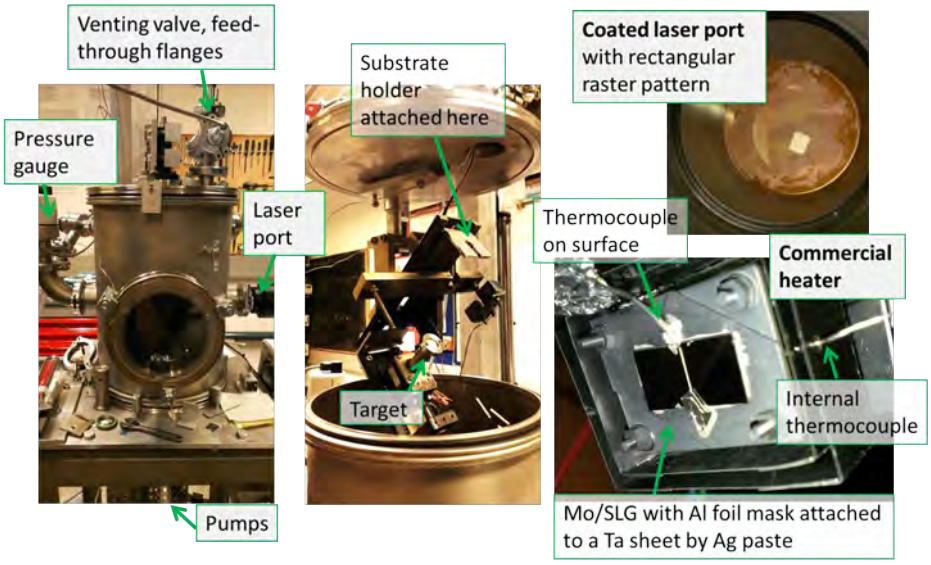

Figure 5.1: The 355 nm PLD setup: the vacuum chamber used with the 355 nm laser at Risø. The target rotation motor, sample holder and thermocouples etc. are attached to or fed in through the lid, which opens up. The window quickly is coated by ablated material, though the laser 'cleans' a hole for itself (here the beam had been moved in a rectangular raster pattern). The heater shown is the Boralectric heater used for CTS deposition on Mo-coated soda lime glass substrates (Mo/SLG).

The 355 nm laser is a Q-switched frequency-trebled 1064 nm Nd:YAG laser from Coherent with a 5-7 ns pulse width. The setup is shown in Fig. 5.1. The pulse energy sometimes fluctuated from pulse to pulse and contributed to the error in our fluence measurements. The stability was influenced by the difference in the time delay of the capacitor bank that triggered the flash lamps pumping the laser and the Q-switching delay. A stable laser temperature was also important and at one point the electronics controlling the cooling had to be exchanged. Even after warming up according to the manual, the laser was not always stable during long depositions. We used a 10 Hz repetition rate except in the early work with metal and ZnS ablation where we used 5 Hz for some of the deposition rate measurements.

The target could be rotated and the distance from target to substrate could

be varied from 3-7.5 cm. We always used 4.5 cm to be able to compare easily to the 248 nm setup. Prior to deposition, the chamber was always pumped down to below 10^{-5} mbar, usually to about $2*10^{-6}$ mbar.

The laser beam was raster scanned across the target by a motor-controlled mirror to increase the ablated area, reducing target roughening. For most of this work we used a rectangular raster pattern on one quarter of the circular target. After we realized how important the precise value of the fluence was for the composition of the CTS films, A. Cazzaniga proposed that we only raster the beam in the direction on the target surface where the spot size would be constant, as he calculated that moving the spot in the orthogonal direction could change the spot size by 10 % as described in his PhD thesis [135].

The laser passed through a quartz window on its way to the target. The transmission was measured before and after the deposition and an average value was used for calculating the transmission. The window was cleaned occasionally; the best method was with HCl under a fume hood (it is important not to etch the front of the window which has anti-reflective coating). The transmission decreased rapidly after cleaning but reached more of a steady state after some coating. Right after cleaning the transmission was generally about 90 % in CTS depositions, decreasing to about 75-80 % after 1-2 depositions (the first coating deposition run could be used to preablate the target).

5.1.1.1 Spot size

Within the first year of this work we increased the spot size in the 355 nm setup from 0.2-0.3 mm^2 to 2.5 mm^2 as a larger spot size yielded a higher deposition rate, required less attenuation of the laser beam, and caused less error in fluence calculation as the size could be determined more accurately. For some later experiments we increased the spot size further to deposit at very low fluence within a reasonable amount of time. We evaluated the spot size by measuring the size of single laser pulses on Ag and Cu foil at high fluence. For low fluence values, the full area of the laser spot was not ablated, showing the gradient in intensity from the edge of the spot to the center. See Figure 5.2. For the 248 nm laser with a rectangular top hat beam we calculated the size of the spot based on the size of the rectangular aperture and the lens position.

5.1.2 PLD: 248 nm setup

The 248 nm laser was a Lambda Physik LPX KrF excimer laser with 20 ns pulse width which varied in output energy from about 200-400 mJ/pulse depending on the amount of gas in the system and the voltage applied during lasing. At the lens in front of the viewport to the chamber the maximum energy was about 70 mJ per pulse due to attenuation from several mirrors and two apertures in the

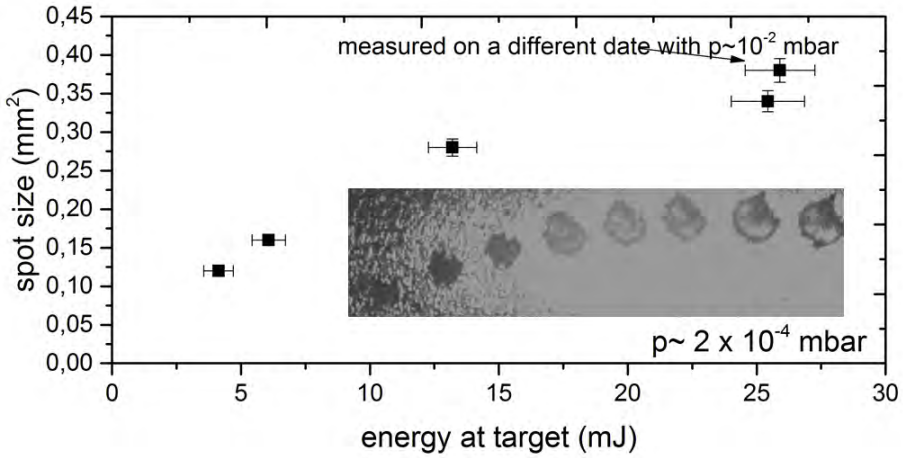

Figure 5.2: Variation of spot size with laser energy: the imprinted area of a single shot of the 355 nm laser on an Ag target varied significantly depending on the energy per shot. Inset: Optical microscope image of the Ag target with a series of single shots at three different fluence values (the target was rotated a little between each shot). The shape of the spot is not exactly round because the iris used to cut off the low-energy fringes of the laser beam had been ablated. In later experiments the iris was exchanged.

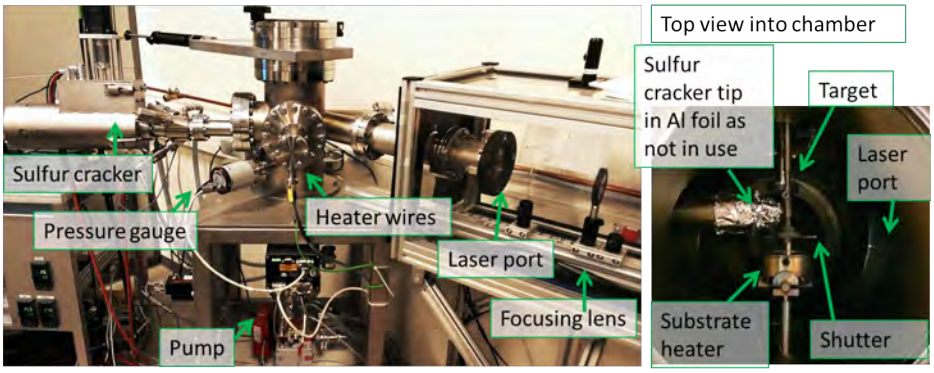

Figure 5.3: The 248 nm PLD setup: the vacuum chamber used with the 248 nm laser at Risø. The sulfur cracker was not used in the experiments conducted in this thesis.

path. The setup is shown in Figure 5.3. The beam passed through a rectangular slit to cut off any low-intensity fringes at the edges before reaching the focusing lens. As in the 355 nm setup, the laser spot was scanned across the target by a motor-controlled mirror to avoid crater formation. The spot size could be varied by moving the focusing lens.

In the experiments described in Chapter 8, the spot size was approx. 5 mm^2 and the fluence was about 0.3 to 0.5 $J\,cm^{-2}$, the target-substrate distance was 4.5 cm, and the target rotated during the deposition. The chamber pressure prior to each deposition was $< 5 \times 10^{-5}$ mbar for heated films and $< 2 \times 10^{-6}$ mbar for films at room temperature. The fluence decreased about 30 % during the CZTS depositions due to increasing window coating; the fluence values quoted here are averages. For the CZTS depositions the window was cleaned and the target refreshed prior to each deposition. The pulse repetition rate was 15 Hz except as noted in Chapter 8. The deposition rate measurements on ZnS and CTS were done at 5-10 Hz and film deposition of CTS was done at 10 Hz to be comparable to the depositions done with the 355 nm laser.

5.1.3 Heating the films

The 355 nm, 248 nm, and PED setups had different heaters. Some observations based on working with the different configurations include:

On attaching the substrates: The substrate could be attached by clamping with clips on springs (355 nm setup), with silver paste (248 nm setup, 355 nm setup) or with a mask around the edge of the film (PED setup). All three methods had drawbacks: The contact between heater and substrate was uneven in all cases, clips on springs applied pressure to the substrate that visibly changed the reflectivity of the film near the clip, and the silver paste had to be carefully removed if the films were to be annealed or otherwise post-treated. A metal mask as used in the PED setup is probably the best option for making solar cells.

On temperature monitoring: This was best done with a thermocouple on the edge of the heater surface (355 nm and PED setup). In some cases we also used a thermocouple touching the front of the substrate (355 nm setup for control) or internally in the heater (355 nm and 248 nm setup). The temperature was highest inside the heater and lowest on the surface of quartz samples (which could be 50 °C less than the heater surface when clamped to the heater at 300 °C). The heat transfer was much better to the Mo-coated substrates attached by Ag-paste.

The 248 nm setup had a commercial resistive heater (TSST B. V., The Netherlands) and no option of using an external thermocouple to monitor the temper-

ature. For the the 355 nm work on ZnS and CTS deposited on fused silica for the article in Applied Surface Science [211] (Appendix A), we used a home built heater which suffered from non-uniform heating (up to 30 °C across the surface when set to 250 °C). Heating above 300 °C was not possible as the resistive wires melted. For later experiments with CTS deposited on Mo-coated soda lime glass we used a commercial Boralectric heater with a built-in thermocouple (see Figure 5.1). To improve the contact between film and substrate and increase the comparability of the experiments to the ones in the 248 nm setup, we placed a Ta sheet above the ceramic heating element and attached our substrates with Ag paste to the sheet. In the PED setup, the substrates were attached to a graphite susceptor that was heated by an infrared bulb and the heating was controlled manually by adjusting the voltage applied to the bulb, which led to some difficulty in keeping the temperature constant.

5.2 Pulsed electron deposition

The PED setup at IMEM-CNR in Parma is shown in Figure 5.4. The PED gun was a commercial PEBS-20 source from Neocera Inc., USA. The discharge voltage was varied from 10-19 kV and the pulse repetition rate varied from 6-10 Hz depending on the voltage (at high voltage, the repetition rate had to be lower: 6 Hz at 19 kV, 7 Hz at 18 kV, 9 Hz at 16 kV and 10 Hz at 15 kV and below). The target-substrate distance was fixed at 8 cm and the target was rotated to ensure a uniform material removal and to avoid local overheating. The distance between the end of the alumina cathode tube and the target distance was approx. 3-5 mm and the size of the electron beam spot on the target was approx. 7-8 mm^2. A new alumina tube had to be cut and inserted occasionally. Prior to each deposition, the chamber was pumped down to about 5×10^{-5} mbar, then filled with Ar to $\approx 1 \times 10^{-3}$–2×10^{-3} mbar.

5.2.1 Optical Emission Spectroscopy

The composition of the PED ablation plume was monitored by optical emission spectroscopy (OES) with a Hamamatsu TM-CCD-A series optical mini-spectrometer. This was not normally in place in the chamber used for the CZTS PED work, and the windows for monitoring the deposition were in the lid of the chamber (Figure 5.4). Therefore the OES detector was mounted in a rather unstable holder and the position relative to the plume was adjusted for every deposition to give a good peak intensity measurement. The emission peaks in the plume were assigned to different elements using the NIST database of atomic spectra [212].

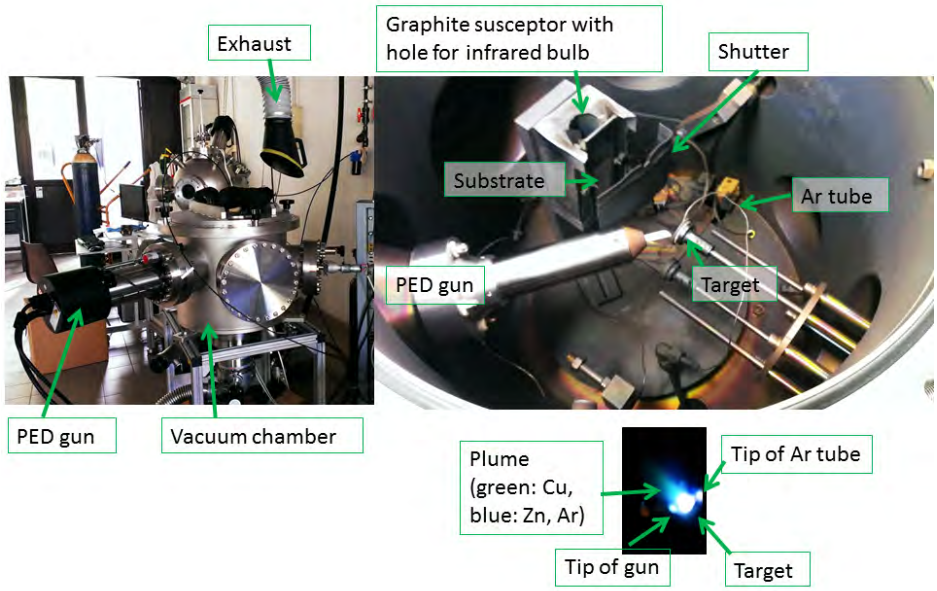

Figure 5.4: The PED chamber used in this study at IMEM-CNR in Parma. This chamber is originally a sputtering chamber and the layout is not ideal for PED. The lid has two glass windows above which the OES detector was aligned manually to detect the plume composition.

A sample optical emission spectrum and the correspondence between the measured Cu/Zn ratio in the film compared to the Cu(I)/Zn(I) ratio is shown in Figure S2 in Appendix D. The detection of the Sn OES peaks had been better if a quartz window had been used rather than glass windows as Sn has relatively strong emission lines just around the absorption onset of glass, above the onset for quartz. As it was, we could most accurately monitor Cu and Zn. The Sn-emission as far as it could be measured was always proportional to Zn.

5.3 Annealing

The annealing setup is shown in Figure 5.5. It consisted of a modified resistive furnace with a quartz tube inserted. The end of the quartz tube stuck out of

the original oven door and was partially insulated while the outer part was not, creating a transition to a cold zone where the tube was joined to a vacuum flange with a rubber o-ring. The quartz tube could be evacuated to 10^{-4} mbar and was flushed and then refilled with N_2 during annealing. Due to the relatively weak construction we did not fill the chamber to more than about 100 mbar N_2 before annealing to avoid cracking the tube as the gas heated when expanded.

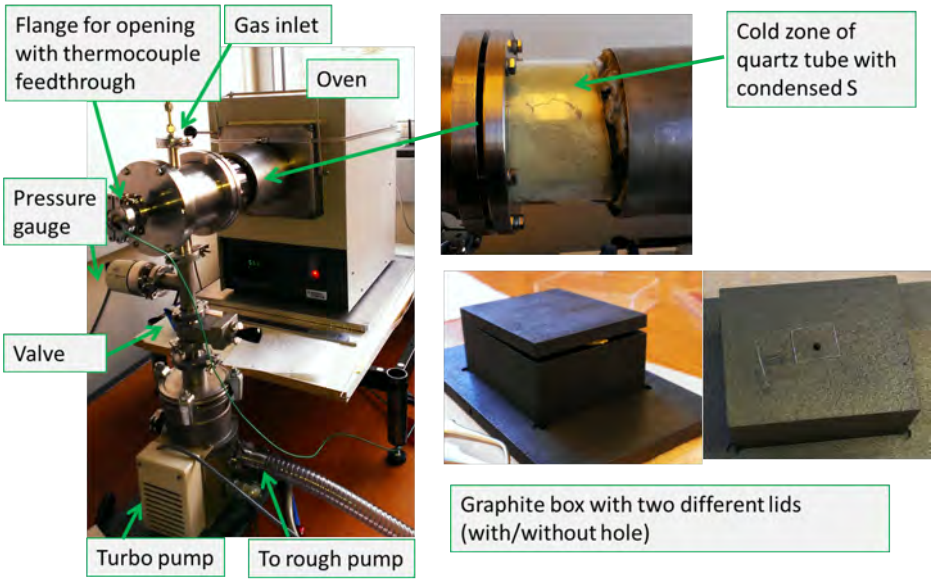

Figure 5.5: The modified furnace used for annealing the CTS samples in this study. The quartz tube stuck out of the oven and was closed by a metal vacuum flange connected to the gas inlet, pressure gauge and pump outlet. We experimented with two types of lids on the graphite box but did not see much difference between them. When using the lid with a hole, we placed a small clean piece of quartz above the lid which blew off as the S gas inside evaporated. With the lid that had no hole, we used S-pieces to keep the box ajar initially, allowing the box to be evacuated by the pumping but ensuring that it would close as the S evaporated.

The samples were placed in a graphite box that was pushed to the end of the quartz tube inside the hot zone of the oven. There were two boxes, one for annealing with S only and one for annealing with S+SnS. We added S (flakes, 50-200 mg per annealing, 99.998 % purity, Sigma-Aldrich) and SnS (powder, 5-35

mg per annealing, 99.99 % purity, Sigma-Aldrich). For most of my work, I used only S-annealing as adding SnS did not seem to make much difference and added an extra variable. For an optimized annealing procedure, however, SnS should help. S evaporated inside the graphite box and condensed in the cold zone of the surface, so that the oven changed over time. We were told by other groups that annealing worked best with neither too much nor too little S in the oven, so it was cleaned periodically.

The temperature was monitored by the oven and by a thermocouple inserted in the base of the graphite box. After we had correlated the temperature of the oven monitor to the thermocouple readout from several heating runs, we removed the thermocouple from inside the quartz tube as we noticed corrosion due to the sulfur.

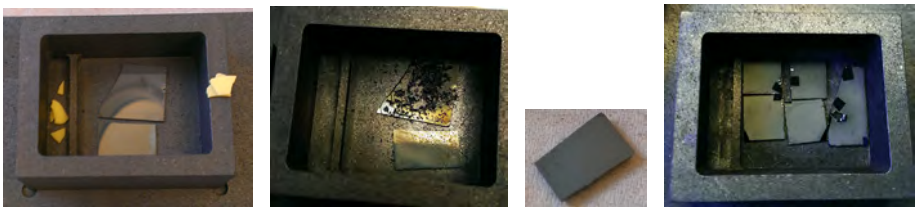

(a) Before annealing (b) After annealing (c) After annealing (d) After annealing

Figure 5.6: Samples in the graphite box before and after annealing. (a): CTS samples with perfect slightly Cu-poor composition ready for annealing with 50 mg S flakes. (b): The same samples after annealing - completely exfoliated including Mo layer (sample thickness about 1600 nm). (c): Very similar sample after annealing (<700 nm thick before annealing). (d): SnS-rich samples after annealing (approx 1200 nm thick before annealing).

Figure 5.6 shows the inside of the graphite box with S before annealing (Fig. 5.6a) and with the S completely gone after annealing (Fig. 5.6b, (d)). The figure illustrates how some CTS films completely exfoliated (relatively thick ones with Cu:Sn:S approx. 40:20:40, Fig. 5.6b) whereas thinner CTS films of similar or slightly more Sn-rich composition did not exfoliate (Fig. 5.6c; the composition was difficult to measure when the films were less than 1 µm as we will see below). Very Sn-rich CTS films (Cu:Sn:S approx. 20:35:45) also did not exfoliate almost no matter the thickness up to 4 µm - the ones in the image were about 1 µm thick.

5.4 Targets and substrates

5.4.1 Targets

The targets were sintered powder targets from Testbourne, Ltd. (90 % density) which consisted of multiple phases as seen in Fig. 5.7. In the CTS targets we detected, e.g., Cu_2S, CuS, Cu_2SnS_3, and SnS by X-ray diffraction. The raw powders that the targets were made from were binary sulfides, e.g., CuS, Cu_2S, SnS, and SnS_2, which decomposed to some extent during hot-pressing. The sintering temperatures were around 750 °C for Cu_2SnS_3 and around 1000 °C for ZnS, while the manufacturer did not tell us the temperature for CZTS.

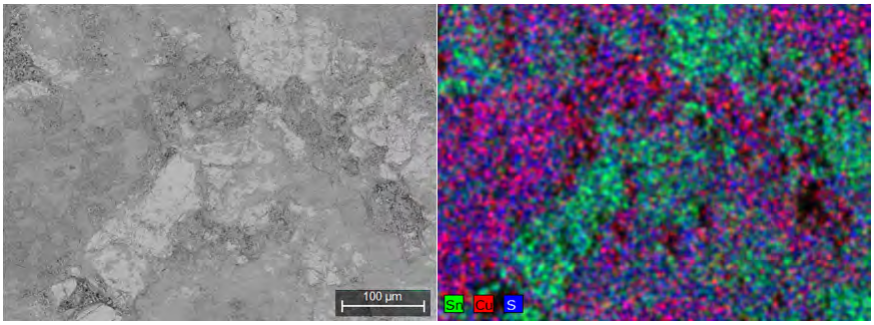

Figure 5.7: EDX map of a fresh CTS target surface showing domains hundreds of microns wide. X-ray diffraction of this target showed a large proportion of CuS and SnS as well as Cu_2SnS_3 in the tetragonal or cubic phase. There is also some cubic-phase Cu_2S.

Figure 5.7 is a compositional map of a CTS target at low magnification indicating the size range of the secondary phase regions in the targets. Figure 5.8 shows X-ray diffractograms of three CZTS targets. In the CZTS targets, we detected SnS_2, SnS, CuS, Cu_2S and Cu_7S_4 as well as "Σ CZTS" peaks that may derive from either CZTS, ZnS, or several different forms of CTS as will be discussed below. EDX-maps of the CZTS targets showed Zn-rich regions as well as Cu- and Sn-rich regions, revealing that there was ZnS present in the target as there are no other Zn-rich secondary phases in the CZTS phase diagram.

We measured the composition of the targets by EDX and noticed a Cu-rich and S-poor composition. The manufacturer said that it was possible that S or Sn could be lost during hot pressing under certain temperatures, adding "but the total loss should not be that great." There can be a great deal of error associated with EDX of a rough surface as will be discussed below, so we could not fully trust our measurement. However, in the CZTS targets for PED and PLD we

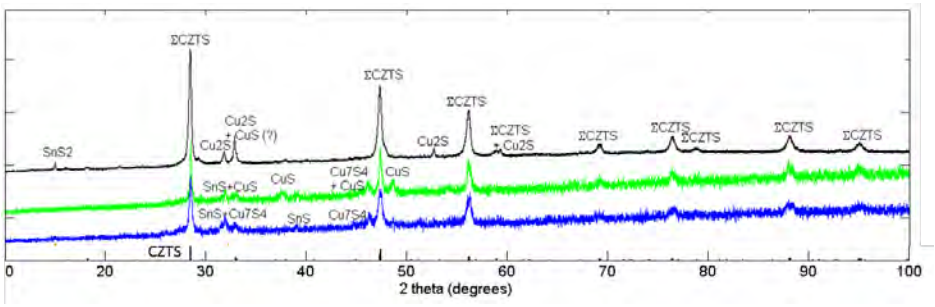

Figure 5.8: X-ray diffractograms for three different CZTS targets used in this study. The bottom reference marks (just above the x-axis) show the CZTS peaks as reported in the ICSD database based on data from Lafond et al. ΣCZTS refers to peaks that may derive from CZTS, ZnS, or several different forms of CTS

measured a S-to-metal ratio of 0.6 where it should have been 1. Following an inquiry to the manufacturer, they delivered new targets with a S-to-metal ratio of 0.9 according to our measurements. It is still difficult to know what the real S-content was, but it seems likely that the initial targets were S-poor.

The targets were 1 cm or 1" in diameter. They were preablated prior to making measurements or depositions. The ZnS and CTS targets were refreshed by sanding down to a uniform but not fully smooth level after each deposition as they were not worn down fast and they were ablated in the 355 nm chamber where no shutter was fitted for easy preablation. Occasionally the CTS target was fully sanded down or refreshed by turning over and was preablated prior to use. The CZTS targets which were used for PED and 248 nm PLD were always fully sanded down and preablated prior to deposition.

5.4.2 Substrates

The substrates were Si, fused silica, soda lime glass and Mo-coated soda lime glass (Mo/SLG) as specified in the results chapters and articles. For most of the work with Mo/SLG, the Mo was sputtered onto SLG by A. Crovetto as described by Cazzaniga & Crovetto et al. [157]. The substrates were cleaned prior to deposition by rinsing in acetone followed by isopropanol and/or ethanol in an ultrasound bath. They were rinsed in DI water in ultrasound and dried with inert compressed air. The transfer times were as short as possible. Note for new researchers: it may be more difficult than one immediately thinks to keep the beakers dust free. This is important to avoid crusts of contaminants on the films.

5.5 Solar cell fabrication

Complete solar cells were fabricated by Andrea Crovetto for annealed CTS films at DTU in Denmark and by Stefano Rampino, Francesco Pattini, Fillippo Bosco, Matteo Bronzoni and Marco Calicchio for PED-deposited CZTS at IMEM-CNR in Italy. The methods for fabrication of the CTS solar cells followed the same procedure as for our in-house CZTS solar cells as described by A. Crovetto in his PhD-thesis, though the steps had not yet been optimized [213]. The CdS layer, deposited by chemical bath deposition at 70 °C, was about 60 nm thick, the i-ZnO layer (sputter deposited) was about 75 nm, the AZO layer (also sputter deposited) was about 200 nm and no anti-reflective coating was used.

The fabrication of CZTS solar cells was with Mo/SLG from DTU (coated by A. Crovetto's process). After CZTS deposition, a CdS layer 90-120 nm thick was deposited by chemical bath deposition at 80 °C in two steps of 10 min each to avoid CdS precipitation. The i-ZnO layer was 120 nm and was grown by RF-magnetron sputtering (100 W for 7 min in Ar). The 800 nm thick AZO layer was also grown by RF-magnetron sputter deposition (120 W for 25 min in Ar).

5.6 Characterization

5.6.1 Deposition rate measurement

The deposition rate could be measured either directly using a quartz crystal microbalance (QCM) or indirectly by measuring the film thickness with a Dektak profilometer after a known number of pulses.

5.6.1.1 Quartz crystal microbalance

A QCM may be used to measure the deposition rate at a pulse by pulse level if one has a sensitive enough frequency counter. The instrument relies on applying an AC voltage across a very thin quartz crystal. The crystal thickness oscillates due to the piezo-electric effect when a voltage is applied to it and the frequency of the oscillations is inversely proportional to the mass of the crystal. On each side of the crystal thin electrodes are deposited, which act as capacitor plates. The crystal is cut to a thickness that will cause a specific frequency of oscillations, e.g., 5 or 6 MHz. Then when material is deposited on one of the electrodes, the total mass increases and changes the frequency instantaneously.

The deposition rate measurements by the QCM are vulnerable to deviation in the density of the laser-deposited film compared to the bulk. Before the deposition rate measurements, it was important to preablate the target until a constant deposition rate was reached

5.6.1.2 Dektak profilometry

A Dektak stylus profilometer was used to measure film thickness. The typical scan length was 1 µm using 210 s scan time. Two examples are shown in Fig. 6.3. For room temperature films, we used sticky tape to mask the films for thickness measurements, creating a clear step between substrate and film once the tape was removed. In the 355 nm setup, we sometimes used clamps to mask the film with small pieces of quartz, Al foil or soda lime glass during depositions at elevated temperature. This was not possible in the 248 nm setup due to the layout of the heater.

In profilometry a small elastic tip is pulled across the film surface and the deflection of the tip is measured. Since the µm-dimension profilometry tip is dragged across the surface, measurements will be error-prone for rough surfaces i.e., PLD films with µm scale droplets. It is likely that the Dektak will overestimate the film height because the tip cannot follow the real surface of the material when the droplets are closely spaced or vary steeply in height.

5.6.2 Transmission and reflection measurements

The transmission of the films deposited on fused silica was measured with a Cary 50 photospectrometer. The full reflectance of the films and targets was measured with an integrating sphere with a deuterium tungsten halogen lamp and an Ocean Optics USB2000 spectrometer (210-900 nm).

Fully measuring the absorption of a thin film requires measuring both the transmission and the reflection [214] and it is necessary to take into account interference from multiple reflections in the material. Our main goal with the transmission measurements was to get a sense of the absorption onset of the materials and to compare them to measurements made by others. In our article we therefore estimated the absorption on the assumption that reflection and scattering were negligible, so that the entire loss in transmitted intensity was due to absorption [210]: $\alpha = 1/d * ln(1/t)$ where t is the transmission. This is probably a very optimistic assumption but is similar to the transmission-only characterization done by Zanettini et al., to whom we wanted to compare our results [83].

From the absorption spectrum, the bandgap can be roughly deduced. A very simple method is to use a Tauc plot, which assumes that all the absorption is due to excitation of electrons above the bandgap, ignoring any exciton or defect absorption [214]. For a Tauc plot for a direct bandgap material, one plots $(\alpha(\hbar\omega))^2$ against $\hbar\omega$ (the photon energy) and the bandgap, E_g, is estimated as the point where a linear fit to the data intersects the x-axis. The original Tauc plot was used for indirect bandgap materials where the exponent in the equation is 2 rather than 1/2 [215]. In our article in Applied Surface Science (Appendix

A [211], we plot $(\alpha\hbar\omega)^2$ against the photon energy rather than simply α^2. This was again done in order to compare our results to those of Zanettini et al. [83]. Murphy also noticed that both of these approaches exist in the literature and remarks that there is not much difference in the final results [215].

Another approach to finding the bandgap is to use the Kubelka-Munk equation based on the diffuse reflectance alone. This equation works best for thick, opaque materials with high scattering and low absorption, e.g., materials that are "dull" in the words of Kubelka [216]. It may be assumed to work reasonably well far away from the bandgap but not so well at or above the bandgap, and does not work well for smooth materials with a high degree of specular reflection. The Kubelka-Munk equation reads [217]:

$$F(R) = \frac{(1-R)^2}{2R} \tag{5.6.1}$$

and if absorption is low, one may assume $F(R) \propto \alpha$. Thus plotting $F(R)^2$ versus photon energy in place of α^2, one may presumably estimate the bandgap of a direct bandgap semiconductor. Lopez and Gomez show that at least for their preparation of TiO_2, using the exponent $1/2$ and assuming an indirect bandgap, the method yields a reasonable bandgap estimate [217].

5.6.3 Scanning Electron Microscopy (SEM)

High-resolution scanning electron microscopy was carried out in a number of different setups: a Zeiss Supra 60 VP, a Zeiss Supra 35, and a Quanta 200 F all equipped with a field emission gun. Additionally, low-resolution imaging was carried out together with EDX measurements in a TM3000 Hitachi Tabletop SEM and in a Phillips 515 SEM.

5.6.4 Energy Dispersive X-ray Spectroscopy (EDX)

Energy Dispersive X-ray Spectroscopy (EDX) for compositional analysis was carried out with 15 kV electrons in a Hitachi tabletop TM3000 SEM with a Bruker XFlash430 silicon drift detector and analyzed using Bruker's Quantax 70 software. The angle of the detector is 25° to the sample plane. Repeated measurements on the same film area with the same instrument gave variation far below 1 %. The error on the absolute numbers was clearly larger than that, however, due to differences in the roughness from film to film and calibration error.

For some measurements, e.g., on the droplet composition presented in our article in Applied Physics A, Appendix B [218], we used an X-MaN 50 EDX silicon drift detector from Oxford Instruments mounted in the Supra 60VP SEM. This instrument allowed point-and-shoot measurements limited in size by the approximately $1\,\mu m^3$ interaction volume of the excitation beam with CTS. From the

Supra/X-ManN 50 data, element ratios were calculated by Oxford Instrument's Aztec software using the Cu K-lines and deconvoluting any Mo contribution to the S peak.

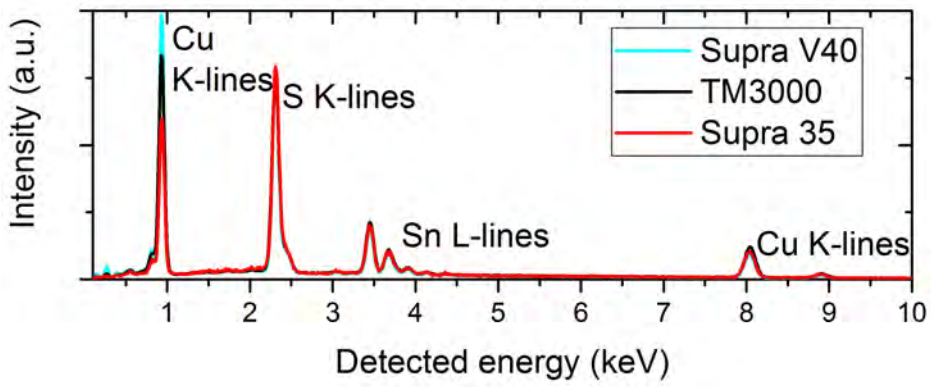

Figure 5.9: Comparison of the EDX spectra recorded by three different instruments at DTU for the same CTS film deposited on Mo/SLG. We see that one instrument, the Supra 35, measures much less Cu-signal than the others. It turned out that this was because it is an old instrument which is less sensitive in the low-energy region. The other two agree reasonably well. The software interpreting the composition based on the spectrum is also different for all three instruments. The Supra V60 calculated Cu:Sn:S=45:15:40, the TM3000 calculated Cu:Sn:S=42:13:45, and the Supra 35 calculated Cu:Sn:S=35:12:52 based on the spectrum recorded by that respective instrument as shown in this figure.

We compared the quantification of the composition of a single film by 3 different EDX systems including the ones mounted in the Supra V60 and the TM3000 instrument (See Fig. 5.9. The quantification by these two instruments was fairly similar and we therefore decided to use the TM3000 for most quantification since this was the most accessible instrument and it was important to perform all measurements with the same setup.

For CTS composition measurements, 10 keV could in principle be used as the excitation voltage, but we mostly used 15 keV as this was the option in the Bruker TM3000. We used the S K-lines, the Sn L-lines and the Cu L-lines for this quantification. For CZTS, the Zn and Cu L-lines overlap strongly, and it is necessary to use the Zn and Cu K-line emission for quantification, which requires at least 15 keV electron bombardment.

Two good introductions to EDX can be found in the treatments by Hafner

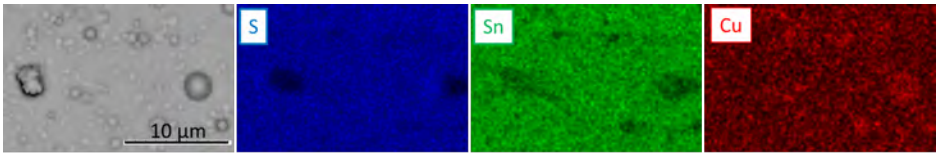

Figure 5.10: EDX map from the TM3000 instrument showing the "shadowing" in EDX detection introduced by droplets on the film surface. In the shadow of the droplet, less S and Sn is detected, while Cu is still detected. This will skew the EDX quantification, perhaps leading to overestimation of Cu.

[219] and Newbury and Ritchie [220]. They list some of the important error sources:

1. Light elements such as S are difficult to quantify accurately by EDX because the single K-line emission peak occurs in the main region of background emission [219]

2. Sample roughness results in quantification errors and Hafner suggests using polished samples with less than 0.1 µm scratches [219]. The PLD films produced in this study are rougher than that, not to mention the targets. In some cases the error introduced by droplets is clearly seen as in Figure 5.10. This means that one cannot use single measurements of e.g. droplets unless the droplets are all of comparable size, in which case they may be compared (though the absolute numbers will be unreliable).

3. lack of standards: we wanted to make Cu-Sn and Cu-Zn calibration standards, but were not able to. However, according to Hafner, it would also have been helpful to calibrate the instruments with single element standards of Cu, Zn and Sn [219]

4. non-uniform distribution of materials both laterally and vertically

The latter point was crucial for evaluating the composition of our targets and therefore evaluating whether we had congruent element transfer from the target to the substrate. Among other issues, non-uniform element distribution results in unreliable quantification of secondary fluorescence, which e.g. happens with quantification of Cu together with Zn: the Zn K-line emission is absorbed by Cu and reemitted at the Cu K-emission-wavelengths. This effect is automatically corrected by the EDX software, which leads to an error if the elements are not mixed and the fluorescence therefore does not occur as the software expects. This would in principle lead to overestimation of Cu. According to Hafner this

will generally happen if the characteristic emission and the ionization energy are within 3 keV of each other [219]. So it also happens for: S to Mo (a lot, as the peaks practically overlap), K from soda lime glass substrates to S, Sn to S, S and Sn to Si (in a soda lime glass or fused silica substrate).

This means that measuring the composition of the targets with their rough surfaces and many distinct domains will be inaccurate as the software will assume a higher degree of secondary fluorescence than there actually is.

5.6.4.1 Casino simulations of EDX signal emission depth

Thin films and layered films also represent examples of non-uniform distribution of materials that in some cases made it impossible to accurately measure the composition of the films. This was partly because of inaccurate quantification of secondary fluorescence but probably most seriously due to overlap of the peaks in the film and the substrate: The Mo and S peaks severely overlap on Mo/SLG substrates and Sn overlaps with K We used the software Casino [155] to estimate the film thickness needed for all (or rather 99 %) the detected signal from 15 keV electrons to originate within the film. For CZTS, the films needed to be $>$ 1 µm assuming uniform and smooth CZTS films with density equivalent to the bulk. For CTS the films had to be at least 900 nm thick, while the relatively low average atomic mass of the elements of ZnS films mean that the films have to be about 2.5 µm thick to avoid any errors from the substrate. Higher energy electrons require even thicker films.

For an imaginary perfectly smooth film of uniform composition, just over 80 % of the Sn and S signal derives from less than 500 nm compared to around 93-95 % of the Cu and Zn signal. If the film is only 500 nm thick, the detector therefore receives a relatively large Cu and Zn contribution compared to what it would from a full thickness film of the same composition (there should not be significant secondary fluorescence from Cu and Zn to Sn and S). The software might then underestimate the S and Sn signal by 10 % relative and overestimate Cu and Zn by 10 % relative as well.

5.6.5 X-ray diffraction

X-ray diffraction (XRD) was carried out in a Bruker D8 diffractometer with Cu Kα and Cu Kβ radiation. The Cu Kα2 signal was stripped with Bruker's EVA software and the PowDLL converter software was used to convert Bruker .raw data into .dat data for further processing [221]. The step size and stepping rate varied from measurement to measurement, but often used parameters were a step size of 0.01° and a rate of 1.1-2 step/s for annealed or heated films as well as the target, where there were many closely spaced peaks and high resolution

was needed. For room temperature films where the peaks were usually few and weak, a larger 0.03° step size and a slower rate of 0.33 step/s was used.

In some cases, the Mo substrates were scanned with Si reference powder (NIST 640d) to correctly identify the position of the Mo peaks, which were at slightly higher 2θ-values than bulk crystals. The position of the Mo peaks were then used to align the diffractograms of the CZTS on Mo-coated substrates to correct for errors from the vertical sample alignment in Bragg-Brentano configuration.

Many good texts introduce X-ray diffraction and crystallography. See for instance Mittemeijer p. 171-189 [222].

The bewildering number of secondary phases of CZTS lead to an equally bewildering array of XRD reference spectra to take into account (there are more reference spectra in the literature for XRD than Raman Spectroscopy, which will be described below). Manual fitting was usually used rather than the EVA database because as noted in Section 3.1.5 there can be stress in the PLD-grown films leading to peak shifting.

The CZTS diffraction pattern nearly overlaps with that of tetragonal Cu_2SnS_3, kuramite Cu_3SnS_4 and $Cu_3SnS_{3.6}$ on all diffraction peaks and it also overlaps in its main diffraction peaks with cubic Cu_2SnS_3 and ZnS. For annealed (equilibrium-phase) films it is good to know that ZnS and cubic and monoclinic Cu_2SnS_3 may be expected at a temperature of 570 °C but not tetragonal Cu_2SnS_3. It is also good to think about which phases would be expected with a given composition. However, with the non-equilibrium method of PLD unusual phases could potentially occur.

5.6.6 Raman spectroscopy

Raman spectroscopy of the CTS films (Chapter 7) and the PED CZTS films (Chapter 8) was done with a DXR Raman Microscope (Thermo Scientific) at 455 nm in the backscattering configuration with a spot size of 1 µm and a power of 0.4 mW, while Raman spectroscopy of the PLD films was done with a Renishaw RL532C diode-pumped solid state laser at 532 nm set to 0.1 mW and a spot size of about 2 μm^2.

The measurements were carried out by A. Crovetto and S. Canulescu, and the results were analyzed by A. Crovetto and myself.

In Raman spectroscopy, the surface of the sample is excited by a laser beam, which is focused onto the sample through a microscope. The phonons excited in the material cause the re-emitted light to be slightly shifted in energy (Raman shifted). This energy shift is measured and shown as intensity of the Raman wavenumber, which is directly related to the wavelength shift of the light by the phonons. Error sources include cosmic rays as well as gamma rays from any decaying radioactive nuclei in the vicinity of the detector, which hit the CCD.

Raman spectroscopy probes phonon modes which are dependent on the crystal structure, so the Raman modes of materials with similar crystal structures may also be similar. Therefore although the different secondary phases that occur in CZTS may more easily be distinguished by Raman spectroscopy than by XRD, the Raman modes of CZTS and CTS still overlap and make it difficult to identify secondary phases that are minor components of the material as shown by Berg et al. [223].

It is important to be aware that different excitation wavelengths are needed to detect different phases in CZTS [224]. In particular, the elusive ZnS-phase can only be probed by UV Raman spectroscopy. This was a problem in our study as we did not have UV Raman equipment available.

The most important Raman references used in this thesis were: CZTS [224], Cu2S and tetragonal and cubic CTS [225], monoclinic CTS [63], and SnS and Sn2S3 [226].

5.7 Photoluminescence and solar cell characterization

Photoluminescence was carried out by A. Crovetto in the steady state on as-deposited PLD films with an Accent RPM2000 spectrometer with 532 nm excitation at 100 $\mathrm{W\,cm^{-2}}$. JV-characterization and External Quantum Efficiency (EQE) measurements for the CTS solar cells was carried out by A. Crovetto at DTU while JV-characterization for the PED solar cells was carried out by S. Rampino and others at IMEM-CNR in Italy.

Chapter 6

Pulsed laser deposition of metals and ZnS

The initial experimental part of this thesis was devoted to becoming familiar with the behavior of the constituents of CZTS during PLD. We deposited Zn, Cu, and Sn at room temperature and compared the deposition rates and the appearance of the resulting thin films to Ag. Additionally, we performed initial depositions of ZnS and CTS at room temperature and up to 300 °C and examined the crystallinity and optical transmission of the films. All of this work was done with the 355-nm laser.

The main part of our work on PLD of metals was presented in the paper "Nanosecond laser ablation and deposition of silver, copper, zinc and tin" in Applied Physics A of which Andrea Cazzaniga is the main author [227]. The preliminary work on CTS and ZnS was presented in the paper "Pulsed laser deposition from ZnS and Cu_2SnS_3 multicomponent targets" in Applied Surface Science [210], which may be found in Appendix A.

The premise was that learning about the nature of each of these materials under PLD would help us understand PLD of CZTS. This chapter will describe the results of our work with metals and ZnS while Chapter 7 will describe the results on CTS.

6.1 Background

Metals are held together by the free energy released by the liberation of conductive electrons throughout the material while the chemical bonds of semiconductors are intermediate between covalent and ionic bonds, mostly covalent in character, e.g., in CZTS [228]. This fundamental difference between metals and semiconductors gives rise to important differences in the way that light can in-

teract with them. The thermal diffusivity in semiconductors is generally lower than that in metals, and energy absorption by semiconductors is inefficient unless there is sufficient energy to excite electrons across the bandgap, in which case free electrons are created that can absorb additional energy much like the electrons in a metal. Additionally a great difference between depositing elemental metal films and compound materials such as ZnS is that there are of course no issues with stoichiometry when depositing single elements.

A number of constants relevant for the deposition of these elements and ZnS are listed in Appendix G.

6.1.1 Literature on UV-PLD of elemental metals

PLD is generally less efficient for ablation of metals than for other materials, such as the ceramic metal oxides used for high-temperature semiconductors [229]. This is due to the high heat conduction and high reflectivity of the metals, which means that the laser energy is coupled less efficiently into the target and is quickly carried away. Additionally, some deposited metal films are fairly easily resputtered with the resputtering rate depending on the cohesive energy as well as the energy of the incoming particles. For example, Fähler et al. found resputtering of > 50 % for Ag but < 20 % for Fe. Co-deposition of Ag and Fe yielded preferential resputtering of Ag, which could be reduced by using a background gas and/or low fluence [230].

Some of the relevant literature on PLD of metals is very briefly referenced in our article [227]. Among the most important references is the work by Thestrup et al. [231] comparing the deposition rates of Ag, Cu, Sn, Zn, and a range of other metals previously made by our group using the 355 nm frequency-trebled Nd:YAG laser also used in the present work. They found a correlation between the ablation rate (the rate of material removal from the target) and the melting point of the metals (as an indicator of their volatility). While the melting point does not always directly reflect the volatility, Schou later made a similar comparison between the ablation rate and the cohesive energy [94].

Much of the remaining literature on metal PLD was described in Chapter 3 in the sections describing the principles of PLD, as metals have been widely used as model systems to understand laser ablation, probably at least partly because their thermal properties are relatively well known. For example, Amoruso and coauthors primarily base their review on laser plasma formation on research on PLD of metals [232].

6.1.2 Quick recap on ZnS

The background on ZnS's material properties were covered in Section 2.3.3 while previous experiments by PLD on ZnS were covered in Section 4.3.

The main lessons from literature were:

- the cubic phase forms at lower temperatures generally - usually below 300-400 °C - while the wurtzite phase is obtained at higher temperatures.
- the substrate impacts the film phase with the wurtzite phase primarily forming on hexagonal substrates
- amorphous substrates usually lead to cubic-phase film growth, sometimes oriented, sometimes not
- the films sometimes become S-poor and/or the deposition rate is reduced at high temperature, indicating a lower sticking coefficient

6.2 Methods

For a description of the 355-nm PLD setup used in the work in this chapter, see Section 5.1.1. The use of the quartz crystal microbalance (QCM) and the Dektak profilometer for measuring the deposition rate was described in Section 5.6.1, while the transmission and reflection measurement methods along with the extraction of the absorption coefficient were described in Section 5.6.2.

For the metal and ZnS depositions, substrates of SiO_2 and Si were used, primarily Si for depositions where the main focus was the deposition rate, and primarily SiO_2 for transmission measurements on ZnS. The spot size was initially very small, only 0.2-0.3 mm^2 for the metals and initial ZnS depositions. For later ZnS depositions, it was adjusted to 1 mm^2.

For ZnS, transmission and reflection measurements of the films were used to estimate the absorption, which was then used to determine the bandgap using a Tauc plot, as described in Section 5.6.2 and in our article (Appendix A [210]).

6.3 Results and discussion: Metal films of Cu, Sn, Zn, and Ag

Our main findings on the deposition of the metal constituents of CZTS, Cu, Zn, and Sn compared to Ag were as presented in our article [227]:

- Zn was deposited more quickly than the other metals (as measured in atoms per pulse using a Quartz Crystal Microbalance, or QCM)
- Sn films were essentially composed of droplets and experienced a high degree of resputtering

The article examined these results in the light of the cohesive energy of the metals: the low cohesive energy of Zn led to a high deposition rate. For Sn, presumably the low melting point led to the prevalence of droplets in the films.

Figure 6.1 illustrates the extreme prevalence of droplets on Sn relative to Zn, Ag, Cu, ZnS, and CTS. CTS also contained many droplets while ZnS contained very few. It is hard to say if this is related to the metal constituents; probably it relates more to the melting and boiling points of the compounds in the targets, but on an intuitive level it is hard not to feel that some of the Sn splashing properties were transferred to CTS.

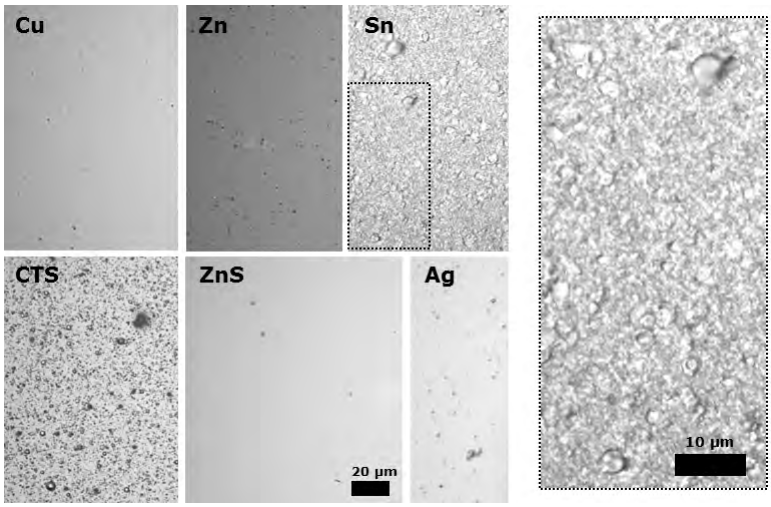

Figure 6.1: Optical microscope images of films deposited by the 355 nm laser. The metal films were deposited with a $\approx$ 0.2-0.3 mm^2 laser spot size and a fluence of $\approx$ 2 J/cm^2 while the sulfide films are made with a $\approx$ 1 mm^2 spot and a fluence of $\approx$ 1 J/cm^2. The images were converted to grayscale due to vivid interference colors (films were on the order of 100's of nm thick). All the images are at the same magnification.

The surfaces of the targets are shown in Figure 6.2. It is clear that the Sn target giving rise to the many droplets is much more rough than the Zn or Cu targets - and also that the Zn target is more rough than the Cu-target, again correlating to the number of droplets on the film. The Sn and Zn target surfaces clearly appear like solidified molten surfaces. The contrast to the smooth appearance of the ablated ZnS target in Figure 6.9 and the smooth ZnS films is striking.

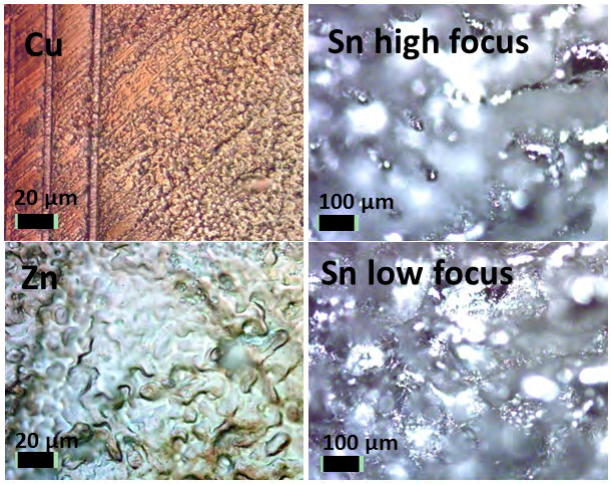

Figure 6.2: Typical metal target surfaces after ablation photographed in an optical microscope. Note the different scales on Cu and Zn versus Sn images. The Cu image shows the transition from the non-ablated (polished) to the ablated part of the target.

The scale of the roughness of the films is also illustrated by profilometer traces of the surfaces - even though these traces cannot be completely trusted when the surface is as rough as what we see on e.g. Sn, as also discussed in Section 5.6.1. Figure 6.3 shows a Dektak profilometer trace on a Cu film compared to a trace on an Sn film. The substrate had been masked by Scotch tape, which was removed after the deposition to enable the thickness measurement.

6.3.1 Metal deposition rates

Figure 6.4 shows the deposition rate of Zn measured by various methods. The measurements show a great variety of values for the deposition rate as measured by the QCM when the fluence is around 2 J/cm^2. In this fluence regime, the deposition rate apparently increases rapidly and small systematic error in the fluence measurement due to a change in spot size between measurement series or perhaps due to higher or lower window coating than expected can lead to a large difference in the magnitude of the deposition rate. When following each series of measurements made by the QCM, it is apparent, however, that the deposition rate seems to change from a slow deposition rate below 2 J/cm^2 to a much higher one at higher fluence. The Dektak measurements of film thickness indicate that at high fluences above 4 J/cm^2, the deposition rate may saturate, as would be

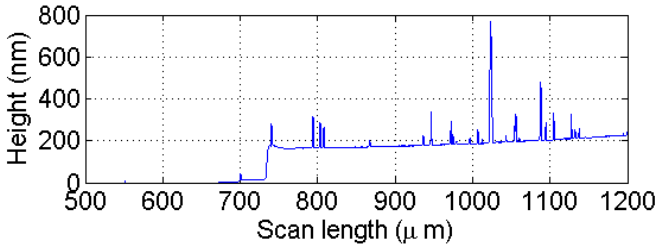

(a)

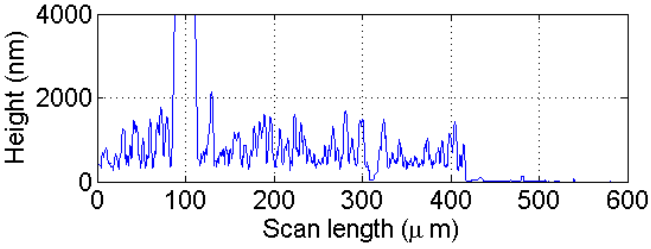

(b)

Figure 6.3: Dektak profilometry of (a) a Cu film made at a fluence of ≈ 4 J/cm^2 and (b) a Sn film made at a fluence of ≈ 2 J/cm^2, both deposited on Si substrates at room temperature using the 355 nm laser. Note the different scales on the y-axis.

expected since the high fluence leads to a higher degree of ionization in the plume, which makes it impenetrable to the laser.

The deposition rate of Zn is compared to the other metals in Figure 6.5. A simplified subset of this data was shown in Fig. 2 in Cazzaniga et al. [227]; the data acquisition and processing was done collaboratively by Andrea Cazzaniga and myself. The main observation to be pointed out here is that deposition rates of Cu, Ag, and Sn increase gradually for all the fluences measured, with no sudden increase like that for Zn. At low fluence the deposition rate of the other metals is similar to that of Zn while at higher fluence values the number of atoms of Zn deposited per pulse suddenly rises compared to the other metals. The figure contains many more data points than the one in our article, giving a better sense of the spread in the measurements, but making it a bit harder for the reader to discern the trends.

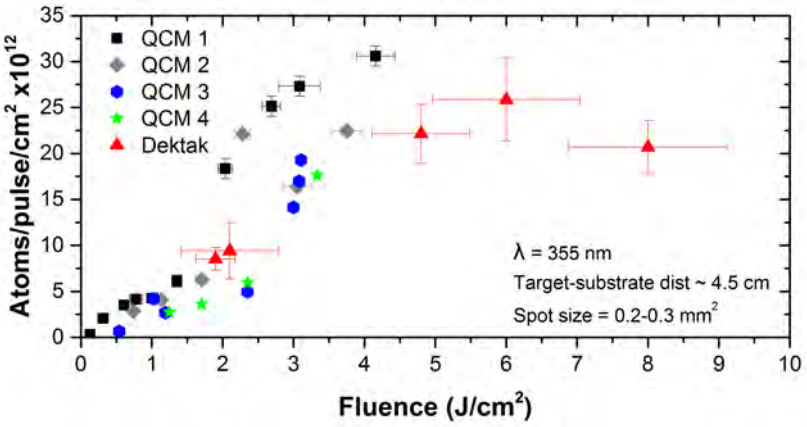

Figure 6.4: Deposition rate of Zn showing transition from low deposition rate, that closely corresponds to the other metals, to a higher deposition rate. Small errors in the fluence measurement for each series caused by systematic variation in the spot size or window coating level could lead to the variation shown in the deposition rate versus the absolute fluence.

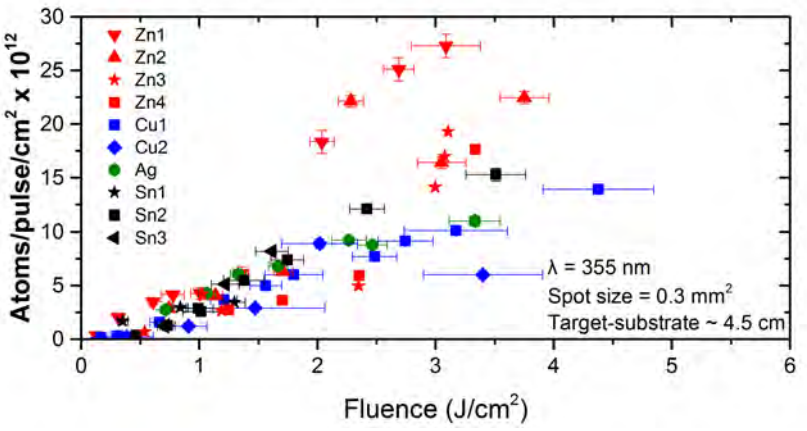

Figure 6.5: QCM measurements of the deposition rates of all the four metals using the 355 nm laser. For most of the metals the deposition rate was measured several times, giving rise to scattering of the data, but the general trends can still be seen as discussed in the text.

6.3.2 What do we learn from the ablation of metals?

In summary, in our deposition of the metals, we saw that Zn was deposited faster than the other metals at high fluence, while it had a similar deposition rate at low fluence. We also saw that the films generally had many droplets, with the Sn films almost entirely consisting of droplets.

Starting with the second point, Timm et al. [130] also saw many large droplets (> 1 µm) on Sn films compared to Ti and Al films made by 248 nm, 17 ns PLD. They explain the high number of Sn droplets simply by the low melting point of Sn (only 232 °C), see Appendix G, combined with a lower degree of plasma heating and consequently a larger amount of bulk heating than in Al and Ti. In our experiments not only Sn but also Zn has a rather low melting point, which might lead one to expect a large amount of droplets in the Zn films as well. The reason we do not see this is probably that Zn has a very low cohesive energy compared to Sn, reflected by its (zinc's) low boiling point (Appendix G).

As discussed in our article [227], the low cohesive energy of Zn can also explain the first point above, namely the high deposition rate of Zn. The observation of a shift from a slower to a faster deposition rate for Zn was not mentioned in the article. It may be that the extreme volatility of Zn coupled with its relatively low thermal diffusion coefficient leads to a higher pressure in the ablation plume of Zn than for the other metals. When the fluence is high enough, this pressure may increase the rate of erosion of the target by the plume and thus result in a higher deposition rate.

In depositions of Ti, Sn, and Al, Timm et al. [130] see a linear dependence of ablation rate on the laser fluence that "bends" with a lower deposition rate at low fluences. However, the bend in their deposition rate curve occurs much closer to the ablation threshold than the effect seen here for Zn. In Fig. 6.5 a low fluence bend in the curve similar to that observed by Timm et al. may be seen for Cu and perhaps for Sn. The "bending" is explained by Timm et al. as a small amount of evaporation that takes place below the ablation threshold because there is no plume to shield the target. Such an explanation could not apply for the bend in the Zn deposition rate curve here, which is far above the ablation threshold.

One surprise that came out of this work was that the deposition rate of Sn was much lower than what would be expected based on the ablation rate measured by Thestrup et al [231]. The term "ablation rate" is different from "deposition rate" because the ablation rate is measured by the weight loss of the target after thousands of shots while the deposition rate is measuerd by the QCM as mass per area deposited on the substrate. In Fig. 6.5 the deposition rate for Sn is very similar to that for Cu and Ag. However, as shown in Table 1 of our article, Thestrup et al. measured a higher ablation yield for Sn than for Zn using the same laser as us with a larger spot size (4 mm^2). As discussed in our article [227],

the comparison can be used to infer that Sn is resputtered from the growing film. This hypothesis is supported by the large number of craters seen in the Sn films, which may be caused by large impinging droplets. The hypothesis could be tested further by placing a substrate behind or next to the target.

What can we take with us? The simplistic version is that phases that easily melt may cause huge numbers of droplets which can in turn erode the growing film, while phases that are highly volatile may be much more easily ablated than non-volatile phases. Both of these lessons may be borne in mind later on when we discuss the deposition of CTS.

6.4 Results and discussion: ZnS

We deposited ZnS at room temperature on both fused silica and silicon and at 100, 200, and 300 °C on fused silica. The latter films were examined by XRD and transmission measurements. We found relatively low crystallinity of the films and a mixture of the hexagonal and cubic phase, interestingly with the cubic phase non-randomly oriented at room temperature and the hexagonal phase occurring at higher temperature. The absorption coefficient was calculated from the transmission measurements and used to make a Tauc plot for extrapolating a tentative value of the bandgap (see Section 5.6.2).

6.4.1 Deposition rate of ZnS versus metals

The 355 nm laser light should not be well absorbed by ZnS as the bandgap of ZnS at 3.54 eV corresponds to 350 nm, so the laser energy is at the threshold for exciting electrons to the conduction band of ZnS. Therefore one might expect inefficient ablation of ZnS. Nonetheless, the deposition of ZnS was much faster than that of Zn and the other pure metals, as seen in Figure 6.6. In our article on ZnS and CTS deposition in Applied Surface Science (Appendix A [211]) we briefly mention this comparison of deposition rates and attribute it to the lower thermal diffusion length in ZnS compared to Zn and the other metals, which means that the absorbed energy is not as easily lost in the bulk target.

While we would expect a much longer absorption length in ZnS than the metals which would reduce the ablation efficiency of ZnS, defects in the target may be causing a higher absorption than in bulk ZnS. We can see that in the visible spectrum there is significant scattering and reflection of the incoming light in the target as it appears off-white and completely non-transparent to the naked eye. Based on the reflectance of the target, the Kubelka Munk function may be calculated according to Equation 5.6.1. This allows us to check that there is absorption also in the low UV spectral region as the Kubelka Munk function is proportional to the absorption in this decidedly dull target material. The

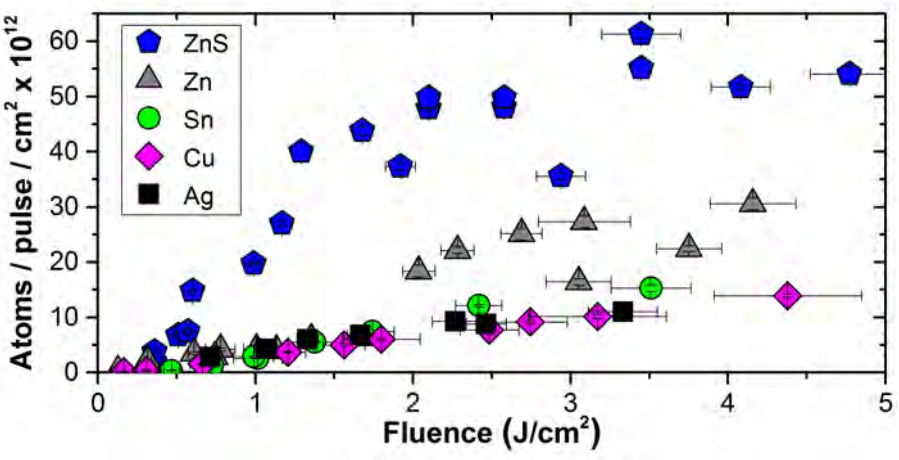

Figure 6.6: Deposition rate of ZnS versus Zn, Cu, Sn, and Ag in atoms per cm^2 using the 355 nm laser with a 0.2-0.3 mm^2 spot size. The mass of material deposited per area was measured by a QCM and the number of atoms per pulse was calculated assuming the densities listed in Appendix G.

resulting function is shown together with the reflectance in Figure 6.7 and shows that the absorption is significant at 355 nm in this target, whether it is occurring through excitons or other transitions in the material.

We determined the reflectance of both the ZnS and the metal targets using a total internal reflection sphere. It is clear that the reflectance of the ZnS target is much lower (at about 20 %) than that of the Zn target (about 60 %) at 355 nm. The other metals vary in reflectivity: the Ag reflectivity is similar to that of Zn, Sn is slightly lower, while Cu is significantly lower (about 40 %). See Figure 6.8. As discussed in our article [233], the differences in target reflectivity could not immediately be related to the metal deposition rates, perhaps because the reflectivity changes rapidly as soon as the surface melts. Nevertheless, the low reflectivity and high Kubelka Munk function of ZnS at 355 nm points to high coupling of light into the target material.

We see from Figure 6.9 that the surface of the ZnS target ends up being much smoother than the metallic target surfaces shown above in Figure 6.2 - even compared to the Cu target. The smoothness of the ablated target matches the smooth appearance of the ZnS films - almost droplet free. Again the reason probably is connected to the melting point: While Zn melts at 420 °C and boils at 907 °C at atmospheric pressure, ZnS only melts at 2100 °C. All other things being equal, this would mean that a smaller melted volume exists in ZnS which

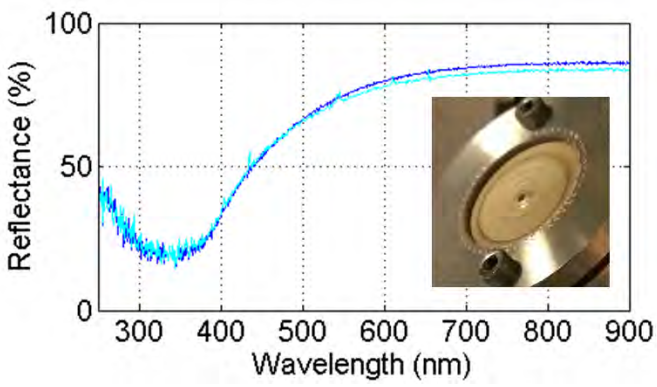

(a)

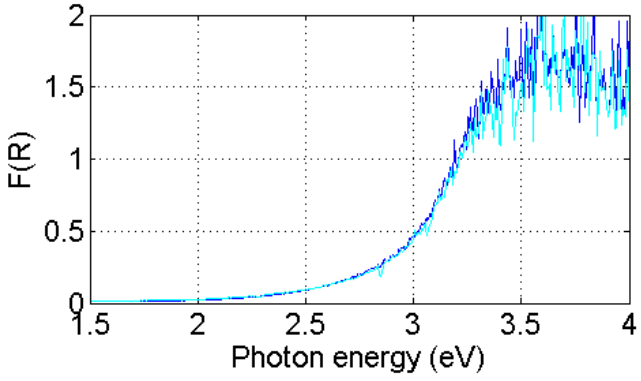

(b)

Figure 6.7: Reflectance and Kubelka Munk function for the ZnS target as measured by a total internal reflection sphere. (a) Reflectance. Inset: photo showing the the dull appearance of the ablated target. (b) Kubelka Munk function, F(R), which is defined in Eqn. 5.6.1 and is proportional to the absorption coefficient.

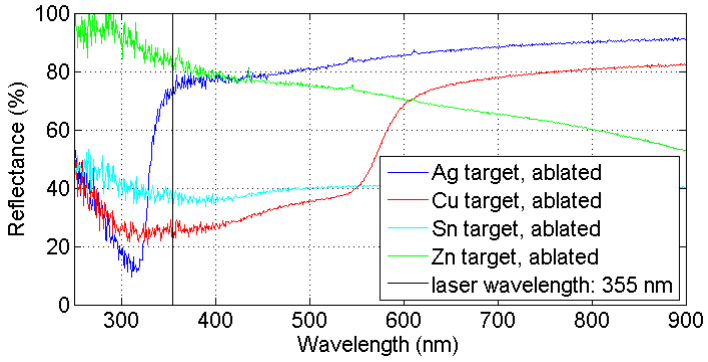

Figure 6.8: Reflectance of the ablated metal target surfaces as measured by a total internal reflection sphere.

may experience subsurface boiling or recoil pressure. In reality, other things are not equal as the absorption depth is larger in ZnS while the thermal diffusion length is not so different from that in Zn. This can intuitively be imagined as a larger volume being heated instantaneously in ZnS than Zn and therefore a larger volume is ablated, while relatively less is heated to the melting temperature, again leading to fewer droplets for a given film thickness.

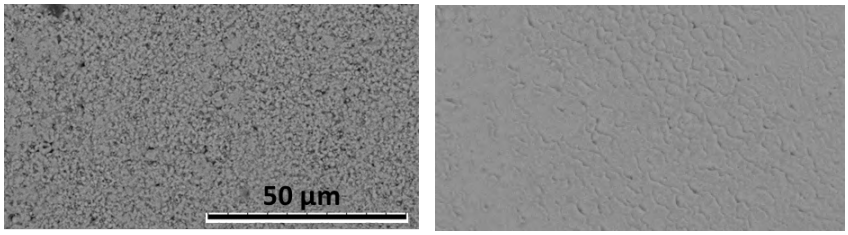

(a) (b)

Figure 6.9: The morphology of the ZnS target viewed by SEM before and after ablation by the 355 nm laser. (a): Fresh target (ridges from polishing by manufacturer). (b): Ablated target The scale bar applies to both images.

For practical film growth applications, we found a ZnS growth rate of 150-200 nm/hr at 1.2 J/^{2} with a laser spot of 0.3 mm^2 while the deposition rate nearly trebled by a tripling of the laser spot size to $\approx$ 500 nm/hr, 1.2 J/cm^2 with a 1 mm^2 spot. This spot size is closer to literature values, e.g., Shen and Kwok use

a 2 mm^2 spot [137].

As shown in Figure 2 of our article (Appendix A), using the 355 nm setup we found no apparent difference between the deposition rate at room temperature and elevated temperatures, although this was not thoroughly investigated as there was no temperature controlled QCM in place in this setup. Surprisingly, in QCM experiments made with the 248 nm laser, we found consistently lower deposition rates at 300 °C than at room temperature for a range of fluences. See Figure 6.10 This contrasts to what we later saw in CZTS depositions and also with what other groups have seen (as noted in the background section, other groups mainly saw decreasing deposition rates at temperatures above 400 °C, although e.g. Xin et al. have large scattering of their data below 400 °C [81]).

Comparing the deposition rate of ZnS to CTS can tell us a little bit more about the effect of the laser wavelength: Using the 355 nm laser, whose energy is extremely close to the bandgap energy of ZnS, the deposition rate of ZnS and CTS are nearly the same. Decreasing the laser wavelength to 248 nm, however, means that the laser energy now comfortably exceeds the bandgap, and we see that the deposition rate of ZnS is much higher than that of CTS - especially at low fluence. See Figure 6.11.

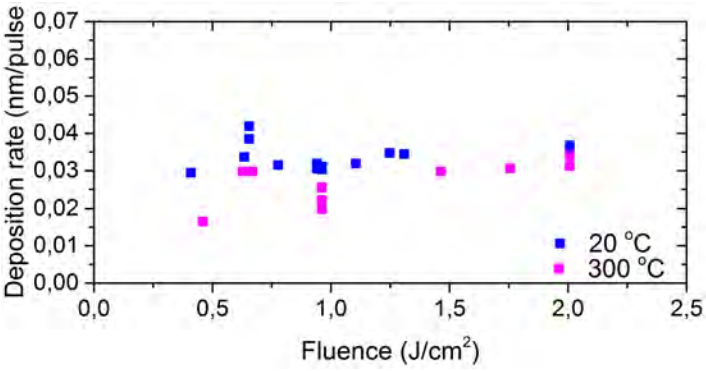

Figure 6.10: ZnS deposition rates at room temperature and 300 °C using the 248 nm laser. Most data recorded by Andrea Cazzaniga.

6.4.2 ZnS film characteristics

The main results regarding ZnS in our article (see Appendix A) were:

- The ZnS films were somewhat crystalline even at room temperature, most likely with a (220)-oriented cubic phase growth at room temperature and a mixture of the cubic and hexagonal phases at higher temperatures.

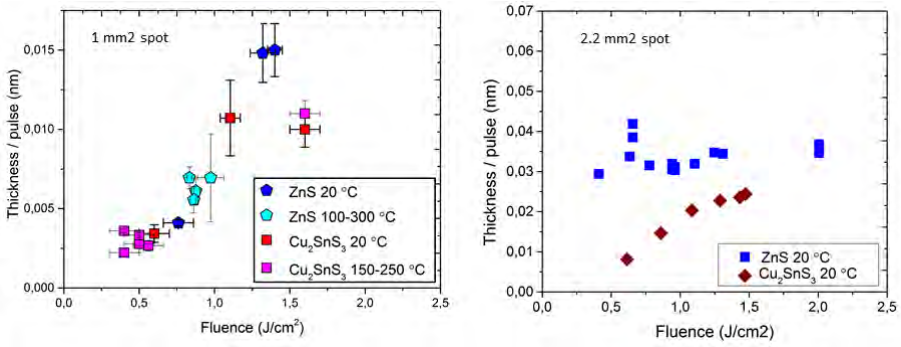

Figure 6.11: The deposition rate of ZnS compared to CTS at 355 nm (left) and 248 nm (right). While the deposition rate of CTS and ZnS are nearly the same at low fluence with the 355 nm laser, they are significantly different at low fluence with the 248 nm laser. As in Figure 6.10, the ZnS data were mostly recorded by Andrea Cazzaniga.

- The bandgap as measured from a Tauc plot increased towards the 3.5 eV bandgap characteristic of the cubic ZnS phase as the deposition temperature increased, similar to observations made in pulsed electron deposition (PED) of ZnS on soda lime glass substrates by Zanettini et al. [83].

Note that the determination of the bandgap based on a Tauc plot is fraught with difficulties as mentioned in Section 5.6.2. Our films most likely contained a mix of phases and probably also an amorphous fraction, so that the term "bandgap" becomes rather imprecise. The term "absorption onset" might more accurately be used. Also, specifically in ZnS, excitonic absorption is known to be significant, so that absorption below the bandgap should be expected [199].

Nonetheless, from the Tauc plots in the article, Figure 4a, Appendix A, we notice a difference between our films and the similar films made by PED: the high temperature (200 - 300 °C films have a longer tail of low-energy absorption (or a lower transmission) than the PED films. This may be due to defects in the films. Note that the figure is missing a label on the y-axis, which should be identical to the insert, namely $(\alpha h\nu)^2$ in units of eV/cm^2.

A fact not shown in the article was that ZnS was deposited at room temperature on both fused silica and crystalline Si substrates. While the crystalline substrates were only used for room temperature depositions and the orientation of the growing films on Si versus fused silica was not explored, it was clear that the substrate played a role in improving film adhesion for films deposited at room temperature. Specifically, for thick films the adhesion was much stronger on Si

than on fused silica even at room temperature.

The stoichiometry of the ZnS films used in the transmission measurements could not be accurately measured by EDX since the films were relatively thin.

6.4.3 Crystalline film texture

Even though we used amorphous silica substrates, we see textured ZnS growth at all temperatures (i.e., a preferential growth direction of the crystal grains). The room temperature films were clearly preferentially oriented with the (220) cubic planes parallel to the surface (or perhaps the (110) hexagonal planes) as seen in Figure 3a in Appendix A. The peak is very broad, indicating very small crystal grains, but it is also quite intense. This is surprising because the amorphous silica substrate should not be imparting a preferential growth direction. The preferential growth must therefore come from an intrinsic minimization of the surface energy by growth in this direction. Apparently this minimization of surface energy changes at higher temperatures, where the growth orientation changes. The size of the peaks detected for our 100, 200, and 300 °C films are small, but it is clear that the cubic (111)/hexagonal(002)-oriented planes are preferentially aligned along the surface at these temperatures since otherwise several other relatively high-intensity peaks would be visible including those from the (220) cubic planes and/or the hexagonal (100) and (101) planes. Additionally, we see clear evidence of the hexagonal phase (100) planes already from 100 °C.

Our finding of a preferential growth direction that changes with temperature and our finding of a mixture of hexagonal and cubic temperatures at elevated temperature is similar to the results of some other authors but not all. Shen and Kwok found exclusively cubic ZnS growth by 193 nm PLD at 300 °C in 0.01 mbar Ar on four different substrates: (111)- and (100)-oriented GaAs, (100)-oriented InP and glass - so no hexagonal phase was present even on an amorphous substrate. On the glass substrates they found random cubic crystal orientation while, as might be expected, they found textured growth on textured substrates [137]. In contrast, Yano et al., like us, see a mix of the cubic and hexagonal phase with a preferential cubic (111) orientation on an amorphous silica substrate using the same type of laser as us (355 nm) but a somewhat higher temperature (400 °C) [199]. By PED, Zanettini et al. [83] also found that the (200) plane peak disappeared when the substrate temperature increased from room temperature to 100 °C and 200 °C, although they did not find as strong a texture as we do (this was not accurately reflected in our article, where we mistakenly write that the PED films were (220)-oriented at room temperature and (111)-oriented at higher temperatures - instead, at room temperature it merely appears that they see random orientation and at 100 °C and 200 °C the (220) peak disappears while the (111) and (311) peaks stay present). Zanettini et al also found the hexagonal

phase mixed with the cubic phase at a temperature $\leq 200\,^{\circ}\mathrm{C}$ while they could show that the growth was fully hexagonal-phase at $300\,^{\circ}\mathrm{C}$ [83].

Thus it appears that despite the findings of exclusively cubic-phase ZnS on untextured substrates by Shen and Kwok, we should use cubic lattice-matched substrates if we wish to obtain exclusively cubic-phase ZnS thin films in PLD. Remembering that the hexagonal and cubic forms of ZnS are polytypes that differ in only the stacking order of the ZnS-motif in one dimension, it does not seem entirely surprising that the two phases might easily co-exist in a non-equilibrium deposition process.

6.5 Summary

Overall, these experiments taught us:

- that the melting and boiling points of the materials have a large influence on the film deposition rate and the number of droplets
- that PLD of ZnS may result in different crystal orientations depending on the temperature
- PLD of ZnS is much more efficient than PLD of Zn or other metals
- that temperature up to $300\,^{\circ}\mathrm{C}$ did not have a large influence on the deposition rate of ZnS (though some effect was measured with the 248 nm laser)
- that PLD onto non-crystalline substrates may lead to low film adhesion and mixed crystalline phases of ZnS
- that PLD and PED of ZnS yielded similar results in terms of crystallization and absorption onset as a function of temperature

Chapter 7

Pulsed laser deposition of copper tin sulfide

A large part of the work of this PhD was done on copper tin sulfide (CTS). There were six main areas of investigation:

- the effect of changing the laser wavelength (especially the effect on the film composition and on the number of droplets)
- the impact of the laser fluence on the film properties(especially the composition)
- deposition of SnS-enriched CTS versus near-stoichiometric Cu_2SnS_3
- deposition at elevated temperatures up to 300 °C
- annealing the as-deposited CTS films
- making CTS solar cells from the annealed films

In the following sections the results will be discussed. Some of the early work on CTS deposition on fused silica with the 355 nm laser was presented together with our results on ZnS in the article "Pulsed laser deposition from ZnS and Cu_2SnS_3 multicomponent targets" (Applied Surface Science 2014), Appendix A [211]. Other results, especially the work on comparing the two different laser wavelengths, are presented in the article "Formation of copper tin sulfide films by pulsed laser deposition at 248 and 355 nm" (Applied Physics A 2016), Appendix B [210]. Preliminary results on annealed CTS films were presented at the WCPEC-6 conference in Kyoto in November 2014 and are included in the conference proceedings in a short article entitled "Pulsed laser deposition of Cu-Sn-S for thin film solar cells", which is included in Appendix C. Finally, ellipsometry

measurements of some of the annealed films were carried out by my colleague Andrea Crovetto and published in a paper entitled "Dielectric function and double absorption onset of monoclinic Cu_2SnS_3: Origin of experimental features explained by first-principles calculations," (Solar Energy Materials & Solar Cells, 2016) [213]. The remaining work on films deposited at elevated temperature and annealed films has not been published.

7.1 Background and aims for PLD of CTS

Copper tin sulfide was introduced in Section 2.3. Briefly, it is a potential solar cell absorber material with a bandgap of about 0.9-1.4 eV depending on the crystal structure. The highest efficiency to date is 4.6 %, which was achieved in a solar cell that used the same cell design as in CZTS and CIGS as described in Section 2.3.2. Additionally, CTS is a secondary phase of CZTS that can be difficult to detect because of overlapping peaks in both X-ray diffractograms and Raman spectroscopy [39]. Cu_2SnS_3 has a complicated phase diagram with a variety of polymorphs, and adjoining phases of different composition including Cu_4SnS_4, $Cu_3Sn_7S_{16}$, and Cu_3SnS_4.

As mentioned at the start of Section 4.3, no previous work had been published on PLD of CTS at the time the CHALSOL project started. Following our own first publication on PLD of CTS, one other paper has been published on this subject by Vanalakar et al. in 2015 [234], demonstrating a 0.82 % solar cell. These authors deposit CTS with a 248 nm KrF laser with a 25 ns pulse width in vacuum and at room temperature. Following the deposition, their films were annealed in a H_2S-N_2 atmosphere for 1 hour at 200 °C, 300 °C, or 400 °C. The best films (largest crystals) were found to be cubic-phase Cu_2SnS_3 at 400 °C and were used in the solar cell.

The primary aim of our investigation of CTS was to better understand the secondary phases formed in CZTS. Initially we had hoped that it would be possible to make as-deposited CZTS solar cells and we also worked with as-deposited CTS. As it became clear that it would be necessary to anneal the CZTS we also began to anneal our CTS films - also because the aim was to make phase-pure films for analysis, and this proved challenging with as-deposited films.

The main issue we had to address was the stoichiometric deviation of the film composition from that expected from the target. Additionally, we were challenged by large droplets in the films, which sometimes had a different composition to the underlying matrix. After initial experiments with the 355 nm laser, we decided to try the 248 nm laser as this was the laser being used for CZTS, so any stark differences in the phases that were most favorably formed with the 248 nm laser compared to the 355 nm laser were important to investigate. We also expected that the 248 nm laser might reduce the amount of droplets in the films, as a

shorter laser wavelength is a frequently cited method for reducing droplets in PLD literature [96]. Droplet generation and the impact of laser wavelength was discussed in Sections 3.3 and 3.4 as well as in our article in Applied Physics A (Appendix B) [210]. In the end we found no impact of the laser wavelength on the amount of droplets in the films.

Many films were made with a SnS-rich target, as our initial investigations (included in the Applied Surface Science paper) indicated that the as-deposited films were Sn-deficient. This target overcompensated for the Sn-deficiency and complicated matters still more. In the end we succeeded in producing thin single-phase and thicker nearly single-phase CTS films from near-stoichiometric Cu_2SnS_3 targets. More work must be undertaken to prove whether these films would yield better solar cells.

The methods and materials for these experiments were described in Chapter 5. Here it is just important to mention that two types of targets were used in the experiments: some with a composition intended to be Cu_2SnS_3 which will in the following be called "near-stoichiometric CTS" and one with a Sn and S-rich composition relative to Cu_2SnS_3, (intended to be $Cu_2Sn_2S_5$), which will be called "SnS-rich CTS". As noted in Section 5.6.4 it was not easy to verify the composition of these targets by EDX measurements.

7.2 Results and discussion: As-deposited films

7.2.1 Deposition rate at different wavelengths

In our article in Applied Physics A (Appendix B) where we compares CTS deposition at 355 nm and 248 nm, we show that the 355-nm laser resulted in a higher deposition rate than the 248-nm laser did at a given fluence. This is probably because the fluence simply does not tell the full story: we should rather look at the intensity (power per unit area rather than energy per unit area). The 355-nm laser has far shorter pulses (approx 6 ns long compared to 20 ns in the 248-nm laser), so the laser power incident on the target is higher for the 355-nm laser.

In the 248 nm setup, we had a temperature-controlled QCM available, and just as we did for ZnS, we were therefore able to check whether the deposition rate of CTS was different for a heated substrate compared to the room temperature deposition rates included in the paper [218]. The deposition rate was slightly lower at elevated temperature than at room temperature, as seen in Figure 7.1. This may mean that the volatile constituents (SnS or S) re-evaporate or have a lower sticking coefficient at 300 °C than at room temperature.

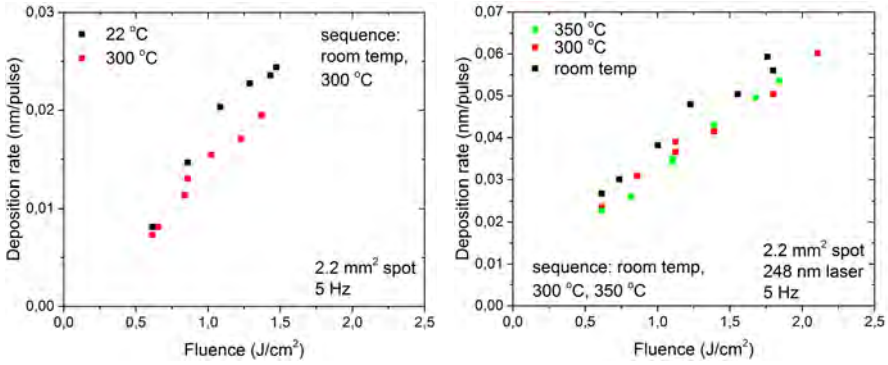

(a) CTS (b) SnS-rich CTS

Figure 7.1: Deposition rate of CTS (a) and SnS-rich CTS (b) at room temperature versus 300 °C using the 248 nm laser. Note different scales on the two graphs. The deposition rate is lower at 300-350 °C.

7.2.2 Fluence effect on composition

In our article in Applied Surface Science (Appendix A), we see a small change in the composition when the fluence was changed (Table 1 in the article): The films deposited at 1.6 J/cm^2 contained relatively more Cu than the films deposited at 0.6 J/cm^2 with the 355 nm laser. While this observation was quite tentative at the time and was not stated clearly in the article, later observations proved that the CTS films indeed become more Cu-rich with increasing fluence. The reason we did not trust the initial observation was that the first films were too thin to enable us to trust the EDX composition measurement quantitatively. However, we were able to qualitatively compare the films made under different circumstances as long as they had the same thickness.

Our initial measurements on the thin films also hinted that the films were Sn-poor relative to the Cu content, prompting us to invest in an Sn-rich target. Since the films were thin, however, this conclusion was not reliable, because according to Casino simulations (Section 5.6.4) the Sn X-ray emission on average derives from deeper in the films than Cu-emission. This means that the detector would receive relatively less Sn emission from a thinner film, leading to underestimation of Sn all other properties being equal. The EDX software quantification of excess Cu relative to Sn in the first films may therefore have been an artifact. Later we saw that some films were indeed Sn-poor while some were Sn-rich as described below.

The fluence dependence of the composition turned out to be most pronounced

when using the near-stoichiometric CTS target. Initially we looked at the composition of SnS-rich CTS (now thick enough to be measured reliably) as shown in Table 7.1. With this starting material we saw:

A that even though these films were made from an SnS-rich target, they were apparently S-poor

B that the composition of two films that were made under identical circumstances could vary by a few atomic percent in the measured composition, exceeding the instrumental variability

C the composition of films deposited at room temperature was not affected by the substrate, as expected, and most importantly,

D there was no significant difference while varying the fluence with a constant spot size from 0.7 to 2.3 J/cm^2, nor a significant difference between thick SnS-rich CTS films (>1700 µm) grown at 1.8 and 4.3 J/cm^2 with the same energy per pulse but different spot sizes.

Table 7.1: The composition of SnS-rich CTS films deposited under different circumstances. The differences in substrate and thickness is not expected to make a difference for these films, which were deposited at room temperature. EDX measurements done in the TM3000 tabletop microscope with ≈ 1 % standard error on measurements made on different locations and different days on the same films.

Substrate	Fluence J cm^{-2}	Thickness µm	Spot size mm^2	Cu %	Sn %	S %
Mo/SLG	0.7	1.9	2.5	20	34	45
Mo/SLG	1.4	1.2	2.5	21	34	44
Mo/SLG	2.3	1.3	2.5	24	33	43
Mo/SLG	2.3	1.2	2.5	21	34	44
fused SiO_2	0.7	4.2	2.5	20	33	47
fused SiO_2	1.7	1.7	2.5	20	35	45
fused SiO_2	2.2	1.2	2.5	21	34	45
fused SiO_2	2.8	1.6	2.5	20	35	45
fused SiO_2	1.8	>6	2.5	29	29	42
fused SiO_2	4.3	1.8	0.9	27	28	44

All this data is included to illustrate that at first we saw no fluence dependence of the composition, whether this was because we did not vary the fluence enough

or because the SnS-rich target responded less to changes in the fluence than the near-stoichiometric target did. When we finally obtained Cu-poor films, this was with the near-stoichiometric CTS target with a fluence values as low as ≈ 0.2 to $0.5\,\mathrm{J\,cm^{-2}}$ as shown in Table 2 in Appendix B [218]. This was attempted after A. Cazzaniga found that CZTS films were extremely Cu-poor at very low fluence with the 248 nm laser. The higher ablation efficiency for CTS with the 355 nm laser compared to the 248 nm laser meant that the change in composition between $0.5\,\mathrm{J/cm^2}$ and $1.6\,\mathrm{J/cm^2}$ was much greater with the 248 nm laser than the 355 nm laser, as seen in the table in the Applied Physics A article. This was probably part of the reason that we did not immediately trust the effect of fluence on the composition with the 355 nm laser.

7.2.3 Fluence and laser wavelength effect on droplets

In our article in Applied Physics A, Appendix B [210], we found that the amount of droplets per area of the film did not depend on the laser wavelength, but instead on fluence. This had not been immediately obvious from initial experiments with the SnS-rich target. Figure 7.2 shows that just as there was no detectable difference in the composition, there was also no difference in the droplet area density for this material even though the fluence was changed from $0.7\,\mathrm{J/cm^2}$, to $2.3\,\mathrm{J/cm^2}$. The fluence was varied among these films by varying the laser energy while keeping the spot size constant at 2.5 $\mathrm{mm^2}$. In Section 3.3 we saw that changing the spot size while keeping the energy per pulse constant resulted in more droplets when we used a very small spot ($<$1 $\mathrm{mm^2}$).

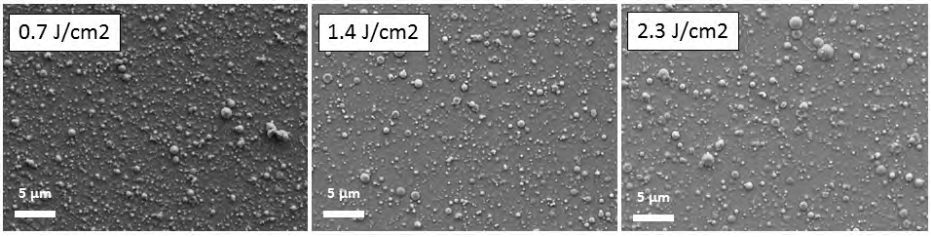

Figure 7.2: SEM images of SnS-rich CTS films made at different fluence, illustrating that at first we saw little change in the area density of droplets when changing the fluence. The films were deposited with a constant spot size (2.5 $\mathrm{mm^2}$) and 40 min, 20 min and 30 min deposition time respectively for the films deposited at $0.7\,\mathrm{J/cm^2}$, $1.4\,\mathrm{J/cm^2}$ and $2.3\,\mathrm{J/cm^2}$

.

The droplets were sometimes Sn-rich and sometimes Cu-rich as seen in Figure 7.3. Similar images have been shown by Che Sulaiman et al. for CZTS: some

Cu-rich droplets and some Sn-rich droplets were observed (no Zn-rich droplets are shown; it is not clear if there were any) [164]. For the Applied Physics A-article, Andrea Crovetto measured the composition of about 70 droplets on our CTS films using the point-and-shoot EDX option in the Supra V40 equipped with an Oxford EDX detector. The width of the measurement spot was on the order of 1 µm, so the accuracy was limited. Nevertheless, it appeared that on near-stoichiometric CTS films the droplets were on average Cu-rich relative to the matrix of the surrounding film. The data are shown in Figure 5 in the paper (Appendix B).

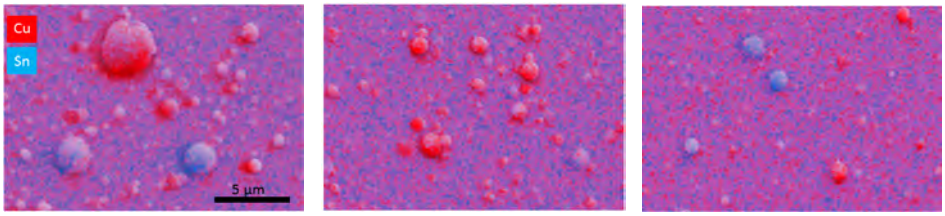

(a) CTS 248 nm (b) CTS 248 nm (c) CTS 355 nm

Figure 7.3: EDX maps showing Cu-rich and Sn-rich droplets on CTS films. (a): 248 nm deposition of a near-stoichiometric CTS film at $\approx 1.6\,\mathrm{J/cm^2}$. (b): Droplets elsewhere on the film imaged in (a). (c): 355 nm deposition of a near-stoichiometric CTS film at low fluence ($\approx 0.2\,\mathrm{J/cm^2}$). All images are at the same magnification. SEM/EDX by A. Crovetto.

The target surface after ablation by the 355 nm laser provides some clues on the origin of the droplets (Figure 7.4). As mentioned in Section 5.4.1, the targets for CTS deposition were multiphase; this is clearly seen in the images of the target before ablation. The difference is striking between the rough appearance of the CTS target after ablation and the smooth appearance of the ZnS target after ablation by the 355 nm laser (Figure 6.9). Many groups have described the appearance of cones on the target after multiple shots, which can easily be imagined as a source of droplets in the extreme process when a new laser pulse hits the same area repeatedly. Minimizing cone-formation leads to fewer droplets according to several authors [136, 129].

Overall we learned that to reduce droplets we had to severely reduce the fluence - to $\approx 0.2\,\mathrm{J/cm^2}$ with the 355 nm laser and $\approx 0.5\,\mathrm{J/cm^2}$ in the 248 nm laser. Reducing the fluence so drastically of course also lowered the deposition rate significantly and changed the composition of the films as we saw above.

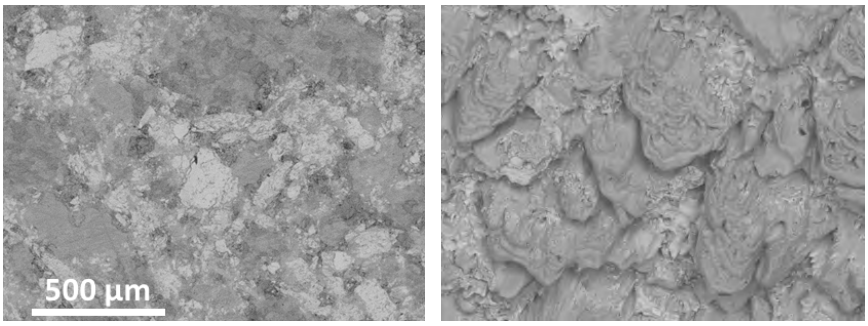

(a) (b)

Figure 7.4: SEM images of the CTS target surface (a) before and (b) after it was ablated by the 355 nm laser. The unablated target consists of Sn-rich and Cu-rich regions (Cu-rich regions appear dark, Sn-rich regions appear bright as seen by EDX, not shown). After ablation the target surface is rough with lobes of material sticking out. The scale bar applies to both images.

7.2.4 CTS films deposited at 150-300 °C

In the Applied Surface Science article (Appendix A [211]) we showed that crystalline CTS forms when the substrate is heated to 150-250 °C. The films shown in the article were made with the 355 nm laser from a near-stoichiometric CTS target on fused silica and we found tetragonal Cu_2SnS_3 at 150 °C, while at 250 °C we found cubic-phase Cu_2SnS_3, as judged by the slight shift in the main XRD peak compared to the 150 °C film, along with secondary phases of Cu_4SnS_4 and orthogonal SnS.

The deposition temperature seemed to change the S-content of the films: surprisingly, the percentage of S in the films apparently increased slightly as the substrate was heated from room temperature to 250 °C. This is shown in Table 1 in our investigation presented in Applied Surface Science (Appendix A). We don't know why the sulfur content increased with temperature, but it may be that the sticking coefficient increased as the S was incorporated in a crystalline film. It is important to note that we did not check for inhomogeneities across the depth of the film. Such inhomogeneities, which were later observed by SEM in some of our CZTS films deposited at high temperature, would cause errors in the EDX measurements, so this result should be considered preliminary.

The initial films included in the Applied Surface Science article were deposited on fused silica and there could be some differences in which phases would most favorably form on Mo/SLG substrates. Subsequent depositions using the 248

nm laser on Mo/SLG painted a similar picture as we will see below: tetragonal CTS and an amorphous appearance at 150 °C (no grains visible in SEM), cubic or monoclinic CTS at 300 °C mixed with Cu_4SnS_4.

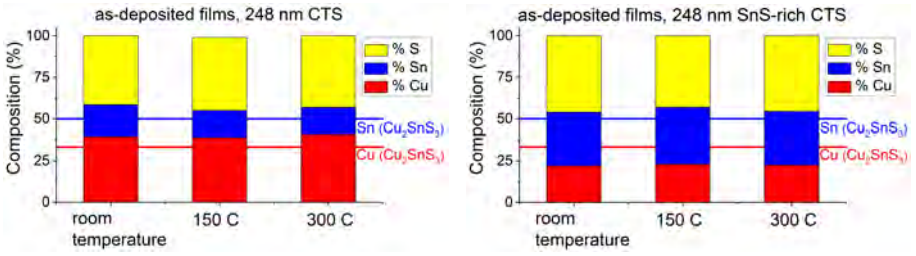

(a) (b)

Figure 7.5: Composition of CTS films deposited on Mo/SLG by the 248 nm laser. (a) shows films made from the near-stoichiometric CTS target grown at $\approx 1.6\,\mathrm{J/cm^2}$ (room temperature) or $\approx 1.4\,\mathrm{J/cm^2}$ (150 °C, 300 °C). (b) shows films of SnS-rich CTS deposited at ≈ 1.6 to $1.8\,\mathrm{J\,cm^{-2}}$. A film deposited at $\approx 1\,\mathrm{J/cm^2}$ had approximately the same composition. These films were all about 800-900 nm thick, thick enough that the EDX measurements may be trusted quantitatively.

With the 248 nm laser, we saw that the deposition rate decreased slightly at higher temperature, which led us to expect a decrease in S and perhaps also Sn in the films deposited at higher temperature. This expectation was not met: Within the error of the EDX measurements, the films deposited with this laser had the same composition at room temperature, 150 °C and 300 °C. See Figure 7.5.

It was encouraging not to find a large S- and Sn-loss due to increased temperature. However, as seen in the figure, the films deposited from the near-stoichiometric CTS target were consistently Cu-rich (the measurements this time were on films thick enough to be trusted), while the films deposited from the SnS-rich target were consistently extremely Sn-rich, neither of which is promising for phase-pure Cu_2SnS_3 whether for solar cells or for advanced characterization. Note that the target stoichiometry could not be accurately quantified as explained in Section 5.6.4. The measured CTS target stoichiometry was quite close to the ideally expected composition, while the measured stoichiometry of the SnS rich target was more Sn-rich and less S-rich than expected.

SEM images of the SnS-rich CTS films deposited at 150 °C and 300 °C on Mo/SLG with the 248 nm laser are shown in Figure 7.6, verifying that these films were uniform in cross-section. X-ray diffractograms showed that the 150 °C-film was completely amorphous while the 300 °C-film contained strong diffraction

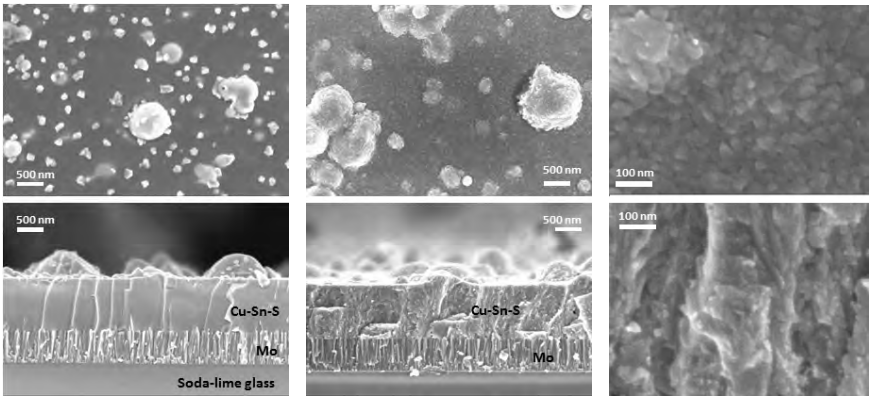

(a) (b) (c)

Figure 7.6: As-deposited SnS-rich CTS films: (a) at a substrate temperature of 150 °C, and (b) at 300 °C. (c) is a close-up of the film in (b). The films were deposited on Mo/SLG with the 248 nm laser at 1.6 to 1.7 J cm^{-2}. Images by L. Ravnkilde and T. Youngman.

peaks most likely of tetragonal-phase Cu_2SnS_3 and orthorhombic SnS (see Figure 7.8a). The co-existence of these two phases is not immediately obvious based on the uniform appearance of the film (Fig. 7.6 (b) and (c)). Based on the strong intensity of the (112) peak relative to the other peaks, the CTS phase appears to be preferentially oriented with the (112) planes parallel to the film surface.

The films deposited from the ordinary CTS target at 300 °C with the 248 nm laser formed crystalline Cu_2SnS_3 together with Cu_4SnS_4 and a large amount of another secondary phase that could be SnS, though this seems surprising based on the Sn-poor composition. See Figure 7.7a. The X-ray diffractogram is similar to what was seen with the 355 nm laser at 250 °C on fused silica (see Appendix A, Figure 3 b). In another similarity to the films made with the 355 nm laser, a film deposited at 150 °C by the 248-nm laser mostly shows crystallization of Cu_2SnS_3, most likely tetragonal phase (Figure 7.7b). Based on the relative peak intensities, this film is less cubic (111)/tetragonal(112) oriented than the 300 °C film - in fact it is apparently preferentially aligned with the cubic or tetragonal (220) planes parallel to the surface. It may be that some of the material is still in an amorphous form at this temperature.

The films deposited with the SnS-rich CTS target at 300 °C with the 248 nm laser formed crystalline Cu_2SnS_3 but like the near-stoichiometric film there is a large amount of secondary phases present. In this case it is clear that it

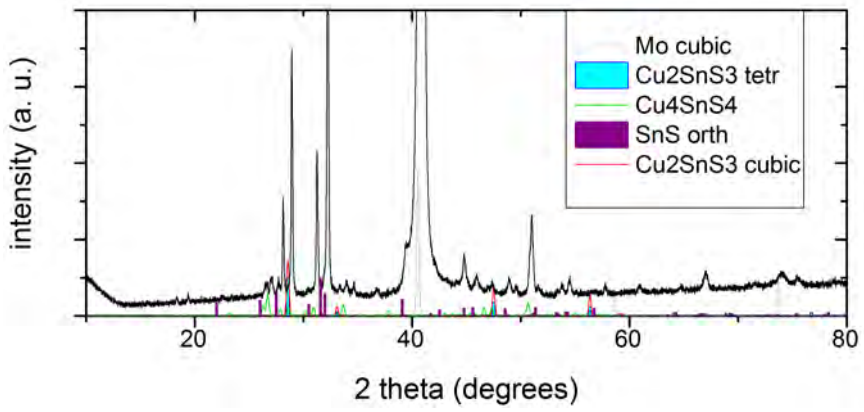

(a)

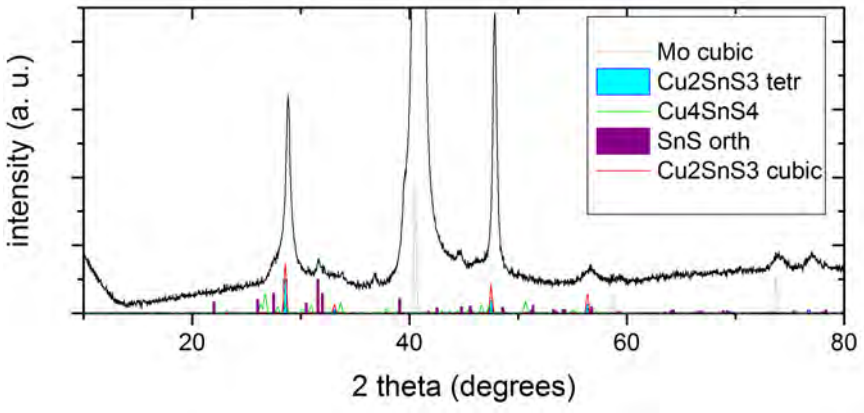

(b)

Figure 7.7: XRD of CTS films as-deposited on Mo/SLG with substrate heating with the 248 nm laser. (a) Near-stoichiometric 300 °C film with main peaks corresponding to Cu_4SnS_4, tetragonal Cu_2SnS_3, and orthorhombic SnS. Small peaks of MoO_x from the substrate also visible. (b): Near-stoichiometric CTS film as-deposited at 150 °C with peaks of Cu_2SnS_3, orthorhombic SnS, and again small peaks of MoO_x.

is orthorhombic SnS (see Fig. 7.8a). Surprisingly, the 150 °C SnS-rich film was completely amorphous (Fig. 7.8b).

These CTS films were deposited at an elevated substrate temperature before we knew that it is possible to change the composition by altering the fluence. Although it would certainly require a persistent effort, perhaps it would be possible to deposit single-phase or nearly single-phase CTS at the right temperature somewhere between 150 and 300 °C with a lower fluence that the $\approx 1.6\,\mathrm{J/cm^2}$ used here. However, it would be difficult to avoid S-poor films.

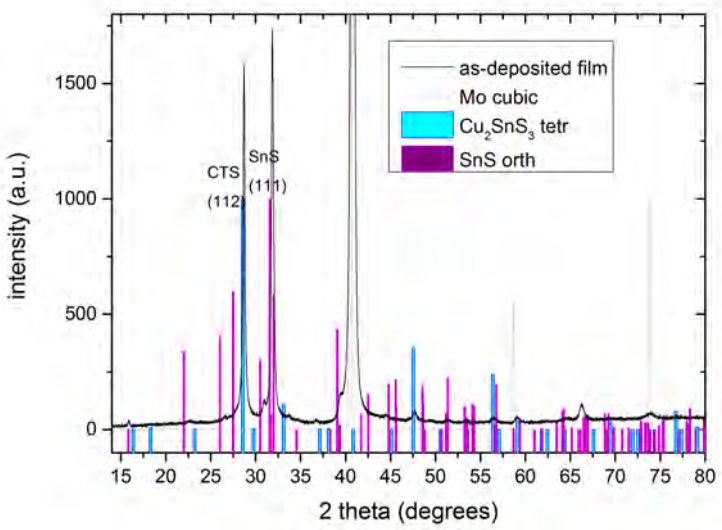

(a)

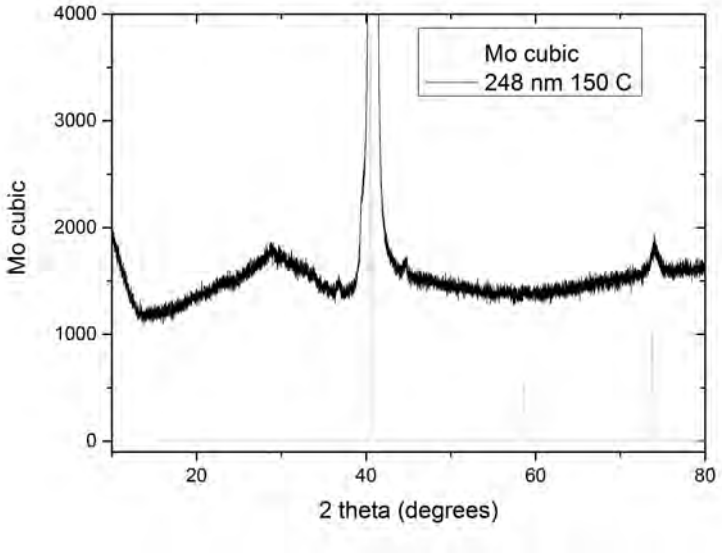

(b)

Figure 7.8: XRD of SnS-rich CTS films as-deposited with substrate heating with the 248 nm laser. (a) SnS-rich CTS film deposited at at 300 °C. The main peaks correspond to Mo (cubic), SnS (orth) and Cu_2SnS_3. SEM images of this film are shown in Fig. 7.6b). (b): SnS-rich CTS film as-deposited at 150 °C with no peaks except those deriving from the substrate.

7.3 Results: Annealed CTS films

A large amount of work was done on annealing a number of CTS films with mixed results. The aim was partly to investigate which phases of CTS would form under the conditions used for CZTS annealing in our group and partly to try to make CTS solar cells.

As described above, we initially found that the as-deposited near-stoichiometric CTS films were Sn- and S-poor relative to the desired stoichiometry. Films with $Cu/Sn > 2$ do not generally lead to good solar cell absorber layers, so initially we focused on annealing SnS-rich films. SEM top view images of our first annealed films looked beautiful compared to the messy droplet-filled surface we were used to from PLD: large crystals had formed apparently uniformly all over the films, at least in some cases. See Figure 7.9.

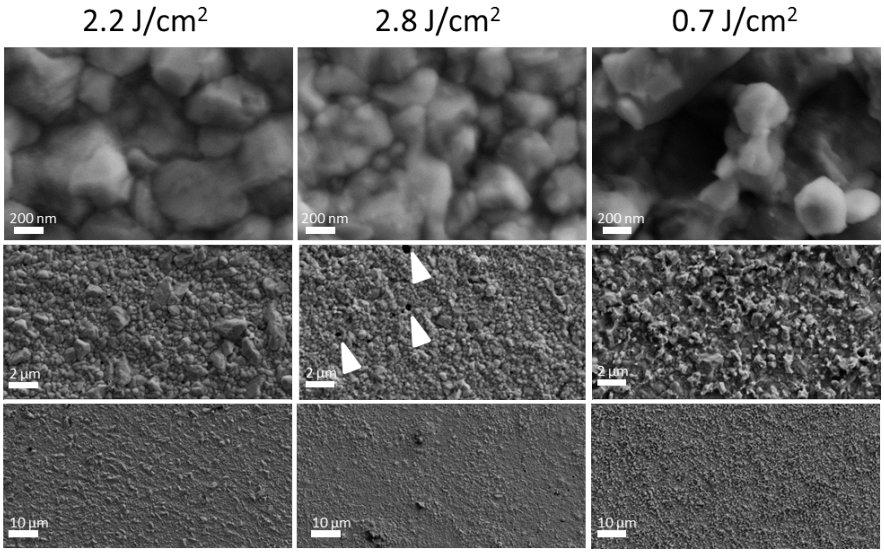

Figure 7.9: SEM top view images of annealed SnS-rich CTS films deposited by the 355 nm laser at various fluences. XRD showed orthorhombic SnS occurring together with Cu_2SnS_3 especially for the two films deposited at higher fluence, which were 1.2-1.7 µm thick. The rough film deposited at $0.7\,J/cm^2$ was 4.2 µm thick due to overcompensating for the low deposition rate at low fluence by increasing the deposition time. Small holes may be seen in the central panel of the $2.8\,J/cm^2$ film as indicated by the white arrows. We were later to see that these films contained huge amounts of SnS in cross-section. Images by E. Bosco.

As shown in the technical paper presented at WCPEC-6 (Appendix C), X-ray diffractograms of the films in Fig. 7.9 revealed SnS, which was not visible in the SEM top view images, and we assumed that evaporation of SnS was the reason for small holes in some of the films (can be seen in the technical paper and in the middle panel in Fig.7.9 upon close inspection). When we later looked at the films in cross-section, we found that most of the films showed a layered structure with sheets of SnS near the back (Figure 7.10). This meant that any measurement of the composition would be unreliable. It also posed an immediate problem for a solar cell material - it was remarkable that the solar cells we made worked at all. The characterization of the full solar cells will be described below in Section 7.4. In Fig. 7.11, we see that there were also other issues such as cracks and impurity phases on the surface. In our best solar cell (7.11b) the bubbles were relatively small and very rarely burst compared to other films, but certainly the voids beneath the bubbles would impede current transport across the cell and even a few burst bubbles would still shunt the cell.

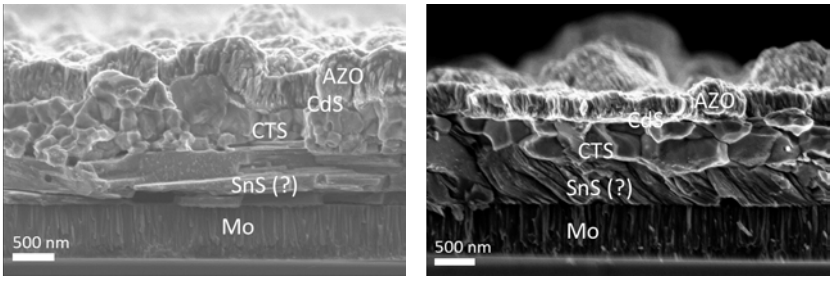

(a) (b)

Figure 7.10: Cross-sectional SEM images of two CTS solar cells. (a) Solar cell with 0.01 % efficiency. It has a dense SnS layer at the bottom. (b) Solar cell with 0.3 % efficiency. This film had larger CTS grains but there is still SnS at the bottom (perhaps with a different orientation). SEM imaging by A. Crovetto and/or E. Bosco).

While exploring the uniformity of the near-stoichiometric CTS films at a distance up to about 2.5 cm from the plume center (the thickest part of the film), I found that off-axis the film composition was in fact not Cu-rich relative to the Sn-content as shown in Figure 3.7 in the far corner of the deposited area, where the Cu/Sn ratio was <2. This was confirmed in measurements of other films and encouraged us to explore annealing of the near-stoichiometric CTS films as well, as the shortage of S could be remedied by annealing with S as described in Section 5.3. When we discovered that the composition could be tuned by reducing the

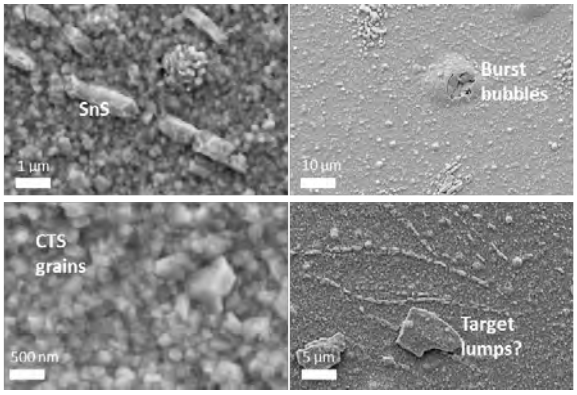

(a)

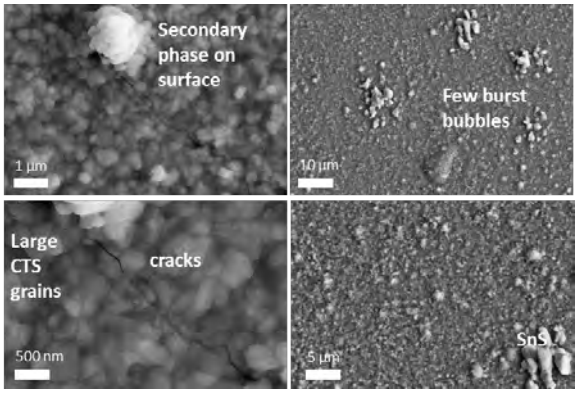

(b)

Figure 7.11: Surface of SnS-rich CTS layers used for solar cells. (a): Surface of the absorber layer in the film used for our 0.01 % efficient solar cell. The burst bubbles are probably the worst of the many offenders. (b): Surface of the absorber layer in the film used for our 0.3 % efficient solar cell. This film had fewer bubbles and very few of them were burst, but there are many other possibly problematic issues apart from the SnS seen in the cross section above.

fluence rather than increasing the angle away from the normal to the target, we used that strategy instead. The results of annealing these films will be described in the following.

7.3.1 Effect of different annealing conditions

The most obvious lesson learned on CTS annealing was that annealing too long at 570 °C leaves only Cu and S behind - the Sn evaporates completely in the form of SnS. A similar effect has been shown previously: when co-deposited precursor CZTSe films were annealed for a long time (5-6 hours), only Cu, Zn and Se was left behind in the films while all the Sn disappeared [235, 57].

Another crucial lesson was that the films peeled off unless they were very thin. Peeling off of annealed CZTS films is a well known problem and the main remedy offered by other groups is to limit the thickness of the film. This also worked for our CTS films eventually. At first we were able to anneal quite thick near-stoichiometric CTS films ($< 1.6\,\mu m$) without exfoliation, but these films contained bubbles, some of them burst, which may have provided an alternative form of strain relief. The annealed SnS-rich films also never exfoliated even at thicknesses of $> 4\,\mu m$ but apart from bubbles and holes, as we saw above these films had a SnS-layer near the bottom which may have improved the adhesion. Ultimately we were able to produce films around 700-1000 nm thick without bubbles or exfoliation as shown in Section 7.3.2.

A number of different annealing procedures were tried - with a slow heating ramp versus a fast ramp, with a maximum temperature of 575 °C or 550 °C and with long or short holding times at the top temperature. XRD and SEM images of the film surfaces were used as initial markers of the suitability of the annealing procedure, as this revealed the presence of the worst secondary phases (SnS_y and Cu_xS and the size of the grains and any bubbles and holes in the film.

Annealing hot (up to 580 °C) yielded larger grains. A long holding time at this temperature increased grain size the most but also led to large (several micron sized) holes in the films. Annealing at 575 °C yielded cubic or monoclinic-phase Cu_2SnS_3 as well as orthorhombic-phase SnS in the SnS-rich films. As noted, at least some of the annealed films segregated into different layers, which made it impossible to measure their composition by EDX.

Two annealing runs made with precursor films deposited using different lasers but otherwise similar conditions are shown in Figure 7.12. The films in the figure were annealed with a very slow ramp (in the hope of preventing bubbles, though clearly it did not), a maximum temperature of ≈ 575 °C, about 10 minutes annealing time above 570 °C and just over 1.5 hours above 500 °C. We see that the films contained multiple phases with both monoclinic-phase and cubic-phase CTS (possibly mixed with some tetragonal phase; the peaks are closely spaced

in Raman and even more closely in XRD, making the distinction difficult). The distinct layers formed by one the films allowed Andrea Crovetto to exfoliate them and measure with Raman spectroscopy on both the front and the back of the film. This showed us that the film in Fig. 7.12b contained cubic/tetragonal CTS at the front and monoclinic/tetragonal CTS at the back. A similar procedure told us that the slanted layers at the back of the SnS-rich films were in fact SnS. XRD of the film in Fig. 7.12b showed tiny SnS peaks, which were corroborated by XPS measurements (not shown) that indicated that the surface was Sn-rich. This could be a sign of SnS migrating to the top due to evaporation of SnS.

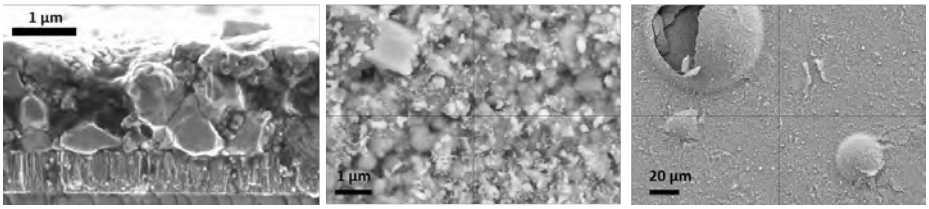

(a)

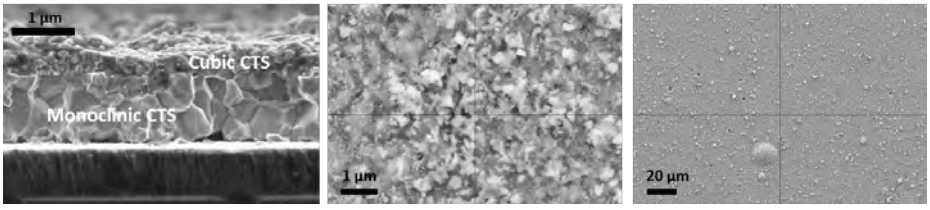

(b)

Figure 7.12: SEM images of annealed films made from near-stoichiometric CTS precursors deposited with 1.6 J/cm^2 using (a) the 248 nm laser and (b) the 355 nm laser and annealed under identical conditions. (a): Annealed film from precursor made with the 355 nm laser. XRD showed Cu_2SnS_3 and Raman spectroscopy revealed that the film contained a mix of cubic and monoclinic Cu_2SnS_3. Large bubbles occurred all over the film, some of them burst. (b): Annealed film from precursor made from the 248 nm laser. Again, Raman spectroscopy revealed a mix of cubic and monoclinic Cu_2SnS_3, with cubic Cu_2SnS_3 dominating on top of the film and monoclinic at the bottom. Tiny SnS peaks in XRD may correspond to the "white fluff" on the top of the film. Bubbles were fewer and smaller than in (a). Cross-sectional SEM images, XPS and Raman analysis by A. Crovetto.

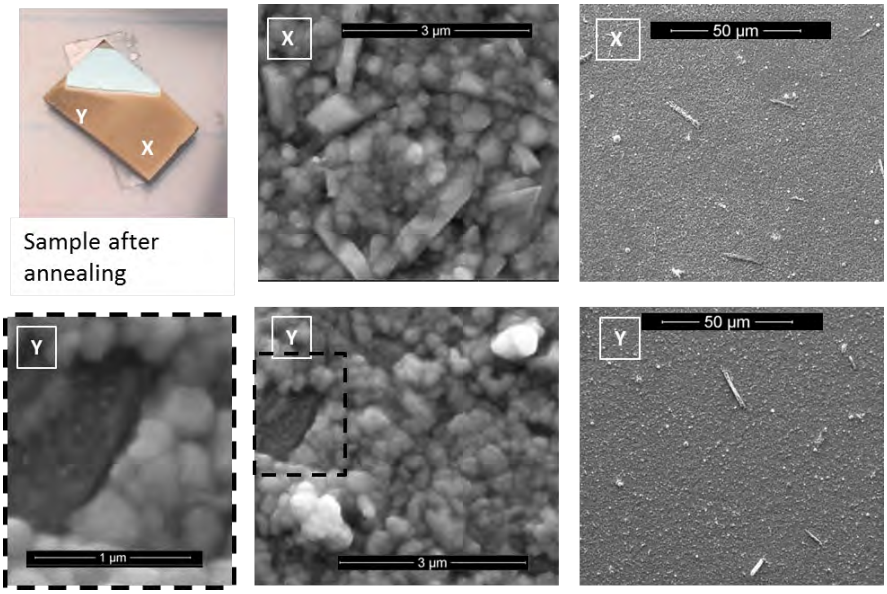

Figure 7.13: SEM images of an improved annealed CTS film (max. thickness about 700 nm measured at the masked edge). There were almost no bubbles seen in SEM of this annealed film. The thinner part of the film (furthest away from the PLD plume center, labeled **X**) looked uniform to the naked eye. The thicker part of the film had black specs visible by eye (area labeled **Y**). SEM images of region **X** reveal two different crystalline growth modes. SEM images of region **Y** show spires that appear bright as well as holes as seen in the enlarged image.

7.3.2 Example: Phase analysis in an improved annealed film

Figure 7.13 shows an annealed near-stoichiometric CTS film where there were only few bubbles or other obvious deficiencies. This film was max. 700 nm thick. The thickness gradient in the film was rather large as a relatively large spot was used (3.3 mm^2) and the laser was moved in a line rather than a rectangle to avoid changes in the spot size when moving the laser spot on the target. It was deposited on Mo/SLG and annealed with 50 mg S (no SnS) at 550 °C, the temperature generally used by my colleagues in CZTS annealing. The annealed film looks fairly smooth, but clearly contains two phases at the surface as seen in the SEM images. Cross-sectional SEM would be needed to confirm that there are no inhomogeneities across the depth of the films.

The difficulties associated with assigning the correct material phases by Ra-

man and XRD measurements is illustrated in Figure 7.14, which were measured on a film that was very similar to part **Y** of the film shown in Fig. 7.13 (the precursor was deposited adjacent to it, they were annealed together and the annealed film contained little black specks just as we see in Fig. 7.13). The main Raman peaks belong to Cu_2SnS_3, though it is hard to tell if they represent the monoclinic or the cubic phase as the monoclinic peaks should be at 290 cm^{-1} and 352 cm^{-1} [63] while the cubic phase peaks should be at 303 cm^{-1} and 355 cm^{-1} [236] and we see peaks at 292 cm^{-1} and 354 cm^{-1}. The peak shoulder at 299 cm^{-1} hints that perhaps we have a mixture between somewhat strained monoclinic and cubic phases as seen in previous films. The peak at 318 cm^{-1} could potentially also belong to Cu_3SnS_4 [236] but we see no sign of that in the XRD spectrum.

The small peaks labeled by stars at ≈227 cm^{-1}, 313 cm^{-1}, and 372 to 373 cm^{-1} are similar to impurity phase peaks observed by others in films where the main phase is monoclinic or cubic Cu_2SnS_3 [63, 237]. These authors attribute it tentatively to a "$Cu_2Sn_3S_7$" phase, but another group has reported that this phase does not even exist and is rather $Cu_4Sn_7S_{16}$ [64]. Recently de Wild et al. saw similar peaks at 310 to 320 cm^{-1} and 375 to 380 cm^{-1} and convincingly attributed them to a phase containing Na [238], as Na can migrate into the film during annealing as described in Section 2.3.2. More probing would be necessary to see if this is the phase also formed here.

Additionally, in Fig. 7.14a we see signature Raman peaks of Cu_xS. Others have shown that covellite, CuS, has Raman peaks at 471 cm^{-1} (primary peak) and 263 cm^{-1} (secondary peak) [239], while we found the Raman peak for our CuS target at 477 cm^{-1}. The Cu_xS peak was most pronounced on certain spots on the annealed films that looked dark in the Raman microscope probably corresponding to the dark splotches visible by eye on the thick part of the film; this makes sense in the light that the part of the film closest to the plume center is richest in Cu. The X-ray diffractogram of the film (Fig. 7.14b) shows only the Cu_2SnS_3 phase(s), confirming that there is at least some monoclinic phase present due to the peak at about 16° 2θ, while the other phases detected by Raman spectroscopy (Cu_xS and mystery $Cu_4Sn_7S_{16}$-or-Na-containing-CTS) must be minor constituents.

7.3.3 Films for ellipsometry

The main published result based on our work on annealed CTS was the ellipsometry measurement performed by my colleague Andrea Crovetto on near-stoichiometric CTS which in some cases formed single-phase monoclinic CTS films. Andrea measured a double bandgap previously seen in literature (e.g., [17]), and Rongzhen Chen and Clas Persson were able to match to it to a detailed theoretical band model, showing that the double bandgap could be an intrinsic

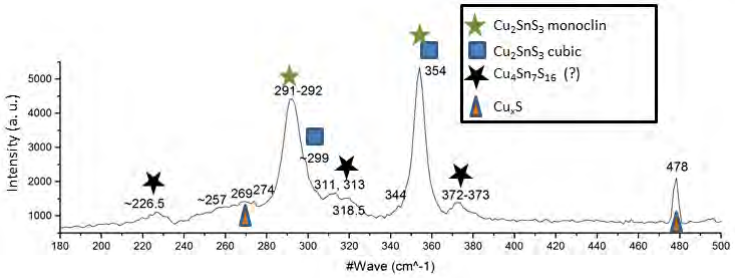

(a)

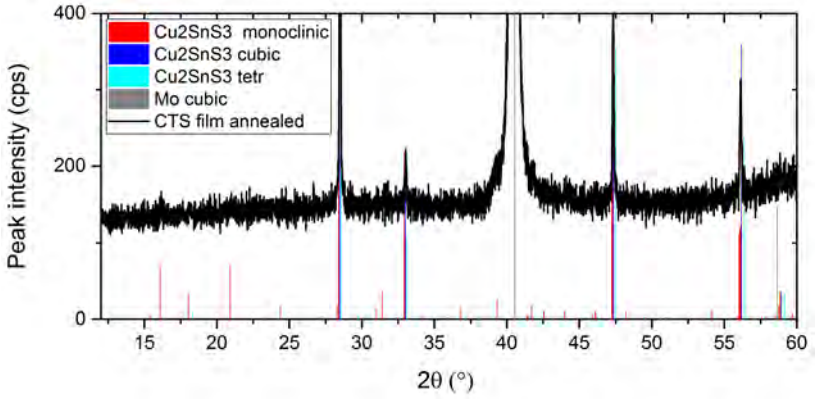

(b)

Figure 7.14: Analysis of the crystalline phases in the annealed film deposited adjacent to the one in Fig. 7.13 and annealed under the same circumstances. (a) shows a sample Raman spectrum for this film. There are signature Cu_2SnS_3 peaks as well as Cu_xS and mystery phase peaks. See text. Raman measurements carried out together with Stela Canulescu. (b) shows the XRD diffractogram which confirms that monoclinic Cu_2SnS_3 is present.

property of monoclinic CTS due to its asymmetric crystal structure rather than an artifact due to multiple phases in the film [213].

Films for ellipsometry measurements had to be quite thin ($\approx$ 100 nm) and some of them had to be deposited on SLG to allow deconvolution of the reflection from more layers (MoS_2 formed on top of the Mo layer during annealing, leading to a complicated structure). To make these films, we first deposited relatively thick films to be able to verify the composition before and after annealing and then we deposited very thin films under exactly the same circumstances and annealed them together. The thick film made it easier to measure which phases were present in the film by XRD because of the stronger signal intensity from a larger amount of material. As shown above in Figure 7.12, we sometimes saw co-existence of the cubic and monoclinic phase. In the thin films for ellipsometry, SEM, XRD and Raman spectroscopy together pointed to films dominated by the monoclinic phase. Apart from XRD, the work on characterization was carried out by Andrea Crovetto. One of the films used in the study is shown in Fig. 7.15, illustrating that annealing does not eliminate the problem of film inhomogeneity due to craters and droplets, but that the material was otherwise highly homogeneous.

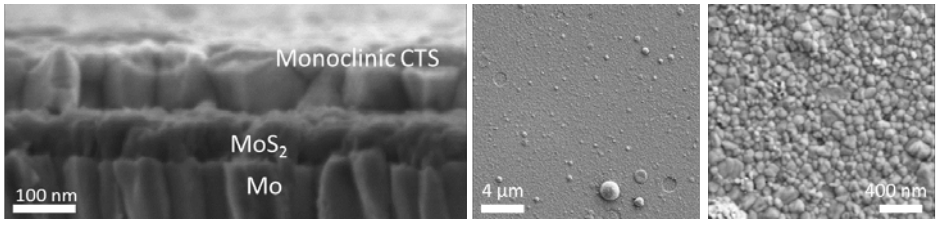

Figure 7.15: 100 nm monoclinic CTS film for ellipsometry: high resolution shows a uniform film crystallinity, while lower resolution reveals droplets and craters from the PLD process. SEM images by A. Crovetto; two of the images were included in similar form in [213]).

Aihara et al. [240] recently measured the photoluminescence of monoclinic Cu-rich single crystals of CTS showing a free exciton occurs and indicating that the bandgap should be at 0.93 eV. They commented that there could be more than one valence band energy due to the monoclinic structure but did not prove it. Our article does, which is a valuable contribution to research in this material.

7.4 Results: Solar cells

This section would not be complete without the presentation of the working solar cells assembled and measured by Andrea Crovetto using some of the annealed

films. The current-voltage characteristics of two working solar cells are shown in Figure 7.16a along with the external quantum efficiency in Figure 7.16b. The external quantum efficiency is the fraction of photons shining on the solar cell that are converted into electricity, in contrast to the internal quantum efficiency (a little harder to measure) that considers the fraction of photons absorbed by the material that are converted into electricity, i.e., taking into account reflection losses.

We see that the JV curves do not look much like the usual nearly rectangular curves seen in solar cell literature. As we saw in Section 2.1, the voltage when the current is zero is called the open current voltage (V_{oc}) and corresponds to a solar cell under illumination that generates charge carriers and therefore an internal field but has nowhere for the charge carriers to go. As mentioned previously, the current where the voltage is zero is called the short-circuit current (J_{sc}) and shows the maximum amount of light-generated charge carriers that are collected at the contacts. Ideally the curve should be rectangular and V_{oc} would depend only on the temperature and J_{sc}. In real solar cells, the amount of "rectangularness" is quantified by the fill factor, which for good solar cells can be 60-90 % but which for our solar cells is very low (closer to 20-30 %). The fill factor depends on the shunt resistance and the series resistance as well as the diode ideality factor, which takes into account how recombination takes place in the cell. The shunt resistance should be high (no shunts of current from the front to the back of the solar cell) while the series resistance should be low (easy transport of current from the back to the front). A low fill factor can derive from deficiency in both of these factors. The shape of the JV curve here especially points to an extremely low shunt resistance.

These preliminary solar cells had an unintended bilayer structure of CTS on top of SnS as we saw in Figure 7.10, which could lead to high series resistance. Additionally, we saw in Figure 7.11 that there were bubbles in some of these films, sometimes burst, just as there were in near-stoichiometric CTS films. Together with the smaller holes we saw, the burst bubbles could easily cause shunt paths when the subsequent layers of the solar cell are deposited.

The EQE curve (Fig. 7.16b) shows a high collection efficiency only near the CdS bandgap, perhaps indicating that primarily the carriers reaching the front contact are the ones created near the interface with CdS, as the shorter wavelength light is absorbed closer to the interface than the longer wavelengths. Nakashima et al. show an EQE curve with a similar shape when they do not use so-called white light biasing during the measurement (i.e., illuminating the cell with white light plus low-intensity additional illumination at the wavelength being measured). However, when using white light biasing, their EQE improves over the lower wavelengths [68]. Umehara et al. see a similar behavior in CTGS (Ge-alloyed CTS) solar cells and attribute it to defects in the CdS layer [241].

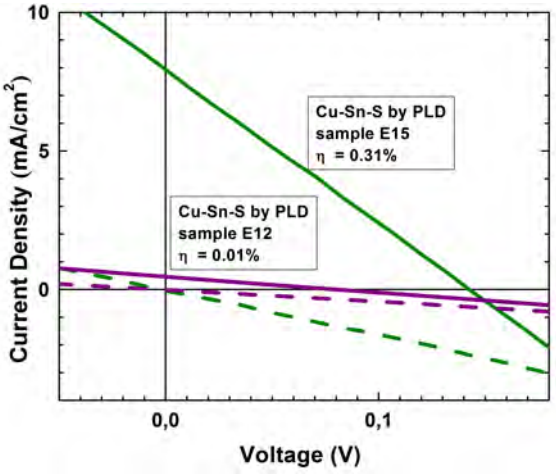

(a)

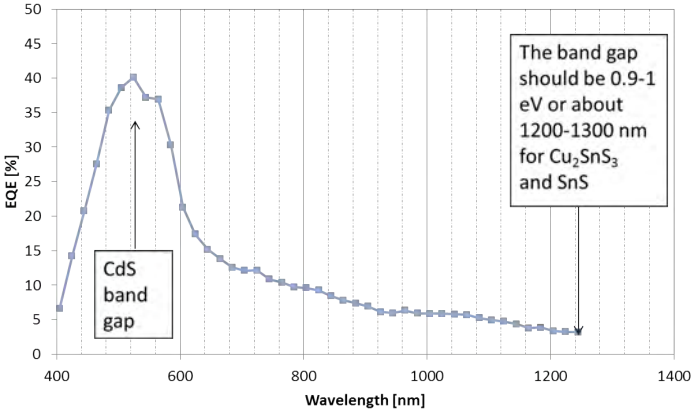

(b)

Figure 7.16: Current-voltage and external quantum efficiency (EQE) measurements for the CTS solar cell. (a): JV curves for two solar cells made from a SnS-rich CTS film. V_{oc} and J_{sc} for the best cell: 140 mV and 8 mA/cm^2. Solid lines: under illumination. Dashes: in the dark. The curve should ideally be horizontal at the current axis intercept and vertical at the voltage axis intercept, showing that there is low shunt resistance, probably coupled with high series resistance. (b): EQE for the 0.3 % efficient cell (the fraction of photons at a given wavelength that are converted to electrical energy). Only the highest-energy photons just below the CdS bandgap are efficiently collected - these are generally absorbed close to the surface of the solar cell and do not have to travel as far through the bulk. Raw plots and measurements by A. Crovetto.

They suggest that the CdS layer may have acceptor-like (positively charged) defects, which must be compensated by exciting a large number of electrons to the bandgap in the CdS layer to avoid it acting as a barrier. These carriers in the CdS layer are only generated above the bandgap of CdS, so short wavelength light must be present. The same mechanism may be contributing to the low EQE in our films - the measured EQE is too low to account for all the current measured by the J_{sc} value.

Overall, our 0.3 % cell with V_{oc}=140 mV and J_{sc}=8 mA/cm^2 has some way to go to compete with the best CTS solar cell in the literature, which has η=4.6 %, V_{oc} of 0.283 V, and J_{sc}=37.3 mA cm^{-2} [68]. It would be interesting to see how well a non-SnS-rich film would work as a solar cell absorber. It may be advantageous to maintain slightly Sn-rich growth conditions as this has been shown to improve the electrical properties of CTS [70].

7.5 Summary

The CTS depositions were to our knowledge the first by PLD. The substrates used for CTS initially (and for our article in Applied Surface Science) was fused silica, which was chosen to enable transmission measurements. This also influenced film growth. For obtaining, e.g., the cubic phase, lattice matched substrates would have been the best choice, while for obtaining the phases seen in our group's CZTS films, using Mo/SLG substrates like we did for CZTS was important, and we proceeded with this substrate for the films.

For the as-deposited CTS films, we found at room temperature that the films were generally Cu-rich and S-poor compared to the expected composition, but that the Sn and S-content in the films could be increased by using a lower fluence. Reducing the fluence also reduced the amount of droplets in the films, as previously seen by other authors. In contrast, the droplet area density on the films was not reduced by using a shorter-wavelength laser, even though this is a rule of thumb in PLD. Instead it was clear that the laser pulse length (and therefore the intensity on the target) was important for the film growth, with a high deposition rate when using the laser with the highest intensity at a given fluence.

The as-deposited CTS films at 150-300 °C substrate temperature were crystalline with evidence of the tetragonal phase in 150 °C films and the cubic phase in 300 °C films. However, the films deposited from the near-stoichiometric CTS target were plagued by Sn- and S-loss and contained Cu-rich secondary phases which would preclude any solar cell efficiency. The films from the Sn-rich CTS target on the other hand were too Sn-rich. In order to obtain crystalline as-deposited CTS films at high temperature, it will be necessary to decrease the fluence significantly, using the fluence and/or slightly off-axis deposition to tune

the Cu/Sn ratio of the film deposited from the near-stoichiometric CTS target. However, a lower fluence and off-axis deposition both lead to a lower deposition rate, making it necessary to keep the films at an elevated substrate temperature for longer. This could exacerbate any loss of S or SnS from the growing films, so it is likely that an additional sulfur source would be needed.

The annealed CTS films from the SnS-rich target were used for solar cells with small but measurable efficiencies up to 0.3 %. The films contained layers of SnS, pinholes and other defects that could cause both shunting and blocking of charge carriers. For better solar cells using annealed films, the near-stoichiometric CTS target would probably be a better starting point, once again using the fluence and/or off-axis deposition to tune the composition of the as-deposited films to Sn-rich and Cu-poor. Extra thin ($\approx$ 100 nm) films made in this way were in some cases phase-pure monoclinic Cu_2SnS_3 and were used for characterization by ellipsometry, the results of which were published.

Chapter 8

Pulsed electron deposition compared to pulsed laser deposition of CZTS

The last major part of the work comprising this thesis was the comparison of CZTS deposition by PLD and PED. This work came about in collaboration with the PED group at IMEM-CNR in Parma, Italy, because of their successful work on PED deposition of CIGS. At the time we met them, their solar cells using CIGS films deposited and post-annealed at a temperature as low as 270 °C had reached 15 % efficiency [148] and today they have achieved more than 17 % [242]. Since the CZTS solar cell is fully modeled on the CIGS system except for the composition of the absorber layer itself, it was an interesting comparison to make and a great opportunity to learn from the experiences of another group.

The main similarities between PED and PLD are the high energy of the species arriving on the substrate, enabling deposition of crystalline films at relatively low temperature, and the ability to ablate the material in an ideally congruent process that reproduces the composition of the target in the growing film. We already knew that congruent ablation did not take place in PLD of CZTS. The group in Parma had also found some deviations between the film and target composition in PED of CIGS, but they had found ways to overcome this [153, 243]. Additionally, they had found ways to reduce the amount of droplets on the PED films [132]. We therefore hoped that their success in addressing these issue could be transferred to CZTS.

Our initial experiments on CZTS by PED yielded highly non-stoichiometric films and a large part of our work with PED therefore focused on the composition as a function of different voltage and pressure. We were able to deposit CZTS at the relatively low temperatures of 250-325 °C, though with secondary phases

and possibly S-poor films, resulting in low-efficiency solar cells. The work was compared to my colleague Andrea Cazzaniga's work on PLD of CZTS at room temperature at different fluences. I verified his work at the optimal fluence range and compared the PED films at $\approx 300\,^{\circ}\mathrm{C}$ to PLD films deposited at $300\,^{\circ}\mathrm{C}$.

A manuscript describing the results is currently in preparation and the preliminary article is included in Appendix D [244]. The paper is in principle ready for submission, but we are awaiting more PED results at $300\,^{\circ}\mathrm{C}$ with the aim of making Cu-poor CZTS films at this temperature, hopefully resulting in a better solar cell efficiency. This chapter presents the main results included in the manuscript and adds some subsidiary observations.

8.1 PED versus PLD - background on other materials

Already in our work on PLD of ZnS we were able to compare some of our results to those by PED and it was clear that there were many similarities between the techniques, especially the capacity to deposit a high-temperature phase at a much lower substrate temperature, namely hexagonal ZnS deposited at $300\,^{\circ}\mathrm{C}$ on an untextured substrate even though under equilibrium conditions this phase occurs above $1120\,^{\circ}\mathrm{C}$. A number of authors have compared the two techniques for other materials, including Nistor et al. (2012) [245] for $Ba_xSr_{1-x}TiO_3$ (BST), Monaco et al. [246] for silicon carbide (SiC), and Nistor et al. (2008) [146] for the wide band-gap oxides including ZnO, $Zr_{0.8}Sn_{0.2}TiO_4$ (ZST) and $Ca_3(PO_4)_2$. Nistor et al. [146] found that PED was an excellent deposition method for the many oxide compounds investigated: with optimization, PED could yield near-stoichiometric transfer comparable to PLD and a much better surface morphology than ns-PLD with much fewer droplets (comparable to fs-PLD for ZnO). They explained the success of PLD for these materials with a more efficient energy transfer from the PED beam than ns UV lasers with a photon energy below the bandgap energy of the materials.

Monaco et al. [246] also found stoichiometric transfer of SiC from target to substrate with both PLD and PED, but in their preliminary PED experiments they were not able to demonstrate crystalline SiC at $800\,^{\circ}\mathrm{C}$, which had been achieved by others in PLD. In another example where PED did not work as well as PLD, Mathis and Christen [247] compared the results of PLD from literature with their experimental results of PED of YBCO and noted that PLD of YBCO has generally been more successful. They found that PED resulted in more droplets on the YBCO films and that the high-energy species ejected from the target damaged the film properties because the background pressure had to be lower in PED than PLD for this material.

There are only a few comparisons of ns-PLD and PED of chalcogenides. Sava et al. [248] deposited $SnSe_2$ by both PED and PLD (with 248 nm, 7 ns pulses)

and apparently found no major differences in the amorphous films produced by the two techniques at room temperature. We saw that ZnS deposition by PED and PLD was also fairly similar. However, both of these materials might behave quite differently to the more complex CZTS.

For CIGS, PED done by the group at IMEM-CNR in Parma has been more successful than PLD, which to our knowledge has never yielded solar cells with an efficiency above the 8 % achieved for CISe by Dittrich et al. [172]. As discussed in Section 4.2.1, it appears that Se-loss was in many experiments an important drawback of CIGSe deposition by PLD. In PED, in contrast, as-deposited CIGS and CGSe films were Se-rich and Cu-poor at room-temperature [243, 153]. When the temperature was increased, the films became slightly Se-poor, just below the ideal Se-content of 50 %, which was ascribed to evaporation of the excess Se not incorporated in the growing crystalline CIGSe film. While In and Ga also re-evaporated to some extent from the heated films, increasing the relative Cu-content of the film, the overall composition remained Cu-poor, which is favorable for CIGS solar cells [243]. In CGSe, the films were always found to be Se-rich at temperatures from room temperature to 475 °C with a slight decrease in the Se-content when the temperature was raised from room temperature to 100 °C and above [249]. The Cu/Ga and Cu/Se ratio in the CGSe films could be tuned to some extent by changing the voltage, and a lower voltage leads to a higher proportion of Ga and Se in the films because there are more low-energy electrons at this voltage leading to evaporation of these elements due to their lower cohesive energy. Thus at low voltage the thickness distribution of the film showed a greater cosine-distributed component characteristic of evaporation, while a higher voltage more closely resembled a $cos^4\theta$ distribution, showing a greater evaporative component at low voltage and a greater ablated component at high voltage [153].

The main question in our investigation was whether something similar might come about during PED of CZTS: S-enrichment of the growing films leading to higher material quality than in as-deposited CZTS in PLD in the literature, which appeared plagued with S-loss as we saw in Section 4.1.

8.1.1 Methods for PED and PLD of CZTS

The 248 nm PLD setup was used in this study comparing PED and PLD of CZTS, as this was the setup that had been used by my colleague Andrea Cazzaniga for our previous work on CZTS. The setup and deposition methods are described in Section 5.1.2. Our colleague Stela Canulescu had found that the 355 nm laser was not suitable for CZTS deposition as there was no fluence range that gave rise to Cu-poor films of CZTS with this laser. This is probably because the ablation efficiency of the ZnS phases in the multicomponent target was much lower with

Table 8.1: Deposition parameters for PED and PLD. The PED pulse is polyenergetic; there will be a large amount of electrons with lower energy than the maximum. ‡: For $CuGaSe_2$ at 18 kV.

	PED	PLD (248 nm)
Power (W/cm^2)	Max. 1.2*10^8 ‡	5*10^7 at 1 J/cm^2
Pulse length (ns)	100	20
Spot size (mm^2)	7	5
Target-substrate distance	8	4.5
Pressure (mbar)	$\approx 2 \times 10^{-3}$	$<5 \times 10^{-5}$
Pulse rate (Hz)	6-10	15

the 355 nm laser than with the 248 nm laser.

The PED setup and parameters used in this study are described in Section 5.2. The main deposition parameters for the two techniques are compared in Table 1 of our manuscript, Appendix D, which is reproduced here in Table 8.1.

The targets used for the deposition were nominally all the same, though as previously discussed it is difficult to accurately measure the target composition (See Section 5.4.1). The PED films were made with three different targets (Targets 1-3) as the PED process erodes the target much more rapidly than PLD does. The PLD CZTS films included in this study were all made with a single target (Target 4). Prior to each deposition, the targets were refreshed by polishing and then preablated while the substrate was shielded from the plume by a shutter.

In the PED experiments the preablation lasted until a stable optical emission spectrum was obtained. In the PLD experiments, the preablation was used to obtain a coating of the laser entry port that needed to be similar for every experiment, so a set number of pulses were used to reach approximately 60 % transmission. The transmission further dropped by about 30 % (to 40 %) during the deposition.

The substrates for the room temperature depositions by PED were soda lime glass (SLG), while all the films by PLD and the PED films deposited at higher temperature used Mo-coated SLG substrates.

8.2 Results and discussion: PED and PLD of CZTS

Our investigation of PED of CZTS started with some preliminary films based on the best circumstances for PED of CIGS: the depositions were done at 300 °C and 16 kV (Target 1). The resulting films were surprisingly Sn-rich films and the resulting solar cells had extremely low efficiency (< 1 %) which degraded very quickly over time, something never normally seen with the CIGS solar cells at

IMEM-CNR nor with the CZTS solar cells made from annealed absorber layers at DTU.

Since these initial films showed a Sn-rich, Cu-poor composition which was not optimal for solar cells, subsequent work focused on investigating the composition of films deposited at room temperature (Target 2). This better reflects the combination of species in the ablation plume than do films made at elevated temperature as there is no complicating factor of re-evaporation due to high temperature, though there could be re-sputtering due to high-energy species in the plume.

After we had a stronger knowledge about the behavior of the composition at room temperature, a few more films were deposited at 300 °C and 18 kV (Target 3). The aim of using 18 kV rather than 16 kV was to obtain more Cu in the films, as the room temperature films at 16 kV had generally been Cu-poor. However, as we will see these films were surprisingly Cu-rich. Unfortunately issues with the setup led to a premature stop of the experiments.

8.2.1 Deposition rate and morphology of as-deposited films

The deposition rate of CZTS at room temperature by PED and PLD in our experiments is compared in Table 2 in our manuscript in Appendix D. In the room temperature depositions, the PED deposition rate varied with the voltage and pressure in the chamber from 0.001 nm/pulse at 10 kV to 0.1 nm/pulse at 18-19 kV. The low rate at 10 kV made it impossible to deposit films thick enough for EDX composition measurements: a 500 nm film took nearly 9 hours. Within this wide range of deposition rates, some were comparable to those found by PLD using a similar spot size and an intermediate fluence, and some were slower or faster, keeping in mind that the deposition rate by PLD also varies with the fluence. This information was very useful for practical purposes though it does not provide great physical insights as the deposition conditions were a little bit different (different target-substrate distance and pressure).

Surprisingly, when ablating a new target (target 3) for the higher temperature depositions under nominally similar conditions to room temperature in terms of PED voltage and pressure, the deposition rate doubled as measured by the film thickness after the deposition. This points either to a large change in the film density when the temperature was increased, a difference in the target composition leading to a different interaction with the electron beam, or difficulty controlling the deposition parameters in the setup (during the high-temperature depositions, there were nascent problems with the PED power supply). The composition measurement of target 3 suggested that it might be a little more Zn-rich than target 2 used at room temperature, but the OES measurement of the plume Cu(I)/Zn(I) emission ratio was similar. We will see below in the SEM images in Fig. 8.3 that

the 300 °C films were less dense than the room temperature films. Whether this led to the large change in deposition rate is an open question.

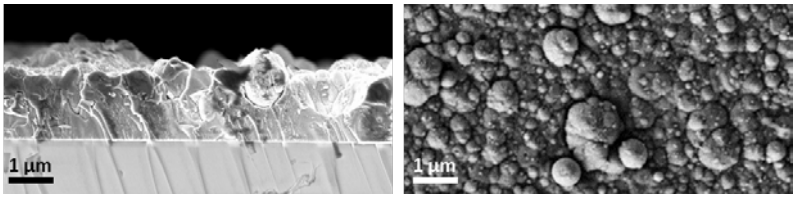

(a) PED

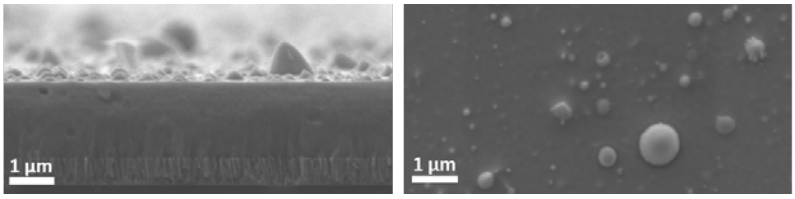

(b) PLD

Figure 8.1: Morphology of as-deposited room-temperature PED and PLD films. There was a larger proportion of droplets in the PED films ((a), as-deposited at room temperature and 18 kV) than in the PLD films ((b), as-deposited, room temperature, 0.5 J/cm^2). This figure is also shown in our manuscript, Appendix D, Fig. 2. Images by E. Bosco, S. Engberg, and this author.

As-deposited room temperature films made by PED looked superficially similar to PLD films, but at high voltages they contained many more droplets than we ever saw in the PLD films (also at higher fluence than the ones shown here); see Figure 8.1. The many droplets in the PED film may partly be due to non-optimized conditions, but could also indicate that the ablation in PED is less efficient than in PLD. This could happen if the electron beam energy is deposited deeper into the target than the laser energy, leading to less intense heating of a larger volume. PED films at high and low voltage are compared in Figure 8.2, and we see that the films made by PED at a lower voltage are much more similar to the ones we saw by PLD. X-ray diffraction was carried out on the films to probe whether the heavily structured surface of the high-voltage films derive from crystallization. This was not the case as only very small unidentified diffraction peaks were detected for the films made at 18 and 19 kV and no peaks at all for films made at lower voltages

As noted above, PED does not always lead to more droplets than PLD: Nistor et al. [146] report that for a number of oxides PLD gave more droplets than PED. They show ZST ($Zr_{0.8}Sn_{0.2}TiO_4$) films with the opposite appearance to our films:

smooth PED films and droplet-filled PLD films and suggest that the explanation is the difference in background pressure leading to higher mobility of the adatoms on their PED films than the PLD films. This could also be part of the story in our study, where the PED background pressure was higher than the pressure in PLD.

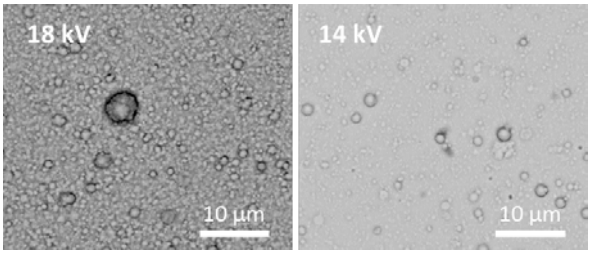

(a) PED

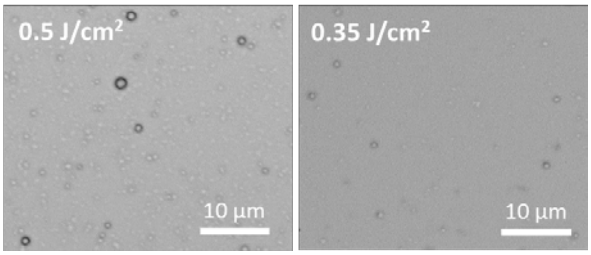

(b) PLD

Figure 8.2: Change in the area density of droplets when the PED voltage / PLD fluence was reduced. Images also shown in the supplementary information of our manuscript (Appendix D, Fig. S1).

In depositions at about 300 °C, the morphology of the films varied widely. This may have derived from differences in composition: Du et al. [38] show similarly varied film morphology depending on whether the films were Cu-rich, nearly stoichiometric, Sn-rich, or Zn-rich. The films made at 300 °C with PED had a porous, popcorn-like texture as seen in Figure 8.3 (these figures are also shown in the manuscript, Appendix D, Fig. 4). We also see that some of the PED films contained secondary phases in the cross-section (either ZnS, an insulator, or SnS, with a high atomic mass, could show up as bright areas in SEM). The porous structure may be due to evaporation of S and SnS or due to the simultaneous growth of two or more phases with different crystal habits as suggested by Du et al. [38].

The PLD films made for this study had an almost completely smooth mor-

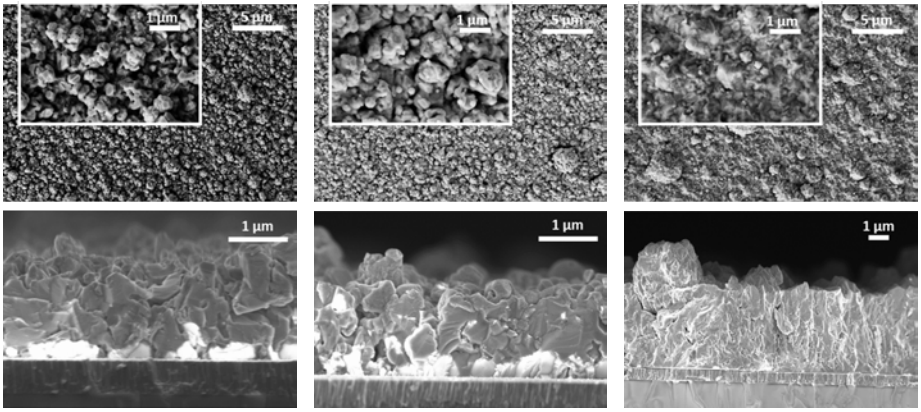

(a) PED 325 °C (b) PED, 300 °C (c) PED, 255 °C

Figure 8.3: Morphology of exploratory as-deposited CZTS films made by PED at 18 kV and a substrate temperature of 300 °C.
(a): Deposition at ≈ 325 °C; (b): Deposition at ≈ 300 °C; (c): Deposition at ≈ 255 °C, longer deposition time than the other two films. SEM images by E. Bosco.

phology contrasting strongly to the PED films (see Figure 8.4a and similar images in Appendix D, Fig. 5). However, the PLD film morphology differed greatly depending on when during the CHALSOL project the films were made: An early Cu-rich, Zn-poor, and S-poor film made by Andrea Cazzaniga looks reminiscent of the PED films with a flaky, porous structure, as seen in Fig. 8.4b. This suggests that the composition rather than the particular differences between PED and PLD gave rise to the morphological differences.

8.2.2 Composition of the as-deposited PLD films

As mentioned in Section 7.2.2 on PLD of CTS, Andrea Cazzaniga showed that the Cu-content of as-deposited CZTS films rose strongly with fluence using the 248 nm laser. He found that the fluence region suited for depositing Cu-poor films as needed for CZTS solar cells was quite narrow [157], as seen in Figure 8.5a. These data are also included in Appendix D, Figure 3. The reason suggested by Cazzaniga and Crovetto et al. [157], agreeing with our observations on CTS, is that at low fluence the SnS_y and ZnS phases were preferentially evaporated while the Cu-rich phases in the target were left behind. As the fluence rose, the Cu-rich phases were ablated too and this ablation was more forward-directed than the

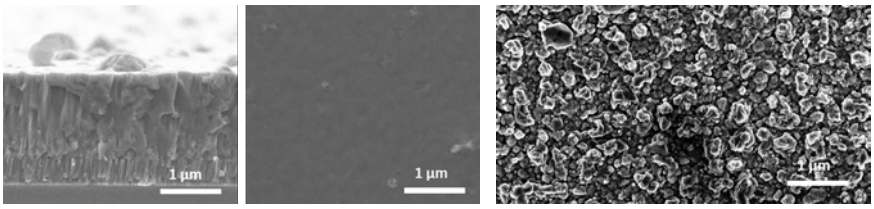

(a) PLD, Cu-poor (b) PLD, Cu-rich

Figure 8.4: Morphology of CZTS films with different composition as-deposited by 248 nm PLD at 300 °C. (a): Cross-section and top view of a Cu-poor, Zn-poor film made in the present study (Cu/(Zn+Sn) ≈ . 0.75, Zn/Sn ≈ . 0.85). (b): Top view of a Cu-rich, Zn-poor and S-poor film deposited at 300 °C by Andrea Cazzaniga early in his PhD thesis work (Cu/(Zn+Sn) ≈ . 1.1, Zn/Sn ≈ . 0.6). SEM images by S. Engberg and A. Crovetto.

evaporative component of SnS and ZnS, leading to Cu-rich films.

Adding to Andrea's work, the present study examined the change in composition between room temperature and high-temperature PLD deposition, as shown in the Supplementary Information, Appendix D, and also the composition at different frequencies. Reassuringly, the difference in composition between different frequencies and between room temperature and 300 °C were too small to be significant.

First, on the temperature: Within the error bars, the composition was the same for films deposited at room temperature and 300 °C, although there was a slight trend of more S-poor films at 300 °C. This is shown in Figure 8.6 here, reproduced from Figure S3, Appendix D. The films made at 0.45 to 0.5 J cm^{-2} had a reasonable metal composition for solar cells with both Cu/(Zn+Sn) and Zn/Sn ≈ 0.8-1, suitable for a subsequent high-temperature annealing where a little bit of Sn might be lost to SnS evaporation while any S-deficiency was replenished, resulting in the good solar cell efficiency reported by Cazzaniga & Crovetto [157]. However, we see in the figure that as-deposited films at 0.45 to 0.5 J cm^{-2} tended to be S-poor even at room temperature, which together with the Sn-enrichment would make them unsuitable as solar cell absorber layers as discussed in Section 2.2.1. A few films were therefore deposited at lower fluence, resulting in a higher S-content at room temperature as expected (Fig. 8.6c). Unfortunately the matching film at 300 °C was S-poor (though as many of the other films it was within the error bar of a stoichiometric film). The lower S-content at 300 °C for the low-fluence film may be due to the much longer deposition time (90 minutes versus 53 minutes), which would exacerbate any tendency towards S-loss at

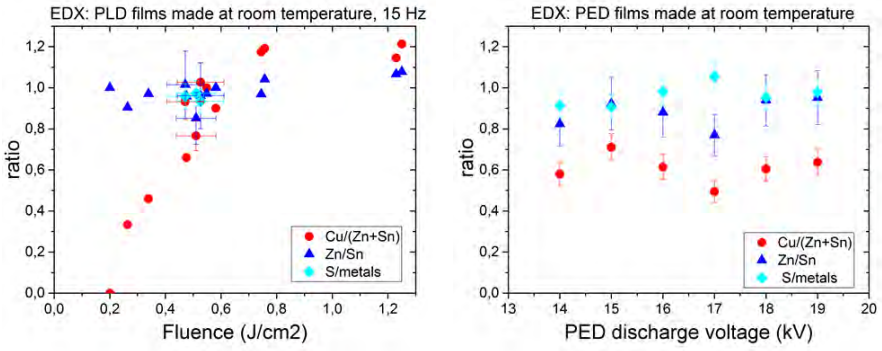

(a) PLD (b) PED

Figure 8.5: Composition of CZTS films made by PLD and PED at room temperature. (a): Composition of PLD films measured by EDX in the same setup and with the same accelerating voltage as the films in (b). The points without error bars are the work of Andrea Cazzaniga as presented in [157]. Error bars represent 95 % confidence intervals for comparisons between measurements; the absolute error in quantification may be larger. (b): Composition of PED films as measured at 15 kV with the TM3000 instrument. The films were on purpose made with a similar Cu(I)/Zn(I) OES peak ratio at all voltages.

this temperature. This low fluence film showed some interesting surface features which will be discussed in Section 8.2.5.

Second, on the repetition rate: It was important to check that using a higher repetition rate of 15 Hz in PLD compared to 6-9 Hz in PED did not result in any differences between the films simply due to the repetition rate. The higher repetition rate was chosen for PLD compared to PED partly because 15 Hz was the repetition rate used in the work of Andrea Cazzaniga, making the present work directly comparable to his, and partly because the deposition rate per pulse was lower for PLD than PED at 300 °C. Since the films had to be of comparable thickness for EDX composition measurements, we could choose either to keep the pulse repetition rate or the deposition time constant. At this temperature the deposition time could influence the film composition because of evaporation of the more volatile elements and we therefore thought it was important to keep the deposition time comparable. To test whether the repetition rate made a difference, a few films were deposited at room temperature at 7 Hz and 45 Hz as well as 15 Hz. This was also briefly discussed in Section 3.4 where we saw that there were more droplets in a film deposited at 45 Hz than in one at 7 Hz (this

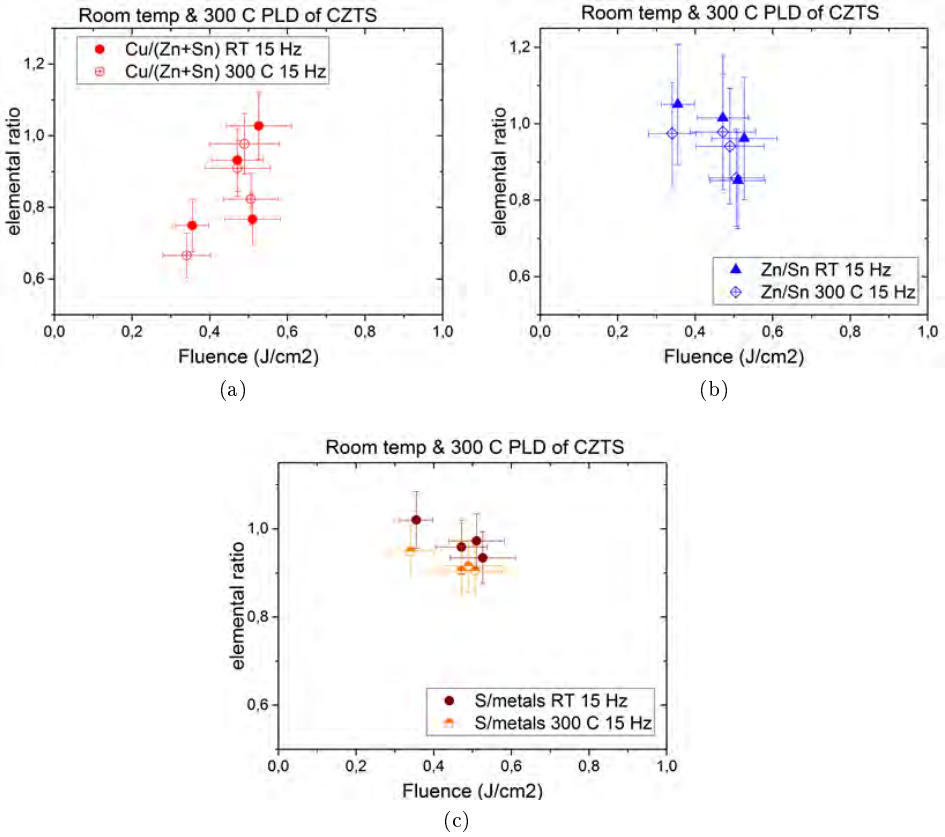

Figure 8.6: Composition of CZTS films made by PLD at room temperature compared to 300 °C. All the films were more than 800 nm thick and were measured with 15 kV excitation in the TM3000 tabletop SEM. (a): Cu/(Zn+Sn) ratio. (b): Zn/Sn ratio. (c). S/metal ratio Error bars represent 95 % confidence intervals for comparisons between measurements; the absolute error in quantification may be larger.

was a general trend confirmed by looking at the 15 Hz films and at the other 45 and 7 Hz films). The composition at 7 Hz was not different from the composition at 15 Hz, whereas the 45 Hz films had a slight tendency to be more Cu-rich. We therefore decided to keep using 15 Hz. Despite the convenience of a shorter deposition time, 45 Hz was clearly out of the question.

8.2.3 Composition of the as-deposited PED films

A prediction of the film composition could be made in the PED setup by OES of the plume emission (Methods, Section 5.2.1). At a given voltage, changing the Ar pressure made it possible to change the intensity of the Cu(I) emission line relative to the Zn(I) emission line. This meant that we could try to see if the composition were different at different voltages while keeping the Cu(I)/Zn(I) emission ratio constant (as far as possible). It turned out that keeping the Cu(I)/Zn(I) emission ratio constant led to a more or less constant composition of the films as seen in Figure 8.5b.

The main result of our room temperature composition investigation was that the elemental transfer in PED was not stoichiometric: the films were Cu-poor, Zn-poor, and often S-poor relative to the expected composition (in other words, they were Sn-rich). EDX of powders scraped from the targets before and after deposition indicated that the target changed over time: there was an increase in the Cu-content and a decrease in Sn and S after the depositions, suggesting that Sn and S were preferentially removed while Cu was left behind. Another hint that the target composition changed during the experiment came from the change in the OES spectrum during preablation: The Cu(I)/Zn(I) intensity ratio was generally lowest when the target was fresh and increased to an approximately stable level during the deposition. Since the Zn(I)/Sn(I) peak ratio was generally constant as far as we could measure, this indicates that at first more Zn and Sn are ablated until a Cu-enriched target surface is obtained during preablation. The Ar pressure sometimes had to be adjusted during the deposition to maintain the Zn(I) peak intensity, however, suggesting a further slow change in the target over time.

The composition of the PED films in Figure 8.5b is similar to the composition of the PLD films made at fluences around 0.4 to 0.45 $J\,cm^{-2}$ (Fig. 8.5a). Below 16 kV, the Cu (I)/Zn (I) emission line ratio could not be increased further than the conditions used to deposit the films in Figure 8.5b, whereas at 16-19 kV changing the Ar pressure led to a higher Cu (I)/Zn (I) ratio in the OES spectrum. By adjusting the Ar-pressure it was therefore possible to deposit a film at 18 kV that had a much higher Cu/(Zn+Sn) ratio while maintaining a similar Zn/Sn ratio as the films shown in Fig. 8.5b. This could suggest a similar dynamic in PED as in PLD: easier ablation of SnS and ZnS compared to the Cu-rich phases

in the target. The Sn-rich but simultaneously slightly S-poor composition of the PED films may indicate that S is scattered more than Sn (and Cu and Zn) by the background gas in PED. Preferential scattering of light elements by a background gas is a well-known effect in PLD and may well be significant in the pressure regime used in PED as seen, e.g., in PLD of Cu-S and Cu-Se films [28]. However, as mentioned the EDX measurement of the S-content of a rough film is not very accurate, so more work is needed to verify this conjecture.

During PED we noticed that portions of the ablation plume originating from distinct points on the rotating target were visibly brighter than the rest of the plume, strongly supporting the idea that the ablation efficiency was higher for some of the phases than others. Such an irregular ablation plume was never observed in PLD. Another clear difference in the beam-target interaction was that when the PED target became thin enough (a few mm), ablation spots became visible on the back of the target, demonstrating that some of the electron energy was deposited very deep in the target indeed. The spotty plume and the occasional plumes on the back of the target may have to do with the different conductivity of different phases.

Due to layering in two of the PED films made at elevated temperature, only the composition of the film made at 255 °C could be measured (the layers in the other films are visible in Fig. 8.3). The measured film was somewhat Cu-rich (Cu/(Zn+Sn)=1.05) and S-poor (S/metals =0.9) with a Zn/Sn ratio of ≈ 1, at least in the top micron probed by 15 kV EDX. The Cu-rich composition was a surprise because the Cu(I)/Zn(I) OES emission ratio had been stable around a value of 1 throughout the deposition and based on the measurements made at room temperature, this predicted a Cu/Zn ratio in the final film of about 1-1.5. Instead the Cu/Zn ratio was just over 2. The Zn/Sn ratio did not change appreciably. More experiments are needed to investigate whether this high Cu-content is reproducible at deposition temperatures of 250 °C-300 °C. The OES spectrum was stable throughout the deposition, so the Cu-rich composition measurement is not expected to be due to any gradient in the film.

8.2.4 Crystallinity of films deposited at 300 °C

The films deposited at high temperature by both PED and PLD were crystalline with XRD and Raman peaks matching CZTS but also some secondary phases. In Sections 5.6.5 and 5.6.6, we saw the difficulty resolving different secondary phases based on Raman and XRD: it is possible to show that a phase may be present but it is hard to rule out that no other phases occur because there are so many competing structures with similar lattice parameters and characteristic phonon frequencies [39]. This is good to bear in mind in the following discussion, which is mostly reproduced from Appendix D.

Raman spectra of the PED and PLD films deposited at $\approx 300\,^{\circ}\mathrm{C}$ are presented in Figure 8.7 (also shown in Fig. 6 in our manuscript, Appendix D). In the PED films (Figure 8.7a) only CZTS peaks and Cu_xS are visible, matching the slightly Cu-rich composition measured by EDX. The copper sulfide phase appeared to be associated with droplets (dark areas) on the surface. In the PLD films (Fig. 8.7b) only traces of Cu_xS are visible but other secondary phases are visible with peaks around 179, 225 and 300 cm^{-1}. These may match orthorhombic Sn_2S_3, orthorhombic SnS, and cubic Cu_2SnS_3 respectively [225, 226]. The secondary phases were associated with a crystalline phase that appeared bright in SEM and was much more pronounced in the low-fluence, Sn-rich film as seen in Fig. 8.7c. The presence of SnS_y matches the Cu-poor nature of the PLD films, but also suggests the possible inclusion of ZnS if $Zn/Sn \approx 1$ as measured by EDX.

XRD of the PED and PLD films made at $300\,^{\circ}\mathrm{C}$ support the Raman observations (Figure 8.8, also shown in Fig. 7 in our manuscript, Appendix D). In the PED film, we see small peaks that belong exclusively to kesterite CZTS around 29° and 36-38° 2θ in the PED film (Fig. 8.8a)(these peaks also match two tetragonal forms of CTS, but this is not supported by the Raman measurement). The remaining major peaks are the Mo substrate peaks and 'ΣCZTS' peaks, where 'ΣCZTS' refers to the 2θ ranges with overlap of the X-ray diffraction peaks for kesterite CZTS, cubic ZnS, and tetragonal and cubic CTS [223]). There are also some extremely small peaks probably belonging to SnS, though they could also derive from different phases (plotting the data with a semilogarithmic y-axis, not shown here, proves that these peaks are not noise). In the PLD films (Fig. 8.8b) again the main peaks apart from the Mo substrate peaks are ΣCZTS peaks. Additionally, a few small peaks are present around 28° and 31-32° 2θ that could belong to SnS, Sn_2S_3, or Cu_2S.

The high intensity of the (211) CZTS peak at 28.4° 2θ in the PLD XRD pattern indicates a preferential growth direction that is stronger than in the PED films. This result is in agreement with Sun et al. [159], reporting a similarly strong preferential orientation of the (211) planes in $300\,^{\circ}\mathrm{C}$, 248 nm PLD of CZTS. Comparison of the insets in Fig. 8.8a and 8.8b shows that the XRD peaks of the PLD films are shifted towards slightly smaller 2θ angles than the PED films, indicating a difference either in the lattice size or in the phase composition. For example, regions of ZnS could shift the PED peaks to larger 2θ values.

The Raman peaks of the PED film appear narrower than those of the PLD film (Fig. 8.7) but this may be an effect of using slightly different wavelengths for the measurements: Dimitrievska et al. [224] show that the shoulder peaks at 353, 366, and 374 cm^{-1} next to the main CZTS peak at 338 cm^{-1} are more prominent with 514 nm Raman excitation than with 458 nm excitation. We used 455 nm excitation in the PED film measurements and 532 nm excitation for the PLD measurements.

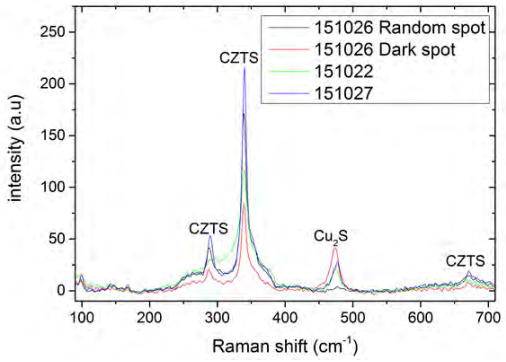

(a) PED

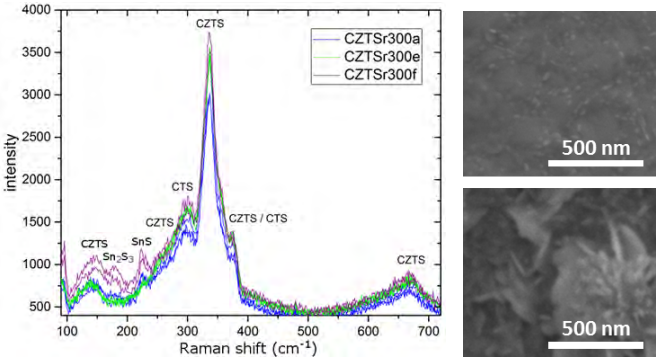

(b) PLD (c) PLD films

Figure 8.7: XRD of CZTS by PED and PLD at elevated substrate temperatures. (a): PED film made at 255 °C-325 °C. All of the films contain some Cu_xS on the surface. In the very thick film made at 255 °C, the Cu_xS was only present in dark spots on the surface but not on other randomly chosen spots. (b): PLD films made at 300 °C. One film apparently included more secondary phase than the other two as seen by the higher peaks at the SnS and Sn_2S_3 peak positions. In this film, small grains were visible on the surface that were not as clear as in the other films. This is seen in (c) (top image) compared to a film made at low fluence (bottom image) which had many more structures visible on the surface in SEM and much higher secondary phase peaks in the Raman spectrum. The scale bars are 500 nm long. Raman spectroscopy by A. Crovetto and S. Canulescu. SEM by Sara Engberg.

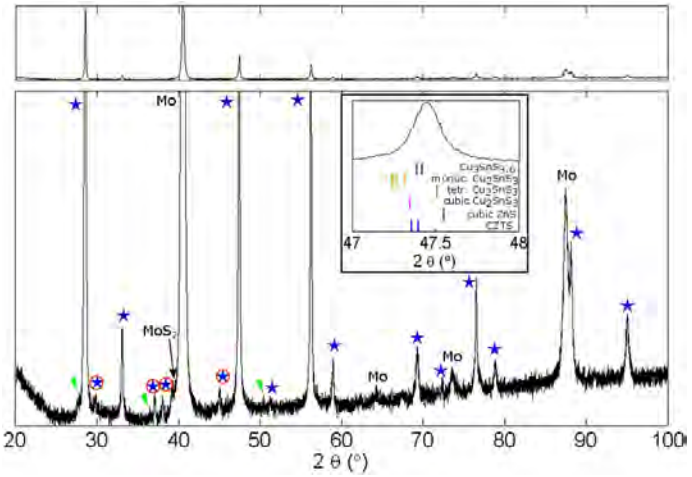

(a) PED

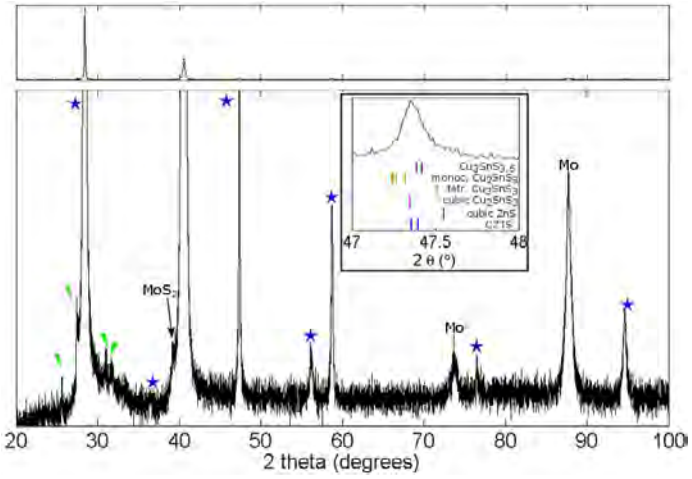

(b) PLD

Figure 8.8: XRD of CZTS by PED and PLD at elevated substrate temperature. (a): PED film made at 255 °C. This data is from the film shown in Fig. 8.3c. Stars: ΣCZTS peaks (CZTS, cubic Cu_2SnS_3, tetragonal Cu_2SnS_3, $Cu_3SnS_{3.6}$, and/or ZnS). Circled stars match only the tetragonal phases: CZTS, tetragonal CTS, and $Cu_3SnS_{3.6}$. Triangles: most likely orthorhombic Sn_2S_3. Inset: the 47.5° peak position compared to reference peaks. Top panel: Comparison of the full height of the peaks for evaluating the preferential growth direction (b): PLD film made at 300 °C. Symbols, inset and top panel as for (a). The Mo peak positions were aligned using Si reference powder (see Section 5.6.5).

Together, the Raman and XRD data point to CZTS and Cu_xS in the PED films and CZTS, Cu_2SnS_3 and SnS_y in the PLD films.

8.2.5 Lessons from a low-fluence PLD film

As mentioned, a few films were deposited at lower than usual PLD fluence to test whether this could enhance the S-content of the films and lead to as-deposited films that were not poor in S even at a deposition temperature of 300 °C. We saw that this was not achieved - the films were slightly S-poor, perhaps due to the long deposition time at elevated temperature. However, two interesting observations could be made regarding the film deposited at low fluence and 300 °C:

- the film formed even smaller crystal grains than the films deposited at higher temperature: the XRD peaks (all ΣCZTS peaks) were very small and broad
- the impurity phases detected by Raman in the other films were much more strongly detected in this film and were visible in SEM as bright, fluffy structures on the film surface

This demonstrates that the strategy of using lower fluence combined with an elevated substrate temperature to obtain a better film quality for solar cells did not work. Instead it helped discern that there really was a secondary phase in the films deposited at higher fluence and to identify this phase as most likely SnS or perhaps Sn_2S_3. This is documented in the Supplementary Information in Appendix D. Despite the stronger Raman peaks of the impurity phase, it was still difficult to assign it/them to one particular SnS_y phase. Most of the peaks match the reference spectrum of SnS, but the peak at 179 cm^{-1} matches Sn_2S_3 better. It may be that we have produced a mix of SnS and Sn_2S_3, perhaps one that would be thermodynamically unfavorable at equilibrium. The low degree of crystallinity of the film is consistent with the idea that evaporation competes with ablation at this low fluence: apparently the particles impinging on the substrate have less energy available to form the crystal structure of CZTS.

8.2.6 Solar cells

The JV curve for one of the CZTS solar cells made by PED is shown in Figure 8.9. The top layers were fabricated by the members of the PED group in Parma as described by Rampino et al. [148]. This solar cell had a very low J_{sc} of 2.1 mA cm^{-2} compared to 17.5 to 19.5 mA cm^{-2} in state-of-the art CZTS solar cells [13, 11] and 4.4 mA cm^{-2} in one of our other PED solar cells. The V_{oc} of 171 mV was also low compared to state-of-the-art solar cells, which display 660-710 mV [13, 11]. The far-from-vertical slope of the JV-curve at the intercept to the

voltage axis points to a low shunt resistance. This solar cell was made from the film shown in Figure 8.3b which clearly has large regions of secondary phases near the back and a highly porous structure.

Our best solar cell was made from the very thick film seen in Figure 8.3c with an efficiency of 0.2 % and a higher J_{sc}, but the JV data for this cell were not saved properly before the solar cell degraded. This degradation is not usually seen for CIGS or CZTS solar cells and may point to oxidation following the scribing of the cell.

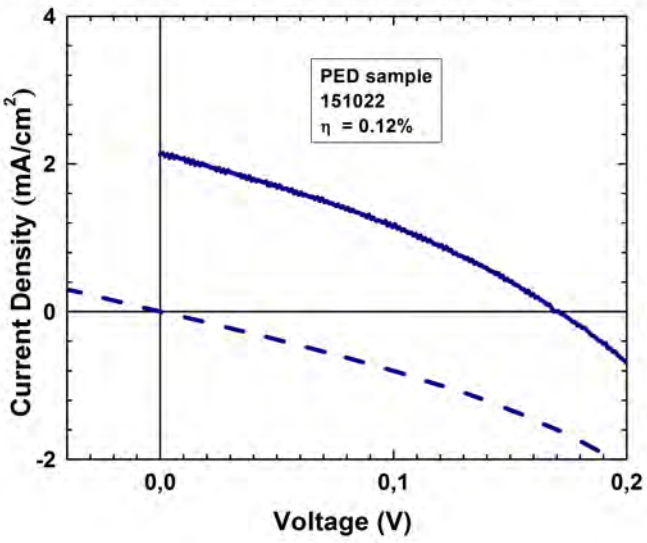

Figure 8.9: Current-voltage measurements for a PED solar cell. Solid line: under illumination. Dashes: in the dark. The curve should ideally be horizontal at the current axis intercept and vertical at the voltage axis intercept, showing that there is low shunt resistance. Additionally the J_{sc} is extremely low. Measurement by S. Rampino.

A few of the PED solar cells were measured by photoluminescence (PL) mapping, as were some of the as-deposited 300 °C PLD films. The results are seen in Figure 8.10. Note that the intensity scale is different for (a) and (b). The as-deposited PLD films (Fig. 8.10a) showed almost no photoluminescence, similar to other previously measured as-deposited PLD samples. This may be because of fatal defects in the material from the S-poor, Sn-rich composition measured

by EDX. When there is no photoluminescence it means that any carriers generated by photoexcitation are lost to non-radiative recombination, which can happen when carriers are trapped in defects with energy levels in the middle of the bandgap. In Section 2.2.1 we saw that both S-vacancies and Sn-substitutions on Cu and Zn lattice sites cause deep donor levels in the bandgap. It may also be that some of the material has formed ZnS rather than CZTS although we saw no sign of large ZnS clusters in the SEM cross section. The presence of ZnS could not be probed by the XRD or Raman measurements that we did and would have no photoluminescence at the excitation wavelength we used.

The PED solar cells did show some photoluminescence and one showed surprisingly high-intensity PL (better than the > 5 % efficient solar cell reported by Cazzaniga and Crovetto [157]). The efficiencies of the PED cells in the map are noted in the caption of Fig. 8.10b. The high photoluminescence sample, A in Figure 8.10b, was very thick, about 3 µm, which could lead to interference in the peak, making the exact peak shape and location unreliable [250]. Thin film CZTS PL peaks are often found at about 1.3 eV, even though the bandgap at 1.5 eV would lead one to expect a higher peak position. In this case it appears that we have a higher PL peak position (or perhaps two peaks) than normal in our annealed PLD CZTS films. EDX measurements of this film indicate a Cu-poor, Zn- and Sn-rich film while XRD showed SnS. It could be that CZTS formed alongside ZnS and SnS in this sample with a high photoluminescence of the CZTS itself. Though such phase segregation could in itself make the EDX measurement unreliable, the high photoluminescence is nonetheless encouraging.

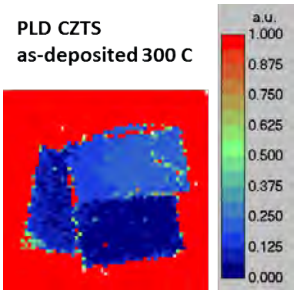

(a)

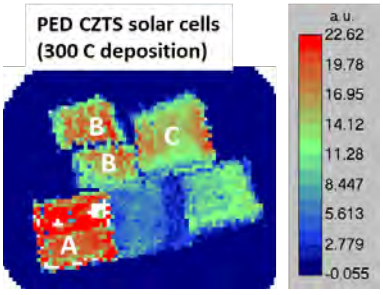

(b)

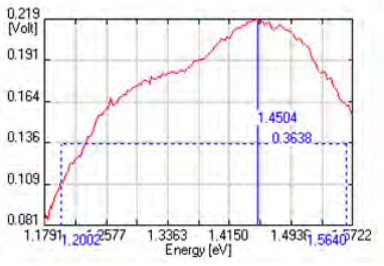

(c)

Figure 8.10: Photoluminescence (PL) mapping of samples made by PLD and PED at a substrate temperature of 300 °C. (a): PL maps of PLD-deposited CZTS films. Almost no photoluminescence. (b): PL maps of PED-deposited finished CZTS solar cells. Sample A: η 0.07 %, V_oc 63 mV, J_{sc} 4.4 mA cm^{-2}. Sample B: η 0.08 %, V_oc 180 mV, J_{sc} very low. Sample C: η 0.01 %. (c): PL peak at a high-intensity spot on sample A. This sample was 3000 nm thick, causing interference. Raw plots and measurements by A. Crovetto.

8.3 Summary and discussion

The most important results of our comparative work on PED and PLD of CZTS were:

- PED at room temperature resulted in preferential ablation of SnS and/or S
- PLD at room temperature and low fluence resulted in preferential ablation of SnS and ZnS

- Changing the discharge voltage and pressure in PED and the fluence in PLD makes it possible to alter the film composition from Cu-poor to Cu-rich
- The composition may have had a large impact on the morphology of the films with a Cu-rich composition apparently resulting in porous, chaotic films
- PLD and PED both result in crystalline CZTS at 300 °C.
- The crystalline CZTS is accompanied by secondary phases by either method: likely ZnS near the bottom and $Cu_{2-x}S$ at the surface in the PED films, and Cu_2SnS_3 as well as Sn_2S_3 near the surface in the PLD films.

Did our initial hope to avoid S-poor films at high deposition temperature in PED work out? Not yet, but it should certainly be possible to tune the deposition parameters in PED so that we get Cu-poor rather than Cu-rich films. This might lead to a higher S-content in the films as well. Achieving single-phase films will be a challenge but may not be impossible. The greatest challenge that I see is increasing the Zn/Sn ratio as the films must not only be Cu-poor but also Zn-rich for high-quality solar cells.

The multiphase nature of the target appears to influence our results strongly for CZTS since we see preferential evaporation or ablation of Sn relative to Cu and Zn at low voltage in PED and at low fluence in PLD. Especially in PED the Sn-content is much higher than expected. This matches our observations of preferential evaporation of Sn at low fluence and overstoichiometric ablation of Cu at higher fluence using the CTS targets in the previous chapter. As in the case for the CTS targets, we believe that we are seeing evaporation of the SnS-rich portions of the target due to the high volatility of SnS. Additionally, as argued by Cazzaniga & Crovetto [157], ZnS is also ablated (or evaporated) more easily than the Cu-rich phases in the target due to a lower heat of fusion.

Highlighting the importance of small differences between setups in the final results, we can compare our results by PLD to those of Moriya et al. [160], who used a very similar setup (a 248 nm laser with 25 ns pulses). We see that they obtain slightly Cu-poor and Sn-rich films relative to the target with a fluence of $1.5\,J/cm^2$ which would result in Cu-rich, Sn-poor films in our experiments. Like us they use no background gas, so scattering in a background gas is not the reason. Instead the difference is very likely due to differences in the target. They use a homemade target but do not describe whether it contains multiple phases.

One question is not completely clear: if the low voltage PED films made at room temperature were enriched in Sn due to preferential evaporation of SnS, then why were the films not stoichiometric in S? During the evaporation, $2SnS_2$ from the target must be broken down into $2SnS + S_2$, but the evaporation plume should in principle have the same shape for both of these evaporating components,

so the resulting composition on the film should also be the same - and the original proportion of Sn to S should be maintained or even enriched in S_2, which is most volatile. If this were the case, a Sn-rich film composition should be accompanied by an S-rich composition. But that was not what we measured.

Initially we blamed the S-poor, Sn-rich nature of the films on the target, which our EDX measurements indicated was S-poor. However, as noted several times during this thesis, the evaluation of the multiphase target composition by EDX is not accurate. An alternative explanation could be that S was scattered preferentially in the plume (or in a dense evaporated gas cloud) by the other, heavier atoms as well as the background gas. In PLD of Cu_2S, scattering of S by the background gas has been observed [114], but the scattering only became significant for pressures about an order of magnitude higher than that used in our PED experiments. Finally it could also be that S is resputtered from the growing film.

It would be interesting to explore the reasons for the S-poor, Sn-rich films further by performing PLD in a background gas of the same pressure as in PED and by testing PED and PLD of a single-phase (or nearly single-phase) target whose composition may be accurately measured. No group has performed PLD of a single crystal CZTS target, but Watanabe et al. [168] synthesized a single-phase polycrystalline target. They found non-stoichiometric film growth and secondary phases, but their films were grown at 500 °C for 5 hours on soda lime glass substrates. It would be interesting to use a similar single-phase target for room temperature depositions to better understand the ablation dynamics. At higher deposition temperature, one could use a larger spot size to reduce the deposition time and use Mo/SLG substrates to get a better idea of the film growth dynamics relevant for solar cells. This could be a path for further research that would help us understand if it is possible either by PED or PLD to deposit CZTS that is not S- and Zn-poor relative to the Sn-content.

Chapter 9

Conclusion

This thesis has explored pulsed laser deposition and pulsed electron deposition for fabrication of thin films of the chalcogenides copper tin sulfide (CTS), copper zinc tin sulfide (CZTS), and zinc sulfide (ZnS) for solar cells and materials studies.

To our knowledge we are the first to have deposited CTS by pulsed laser deposition and the first to have deposited CZTS by pulsed electron deposition.

9.1 Main results on CTS

Annealed CTS films for ellipsometry By annealing PLD-deposited precursor CTS films, we were successful in making very thin films of monoclinic phase Cu_2SnS_3, the form of CTS most commonly used in solar cell research. These films were used for ellipsometry and matched a model that explained the double absorption onset seen in optical characterization. Other authors had seen and commented on this double absorption onset but had not been sure whether it was due to the presence of two different phases in the material or due to the asymmetry of the crystal structure itself [251, 17]. Our paper showed that it is most likely an intrinsic property of the material.

Annealed CTS films for solar cells Preliminary annealed CTS films for solar cells reached 0.3 % efficiency. The CTS in these cells was made from a very SnS-rich starting material and contained layers of SnS, holes and other defects that could cause both shunting and blocking of charge carriers. The CTS films that were less SnS-rich suffered from bubbles in the annealed films and in some cases complete exfoliation. Thinner films seem to be the solution to these problems and should enable us to make better solar cells from annealed films based on precursors from the near-stoichiometric CTS target.

Composition, as-deposited CTS films The composition of the target was not transferred congruently to the growing film. For the as-deposited CTS films, we found that the Sn and S-content in the films could be increased by using a lower fluence. We see this largely as an effect of competition between evaporation and ablation with evaporation leading to SnS-rich films and ablation leading to Cu-rich films because ablation is more forward-directed, so that a greater proportion of ablated material reaches the substrate compared to the evaporated material.

Droplets in CTS films Reducing the fluence also reduced the amount of droplets in the films, as previously seen by other authors, while no change was seen from using a shorter-wavelength laser.

As-deposited crystalline CTS films As-deposited CTS films at 150-300 °C showed evidence of the tetragonal phase in 150 °C films and the cubic or monoclinic phase in 300 °C films. However, the films contained secondary phases and grain growth was limited in the tetragonal-phase 150 °C films. Preliminary films were S-poor and not dense. In order to obtain crystalline as-deposited CTS films at high temperature, it would be necessary to decrease the fluence to tune the Cu/Sn ratio of the film deposited from the near-stoichiometric CTS target.

9.2 Main results on CZTS

Composition: CZTS by PED The composition of the PED films at room temperature could be tuned at high acceleration voltage (16-18 kV) to obtain Cu-rich or Cu-poor films. At low voltage the composition was always Cu-poor.

Differences in composition CZTS by PED versus PLD The PLD films could be made Cu-poor at low fluence but there were slight differences in the balance of Sn to Zn and S compared to Cu-poor PED films: apparently there was more Sn and less Zn+S in the PED films. This could result from the low-energy electrons resulting in preferential evaporation of SnS versus ZnS coupled with scattering of S in the ablation plume and the background gas(the same effect leading to S-poor films in PLD, but smaller). A Zn/Sn ratio <1 would be a problem for our solar cells.

As-deposited crystalline CZTS films PLD and PED both result in crystalline CZTS at 300 °C but as with CTS, the crystalline CZTS is accompanied by secondary phases by either method: likely ZnS near the bottom and $Cu_{2-x}S$ at the surface in the PED films and Cu_2SnS_3 as well as Sn_2S_3 near the surface in the PLD films.

Solar cells from as-deposited PED-grown CZTS Preliminary solar cells of CZTS grown by PED were limited by shunting probably due to the porosity of the films and the maximum efficiency was 0.2 %.

9.3 Observations on PLD and PED of chalcogenides

Composition S-deficiency was a problem in PLD of both CTS and CZTS especially at elevated deposition temperature (300 °C).

Deposition at high temperature We do not see a large change in deposition rate or composition up to 300 °C for the as-grown chalcogenide films, but there may be a small change in the S-content: we saw a small decrease in the deposition rate of ZnS and CTS when the temperature was increased and a small decrease in the S content in CZTS. Perhaps in future this could be verified by other techniques such as Rutherford backscattering spectrometry or X-ray fluorescence spectroscopy.

Target quality One issue that is not discussed very much in our manuscript but which may be an important one is the exact composition of the targets. Our EDX measurements indicated that the targets used in the PED experiments were S-poor and Cu-rich.

Process control We saw that under some circumstances, the PED films were mainly composed of droplets and the deposition rate could be very high though also quite low at high voltages. So the Ar pressure control is crucial for a stable deposition but probably the target also plays a key role.

Finally some observations that are not new but would be useful for a newcomer in this field - at least, they would have been useful to us when we started this project:

- One cannot assume that a multiphase target will be uniformly ablated - the different constituents of the target may not be affected by the laser in the same way.
- Working with a material like Sn with a low melting point and a high boiling point may cause a large amount of droplets in the film.
- The crystal orientation of the substrate strongly influences the film growth and adhesion, especially when the temperature of the film is increased by substrate heating or subsequent annealing.

- For characterization of CTS and CZTS, cross-sectional SEM, Raman spectroscopy, and photoluminescence measurements are important tools alongside surface SEM and XRD. Surface SEM and XRD can reveal whether something is wrong with the material like secondary phases but cannot guarantee that the material quality is high.
- Exact composition control of materials like CZTS is challenging and it is important to be aware of the limitations of measurement techniques like EDX, which may be well suited for some materials but need adjustment for others (e.g., EDX at 25 kV is fine for CIGSe films of 2 µm thickness but not for CZTS of 1 µm thickness as one will detect signal from the substrate as well as the film).

9.4 Discussion

9.4.1 On using a multi-phase chalcogenide target

It is not clear why the different phases in the target behaved so differently under irradiation. Based just on the comparison of the deposition rates of CTS and ZnS by the 248 nm laser, one might expect the CZTS films to be Zn-rich: the deposition rate of ZnS was higher than that for CTS with this laser. However, the CZTS target did not just contain CTS and ZnS but also copper sulfides and tin sulfides and in the end we found the films more Sn-rich than Zn-rich. This has to do with the differences in how the SnS-rich and Cu-rich phases in the target are affected by the laser. We are probably seeing the effect of the extremely low vapor pressure of SnS. As noted briefly in Chapter 8, Cazzaniga & Crovetto [157] suggested that this may be because SnS and ZnS sublime at relatively low temperatures (especially SnS), while vaporization of CuS requires much more energy through intermediate steps where CuS transforms to $Cu_2S + S_2(g)$.

In the CTS films we saw both Sn-rich and Cu-rich droplets, suggesting that both types of phases in the target could melt and be ejected by the extreme pressure created by the laser pulse. However, we saw a majority of Cu-rich droplets which seems to fit well with the idea that SnS was more easily vaporized, leaving more copper sulfide in the molten phase in the target.

As discussed at the end of the previous chapter, it could be interesting to work with a single-phase target, depositing films at room temperature by both PED and PLD to understand if stoichiometric transfer of this chalcogenide would be possible if we were free of the complications of multiple phases in the target. Angle-resolved film measurements could help us understand the dynamics. There might still be problems with S-loss at high temperatures as we saw from the multiphase target, something which could perhaps be addressed by using a separate source of S.

9.4.2 On CZTS by PED and PLD

The greatest challenge we met in our as-deposited CZTS films was obtaining the desired Cu-poor and Zn-rich stoichiometry while avoiding loss of S.

For PLD, we found that CZTS films deposited at 300 °C were always poor in S, though it may be that experiments with the sulfur cracker recently installed in our lab can help solve this problem, enabling us to make as-deposited S at low temperature. However, the S-cracker in itself complicates the deposition process, so this would probably not be the way to develop a simple, single-stage CZTS process.

Another option to explore could be using a background gas. Strikovski et al. write that the ideal energy of incoming adatoms for crystalline film growth should be about 10-20 eV, which is significantly lower than the most energetic species emitted in both PED and PLD. They suggest that apart from working near the ablation threshold with a UV laser (as we do) it is important to adjust the pressure in the chamber and the target-substrate distance [101]. It is conceivable that a background gas could help improve the properties of CZTS and CTS in PLD by slowing down the incoming species, giving rise to fewer defects and randomly occurring secondary phases that do not represent the true thermodynamic minimum energy structure. However, a background gas might lead to scattering of S, making it necessary to perform the deposition a little bit off axis to avoid S-poor films. Like the S-cracker, a background gas would therefore not be a quick and simple fix.

In PED, we saw that changing the discharge voltage and pressure in PED and the fluence in PLD makes it possible to alter the metal part of the film composition from Cu-poor to Cu-rich but we do not completely control the balance yet in PED - one film became Cu-rich at higher temperature despite an OES signal promising a Cu-poor composition but many more experiments could elucidate how to control this.

The first step towards successful as-deposited CZTS solar cells by PED is to ensure that the films are Cu-poor, Zn-rich, and not S-poor. As noted above, this could be challenging with our multiphase targets since it appears that SnS was more easily evaporated than ZnS, resulting in Sn-rich films. A single-phase target could perhaps help correct the Zn/Sn ratio: looking purely at the cohesive energy of each atom, it should be easier to ablate Zn than the other metals. However it is difficult to say how the atoms would behave as part of a CZTS compound target. As in PLD, S-loss from the heated films could be a persistent challenge. It may be that the deposition temperature could be decreased somewhat as has been possible in CIGS deposition. Alternatively perhaps one could increase the fraction of S in the films could by using off-axis deposition if it is correct that S is scattered more than S in the plume and background gas in PED. This would reduce the deposition rate and the efficiency of raw material use, however.

9.5 Perspectives

9.5.1 Non-equilibrium methods for CZTS and CTS

One of the strengths of PED and PLD is that they can be used to obtain material phases that are normally hard to reach because they are far from thermodynamic equilibrium at standard temperature and pressure. For example, we saw that we could obtain the wurtzite phase of ZnS at a much lower temperature than would normally be observed with equilibrium processes. However, for CZTS and CTS this might not be an advantage. These materials are characterized by many secondary phases that are close to each other in potential energy and since PLD and PED allow easy access to non-equilibrium phases, we might actually be increasing the likelihood of obtaining unwanted phases.

In the light of PED and PLD as far-from-equilibrium methods, however, it could be interesting to check our Sn-rich as-deposited CZTS films for the presence of non-equilibrium phases that are not well known such as the elusive phase $Cu_2ZnSn_3S_8$ which was reported by Olekseyuk et al. [40] but has rarely if ever been documented by others [223]. As already proposed by my colleague Andrea Cazzaniga [135], it could also be interesting to delve further into the phases obtained with a low Cu-content both at room temperature and higher temperatures: ZnSnS is a non-equilibrium mixture whose properties are not yet well known.

9.5.2 Epitaxial films of CZTS and CTS

The possibility of obtaining epitaxial growth is another strength of PLD in other contexts. Could it be useful for research on CZTS and CTS? In principle the answer is yes - and indeed this was the first use of PLD in CZTS research by Sekiguchi et al. in 2006 [139]. However, it would be necessary to overcome any problems with S-loss from the films and it is questionable how much we could learn that has not already been seen by work on epitaxial growth of CZTS by other methods.

9.5.3 Single-step CZTS and CTS deposition

Because CZTS deposition today requires high-temperature processing, developing a low-temperature fabrication method could clearly be interesting, e.g., for flexible plastic substrates or for integration with Si substrates in tandem solar cells [252]. A lower processing temperature could also reduce the price of CZTS and perhaps improve the lifetime energy balance of the product, though this also depends on inefficiency in the rest of the process (e.g, a vacuum process will always require pumping energy and an excimer laser will never be an energy efficient production tool though it may allow a lower substrate temperature). While as

noted in Section 2.2.2 the current record solar cell is made by a very complicated method, others have worked to try to achieve a simpler process but none have succeeded, with the lowest-temperature single-step process so far reaching 5.4 % efficiency [20]. There is clearly room, therefore, for a low-temperature single-step deposition method to be developed using PLD or PED. Because PED is more energy efficient and potentially cheaper than PLD, it is probably the best suited of the two methods for developing a low-temperature route to CZTS production for commercialization.

As for CTS production, it is probably better to prove that it is possible to make efficient solar cells of CTS by other routes (e.g., precursor annealing) before embarking on production with a difficult-to-control non-equilibrium process for a material that has even more secondary phases close to each other in potential energy than CZTS.

9.5.4 CZTS as a future solar cell material

The maximum laboratory efficiency of any Si cells is 26.3 % achieved in September 2016 by the company Kaneka as part of a Japanese government research programme. This type of solar cell combines many high-tech innovations in Si solar cells over the last years including an "interdigitated back contact" (which means that the solar cell avoids being shaded by electrodes on the front and therefore appears beautifully and uniformly black) and a so-called HIT design ("heterojunction with intrinsic thin layer"), where a $< 100\,\mu$m monocrystalline Si wafer is coated front and back with ≈ 20 nm amorphous Si to reduce current losses (see [2]). These results are extremely impressive and mean that Si is now very close to the theoretical maximum efficiency for single-junction, non-concentrator solar cells.

The next step for Si solar cells is to combine with other materials to make multi-junction solar cells that have increased efficiency because they use more than one type of light-absorbing material on top of each other [253]. CZTS is a possible candidate material for such a multijunction cell with Si because its bandgap at 1.5 eV is higher than that of Si at 1.2 eV, meaning it can more efficiently convert high-energy photons into electricity. At the same time CZTS maintains its advantage of low-cost, earth-abundant constituents and is lattice matched quite well to Si (it is possible to grow CZTS epitaxially on Si [254]). However, to my knowledge only one study demonstrating a CZTS-Si tandem solar cell has been published which had very low efficiency - much lower than an Si-solar cell [252]. A CZTS-Perovskite tandem solar cell has also been demonstrated, but again so far had lower efficiency than the "parent" solar cells [255].

CTS has also been proposed as a tandem solar cell layer [18]. It would act as the bottom layer because of its low bandgap and in fact purely based on the

bandgap, it could be a better suited bottom layer than Si.

As a solar cell material in its own right, CZTS looks very good in terms of its lifecycle impacts - the only problem is the low efficiency. An accomplished CIGS and CZTS researcher, Susan Schorr, encouraged the research community at her EMRS talk in 2016 by quoting a researcher who in 1983 stated that the open circuit voltage deficit was the key problem preventing the CIS/CIGS community from reaching $>$ 10 % efficiency. Today, many CZTS researchers lament the low open circuit voltage of CZTS as the main problem for the material - perhaps we just have to be patient and keep working just as the CIGS researchers did. This is also necessary if CZTS is to be used in tandem solar cells - it has been shown theoretically that to make an efficient tandem solar cell with a top absorber layer with a 1.5 eV bandgap, the top solar cell must be at least 17 % efficient just to offset the losses it induces in the bottom cell by shading [256].

Finally it is worth noting that both CTS and CZTS have other potential uses than in solar cells. For example, the CZTS solar cell record holders have also worked with CZTS as a photocathode for artificial photosynthesis [257] while others have used CZTS as a counter electrode in dye-sensitized solar cells [258]. Meanwhile CTS has been suggested as a thermoelectric material with both Cu_2SnS_3 and $Cu_4Sn_7S_{16}$ as candidate materials [65, 259].

Appendix A

Article: Pulsed laser deposition from ZnS and Cu2SnS3 multicomponent targets

This article was published in the Applied Surface Science special issue following the laser symposium of the EMRS 2014 spring meeting. The part of the article on ZnS is summarized and referenced in Chapter 6. The part about CTS is summarized and referenced in Chapter 7. Reprinted with permission.

Applied Surface Science 336 (2015) 385–390

Contents lists available at ScienceDirect

Applied Surface Science

journal homepage: www.elsevier.com/locate/apsusc

Pulsed laser deposition from ZnS and Cu_2SnS_3 multicomponent targets

Rebecca Bolt Ettlinger[a,*], Andrea Cazzaniga[a], Stela Canulescu[a], Nini Pryds[b], Jørgen Schou[a]

[a] Department of Photonics Engineering, Technical University of Denmark, DK-4000 Roskilde, Denmark
[b] Department of Energy Conservation and Storage, Technical University of Denmark, DK-4000 Roskilde, Denmark

ARTICLE INFO

Article history:
Received 2 July 2014
Received in revised form
24 December 2014
Accepted 24 December 2014
Available online 6 January 2015

Keywords:
PLD
Pulsed laser deposition
Zinc sulfide
Copper tin sulfide
ZnS
Cu_2SnS_3

ABSTRACT

Thin films of ZnS and Cu_2SnS_3 have been produced by pulsed laser deposition (PLD), the latter for the first time. The effect of fluence and deposition temperature on the structure and the transmission spectrum as well as the deposition rate has been investigated, as has the stoichiometry of the films transferred from target to substrate. Elemental analysis by energy dispersive X-ray spectroscopy indicates lower S and Sn content in Cu_2SnS_3 films produced at higher fluence, whereas this trend is not seen in ZnS. The deposition rate of the compound materials measured in atoms per pulse is considerably larger than that of the individual metals, Zn, Cu, and Sn.

1. Introduction

Pulsed laser deposition (PLD) is a film deposition technique which is well suited for stoichiometric deposition of multicomponent materials [1,2]. PLD has the advantage that the atoms/molecules arriving at the substrate during deposition have a kinetic energy which may exceed the thermal energy with several orders of magnitude [3]. It is therefore possible to grow films which otherwise would require a much higher substrate temperature, and which grow under strong non-equilibrium conditions. Even for compounds with volatile elements the thin films usually exhibit optical, electronic and structural properties similar to the bulk [4–7]. However, for some materials with volatile components such as oxygen or sulfur, a part of the volatile fraction may be lost during the transfer to the substrate or during the film growth [2,8], which, for example, for oxides may lead to "metallic" rather than oxide films [9]. Therefore, in the case of oxides, a background gas is frequently used to ensure correct stoichiometry or structure of the growing film [8].

However, the procedure of compensating the loss of a volatile element with a background gas is undesirable with sulfur-containing compounds such as chalcogenides, as the gas H_2S is toxic and therefore difficult to handle. Though some researchers have used H_2S as background gas for PLD of ZnS [10], other groups have succeeded in using PLD with no background gas or with Ar to make chalcogenide thin films without significant S deficiency or loss of crystallinity, e.g., ZnS, AsS and GeS [5–7,11].

We have previously used PLD to deposit the solar cell absorber material Cu_2ZnSnS_4 (CZTS) in vacuum with no background gas, and we have observed sulfur as well as tin losses at deposition temperatures above 350 °C [12]. We here deposit ZnS and Cu_2SnS_3 at temperatures below 350 °C in a similar single step process with ablation of a multicomponent target made from stoichiometric chalcogenide powders. Our measurements of CZTS films deposited on fused silica demonstrate that many phases occur [12] in contrast to films deposited on typical solar cell substrates such as Mo-coated soda lime glass.

ZnS and Cu_2SnS_3 are interesting materials, not only because they are multicomponent materials with the relatively volatile element sulfur, but also because they are secondary phases in the promising solar cell material CZTS which has a band gap of 1.45 eV [13]. The additional grain boundaries from the secondary phases may trap the charge carriers in the solar cell absorber or directly lead to non-active "dark space" in the case of ZnS with a high band gap

* Corresponding author at: Department of Photonics Engineering, Frederiksborgvej 399, DK-4000 Roskilde, Denmark. Tel.: +45 4677 4587.
E-mail address: reet@fotonik.dtu.dk (R.B. Ettlinger).

http://dx.doi.org/10.1016/j.apsusc.2014.12.165
0169-4332/

of more than 3.5 eV [13]. These two effects are limiting the efficiency of the CZTS cell [13,14]. In addition, the cubic phases of ZnS and Cu_2SnS_3 are particularly hard to detect using X-ray diffraction within Cu_2ZnSnS_4, as the scattering peaks of all three compounds overlap [15]. Another interesting feature is that a pure absorber of Cu_2SnS_3 can be used as a solar cell absorber, albeit with a low efficiency [16].

ZnS is widely used in optical applications. It is a stable material transparent to infrared light, and in crystalline form it displays photo-, cathode- and electroluminescence when doped, e.g., with Mn [5,11]. In its cubic (zincblende) structure it has a direct band gap at about 3.54 eV, while the slightly less stable hexagonal (wurtzite) structure has a direct band gap at about 3.67 eV [17]. ZnS has been deposited by a number of different methods including thermal evaporation [18,19], metal-organic chemical vapor deposition [20], and pulsed electron deposition [21] as well as PLD [5,11,22,23].

Cu_2SnS_3 has previously been deposited as thin films by a variety of vacuum and non-vacuum methods including sulfurization of precursors produced by electron beam evaporation [16], sputtering [24], and electrodeposition [25] as well as, e.g., post-annealing of mixed elemental powders [26] and successive ionic layer absorption and reaction (SILAR) [27]. To our knowledge, Cu_2SnS_3 has not previously been deposited by PLD. Several different crystal structures have been proposed for Cu_2SnS_3 including cubic, tetragonal, and monoclinic phases with reported optical band gaps around 1 eV and with some variation in reported values [16].

In the present work we examine the structural and optical properties as well as the stoichiometry of ZnS and Cu_2SnS_3 films deposited at different fluences and substrate temperatures. Knowledge of these phases may assist us in identifying some of the phases which may occur in films of Cu_2ZnSnS_4 deposited under similar conditions.

2. Materials and methods

2.1. Pulsed laser deposition

Pulsed laser ablation was carried out with a Nd:YAG laser operating at 355 nm with a pulse duration of 6 ns and a repetition rate of 10 Hz. The target rotated as the laser rastered across an area of approx. 0.5 cm^2 at an incident angle of 45° with a spot size of 3 mm^2 (except for the measurements of the deposition rate at room temperature comparing ZnS to Zn, Cu, and Sn, for which the spot size was 1 mm^2). The substrates used in this study were fused silica. The target-substrate distance was kept constant at 45 mm and the substrate was clamped to a heated holder; the deposition temperature was monitored with a thermocouple mounted on the heater surface at the edge of the substrate. The base pressure of the deposition chamber was usually below 10^{-6} mbar.

Multicomponent hot-sintered targets were purchased from PVD products, Inc. The ZnS target was made at 1000 °C from ZnS powder, while the target with 2Cu:Sn:3S stoichiometry was made of a mixture of Cu_2S and SnS_2 powder with 1:1 molar ratio at 750 °C. It is known that the detailed structure of the target does not play a significant role for the film composition except for cases where one or more components are very volatile.

The films of ZnS were deposited at room temperature to 300 °C at a laser fluence ranging from 0.8 to1 J/cm^2 as well as at room temperature at a fluence of 1.4 J/cm^2. All the ZnS films were between 200 and 250 nm thick. The films of Cu_2SnS_3 were deposited at room temperature to 250 °C at a fluence of 0.4–0.6 J/cm^2 as well as at room temperature and at 250 °C at a fluence of 1.6 J/cm^2. The Cu_2SnS_3 films deposited were on average between 400 and 600 nm thick.

2.2. Characterization

Dektak profilometry was used to measure the thickness of deposited films of Cu_2SnS_3 and ZnS. The thickness was converted to the number of atoms per pulse assuming a bulk density of 4.079 g/cm^2 for ZnS and 5.02 g/cm^2 for Cu_2SnS_3 [17].

The transmission of the films was measured with a Cary 50 photospectrometer and the absorption coefficient α estimated from the formula $\alpha = 1/d \times \ln(1/T)$, where d is the film thickness, and T the transmission as a fraction of 1 [28]. Here we make the simplifying assumption that all the incident light is either transmitted or absorbed, with reflection and scattering being negligible. The optical band gap was determined by extrapolating the quantity $(\alpha h\nu)^2$ to zero assuming direct optical transitions.

X-ray diffraction (XRD) was carried out using a Bruker D8 diffractometer in Bragg-Brentano configuration using Cu K_α and Cu K_β radiation. The step size was 0.02° at 1 step/s for the ZnS films (0.01° at 0.75 step/s for the room temperature film shown in Fig. 3a) and 0.01° using 0.75 step/s for the Cu_2SnS_3 films. Peaks were identified manually after stripping the Cu $K_{\alpha 2}$ signal using the program EVA and the peak patterns were matched to the relevant JCPDS files.

Energy dispersive X-ray spectroscopy (EDX) was done with 15 keV electrons with a Bruker Quantax 70 system integrated into a Hitachi TM3000 scanning electron microscope (X-ray take-off angle 25°). The average emission depth of the detected X-rays was modeled with CASINO software version 2.48 assuming a flat sample surface [29]. SEM imaging was carried out both with the Hitachi TM3000 microscope and with a Zeiss SUPRA SEM.

3. Results and discussion

The films of ZnS were transparent, appeared lightly colored due to thin film interference, and looked smooth (Fig. 1a shows a ZnS film made at 200 °C; films made at other temperatures looked very similar). The films of Cu_2SnS_3 (CTS) appeared gray and were rougher than the ZnS films as observed by scanning electron microscopy. From a rather unstructured appearance at room temperature, the Cu_2SnS_3 films changed to a granular structure at 150 °C and 250 °C, as seen in Fig. 1b–d. The SEM analysis revealed the presence of droplets on the surface of the Cu_2SnS_3 films with dimensions ranging from hundreds of nanometers up to one micron (Fig. 1e shows a representative cross-section of the CTS film on fused SiO_2).

3.1. Deposition rate

The deposition rate of ZnS and Cu_2SnS_3 was similar and did not change significantly with increasing deposition temperature from room temperature to 300 °C for ZnS and from room temperature to 250 °C for Cu_2SnS_3 (see Fig. 2). This is consistent with the observations of Xin et al. [5], who found that the growth rate of ZnS was constant from room temperature to about 300 °C.

The deposition rate measurements of Zn, Cu and Sn metals taken under similar conditions [30] is significantly lower than the deposition rate of ZnS. This is partly because the heat conduction of sintered ZnS target is much lower than for the metals and partly because the sintered target may have a high amount of defects at the grain boundaries which absorb photons at the laser energy 3.49 eV, which is slightly below the direct band gap energy of 3.54 eV for a perfect cubic-phase ZnS crystal.

3.2. Crystal structure

Fig. 3 shows X-ray diffraction patterns for films of ZnS and Cu_2SnS_3 deposited at different temperatures.

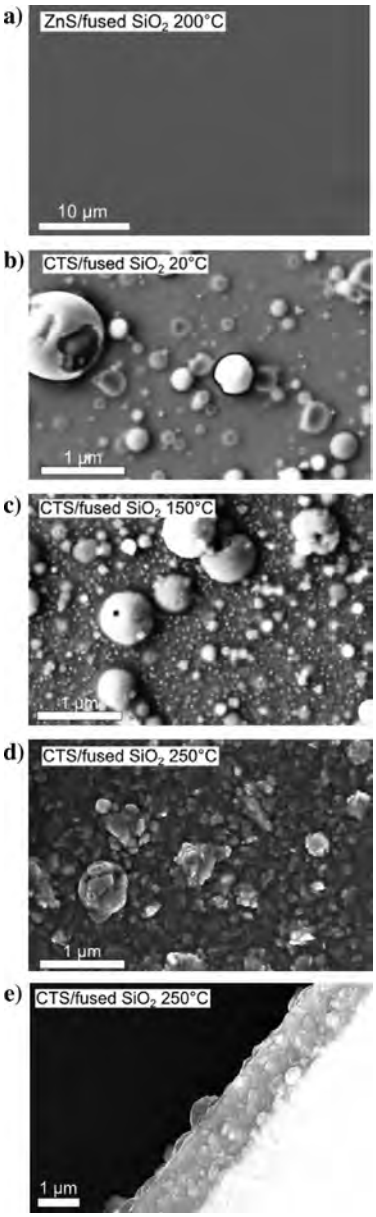

Fig. 1. SEM images of as-deposited films: (a) ZnS deposited at 200 °C at a fluence of 0.9 J/cm^2; (b) Cu_2SnS_3 film deposited at 20 °C, fluence 1.4 J/cm^2, XRD pattern: amorphous; (c) Cu_2SnS_3 film deposited at 150 °C, fluence 0.5 J/cm^2, XRD pattern: Cu_2SnS_3 (tetragonal); d) Cu_2SnS_3 film deposited at 250 °C, fluence 0.4 J/cm2, XRD pattern: Cu_2SnS_3 (cubic), Cu_4SnS_4 (orth), SnS (orth). (e) Cross section of film shown in (d). Note different scales on images.

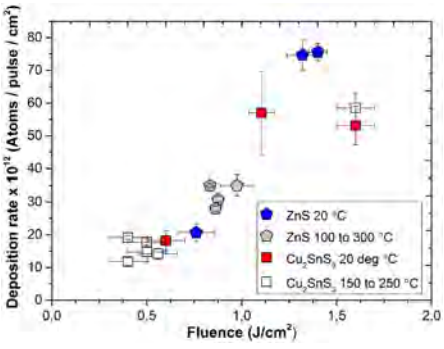

Fig. 2. Deposition rate of ZnS and Cu_2SnS_3 ablated with a 3 mm^2 spot size onto room temperature or heated substrates of fused silica or silicon. Deposition rate error derives from variation in thickness at different locations on the films. Fluence error derives from variation in laser energy and vacuum chamber window transmission during the deposition.

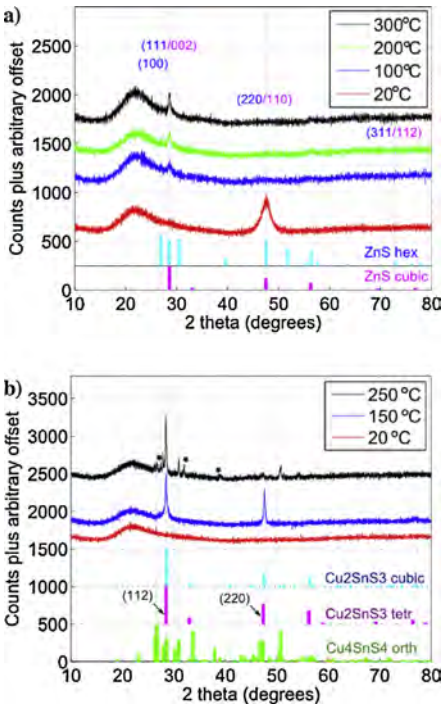

Fig. 3. X-ray diffraction patterns for (a) ZnS thin films and (b) Cu_2SnS_3 thin films. $K_{\alpha 2}$ signal has been removed. The ZnS films were made with a fluence of 0.8–1 J/cm^2 while the Cu_2SnS_3 were made with a fluence of 0.5–0.6 J/cm^2. The stars in (b) denote peaks of orthorhombic SnS (JCPDS 75-2115) Hexagonal ZnS: JCPDS 36-1450; cubic ZnS: JCPDS 05-0566; tetragonal Cu_2SnS_3: JCPDS 89-2877; cubic Cu_2SnS_3: JCPDS 89-4714; orthorhombic Cu_4SnS_4: JCPDS 71-0129.

ZnS films deposited at room temperature show a broad X-ray diffraction peak at the expected position of the cubic (220)/hexagonal (110) reflection (Fig. 3a). As the deposition temperature increases, this peak disappears while reflections appear at about 28.5°, at a slightly smaller angle than the cubic (111) plane/hexagonal (002) plane, as well as at about 56°, at a slightly smaller angle than the cubic (311) plane/hexagonal (112) plane. Additionally, a small peak appears at about 26° which may originate from the hexagonal (100) peak. The relatively high signal-to-noise ratio of the ZnS XRD measurements occurs because the films are thin compared to the penetration depth of the X-rays. With increased temperature the main peak at 28.5° increases in height, which could indicate an increasing fraction of crystalline versus amorphous material.

The observed peak positions are similar to observations using pulsed electron deposition by Zanettini et al. [21]. This group investigated the same range of deposition temperatures using soda lime glass substrates and observed a similar structural modification from preferential cubic (220) growth direction at room temperature to cubic (111)-growth at higher temperature. Unlike Zanettini et al., however, we do not clearly observe a complete transition to the hexagonal phase at 300 °C. In another study using the same third harmonic wavelength of a pulsed Nd:YAG laser as we do (355 nm) and a substrate temperature of 400 °C, Yano et al. [23] find preferential cubic (111) and (311) direction growth similar to our results at elevated temperature. This group also found clear hexagonal-phase peaks at this relatively high growth temperature.

The X-ray diffraction patterns of the Cu_2SnS_3 films vary significantly more with deposition temperature than those of the ZnS films, as seen in Fig. 3b. The films deposited at room temperature appear amorphous. In contrast, the XRD pattern from one of the Cu_2SnS_3 films made at a substrate temperature of 150 °C clearly indicates tetragonal Cu_2SnS_3 with preferential growth in the (112) and (220) directions (expected peaks from the (200) and (312) planes are not visible). At 250 °C the diffraction peaks consistently match a mix of cubic-phase Cu_2SnS_3 with other phases, including clear peaks belonging to Cu_4SnS_4 (orthorhombic) and SnS (orthorhombic). See Table 1 (all JCPDS references in the caption of Fig. 3).

3.3. Elemental composition

Results from energy dispersive X-ray spectroscopy (EDX) show that the expected elements are present in the films (Zn and S for ZnS; Cu, Sn and S for Cu_2SnS_3). Quantifying the amount of each element is difficult as the 15 keV electrons penetrate the layer of interest and enter partly into the substrate, such that the X-ray signal does not derive from a uniform region (see Table 1). This geometry most likely causes overestimation of the signal of Zn in ZnS and of Cu in Cu_2SnS_3. Nonetheless, films of similar thickness may be compared.

On this basis, we can show that for the ZnS films there is less S in films deposited at room temperature than at elevated temperature, while there is no difference between the composition of films deposited at 100 °C, 200 °C, and 300 °C within ±1 at. % equivalent to the variation between measurements of the same film. Changing the fluence from 0.8 J/cm^2 to 1.4 J/cm^2 does not measurably alter the composition of films at room temperature.

Similarly, for the Cu_2SnS_3 films, the S-content increases as the deposition temperature is raised from room temperature to 250 °C. Moreover, an increase in fluence from 0.6 J/cm^2 to 1.6 J/cm^2 results in a decrease in S and Sn content (Table 1). The S:Sn ratio is lower than three for all fluences, indicating S loss at all fluences since the Sn L-lines and S K-lines ideally have a similar emission profile over the sample depth as modeled by Casino. The appearance of Cu_4SnS_4 and SnS together with Cu_2SnS_3 in all films made at 250 °C may be

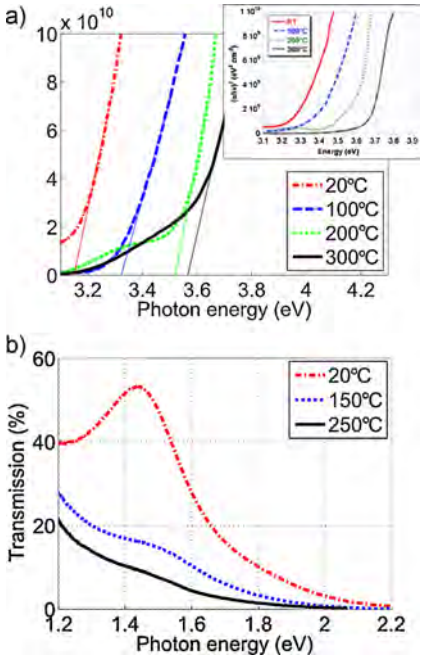

Fig. 4. (a) Optical band gap of (a) ZnS. For ZnS the optical band gap estimate is ~3.15 eV, 3.3 eV, 3.5 eV, and 3.55 eV for films deposited at 20 °C, 100 °C, 200 °C, and 300 °C. The box inset in (a) shows the absorption threshold measured by Zanettini et al. [21] for films made by pulsed electron deposition, reproduced by permission of the authors. (b) Transmission spectrum of Cu_2SnS_3 for films deposited at 20 °C, 150 °C, and 250 °C.

an effect of the S loss, as these compounds are S-deficient relative to Cu_2SnS_3. It is worth noting that even at high fluence at 250 °C, where the films contain least Sn and S, SnS is detected by X-ray diffraction alongside Cu_2SnS_3 and Cu_4SnS_4. However the peaks for Cu_4SnS_4 are relatively more pronounced and the SnS peaks smaller at high fluence than low fluence, matching the lower Sn content (not shown).

3.4. Optical properties

The absorption properties of the ZnS thin films as a function of deposition temperature are shown in Fig. 4a. The optical band gap of ZnS increases with the deposition temperature in a manner very similar to that observed by Zanettini et al. [21] using pulsed electron deposition (inset in Fig. 4a). The trend of increasing optical band gap with increasing temperature was also seen for laser-deposited films at temperatures from room temperature to 660 °C by Xin et al. [5], although this group did not see an optical band gap at all for films deposited at room temperature.

As estimated from Fig. 4a, the value for the optical band gap of the film deposited at 300 °C approaches the expected value of the direct band gap of cubic ZnS, i.e., 3.54 eV. Together with the XRD data, which show an increase in crystallite formation with deposition temperature, the increase in optical band gap with temperature may reflect a change from a material that is partly amorphous with small cubic-phase crystallites to a material with larger crystals and a mix of cubic-phase and hexagonal-phase crystals, increasing the average absorption threshold.

Table 1

	Fluence (J/cm^2)	Thickness (nm)[a]	Mean EDX emission depth (nm)[b]	Zn (%)[c]	S (%)	X-ray pattern matches
EDX and X-ray diffraction data for films made from the ZnS target						
RT	0.8	230	600	60	40	ZnS cubic (220)
100	0.8	250	600	57	43	ZnS cubic (111), hex (100)
200	0.9	200	600	56	44	"
300	1.0	250	600	57	43	"
Target, unablated		-	-	53	47	-

EDX and X-ray diffraction data for Cu–Sn–S films made from the Cu_2SnS_3 target

	Fluence (J/cm^2)	Thickness (nm)[a]	Mean EDX emission depth (nm)[b]	Cu (%)[c]	Sn (%)	S (%)	X-ray pattern matches
RT	0.6	400	250	43	19	38	Amorphous
"	1.6	400	250	52	15	33	"
150	0.5	500	250	40	18	42	Cu_2SnS_3 tetragonal
250	0.6	500	250	41	17	42	Cu_2SnS_3 cubic, Cu_2SnS_4 orth, SnS orth
"	1.6	400	250	46	16	38	"
Target, unablated		-	-	36	19	43	-

[a] Thickness of ZnS films averaged to nearest 10 nm; thickness of Cu_2SnS_3 films averaged nearest 100 nm (due to droplets on Cu–Sn–S film surfaces, some parts of these films are thicker).

[b] 50% of the X-rays reaching the EDX detector come from this depth or less; emissions are averaged from Zn and S K-lines or, as appropriate, from Cu K-lines, Sn L-lines and S K-lines (15 keV electron excitation modeled by Casino [29]).

[c] Zn and Cu K-lines are used. Cu and Zn are overestimated in films thinner than the penetration depth of the electrons. The variation in measurements made on different films made under the same circumstances and on the same film measured on different days is approx. 1–2% absolute.

On close comparison to the data of Zanettini et al. [21], it is interesting to note that the highest optical band gap observed by Zanettini et al. is slightly higher than that observed here, and is closer to the direct electronic band gap of hexagonal-phase ZnS, which is 3.67 eV. This may reflect a difference between pulsed laser and pulsed electron deposition, with a clearer transition to the hexagonal phase already at 300 °C with pulsed electron deposition. This would parallel the observed difference in the X-ray diffraction patterns, where Zanettini et al. observe a change to a pattern that more closely matches the hexagonal phase at 300 °C.

The transmission spectrum of the Cu_2SnS_3 thin films deposited at different temperatures is shown in Fig. 4b. It is clear that the threshold of transmission increases with temperature and the data indicate that the optical band gap of the Cu_2SnS_3 films decreases with increasing deposition temperature from about 1.55 eV to 1.35 eV. The peak or shoulder at about 1.5 eV is possibly due to thin film interference. As the temperature increases, the value of the energy gap approaches those found in literature for cubic-phase Cu_2SnS_3 of about 1 eV. However, as noted earlier, the literature values for the optical band gap vary widely. The measured band gap of ~1.45 eV for the 150 °C film, which appears from its XRD pattern to be tetragonal-phase Cu_2SnS_3, is not far from the previously reported band gap of 1.35 eV for this phase [31]. The XRD patterns of the 250 °C films indicate that we do not have pure phase Cu_2SnS_3 at this temperature but rather a mix of phases and the optical band gap must therefore reflect a mix of the absorption of these different phases.

4. Conclusion

In this work we have shown that pulsed laser deposition of ZnS can result in a high deposition rate, with films most likely consisting of a mix of cubic and hexagonal phases. The film quality appears to improve with substrate temperature up to 300 °C: with increasing temperature the optical band gap approaches that of the direct band gap of cubic-phase ZnS while the X-ray diffraction pattern indicates an increasing crystalline fraction. These results are in close agreement with results from both pulsed laser deposition and pulsed electron deposition [5,21,23].

We have successfully used pulsed laser deposition to create films of Cu_2SnS_3 in the tetragonal phase at 150 °C, though more work is needed to confirm that the films are stoichiometric. These films are covered by particulates, but this issue can, for example, be reduced by applying a shorter wavelength, e.g. 248 nm, in the PLD-process [3]. At 250 °C the X-ray diffraction patterns indicate that Cu_4SnS_4 and SnS form in addition to cubic-phase Cu_2SnS_3. Energy dispersive X-ray spectroscopy shows that S and Sn content declines in the Cu_2SnS_3 films with increasing fluence. Further studies will cast more light on the secondary phases that may be formed within the range of conditions used to deposit the solar cell absorber material Cu_2ZnSnS_4. However, a complete analysis of the temperature dependence of the phase growth is not straightforward because of the many possible phases during film growth, which also may be promoted by the high kinetic energy of the arriving particles.

Acknowledgments

This work has been supported by a grant from the Danish Council for Strategic Research. The authors thank Jørgen Stubager for competent technical assistance.

References

[1] R.W. Eason (Ed.), Pulsed Laser Deposition of Thin Films, Wiley, Hoboken, NJ, 2007.
[2] J. Schou, Physical aspects of the pulsed laser deposition technique: the stoichiometric transfer of material from target to film, Appl. Surf. Sci. 255 (2009) 5191–5198.
[3] D.H. Lowndes, Laser ablation and desorption, in: J.C. Miller, R.F. Haglund (Eds.), Exp. Methods Phys. Sci., vol. 30, Academic Press, New York, 1998, pp. 475–571.
[4] C. Karner, P. Maguire, M. McLaughlin, S. Laverty, W.G. Graham, T. Morrow, et al., Pulsed-laser deposition of ZnS and SrS for ACTFEL and field-emission displays, in: Second Int. Conf. Sci. Technol. Disp. Phosphors, 1996.
[5] Z.-J. Xin, R.J. Peaty, H.N. Rutt, R.W. Eason, Epitaxial growth of high-quality ZnS films on sapphire and silicon by pulsed laser deposition, Semicond. Sci. Technol. 14 (1999) 695–698.
[6] J. Lanèok, M. Jelí, L. Jastrabí, L. Soukup, J. Oswald, K. Jurek, et al., Laser deposition of waveguiding Ti: sapphire and chalcogenide glass AsS films, in: Superf. Y Vacio, 1999, pp. 316–319.
[7] H. Ogura, K. Matsuishi, S. Onari, Raman scattering and photodarkening of amorphous $Ge(1-X)S(X)$ ($0<X<0.62$) films, J. Non-Cryst. Solids 270 (2000) 147–153.
[8] S. Canulescu, T. Lippert, A. Wokaun, R. Robert, D. Logvinovich, A. Weidenkaff, et al., Preparation of epitaxial $La0.6Ca0.4Mn1-xFe_xO_3$ ($x=00.2$) thin films: variation of the oxygen content, Prog. Solid State Chem. 35 (2007) 241–248.
[9] B. Thestrup, J. Schou, A. Nordskov, N.B. Larsen, Electrical and optical properties of thin indium tin oxide films produced by pulsed laser ablation in oxygen or rare gas atmospheres, Appl. Surf. Sci. 142 (1999) 248–252.
[10] H. Hiramatsu, H. Ohta, M. Hirano, H. Hosono, Heteroepitaxial growth of single-phase zinc blende ZnS films on transparent substrates by pulsed laser deposition under H_2S atmosphere, Solid State Commun. 124 (2002) 411–415.

[11] M. McLaughlin, H.F. Sakeek, P. Maguire, W.G. Graham, J. Molloy, T. Morrow, et al., Properties of ZnS thin films prepared by 248-nm pulsed laser deposition, Appl. Phys. Lett. 63 (1993) 1865.
[12] A. Cazzaniga, A. Crovetto, S. Canulescu, J. Schou, N. Pryds, O. Hansen, Thin films of CZTS for solar cells prepared by pulsed laser deposition, Appl. Phys. B, submitted for publication.
[13] B. Shin, O. Gunawan, Y. Zhu, N.A. Bojarczuk, S.J. Chey, S. Guha, Thin film solar cell with 8.4% power conversion efficiency using an earth-abundant Cu_2ZnSnS_4 absorber, Prog. Photovoltaics Res. Appl. 21 (2013) 72–76.
[14] S. Siebentritt, Why are kesterite solar cells not 20% efficient? Thin Solid Films 535 (2013) 1–4.
[15] P.J. Dale, K. Hoenes, J.J. Scragg, S. Siebentritt, A review of the challenges facing kesterite based thin film solar cells, in: 2009 34th IEEE Photovolt. Spec. Conf., 2009, pp. 002080–002085.
[16] N. Aihara, H. Araki, A. Takeuchi, K. Jimbo, H. Katagiri, Fabrication of Cu_2SnS_3 thin films by sulfurization of evaporated Cu-Sn precursors for solar cells, Phys. Status Solidi 10 (2013) 1086–1092.
[17] L.I. Berger, Properties of semiconductors, in: W.M. Haynes (Ed.), Handb. Chem. Phys., 95th ed., Taylor and Francis Group, LLT, 2014, pp. 80–85.
[18] J.T. Cox, G. Hass, Optical properties of zinc sulfide in the vacuum ultraviolet, J. Opt. Soc. Am. 49 (1959) 807–810.
[19] X. Wu, F. Lai, L. Lin, J. Lv, B. Zhuang, Q. Yan, et al., Optical inhomogeneity of ZnS films deposited by thermal evaporation, Appl. Surf. Sci. 254 (2008) 6455–6460.
[20] A. Abounadi, M. Di Blasio, D. Bouchara, J. Calas, M. Averous, O. Briot, et al., Reflectivity and photoluminescence measurements in ZnS epilayers grown by metal-organic chemical-vapor deposition, Phys. Rev. B 50 (1994).
[21] S. Zanettini, F. Bissoli, L. Nasi, P. Ranzieri, E. Gilioli, Low temperature pulsed electron deposition and characterization of ZnS films for application in solar cells, Cryst. Res. Technol. 46 (2011) 881–884.
[22] J.W. McCamy, D.H. Lowndes, J.D. Budai, R.A. Zuhr, X. Zhang, Epitaxial ZnS films grown on GaAs (001) and (111) by pulsed-laser ablation, J. Appl. Phys. 73 (1993) 7818.
[23] S. Yano, R. Schroeder, H. Sakai, B. Ullrich, Absorption and photocurrent properties of thin ZnS films formed by pulsed-laser deposition on quartz, Thin Solid Films 423 (2003) 273–276.
[24] H. Zhang, M. Xie, S. Zhang, Y. Xiang, Fabrication of highly crystallized Cu_2SnS_3 thin films through sulfurization of Sn-rich metallic precursors, J. Alloys Compd. 602 (2014) 199–203.
[25] D.M. Berg, R. Djemour, L. Gütay, S. Siebentritt, P.J. Dale, X. Fontane, et al., Raman analysis of monoclinic Cu_2SnS_3 thin films, Appl. Phys. Lett. 100 (2012) 192103.
[26] T. Nomura, T. Maeda, T. Wada, Preparation of narrow band-gap $Cu_2Sn(S, Se)_3$ and fabrication of film by non-vacuum process, Jpn. J. Appl. Phys. 52 (2013) 04CR08.
[27] H. Guan, H. Shen, C. Gao, X. He, Structural and optical properties of Cu_2SnS_3 and $CuSnS_4$ thin films by successive ionic layer adsorption and reaction, J. Mater. Sci.: Mater. Electron. 24 (2013) 1490–1494.
[28] M. Fox, Introduction, in: Opt. Prop. Solids, Oxford University Press, 2001, pp. 3.
[29] D. Drouin, A.R. Couture, D. Joly, X. Tastet, V. Aimez, R. Gauvin, CASINO V2.42: a fast and easy-to-use modeling tool for scanning electron microscopy and microanalysis users, Scanning 29 (2007) 92–101.
[30] A. Cazzaniga, R.B. Ettlinger, S. Canulescu, J. Schou, N. Pryds, Nanosecond laser ablation and deposition of silver, copper, zinc and tin, Appl. Phys. A 87 (2014) 89–92.
[31] P.A. Fernandes, P.M.P. Salomé, A.F. da Cunha, A study of ternary Cu_2SnS_3 and Cu_3SnS_4 thin films prepared by sulfurizing stacked metal precursors, J. Phys. D: Appl. Phys. 43 (2010) 215403.

Appendix B

Article: Formation of copper tin sulfide films by pulsed laser deposition at 248 and 355 nm

This article was published in Applied Physics A following the 2015 COLA conference. The article is briefly summarized and referenced in Chapter 7. Reprinted with permission.

Appl. Phys. A (2016) 122:466
DOI 10.1007/s00339-016-9939-4

Applied Physics A
Materials Science & Processing

Formation of copper tin sulfide films by pulsed laser deposition at 248 and 355 nm

Rebecca Bolt Ettlinger[1] · Andrea Crovetto[2] · Stela Canulescu[1] · Andrea Cazzaniga[1] · Lasse Ravnkilde[2] · Tomas Youngman[2] · Ole Hansen[2] · Nini Pryds[3] · Jørgen Schou[1]

Received: 16 October 2015 / Accepted: 23 February 2016 / Published online: 29 March 2016

Abstract The influence of the laser wavelength on the deposition of copper tin sulfide (CTS) and SnS-rich CTS with a 248-nm KrF excimer laser (pulse length $\tau = 20$ ns) and a 355-nm frequency-tripled Nd:YAG laser ($\tau = 6$ ns) was investigated. A comparative study of the two UV wavelengths shows that the CTS film growth rate per pulse was three to four times lower with the 248-nm laser than the 355-nm laser. SnS-rich CTS is more efficiently ablated than pure CTS. Films deposited at high fluence have submicron and micrometer size droplets, and the size and area density of the droplets do not vary significantly from 248 to 355 nm deposition. Irradiation at low fluence resulted in a non-stoichiometric material transfer with significant Cu deficiency in the as-deposited films. We discuss the transition from a non-stoichiometric material transfer at low fluence to a nearly stoichiometric ablation at high fluence based on a transition from a dominant evaporation regime to an ablation regime.

1 Introduction

Research in thin-film solar cells based on p-type semiconductors has mainly been focused on $Cu(In,Ga)(S,Se)_2$ (CIGS) and CdTe. However, due to the limited availability of elements such as In and Te and the toxicity of Cd, alternative absorbers such as Cu_2ZnSnS_4 (CZTS) are being investigated [1], and recently, a thin-film solar cell based on a CZTS absorber layer has reached an efficiency of 8.8 % [2]. Other p-type semiconductors with fewer elements are also available, including members of the ternary Cu–Sn–S system [3]. Among the Cu–Sn–S compounds, Cu_2SnS_3 (CTS) has been suggested as potential solar cell absorber because it has an absorption coefficient comparable to CZTS and a band gap of 0.9–1.35 eV depending on the crystal structure [4–6]. The highest efficiency of CTS solar cells of 4.65 % was achieved by thermal evaporation [7]. CTS thin films have also, more recently, been fabricated by pulsed laser deposition (PLD) [8]. Vanalakar

✉ Rebecca Bolt Ettlinger
reet@fotonik.dtu.dk

Andrea Crovetto
ancro@nanotech.dtu.dk

Stela Canulescu
stec@fotonik.dtu.dk

Andrea Cazzaniga
andcan@fotonik.dtu.dk

Lasse Ravnkilde
s122729@student.dtu.dk

Tomas Youngman
s123603@student.dtu.dk

Ole Hansen
ole.hansen@nanotech.dtu.dk

Nini Pryds
nipr@dtu.dk

Jørgen Schou
josc@fotonik.dtu.dk

[1] DTU Fotonik, Technical University of Denmark, Frederiksborgvej 399, 4000 Roskilde, Denmark

[2] DTU Nanotech, Technical University of Denmark, 2800 Kgs. Lyngby, Denmark

[3] DTU Energy, Technical University of Denmark, 4000 Roskilde, Denmark

et al. [9] have reported on the first CTS solar cell prepared by pulsed laser deposition with an efficiency of 0.82 %.

PLD is a suitable technique for the deposition of films with complex structures [10]. The presence of droplets (in some papers called particulates) in the growing films is a well-known problem, which can be addressed in a number of ways [11]. Particularly, droplets up to 1 micron in diameter or larger were observed in the films of CTS deposited by PLD [8, 9]. The influence of droplets on the overall efficiency of the solar cell is not well understood, but it is clear that it can be detrimental for the cell performance for the following reasons: (1) The droplet size can be larger than the overall thickness of the absorber layer, resulting in a rough interface and possible shunt paths between the CTS film and the subsequent solar cell layers [12], and (2) the droplets can have a different composition than the matrix of the CTS film [13, 14], resulting in non-homogeneity in composition and therefore different charge carrier transport properties.

Round droplets of micrometer or submicrometer size result from solidification of molten droplets ejected from the target by laser-induced recoil pressure or subsurface boiling [11]. A common approach to minimize droplets is to reduce the irradiation wavelength, as previously reported for Si [15], ZnO [16], and $YBa_2Cu_3O_{7-x}$ (YBCO) [17, 18] with comparisons of PLD using IR, visible, and UV laser wavelengths. Several mechanisms have been proposed to explain the better morphology of films deposited at UV wavelengths. First, the absorption depth (α^{-1}) in the material is usually short at UV wavelengths, resulting in a thin layer being ablated and thus formation of a hot plasma plume [17]. Second, if the absorption does not vary significantly with irradiation wavelength, droplet minimization may result from absorption of UV light by the droplets in the near-surface region, resulting in fragmentation down to a very small size. The second mechanism may be more dominant when comparing the morphology of films deposited at different UV wavelengths [17].

Apart from changing the laser wavelength, it is also known that a reduction in fluence can lead to a reduction in droplet area density and size [19]. A reduction in droplet density and size with a reduction of the fluence from 1.5 to 0.7 J/cm^2 has been seen in PLD of CZTS with a 248-nm laser by Moriya et al. [20] and with a reduction in fluence from 4 to 0.5 J/cm^2 on CZTS using a 355-nm laser by Sulaiman et al. [13]. Pawar et al. [21] also observed smaller and fewer droplets at 1 J/cm^2 than at 1.5 and 2 J/cm^2 using a 248-nm laser with CZTS. Similarly, Ujimoto et al. [22] observed a reduction in droplet density from 1.5 to 0.5 J/cm^2 using a 193-nm excimer laser to deposit $BiFeO_3$, while noting that in their case droplets could not be completely avoided simply by decreasing laser fluence.

The aim of this paper is to examine the influence of two different UV laser wavelengths on the deposition rate and the size, density, and composition of the droplets in films deposited by PLD from targets of CTS and SnS-enriched CTS. The SnS-rich composition was chosen for comparison because deficiency of Sn and S had previously been observed in CTS films deposited with 355-nm laser irradiation [8].

2 Materials and methods

2.1 Pulsed laser deposition

Pulsed laser deposition was carried out using a Nd:YAG laser operating at 355 nm (third harmonic) with a pulse duration of 5–7 ns and a KrF excimer laser operating at 248 nm with a pulse duration of 20 ns (see Fig. 1; Table 1). The depositions were made in vacuum at a pressure of 1–5 $\times$ 10^{-6} mbar. The target was placed at an angle of 45° with respect to the incoming laser beam, and the beam was rastered across the target. The substrate material was Mo-coated soda-lime glass, which is typically used for CTS solar cell preparation. The fluence was varied from 0.2 to 2.3 J/cm^2 and was calculated based on a measurement of the spot size on a Cu foil. The substrate–target distance was 4–4.5 cm due to constraints in the setups for ensuring similar deposition conditions. Films made using the 355 nm laser with target–substrate distances ranging from 4 cm to 7.5 cm were similar in composition and droplet density (not shown), as expected for depositions made in vacuum [19].

Single samples were made at different fluence values and spot sizes. The representativeness of the single samples was verified by repeated depositions of some of the films under identical circumstances. With the 355-nm laser and

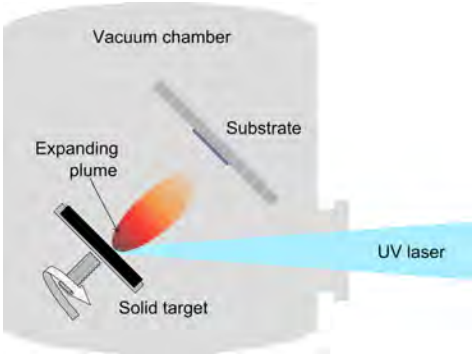

Fig. 1 Setup. See Table 1 for comparison of the 248 and 355 nm setups

Table 1 Laser and setup comparison

Wavelength (λ)	248 nm	355 nm
Laser type	KrF excimer	Nd:YAG solid-state
Pulse width (ns)	20	5–7
Frequency (Hz)	10	10
Target–substrate distance (cm)	4	4–4.5[a]
Spot size (mm^2)	2.2 ± 0.1[a]	2.2 ± 0.1[a]
Fluence range (J/cm^2)	0.2–2.1	0.2–2.4
Duration of deposition (min)	45–94	20–180

[a] All measurements with the quartz crystal microbalance were made with a target–substrate distance of 4 cm and a spot size of 2.2 ± 0.1 mm^2. The films at low fluence (0.2–0.5 J/cm^2) were made with a larger spot size (up to 5 ± 0.2 mm^2) in order to make a relatively thick film within a reasonable amount of time

the SnS-rich CTS target, nine films were made under exactly the same circumstances, confirming that the deposition rate, droplet density (appearance in SEM), and composition were reproducible. With the non-SnS-enriched CTS target, films made at 1.6 J/cm^2 were reproduced with both lasers and it was confirmed that samples produced under the same circumstances were similar regarding thickness, droplet density, and composition.

The number of pulses at the two different wavelengths was adjusted to deposit films sufficiently thick for reliable energy-dispersive X-ray spectroscopy (EDX) at most fluences. According to the model CASINO [23], 99 % of the EDX signal for CTS derives from below 900 nm thickness and 90 % from below 750 nm, assuming a smooth surface and a bulk density of 5.02 g/cm^3 for Cu_2SnS_3 [24].

Multicomponent targets of CTS and SnS-rich CTS were purchased from PVD products. The targets named "CTS" in the present work had a Cu:Sn:S ratio of about 2:1:2.5 (measured by EDX; see Table 2), while the one called "SnS-rich CTS" had a Cu:Sn:S ratio of about 1:2:3. The targets consisted of multiple crystalline phases identified by XRD including Cu_2SnS_3 (tetragonal, JCPDS 89-4714), SnS (cubic, JCPDS 89-2755, and orthorhombic, JCPDS 75-1803), CuS (cubic, JCPDS 78-877), and Cu_2S (cubic, JCPDS 53-522). EDX mapping of the targets showed regions of hundreds of micrometers in diameter with either Cu-rich composition, Sn-rich composition, or a mixture of different phases.

2.2 Characterization

The deposition rates were measured with quartz crystal microbalances (QCM, Colnatec, Inc) and converted to film thickness, assuming a bulk density of 5.02 g/cm^3 for both Cu_2SnS_3 and SnS-rich CTS (the bulk density of SnS of 5.08 g/cm^3 is similar to that of CTS) [24, 25]. The targets were pre-ablated by 15.000–18.000 pulses before the measurement of the deposition rate in order to ensure a stable deposition. As shown in Table 1, the ablation parameters were similar for the comparison of the deposition rate between the different wavelengths. The deposition rates measured by QCM were systematically larger (by about 20–30 %) than the deposition rates determined from thickness measurements of films made at different fluence values (data not shown). This was most likely due to the measurement method: In SEM, the measurement excluded droplets sticking up above the film surface, while Dektak measurements are not highly accurate for surfaces with a high density of micrometer-scale droplets.

X-ray diffraction (XRD) measurements were carried out with a Bruker D8 diffractometer in Bragg–Brentano configuration using Cu K_α and Cu K_β radiation. The diffraction pattern of the as-deposited films was measured using a step size of 0.03° and a rate of 0.33 step/s.

Scanning electron microscopy was performed at 5–15 kV using the in-lens and secondary electron detectors of two SEMs equipped with field emission guns (FE-SEM, Supra 60VP and Supra 35, Zeiss). The droplet size distributions were determined by processing SEM images of 20 × 30 µm size with image analysis software (ImageJ). The droplets were discriminated from the homogeneous

Table 2 Composition of the CTS target and selected films deposited at room temperature

	Fluence (J/cm^2)	Spot size (mm^2)	Thickness (nm)	Cu (%)	Sn (%)	S (%)	Cu/Sn
CTS target	–	–	–	38.6 ± 1.0	17.1 ± 1.0	44.4 ± 0.3	2.3 ± 0.5
355-nm laser	1.6	2.5	1500	43.3 ± 0.4	18.7 ± 0.5	38.1 ± 0.1	2.3 ± 0.1
	0.5	5	1000	28.8 ± 0.5	25.8 ± 0.5	45.5 ± 0.1	1.1 ± 0.1
	0.2	3.3	1200	27.4 ± 0.7	25.3 ± 0.3	47.3 ± 0.5	1.1 ± 0.1
248-nm laser	1.6	2.2	850–900	38.9 ± 0.6	19.3 ± 0.2	41.8 ± 0.6	2.0 ± 0.1
	0.5	5	800	11.1 ± 1	29.2 ± 2.1	59.8 ± 2.3	0.4 ± 0.1
	0.2	4	450	*ND*	*ND*	*ND*	*ND*

Uncertainties are the standard error of repeated measurements with the same instrument. The standard error on the Cu/Sn ratio is calculated, assuming that the Cu and Sn content are fully anti-correlated. All the film measurements in this table were made with the Bruker detector

film using a semiautomatic procedure with the signal intensity contrast as selection criterion and the area of each droplet was calculated automatically. Energy-dispersive X-ray spectroscopy (EDX) was performed at 15 kV in a Hitachi TM3000 tabletop SEM using a built-in Bruker detector with Quantax 70 software that performed mapping and quantification of the element ratios with Cu K-lines. Additional EDX measurements were performed in the Supra 60VP SEM with a silicon drift detector (X-Man^N 50, Oxford Instruments), which allowed measurement on specific areas identified in SEM images of the films including individual droplets. From the Supra/X-Man^N 50 data, element ratios were calculated by Oxford Instrument's Aztec software using the Cu K-lines and deconvoluting any Mo contribution to the S peak.

3 Results

3.1 Deposition rates

The deposition rate of CTS and SnS-rich CTS as a function of laser fluence is shown in Fig. 2. At any given fluence, the deposition rate of CTS and SnS-rich CTS at 355 nm is three to four times higher than at 248 nm.

Two main factors may explain the difference in deposition rate between the two lasers. Firstly, the effective intensity at 248 nm (1.2×10^8 W/cm^2) was about three times lower than at 355 nm (3.8×10^8 W/cm^2) due to the longer pulse duration at 248 nm. Secondly, the photon energy of 5 eV (corresponding to 248 nm) and 3.5 eV (corresponding to 355 nm) is much larger that the band gap energy of the constituent phases of the target, which was mainly composed of SnS, CuS, Cu_2S, and tetragonal-phase Cu_2SnS_3 (see Sect. 2.1) [4, 26, 27]. However, it is possible that the absorption coefficient of the individual phases varies from 248 to 355 nm even though the photon energies are greater than the band gap energy. For example, for a mixture of the two related phases, cubic-phase and monoclinic-phase Cu_2SnS_3, the absorption coefficient was found to vary by a factor 3 from 1.6×10^5 cm^{-1} at 3.5 eV to 4.3×10^5 cm^{-1} at 5 eV [28]. For SnS, the absorption coefficient varies less between the two wavelengths (both approx. 1×10^6 cm^{-1} as estimated from plots of the dielectric functions) [29]. The variation in the absorption coefficient means that the light penetration depth may vary from phase to phase in the target. Overall, the lower deposition yield at 248 nm compared to 355 nm probably may be attributed to the lower laser intensity, possibly in combination with a smaller light penetration depth in some of the phases in the target.

Figure 2 furthermore shows that the deposition of SnS-rich CTS (Cu:Sn:S 1:2:3) was faster than the deposition of CTS (Cu:Sn:S 2:1:2.5), independent of the irradiation wavelength. This is expected since both S and SnS have a higher vapor pressure than the copper-containing phases in the target [30, 31]. An increase in the concentration of high vapor pressure components in the target results in a higher ablation yield [10, 11].

3.2 Droplets

SEM images of several CTS and SnS-rich CTS films deposited at a laser fluence of 0.2–1.8 J/cm^2 are shown in Fig. 3a–f. The surface of the films is covered with large circular droplets ranging from tens of nanometers to

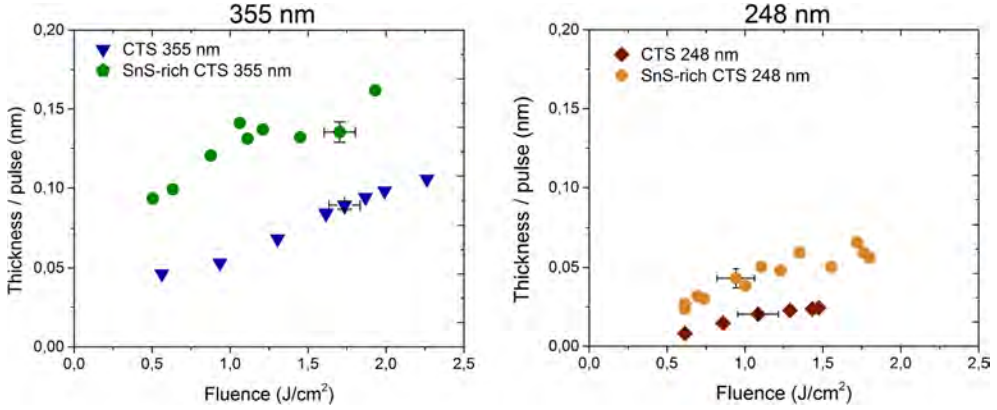

Fig. 2 Deposition rates of CTS and SnS-rich CTS at 355 nm (Nd:YAG laser, $\tau = 6$ ns) and 248 nm (KrF laser, $\tau = 20$ ns). The estimated error is similar for all the measurements, increasing proportionally with the fluence. Due to constraints in the 248 nm setup, it was not possible to measure the deposition rate at higher fluence without changing the spot size

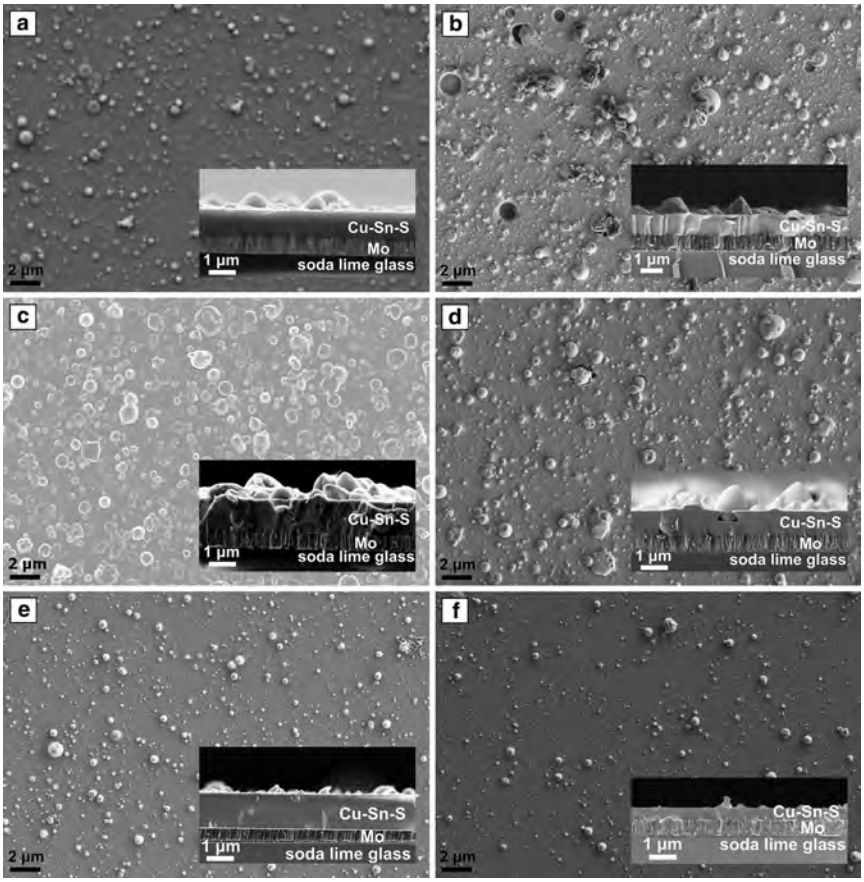

Fig. 3 SEM images (*top* and *side view*) of as-deposited films on Mo-coated soda-lime glass made at room temperature with 355 nm (**a**, **c**, **e**) and 248 nm (**b**, **d**, **f**) laser pulses. **a** 355 nm SnS-rich CTS 1.4 J/cm^2, **b** 248 nm SnS-rich CTS 1.8 J/cm^2, **c** 355 nm CTS 1.6 J/cm^2, **d** 248 nm CTS 1.6 J/cm^2, **e** 355 nm CTS 0.2 J/cm^2, **f** 248 nm CTS 0.2 J/cm^2 (note that this film was not used for EDX as it was too thin). While the 355-nm film shown in (**a**) was made at 1.4 J/cm^2, this film was highly similar to a series of films made at 2.3 J/cm^2 by the same laser. Image (**c**) was taken with the backscattered electron detector, while the others were taken with the more surface-sensitive secondary electron detectors

several microns in diameter. Our findings indicate that at a given fluence, the surface morphology of the as-deposited CTS films does not vary significantly from 355 to 248 nm. On the other hand, a decrease in the laser fluence to 0.2 J/cm^2 results in a decrease in the size and density of the droplets at both wavelengths (Fig. 3e–f).

The size distribution of the droplets extracted from SEM images in Fig. 3c–f is shown in Fig. 4. Note that we could not accurately identify small (<200 nm) particulates nor overlapping droplets by this method. The incidence of large droplets is also determined with a considerable uncertainty in the histograms as they were relatively rare. Nonetheless, Fig. 4 shows that there is no reduction in droplet area density for the 248-nm laser compared to the 355-nm laser. At high laser fluence, the distribution profile is broad, while at low fluence, the average size of the droplets decreases. The data suggest that the size and density of the droplets are strongly dependent on the laser energy and, for a given fluence, less dependent on the UV irradiation wavelength. This will be discussed in Sect. 4.

No diffraction peaks were observed beside Mo and MoO_x in X-ray diffractograms of the as-deposited films,

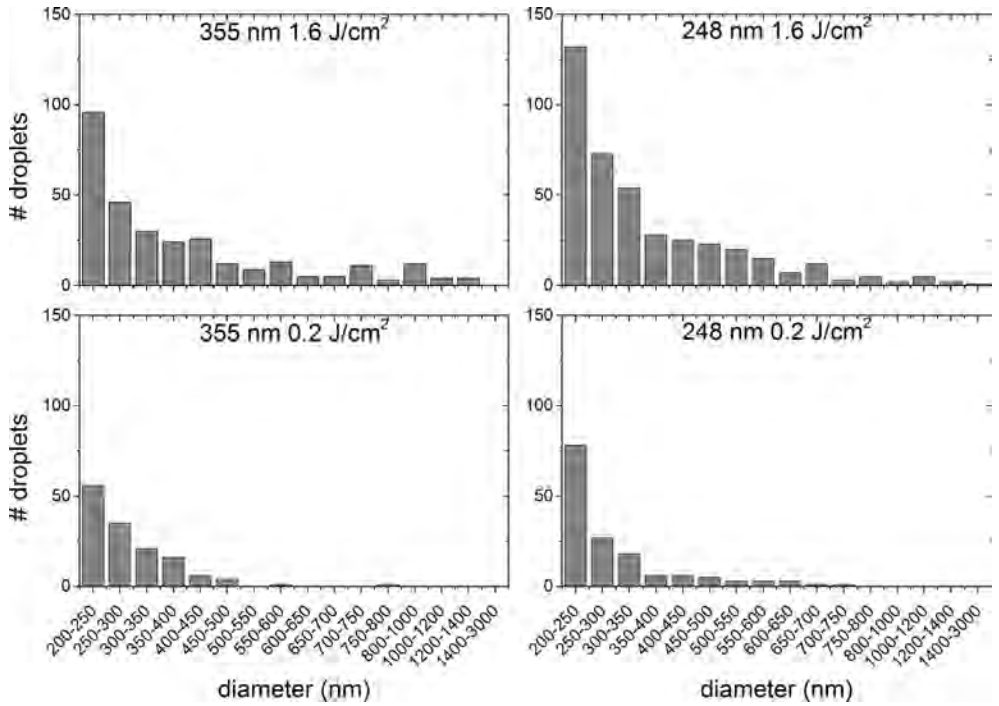

Fig. 4 Distribution of droplet size at 0.2 and 1.6 J/cm^2 with the 355- and 248-nm laser in a film made from the non-SnS-enriched target. Smaller droplets were present but could not be accurately quantified with the image processing software. Large droplets were rare and are therefore not accurately portrayed in the histograms

indicating that the films were mostly amorphous (X-ray data not shown).

3.3 Composition

Sulfur content The CTS films deposited at high fluence (1.5–1.6 J/cm^2) show S deficiency, and the deficiency appears to be larger at 355 nm than at 248 nm (Table 2). In contrast, the S content increased markedly in the films made at low fluence (0.5 J/cm^2 with the 355 nm and 0.2 J/cm^2 with the 248-nm laser). Thus, the S content increased from S/(Cu + Sn) = 0.8 ± 0.2 in the target to S/(Cu + Sn) = 1.5 ± 0.6 in the film made at 0.5 J/cm^2 by the 248-nm laser.

Metal content The Cu/Sn ratio of the target is maintained within the error bar in the CTS films made at 1.6 J/cm^2 by the 355-nm laser (Table 2). In comparison, the CTS film deposited at 248 nm at a similar fluence has a somewhat lower Cu concentration, though still within the error bar. The low-fluence depositions resulted in CTS films with a significant Cu deficiency at both wavelengths. The Cu/Sn ratio varies from 1.1 ± 0.1 for films made at 0.2–0.5 J/cm^2 at 355 nm to only 0.4 ± 0.1 for a film made at 0.5 J/cm^2 at 248 nm. These values should be compared with the Cu/Sn ratio in the target of 2.3 ± 0.5. As a general trend, we observe that as the incident laser energy is reduced, incongruent evaporation becomes dominant, and the Cu content in the as-deposited films decreases progressively (see Sect. 4). We have previously reported a similar but less dramatic increase in the S and Sn content of films made at low fluence with the 355-nm laser [8].

Composition of SnS-rich films The composition of the SnS-rich films does not vary much for films made at fluences between 0.7 and 2.3 J/cm^2 with the 355-nm laser or for films made at 1–1.8 J/cm^2 for the 248-nm laser (data not shown). In general, the films appear S- and Sn-poor compared to the target, but highly Sn-rich (Cu/Sn ~0.6) as well as somewhat S-poor compared to the desired stoichiometry of Cu_2SnS_3.

Composition of droplets The chemical composition versus the diameter of the droplets of the CTS films deposited at 1.6 J/cm^2 at 248 nm is shown in Fig. 5. EDX measurements

were carried out on a random selection of individual droplets with an average diameter larger than 1 μm. Figure 5 shows a significant deficiency of S and Sn and, consequently, enrichment of Cu in the Cu–Sn–S droplets. Despite the scattering of the data due to the relatively high uncertainty of the EDX analysis, we note that the deficiency of S and Sn increases as the droplet size decreases. The underlying film denoted by the "matrix" in Fig. 5 shows enrichment in the Sn content relative to the average target composition, which may derive from Sn loss from the droplets or from more efficient ablation of the Sn-rich phases in the target compared to the Cu-rich phases. The underlying film matrix is still slightly S deficient relative to the target, suggesting that sulfur losses occur both by evaporation from the film and by sulfur-deficient droplet solidification into the film.

It should be noted that the spot size was increased from 2.2 to 5 mm^2 in order to deposit films at low fluence due to the low deposition rate. The change in spot size may have had some influence on the off-axis composition, as the ablation plume becomes more forward-directed when the spot size is increased. However, we have in the present work considered the on-axis composition.

4 Discussion

Our ablation studies of CTS and SnS-rich CTS films indicate that the number of droplets is significantly reduced at lower laser fluence, while the irradiation wavelength does not significantly influence the surface morphology of the as-deposited CTS films. We observe a reduction in the average size of the droplets at low laser fluence accompanied by a change to non-stoichiometric material transfer with an increase in the S and Sn content. This trade-off

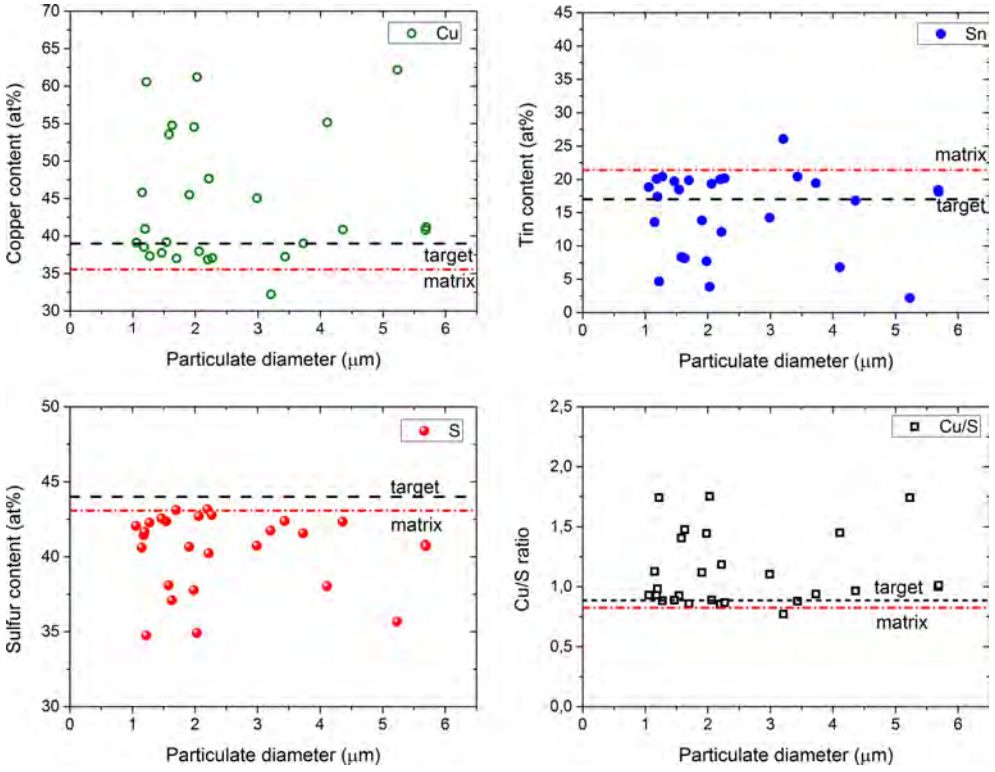

Fig. 5 Compositional analysis of the droplets as a function of droplet diameter for a film made from the non-SnS-enriched CTS target at 1.6 J/cm^2 at 248 nm (note that this target was Cu-rich and S-poor relative to the ideal composition as measured by our EDX analysis; see also Table 2). The Cu, Sn, S content, as well as the Cu/S ratio are given for a random selection of droplets with an average diameter larger than 1 μm. The composition of the target is indicated as "target", while the composition of the underlying film is indicated by "matrix"

between congruent material transfer and the amount of droplets on the films depending on fluence was previously mentioned in the literature, e.g., by Lowndes [11].

An incongruent transfer at low fluence has been observed for other materials (e.g., $SrTiO_3$ [32, 33] and YBCO [34]), and different explanatory models have been offered [11, 33, 34]. Venkatesan et al. [34] pointed out that the non-stoichiometric transfer of the material in the low-fluence regime is correlated with preferential evaporation of the elements with high vapor pressure and low cohesive energy in the multicomponent target. In the case of CTS, Cu has a higher cohesive energy (3.5 eV/atom) than Sn (3.12 eV/atom) (Table 3) [35]. While the cohesive energy of atoms in alloys has only been investigated by a few groups, alloyed atoms nevertheless show a cohesive energy similar to the pure elements [10]. Therefore, it may be expected that in the evaporative regime, the CTS films are Cu-deficient, as seen in the low-fluence films, as this is the least volatile element and thus the most difficult one to ablate.

In the high-fluence regime, ablation results in a distribution of droplets of the order of micrometer size embedded in the CTS films, independent on the irradiation wavelength. In this regime, the transfer of the ablated material is nearly stoichiometric. The films deposited at 355 nm are slightly Cu- and Sn-rich, while the films deposited at 248 nm are slightly Cu-poor. The lower Cu content of the 248-nm films may be linked to the lower intensity of the 248-nm laser pulses, since this would lead to a higher evaporative component for a given fluence. Interestingly, Kautek et al. [18] saw a similar trend in YBCO films made at 266 and 355 nm: The element transfer was incongruent at somewhat higher fluence at 266 nm than at 355 nm, even though in their experiment, both lasers had the same pulse length.

Our observation of a transition from a Cu-poor to a Cu-rich regime with increasing fluence with the 355-nm laser is similar to the transition from Sr-rich to Ti-rich $SrTiO_3$ seen by Ohnishi et al. [32] with increasing fluence. For the deposition of a bimetallic material in an oxygen background gas, it was possible for Onishi et al. to identify a fluence that perfectly balanced the Sr:Ti ratio. In contrast, for the tri-component chalcogenide CTS, it may be that no fluence exists that ensures perfectly stoichiometric transfer. However, we see that it is possible tune the ratio of Sn to Cu by fluence adjustment and to compensate for any S deficiency using a post-deposition sulfurization step, as performed for CZTS films by Moriya et al. [20].

Table 3 Cohesive energy and temperature at which the vapor pressure is 1 Pa for the constituent elements of CTS as well as SnS and Cu_2SnS_3

	Cohesive energy (eV/atom) [35]	Temperature at which the vapor pressure is 1 Pa (°C)
Cu	3.5	963 [31]
Sn	3.12	951 [31]
S	2.86	102 [31]
SnS	NA	590 [38, 39]
Cu_2SnS_3	NA	higher than SnS [30]

Detailed characterization of the droplets embedded in the CTS film deposited at 1.6 J/cm^2 at 248 nm reveals a large depletion in S and Sn relative to Cu in the droplets. The degree of depletion increases with decreasing droplet size. Sulaiman et al. [13] have observed that both Cu- and Sn-rich droplets were transferred onto films of CZTS made by PLD at 355 nm without a detailed qualitative analysis. Chen and Hall [14] have shown that in binary metallic systems of Nb–Al and Nb–Cr, the droplets are usually deficient in the element with high vapor pressure and the deficiency of the volatile elements increases with decreasing droplet size. In the Cu–Sn–S system, the vapor pressure of Cu and Sn is much lower than that of S (see Table 3). As a result, preferential evaporation of S is likely and would result in Cu- and Sn-rich droplets. However, the EDX analysis indicates a deficiency of Sn in the solidified molten droplets in addition to an S deficiency. Since SnS is far more volatile than Sn (Table 3), it is likely that the Sn deficiency is caused by the evaporation of SnS, as proposed by Weber et al. [30] in an investigation of Sn loss from heated films of CZTS.

We do not see a droplet reduction with a change between the two UV laser wavelengths 355 and 248 nm. As described in the introduction, droplet reduction might have been expected if the target absorption of the 248-nm laser was higher than the 355-nm laser so that subsurface boiling would be reduced, or if the 248 nm light was able to more efficiently break up the ejected droplets. As discussed in Sect. 3.1, the absorption of different UV wavelengths in the target is not easily predicted, and the increased photon energy at 248 nm may be offset by the longer pulse length, leading to a lower pulse power. The combined effect of the differences between the lasers in wavelength and pulse length seems to have little influence on this particular material.

For the fabrication of the thin-film absorber layers of CTS for thin-film solar cells, it is desirable to have Cu-poor films [36] and a uniform composition. Since the composition of the droplets can be different to the underlying film, it is important to minimize their occurrence. We observe that splashing and associated Cu-rich droplets can be minimized by reducing the fluence, although the droplet reduction has to be balanced against the appropriate composition. Additional strategies to reduce droplets are to use off-axis deposition, a mechanical velocity filter, or a voltage across the ablation plume [11, 19]. However, these

methods mean that the deposition process becomes far more complex.

5 Conclusion

We have reported on the fabrication of copper tin sulfide (CTS) and SnS-rich CTS thin films in vacuum for two UV wavelengths, 355 and 248 nm. The deposition rate was about four times higher at 355 nm than at 248 nm for both CTS and SnS-rich CTS. The morphology studies of the as-deposited films showed that the area density of the droplets was not reduced by increasing the photon energy from 355 to 248 nm.

For both lasers, the laser fluence significantly affects the density and average size of the droplets. At high fluence (1.6 J/cm^2), UV irradiation leads to near-congruent transfer of the ablated material. Droplets produced by the 248-nm KrF-excimer laser ablation at high fluence were mainly S- and Sn-poor, and the deficiency seemed more pronounced with decreasing droplet size. A reduction in the laser fluence down to 0.2 J/cm^2 resulted in smaller droplets and lower droplet area density for both lasers.

The low-fluence regime leads to incongruent evaporation of films with typically large copper deficiency and therefore films that were S- and Sn-rich relative to the target. The Cu deficiency was most pronounced for the 248-nm laser, possibly due to the lower intensity of the 248-nm laser pulses.

Films deposited by either laser from the SnS-rich CTS target were Sn-rich relative to the desired composition for solar cell absorber layers. Films deposited from the CTS target at 1.6 J/cm^2 by either laser were somewhat Cu-rich for solar cells (we found Cu/Sn $\sim$ 2.0 compared to Cu/Sn $\sim$ 1.7–1.9 in successful solar cells [36, 37]). However, by reducing the fluence somewhat, it will be possible to reach the optimal Cu/Sn ratio with both the 248- and the 355-nm laser.

Overall, our study illustrates the commonly observed trade-off in PLD between reduction in the droplet density and change in the composition with a reduction in the laser fluence.

Acknowledgments This work has been supported by a grant from the Danish Council for Strategic Research.

References

1. D.B. Mitzi, O. Gunawan, T.K. Todorov, D.A.R. Barkhouse, Philos. Trans. R. Soc. A **371**, 20110432 (2013)
2. S. Tajima, T. Itoh, H. Hazama, K. Ohishi, R. Asahi, Appl. Phys. Express **8**, 082302 (2015)
3. T.A. Kuku, O.A. Fakolujo, Sol. Energy Mater. **16**, 199 (1987)
4. P.A. Fernandes, P.M.P. Salomé, A.F. da Cunha, Phys. Status Solidi C **7**(3–4), 901 (2010)
5. P. Zawadzki, L.L. Baranowski, H. Peng, E.S. Toberer, D.S. Ginley, W. Tumas, A. Zakutayev, S. Lany, Appl. Phys. Lett. **103**, 253902 (2013)
6. N. Aihara, H. Araki, A. Takeuchi, K. Jimbo, H. Katagiri, Phys. Status Solidi C **10**, 1086 (2013)
7. M. Nakashima, J. Fujimoto, T. Yamaguchi, M. Izaki, Appl. Phys. Express **8**, 042303 (2015)
8. R.B. Ettlinger, A. Cazzaniga, S. Canulescu, N. Pryds, J. Schou, Appl. Surf. Sci. **336**, 385 (2015)
9. S.A. Vanalakar, G.L. Agawane, A.S. Kamble, C.W. Hong, P.S. Patil, J.H. Kim, Sol. Energy Mater. Sol. Cells **138**, 1 (2015)
10. J. Schou, Appl. Surf. Sci. **255**, 5191 (2009)
11. D.H. Lowndes, in *Laser Ablation Desorption, Experimental Methods in the Physical Sciences*, vol. 30, ed. by J.C. Miller, R.F. Haglund (Academic Press, New York, 1998), pp. 475–571
12. K. Ito, in *Copper Zinc Tin Sulfide-Based Thin Film Solar Cells*, 1st edn., ed. by K. Ito (Wiley, Chichester, West Sussex, 2015), pp. 34–35
13. N.S. Che Sulaiman, C.H. Nee, S.L. Yap, Y.S. Lee, T.Y. Tou, S.S. Yap, Appl. Surf. Sci. **354**, 42 (2015)
14. L.-C. Chen, E.L. Hall, Mater. Res. Soc. Symp. Proc. **285**, 519 (1993)
15. W.O. Siew, S.S. Yap, C. Ladam, Ø. Dahl, T.W. Reenaas, T.Y. Tou, Appl. Phys. A **104**, 877 (2011)
16. N.J. Ianno, L. McConville, N. Shaikh, S. Pittal, P.G. Snyder, Thin Solid Films **220**, 92 (1992)
17. G. Koren, A. Gupta, R.J. Baseman, M.I. Lutwyche, R.B. Laibowitz, Appl. Phys. Lett. **55**, 2450 (1989)
18. W. Kautek, B. Roas, L. Schultz, Thin Solid Films **191**, 317 (1990)
19. L.-C. Chen, in *Pulsed Laser Deposition. Thin Film*, 1st edn., ed. by D.B. Crisey, G.K. Hubler (Wiley, New York, 1994), pp. 167–198
20. K. Moriya, K. Tanaka, H. Uchiki, Jpn. J. Appl. Phys. **47**, 602 (2008)
21. S.M. Pawar, A.V. Moholkar, I.K. Kim, S.W. Shin, J.H. Moon, J.I. Rhee, J.H. Kim, Curr. Appl. Phys. **10**, 565 (2010)
22. K. Ujimoto, T. Yoshimura, A. Ashida, N. Fujimura, Jpn. J. Appl. Phys. **52**, 045803 (2013)
23. D. Drouin, A.R. Couture, D. Joly, X. Tastet, V. Aimez, R. Gauvin, Scanning **29**, 92 (2007)
24. L.I. Berger, in *CRC Handbook of Chemistry and Physics*, 96th edn., ed. by W.M. Haynes, T.J. Bruno, D.R. Lide (CRC Press, Boca Raton, 2015), pp. 12-80–12-93
25. W.M. Haynes, T.J. Bruno, D.R. Lide (eds.), *CRC Handbook of Chemistry and Physics*, 96th edn. (CRC Press, Boca Raton, 2015), pp. 4–43–4–101
26. L.A. Burton, D. Colombara, R.D. Abellon, F.C. Grozema, L.M. Peter, T.J. Savenije, G. Dennler, A. Walsh, Chem. Mater. **25**, 4908–4916 (2013)
27. O. Madelung, U. Rössler, M. Schulz (eds), *Springer Materials Series Landolt-Börnstein - Gr. III Condensed Matter, Subvolume 41C, Non-tetrahedrally Bonded Elements and Binary Compounds I* (Springer, Berlin, 1998), pp. 1–2
28. A. Crovetto, R. Chen, B. Ettlinger, A.C. Cazzaniga, J. Schou, O. Hansen, C. Persson (2016) (submitted)
29. O. Madelung, U. Rössler, M. Schulz (eds.), *Non-tetrahedrally Bonded Elements and Binary Compounds I* (Springer, Berlin, 1998), pp. 1–8
30. A. Weber, R. Mainz, H.W. Schock, J. Appl. Phys. **107**, 013516 (2010)
31. W.M. Haynes, T.J. Bruno, D.R. Lide (eds.), *CRC Handbook of Chemistry and Physics*, 96th edn. (CRC Press, Boca Raton, 2015), pp. 6-88–6-116

32. T. Ohnishi, T. Yamamoto, S. Meguro, H. Koinuma, M. Lippmaa, J. Phys. Conf. Ser. **59**, 514 (2007)
33. B. Dam, J.H. Rector, J. Johansson, J. Huijbregtse, D.G. De Groot, J. Appl. Phys. **83**, 3386 (1998)
34. T. Venkatesan, X.D. Wu, A. Inam, J.B. Wachtman, Appl. Phys. Lett. **52**, 1193 (1988)
35. C. Kittel, *Introduction to Solid State Physics*, 3rd edn. (Wiley, New York, 1966) p. 78
36. A. Kanai, K. Toyonaga, K. Chino, H. Katagiri, H. Araki, Jpn. J. Appl. Phys. **54**, 08KC06 (2015)
37. M. Nakashima, T. Yamaguchi, H. Itani, J. Sasano, M. Izaki, Phys. Status Solidi C **12**, 761 (2015)
38. B. Richards, Trans. Faraday Soc. **51**, 1193 (1955)
39. V. Piacente, S. Foglia, P. Scardala, J. Alloys Compd. **177**, 17 (1991)

Appendix C

Conference Proceedings: Pulsed laser deposition of Cu-Sn-S for thin film solar cells

This text was included in the proceedings of the WCPEC-6 conference in Kyoto, Japan, November 2014, at which I presented a poster on the same topic (deposition and annealing of CTS for solar cells). Note that Fig. 2 erroneously quantifies the composition of the annealed films, which turned out to have a composition gradient across the film thickness and therefore could not reliably be measured by EDX. The subject of the proceedings article is treated in Section 7.3.

Pulsed laser deposition of Cu-Sn-S for thin film solar cells

Rebecca Bolt Ettlinger[1], Andrea Crovetto[2], Edoardo Bosco[2], Philip Rasmussen[2], Ole Hansen[2] and Jørgen Schou[1]
1. Department of Photonics Engineering, Technical University of Denmark, DK-4000 Roskilde, Denmark
2. Department of Nanotechnology, Technical University of Denmark, DK-2800 Lyngby, Denmark

ABSTRACT

Thin films of copper tin sulfide were deposited from a target of the stoichiometry Cu:Sn:S ~1:2:3 using pulsed laser deposition (PLD). Annealing with S powder resulted in films close to the desired Cu_2SnS_3 stoichiometry although the films remained Sn rich. X-ray diffraction showed that the final films contained both cubic-phase Cu_2SnS_3 and orthorhombic-phase SnS.

1. INTRODUCTION

The ternary chalcogenide Cu_2SnS_3, like the more widely researched material Cu_2ZnSnS_4 (CZTS), can be used as the absorber layer of thin film solar cells [see, e.g, 1, 2]. Pulsed laser deposition is a well-recognized deposition method for compound materials and several groups have used it to deposit CZTS [see, e.g., 3]. We have deposited Cu_2SnS_3 at temperatures below 300 ºC, where, however, a number of secondary phases formed. A loss of S and Sn is anticipated with higher deposition or annealing temperature, as needed to obtain good crystal quality [1, 2]. Therefore a Sn and S enriched target was used to deposit precursor films, which were annealed with S powder. The resulting films contain cubic-phase Cu_2SnS_3 with a stoichiometry near the desired Cu:Sn:S ratio of 2:1:3.

2. METHODS

2.1 Pulsed laser deposition

Pulsed laser deposition was done using a 355 nm Nd:YAG laser with 5-7 ns pulses at 10 Hz. The laser beam was rastered across a rotating target in vacuum ($p < 5*10^{-6}$ mbar) and the ablated material was deposited on substrates placed 4.5 cm from the target (Fig. 1); the substrates were fused silica or molybdenum- coated soda-lime glass (Mo/SLG). All depositions took place at room temperature. The target was a sintered pellet of copper and tin sulfides (PVD products). The laser spot size was 2.5 mm^2, the fluence varied from 0.7-2.8 J/cm^2, and the film thickness varied from ~1300 nm to ~4200 nm. Annealing was done with S powder in a graphite box held inside a quartz tube with >100 mbar N_2. The temperature was ramped to 500 ºC at 12 ºC/min, then to 570 ºC at 1 ºC/min. It remained above 570 ºC for 10 min, reaching a maximum of 580 ºC, after which the system cooled naturally.

2.2 Characterization

Scanning electron microscopy was performed at 5 keV using the secondary electron detector of a SEM equipped with a field emission gun (FE-SEM, Supra 60VP, Zeiss). Energy dispersive X-ray spectroscopy (EDX) was performed in this SEM using a silicon drift detector (X-Man^N 50, Oxford Instruments) and a beam voltage of 15 kV. On films, full area scans were made at 1000x magnification; on targets, 250x magnification was used. Several measurements were averaged for each sample. The element ratios were calculated using Cu K-lines with Oxford Instruments' Aztec software. When the Mo contribution to the S peak was detectable, the Mo peak was deconvoluted from the spectrum.

X-ray diffraction was done in Bragg-Brentano mode with a Bruker D8 powder diffractometer using a step size of 0.01° and a measurement interval of 1.5 s/step. $K_{\alpha 2}$ radiation was subtracted from the data using the program EVA. The diffraction peaks were identified manually and matched to JCPDS files.

3. RESULTS

3.1 Morphology

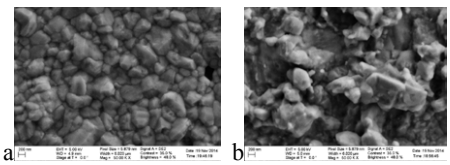

Fig. 1 SEM images of annealed Cu-Sn-S films on Mo/SLG. **a**: deposited at 2.2 J/cm2, precursor ~1320 nm thick; **b**: deposited at 0.7 J/cm2, precursor ~4200 nm thick. Magnification 50k.

As-deposited films displayed an underlying film dotted with round droplets, similar to CZTS films produced by PLD [4]. The laser fluence had little influence on film appearance.

After annealing, several films contained relatively large grains and visible pinholes (Fig. 1 a) while one thicker film deposited at lower fluence appeared rougher with less well-defined grains (Fig. 1 b). The films with large grains are similar in appearance to Cu_2SnS_3 films annealed in a similar manner by Chino et al. [2].

3.2 Energy dispersive X-ray spectroscopy

The composition of the Sn- and S-enriched target, as-deposited films and annealed films is shown in Fig. 2. Measurements on as-deposited films were made on films on fused silica substrates, whereas annealed films were deposited on Mo/SLG. As-deposited films on Mo/SLG were generally a few absolute percent more Sn and S rich than those on fused silica.

The as-deposited films were Sn- and S-poor compared to the target. The composition did not depend significantly on fluence or laser spot size. Annealing decreased the Sn content while increasing the S content slightly. The stoichiometry of the annealed films is close to Cu_2SnS_3; the thickest film is closest. All the films retained an excess of Sn.

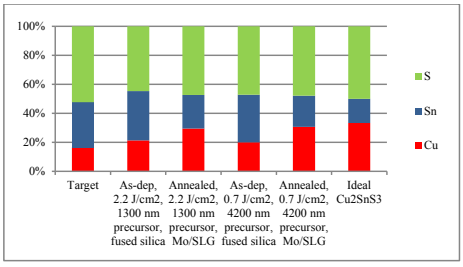

Fig. 2 Composition from EDX of target and selected films.

3.3 X-ray diffraction

As-deposited films on fused silica displayed no obvious X-ray diffraction peaks; films on Mo/SLG were assumed to be similar. After annealing, films form Cu_2SnS_3 (cubic phase) alongside SnS (orthorhombic) (Fig. 3). The thick film shown in Fig. 1 b is dominated by cubic-phase Cu_2SnS_3, while the thinner films were dominated by SnS (orthorhombic phase).

4. Discussion and conclusion

As seen from the EDX data, S and Sn was lost relative to the target during pulsed laser deposition at room temperature. Annealing further caused loss of Sn, probably in the form of SnS, where the S loss was compensated by the S powder. The pinholes seen in the thinner films (Fig. 1 a) may be evidence of SnS evaporation [1]. Compared to the thickest film, the pinholes may appear clearly in the thinner films due to more uniform crystallization. The relatively small X-ray diffraction peaks for the thick film may indicate that it is not fully crystallized but contains amorphous regions.

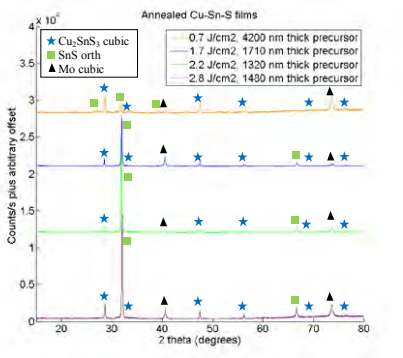

Fig. 3 X-ray diffractograms of films of different thickness made at different fluences. Cubic Cu2SnS3: JCPDS 89-2877; orthorhombic SnS: JCPDS 39-354; cubic Mo: JCPDS 42-1120

In summary, using a Sn- and S-enriched target for pulsed laser deposition of copper tin sulfide, we obtained near-stoichiometric Cu_2SnS_3 thin films after annealing with S above 570 ºC. However, the films remain Sn rich and contain SnS. In future work a less enriched target may be used.

REFERENCES

[1] N. Aihara, H. Araki, A. Takeuchi, K. Jimbo, and H. Katagiri, "Fabrication of Cu_2SnS_3 thin films by sulfurization of evaporated Cu-Sn precursors for solar cells", *Phys. Stat. Sol. C,* **10**, No. 7-8, 1086-1092 (2013).

[2] K. Chino, J. Koike, S. Eguchi, H. Araki, R. Nakamura, K. Jimbo, H. Katagiri, "Preparation of Cu_2SnS_3 Thin Films by Sulfurizaiton of Cu/Sn Stacked Precursors", *Jpn J Appl Phys* **51**, 10NC35 (2012).

[3] A. V. Moholkar, S. S. Shinde, G. L. Agawane, S. H. Jo, K. Y. Rajpure, P. S. Patil, C. H. Bhosale, and J. H. Kim, " Studies of compositional dependent CZTS thin film solar cells by pulsed laser deposition technique: An attempt to improve the efficiency", *J. Alloys Compounds,* **544**, 145-151 (2012).

[4] S. M. Pawar, A. V. Moholkar, I. K. Kim, S. W. Shin, J. H. Moon, J. I. Rhee, and J. H. Kim, "Effect of laser incident energy on the structural, morphological and optical properties of Cu_2ZnSnS_4 (CZTS) thin films", *Current Appl. Phys.* **10,** 565-569 (2010).

Appendix D

In prep: Pulsed Electron vs. Pulsed Laser deposition for the growth of CZTS films

Manuscript draft on PLD versus PED of CZTS for solar cells including Supplementary Information. The main results and part of the discussion in this paper are presented in Chapter 8. We are awaiting possible further results of PED of CZTS at IMEM-CNR before submitting the paper.

Pulsed Electron vs. Pulsed Laser deposition for the growth of CZTS films

Rebecca B. Ettlinger[(1)]*, Francesco Pattini[(2)], Stefano Rampino[(2)], Matteo Bronzoni[(2)], Filippo Annoni[(2)], Andrea Crovetto[(3)], Edoardo Bosco[(3)], Andrea C. Cazzaniga[(1)], Edmondo Gilioli[(2)], Ole Hansen[(3)] and Jørgen Schou[(1)]

[(1)] DTU Fotonik, Technical University of Denmark, DK-4000 Roskilde, Denmark

[(2)] IMEM-CNR, Institute of Materials for Electronic and Magnetism, 43124 Parma, Italy

[(3)] DTU Nanotech, Technical University of Denmark, DK-2800 Kgs. Lyngby, Denmark

* corresponding author: reet@fotonik.dtu.dk

Abstract

We have investigated the use of pulsed electron deposition (PED) and pulsed laser deposition (PLD) for the growth of copper zinc tin sulfide (CZTS), a complex material used as absorber layer in thin film solar cells. PED and PLD are high energy vacuum deposition techniques sharing common features such as the ability to grow complicated crystalline compounds at low temperatures. The films were grown at temperatures ≤ 300 °C and characterized with EDX, SEM, XRD, and Raman spectroscopy. We find that PED and PLD behave similarly; in both cases the composition is generally non-stoichiometric and can be widely varied depending on the deposition parameters. With both techniques, crystalline CZTS is obtained at temperatures around 300 °C with comparable deposition rates. Some fundamental differences between the two techniques impose the need for careful control of the process parameters in order to make both PED and PLD suitable techniques for the growth of high-quality CZTS films in a rapid single-step process.

1 Introduction

Pulsed electron deposition (PED) and pulsed laser deposition (PLD) are high energy vacuum deposition techniques with common characteristics as reported for example by Strikovski et al. [1]. In PED and PLD, the ablation of a bulk target material creates a plasma "plume" that condensates on a substrate. A peculiar characteristic of both techniques is the high kinetic energy of the ablated species in the plasma plume and on the substrate, which allows complex material to form under non-thermodynamic equilibrium conditions.

In PED, a triggered electrical discharge ignites the plasma inside a hollow cathode and the high acceleration voltage applied (10-20kV) draws out and accelerate the electrons of the plasma towards the target, inducing the ablation process (Figure 1 a). The target connected to the grounded vacuum chamber, acts as the anode and attracts the focused electron beam through a dielectric tube. The extremely high power density of the electron pulse (on the order of 10^8 W/cm^2 [2,3]) induces the sudden ablation of the target. Slow heating and evaporation of the target material must be minimized by adjusting the process conditions. Because of the far-from-equilibrium conditions, in the ablation regime all the elements are transferred from the bulk target to the growing film, ideally maintaining the desired stoichiometry, in contrast to the lower-energy evaporative regime [4].

For PLD, the ablation is caused by a high power pulsed laser hitting the target in a similar manner to the pulsed electron beam (Figure 1 b). The plasma formation process and the required power density of the laser pulses differ for a given material depending on the laser wavelength (λ) and pulse duration (τ). The main differences between the two techniques include: 1) the requirement of a background gas for PED and 2) the material interaction of electrons and photons. While PLD may be carried out in a vacuum or within a wide range of background gas pressures, a background gas (typically Ar) on the order of 10^{-3} mbar is needed in PED for the initiation of the electric discharge and for the self-focusing of the beam [2]. Additionally, in PLD of semiconductors with a laser energy greater than the material's band gap, the main part of the laser energy will be deposited in the top hundred nm range of the target, while the energy of a polyenergetic PED beam of up to 10-20 keV may be deposited down to micrometer depth. Typical parameters of the PED and PLD systems used in this study are compared in Table 1.

In this paper, we used PED and PLD to grow film of Cu_2ZnSnS_4 (CZTS), a structurally and chemically complex material. It is a quaternary compound characterized by a complicated phase diagram and a narrow stability region [5]. The deposition of high quality film of CZTS is extremely difficult, and the development of a simple (possibly single stage) and fast method to control the stoichiometry would be a fundamental step towards its use as an absorber layer in thin film solar cells. Current methods for making CZTS usually require deposition of a precursor layer followed by high-temperature annealing, as detailed below.

To the best of our knowledge, no CZTS solar cells have been reported by PED, but recently, isostructural $Cu(In,Ga)Se_2$ (CIGSe)-based thin film solar cells with 17% efficiency has been reported, grown by PED in a single-stage process starting from a quaternary target [6,7]. Remarkably, the deposition temperature for CIGSe by PED is only 270 °C, significantly lower than the values required by the usual methods such as sputtering [8] or co-evaporation, the latter holding the world record of 22.6 % efficiency for CIGSe solar cells [9]. CZTS is attracting interest as an alternative to CIGS because it has similar material properties but is made up only of Earth-abundant elements. The record solar cell to date with 9.4 % active area efficiency was achieved with vacuum processing and no less than two precursor/annealing steps (four steps in total) for the CZTS layer with a maximum annealing temperature of 570 °C in an H_2S/N_2 atmosphere [10]. The highest efficiency for a sulfo-selenide variety ($Cu_2ZnSn(S,Se)_4$ or CZTSSe) is 12.6 % by solution processing with hydrazine followed by annealing > 500 °C [11], while a recent record for CZTS solar cells made by pulsed laser deposition (PLD) with a 560 °C annealing step is 5.2 % [12]. The highest value achieved with a one-step method was likewise 5.2 % using co-evaporation with a deposition temperature of 460 °C [13]. On this backdrop, it is worthwhile to investigate low-temperature deposition of CZTS.

Owing to the experience acquired on CZTS deposition by PLD at DTU (Denmark) and on CIGSe by PED at CNR (Italy), we compare the properties of the material grown by both methods and explore the use of PED to deposit CZTS for solar cells. Although the optimization of the CZTS-based solar cells goes beyond the scope of this paper, some preliminary results are presented.

2 Methods

2.1 Pulsed electron deposition

Pulsed electron deposition was carried out with a commercial PED source (PEBS-20, Neocera Inc., USA). The pulse repetition rate varied from 7-10 Hz depending on the voltage, the target-substrate distance was 8 cm, the dielectric tube-target distance was approx. 3-5 mm, and the size of the electron beam spot on the target was approx. 7 mm^2. The target was kept in rotation to ensure a uniform material removal and to avoid to local overheating, thus limiting the evaporation. Prior to each deposition, the chamber was pumped to about $5*10^{-5}$ mbar, then filled with Ar to ~ $1\text{-}2*10^{-3}$ mbar. The composition of the PED ablation plume was monitored by optical emission spectroscopy (OES) with an optical mini-spectrometer (Hamamatsu TM-CCD-A series), and the emission peaks in the plume were assigned to different elements using the NIST database of atomic spectra [14].

2.2 Pulsed laser deposition

Pulsed laser deposition was carried out with a 248 nm KrF excimer laser (Lambda Physik LPX) with a spot size of approx. 5 mm^2 and a fluence of 0.3-0.5 J/cm^2. The target-substrate distance was 4.5 cm, the target rotated during the deposition, the laser spot was scanned across the target to avoid crater formation, and the chamber pressure prior to deposition was < $5*10^{-5}$ mbar for heated films and < $2*10^{-6}$ mbar for films at room temperature. The fluence decreased about 30 % during the deposition due to increasing window coating; the fluence values quoted here are averages. The pulse repetition rate was 15 Hz except as noted. A higher repetition rate for PLD compared to PED was chosen because the deposition rate per pulse was lower for PLD than PED at 300 °C, and at this temperature the deposition time could influence the film composition due to evaporation of the more volatile elements.

2.3 Targets and substrates

The CZTS targets were commercial hot-sintered pellets made from binary sulfides powders (Testbourne, Ltd., UK). They contained multiple phases including ZnS, Cu_xS and SnS_y identified by X-ray diffraction and EDX-mapping, which showed Zn-, Sn- and Cu-rich regions up to hundreds of microns across. Prior to each ablation, the target was polished and pre-ablated until a stable OES signal was reached (PED) or until a somewhat eroded target surface and a ~ 60 % transmitting window coating had been obtained (~15 min at 15 Hz, PLD).

Soda lime glass (SLG) substrates were used for the PED at room temperature depositions, while sputtered Mo-coated SLG was used for all films made by PLD and for the heated films by PED, as Mo is commonly used as the back contact of CIGSe and CZTS thin film solar cells.

For PED, the substrates were placed on a graphite susceptor heated by an infrared bulb and the temperature was monitored by a thermocouple in contact with the substrate surface. For PLD, the samples were mounted with silver paste on a resistive heater (TSST B. V., The Netherlands), and the temperature was monitored with an internal thermocouple.

2.4 Characterization

The morphological characterization was done by scanning electron microscopy (SEM, Zeiss Supra 40 VP and FEI Quanta 200 F) equipped with a field emission gun. Energy Dispersive X-ray Spectroscopy (EDX) for compositional analysis was carried out with 15 kV electrons in a Hitachi tabletop TM3000 SEM with a Bruker XFlash430 silicon drift detector and analyzed using Bruker's Quantax 70 software. The deposition rates were calculated from the measurements of film thickness in a Phillips 515 SEM as well as the Supra and the FEI Quanta 200 F. The room temperature PLD films were masked with sticky tape and the deposition rates confirmed with a Dektak profilometer.

X-ray diffraction (XRD) was carried out in a Bruker D8 diffractometer with Cu K_α and Cu K_β radiation, a step size of 0.01° and a rate of 1.1-2 step/s (heated films, target) or 0.03° at 0.33 step/s (room temperature films). Mo substrates were scanned with Si reference powder (NIST 640d) to correctly identify the position of the Mo peaks that, in turn, were used to align the diffractograms of the CZTS on Mo-coated substrates. The Cu $K_{\alpha 2}$ signal was stripped with Bruker's EVA software and the peaks were identified manually using PDF files from the ICSD (Karlsruhe). References from the ICSD: CZTS: Lafond et al., 2014, Zeit. Anorg. Allg. Chem.; ZnS: PDF 01-071-5976; cubic CTS: PDF 01-089-2877; tetragonal CTS: PDF 29-570; monoclinic CTS: PDF 01-070-6338; $Cu_3SnS_{3.6}$: Goto et al., 2013, Inorg. Chem.; orthorhombic SnS: PDF 01-073-1859; orthorhombic Sn_2S_3: PDF 01-075-2183; hex. MoS_2: PDF-01-072-1508; cubic Mo: PDF 01-071-3771.

Raman spectroscopy of the PED films was done with a DXR Raman Microscope (Thermo Scientific) at 455 nm in the backscattering configuration with a spot size of 1 μm^2 and a power of 0.4

mW. Raman spectroscopy of the PLD films was done with a Renishaw RL532C diode-pumped solid state laser at 532 nm set to 0.1 mW.

Photoluminescence spectra and maps were measured in the steady state on as-deposited PLD films with an Accent RPM2000 spectrometer with 532 nm excitation at 100 W/cm2.

3 Results and discussion

3.1 CZTS @ room temperature: deposition rates, morphology and composition

Deposition rates: The deposition rates of PED (CZTS and CIGSe) and PLD (CZTS) are compared in Table 2. The rates depend on the spot size and the power density of the electron/laser pulses. Nonetheless, in the voltage/fluence range used here, the deposition rates are comparable for the two techniques, allowing growth of micrometer-thick films in about half an hour with a pulse repetition rate of 7-15 Hz. The growth rates of CZTS and CIGSe by PED under the same conditions are similar.
Morphology: The surface roughness of the grown film is a typical issue of pulsed, high energetic deposition techniques due to debris or molten droplets ejected from the target. SEM images of PED and PLD films deposited at room temperature are shown in Figure 2. Droplets up to μm size cover the films with large droplets deeply embedded. The as-deposited room temperature PED film (Figure 2a, b) contains many more droplets than the PLD film (Figure 2c, d). This is not always the case: for example, Nistor et al. saw the opposite for ZST ($Zr_{0.8}Sn_{0.2}TiO_4$) film with fewer droplets in PED than PLD [15]. The amount of droplets decreased when the deposition voltage decreased (Supplementary Figure S1), similar to the droplet reduction with decreasing fluence seen in PLD, e.g., for CZTS and CTS [16,17]A larger incidence of droplets can point to less efficient coupling of energy into the target: a larger volume is heated enough to melt or explode but not enough to be atomized.

Composition: The film composition can be modified in the PED setup. Depending on the Ar pressure, it possible to change the intensity of the Cu (I) vs. Zn (I) emission lines, as detected by OES of the plume emission (Supplementary Figure S2). Figure 3a shows the Zn/Sn, S/metals and Cu/(Zn+Sn) ratios in films made at different PED discharge voltages at room temperature. The Ar pressure was adjusted during the depositions to allow for a stable ablation plume and a constant Cu (I)/Zn (I) OES ratio; under these conditions, it possible to keep the composition of the films constant at 14-19 kV. Below 16 kV, changing the Ar pressure did not increase the Cu (I)/Zn (I) line ratio,

indicating that the Cu-content of the emission plume could not be increased. At 16-19 kV a far higher Cu (I)/Zn (I) emission line ratio could be obtained in the plume. As expected, the Cu/(Zn+Sn) ratio was higher in films deposited with higher Cu (I)/Zn (I) OES ratios (not shown in the figure). This increase in the Cu/(Zn+Sn) ratio was accompanied by a decrease in the S/metal ratio.

Figure 3a shows that the elemental transfer to the PED films is not exactly stoichiometric: the films results Cu-poor, Zn-poor and often S-poor relative to the expected composition of Cu_2ZnSnS_4 (in other words, the films were Sn-rich). The ideal CZTS composition for solar cells is slightly Cu-poor and Zn-rich compared to stoichiometric CZTS, with Cu/(Zn+Sn) ~ 0.8-0.9 and Zn/Sn ~ 1.1-1.3 [18], so the Cu-poor nature of the PED films is desirable, while Sn-rich films pose a problem. EDX of powders scraped from the targets before and after deposition showed that the target changed over time: there was an increase in the Cu-content and a decrease in Sn and S after the depositions. Together, these observations point to preferential evaporation of the most volatile target constituents (S and SnS).

Figure 3b shows the same element ratios for films made by PLD at room temperature. The Cu/(Zn+Sn) ratio rises strongly with fluence, saturating above 0.8 J/cm^2, while the Zn/Sn ratio stays nearly constant or rises slightly rising with the fluence. Most of these data have been reported by Cazzaniga & Crovetto et al. [12] where the authors related the increasing Cu/(Zn+Sn) ratio with increasing PLD fluence to the multiphase nature of the target: SnS_y and ZnS may be more easily vaporized than $Cu_{2-x}S$ due to their lower specific heat, enthalpy of evaporation, and enthalpy of fusion.

To confirm that the composition differences between the PLD and the PED films did not derive from the difference in repetition rate (7 Hz for PED, 15 Hz for PLD), PLD films were also deposited at 7 Hz and 45 Hz at room temperature. The composition of the 7 Hz film did not vary significantly from the 15 Hz films. The PLD film composition at a fluence value around 0.4-0.5 J/cm^2 is similar to the composition of the PED films (compare Fig. 3a and 3b).

The data shown here suggests a similar dynamic in PED and PLD: easier ablation of SnS and ZnS (especially SnS) compared to the Cu-rich phases in the target. The slightly Sn-rich but simultaneously slightly S-poor composition of the PED films may indicate that S is scattered more than Sn by the background gas in PED. Preferential scattering of light elements by a background gas is a well-known effect in PLD, although a pressure equivalent to that used in PED was not high enough to cause a significant effect in PLD of Cu_2S [19]. It is worth noting that during PED, portions of the ablation plume originating from distinct points on the rotating target were visibly brighter than the rest of the

plume, strongly supporting the idea that the ablation efficiency was higher for some of the phases than others. Such an irregular ablation plume was never observed in PLD.

There are few previous reports on the composition of as-deposited 248 nm PLD CZTS films at room temperature in vacuum, but an early study by Moriya et al. shows somewhat Cu- and Zn-poor, Sn-rich as-deposited films similar to the films made in the present study at around 0.5 J/cm^2, though they use a higher fluence (1.5 J/cm^2) and a shorter pulse length (10 ns) [20]. The PLD films made here tend to be S-poor, though the EDX quantification of S is uncertain due to its low elemental mass.

3.2 CZTS @ 300 °C: morphology, composition and crystallographic structure

Morphology: Figure 4 shows SEM images of PED films made at 18 kV at 255°C-325°C. The film cross sections reveal a porous structure even for the most tightly packed of the three films (Fig. 4 c) while secondary phases are visible near the bottom in the others (Fig. 4 a and b). The porous structure in comparison to the room temperature films could point to re-evaporation of S or SnS from the film and/or secondary phases with different crystal habits to CZTS [5]. The brightly visible secondary phases are most likely either ZnS, bright in SEM as an insulator, or SnS, bright due to the high atomic weight of Sn. Droplets of μm size are clearly visible; the droplet surfaces appear crystallized compared to the droplets in Fig. 2. Figure 5 shows SEM images of a PLD film made at 0.5 J/cm^2 and 300°C which appears completely different to the PED films: it is dense and does not show any large grains. Films deposited at slightly lower fluence (0.45 J/cm^2) or higher pulse rate (45 vs. 15 Hz) looked the same.

Composition: The PLD films made at 300 °C had a similar composition to the ones deposited at room temperature, although there was a slight tendency for the 300 °C films to lose S (Supplementary Figure S3). The composition of the PED film shown in Fig. 4 c was somewhat Cu-rich (Cu/(Zn+Sn)=1.05) and S-poor (S/metals =0.9) with a Zn/Sn ratio of ~1, at least in the top micron probed by 15 kV EDX.

Crystalline phases: Figure 6 shows Raman spectra of the PED and PLD films deposited at 300 °C. The PED films (Fig. 6a) show only CZTS peaks and Cu_xS, which appeared to be associated with droplets on the surface, matching the slightly Cu-rich composition measured by EDX. The PLD films (Fig. 6b) show only traces of Cu_xS but instead have peaks around 300 cm^{-1},179 cm^{-1} and 225 cm^{-1}

matching the cubic Cu_2SnS_3 (CTS), orthorhombic Sn_2S_3 and orthorhombic SnS phases, respectively [21,22] (see discussion of these peaks in Supplementary Figure S4 and associated text). The presence of SnS_y matches the Cu-poor nature of the PLD films, but also suggests the possible inclusion of ZnS if Zn/Sn~1 as measured by EDX. XRD of the PED and PLD films made at 300 °C support the Raman observations (Figure 7). Small peaks that belong exclusively to kesterite CZTS are present around 29° and 36-38° 2θ in the PED film (Fig. 7a) (these peaks also match two tetragonal forms of CTS, but this is not supported by the Raman measurement). The remaining peaks are "∑CZTS" peaks, where "∑CZTS" refers to the narrow 2θ ranges where the X-ray diffraction peaks overlap for kesterite CZTS, cubic ZnS, and tetragonal and cubic CTS [23]). In the PLD films, apart from the ∑CZTS peaks, extremely small peaks are present around 28° and 31-32° 2θ that could belong to SnS, Sn_2S_3 or Cu_2S (Fig. 7c). Raman and XRD therefore point to CZTS and Cu_xS in the PED films and CZTS and SnS_y in the PLD films. The high intensity of the 28.4° CZTS (211) peak in the PLD XRD pattern indicates a preferential growth direction, stronger than in the PED films. This results is in agreement with Sun et al., reporting a similar strong preferential orientation of the (211) planes parallel to the sample surface in 300 °C 248 nm PLD of CZTS [24]. Comparison of Fig. 7b and 7d shows that the XRD peaks of the PLD films are shifted towards slightly smaller 2θ angles than the PED films, indicating a difference either in the lattice size or in the phase composition. In the latter case, regions of ZnS could shift the PED peak to larger 2θ values.

3.3 Preliminary solar cells from PED films

The PED films made at 255-325 °C were used to make solar cells following the recipe used for CIGSe by Rampino et al. [3]. A specific optimization is clearly required; however, the very preliminary solar cells displayed some photo-response with efficiencies of about 0.2 %. As mentioned, the SEM-cross sections show porous films and in some cases also reveal secondary phases near the bottom of the films, while Raman measurements showed Cu_2S on the surface, and the film for which the composition could be measured was somewhat Cu-rich and S-poor. A Cu-rich, porous film is not suitable for CZTS solar cells and future work would need to focus on these issues. While the ZnS has been detected near the back of even very good CZTS solar cells [25], it must not occur in large enough quantities to block

electron transport. S-vacancies and $Cu_{2-x}S$ on the surface are known to be highly detrimental to solar cell performance and may also explain the low performance [26,18].

3.4 Perspectives for CZTS deposition by PED and PLD

The temperature of 300 °C was chosen in this study because it is high enough to induce the CZTS crystallization while avoiding Sn-loss as SnS sublimation from the growing films, as many authors have reported on the SnS evaporation from CZTS films heated in vacuum [27,28]. In the past in 248 nm PLD at 300 °C, the general problem has been lack of S in the as-deposited films [24,29,30]. This was also the case in this study, where the composition at room temperature and 300 °C was nearly identical and the S/metal ratio was relatively close to 1 but nonetheless S-poor according to EDX-measurements. Photoluminescence measurements of the PLD films yielded zero intensity, indicating serious shortcomings for solar cell absorbers. This may derive for example from S-vacancies or Sn-induced defects, which both may cause deep defects that are highly detrimental to the solar cell efficiency [5,26].

In previous studies of PED of CIGSe and CGSe, the composition of the films depended strongly on both the deposition voltage [31] and the substrate temperature [32]. Highly Se-rich films occurred at room temperature, whereas near-stoichiometric, somewhat Cu-poor films occurred at temperatures from 200-500 °C. The amount of Se in the films decreased with increasing temperature and increasing voltage and the change in composition was attributed to the changing balance between the amount of material ablated from the target or evaporated from either the film (high substrate temperature) or the target (high voltage). The Se-loss can be limited by reducing the PED deposition temperature, while the enrichment of Se in the plume due to evaporation from the target turned out to be an advantage that was able to counterbalance the loss that does occur from the growing film. In contrast, in ns-laser PLD of CIGSe, Se-loss was a problem at high deposition temperatures [33].

In the PED CZTS films, the Cu-rich composition and the associated occurrence of $Cu_{2-x}S$ on the surface could be resolved by adjusting the deposition parameters (reduced voltage and optimized Ar-pressure). Concerning the possible S loss, we assume that the low-energy electrons present in PED could provide extra S-evaporation from the target, similar to the extra Se-evaporation seen in CIGSe.

To provide enough S during PLD, a sulfur cracker is another option to improve the quality of the as-deposited films; this solution is currently being investigated in the PLD lab at DTU. Finally, in view of applications as solar cell absorber, it will be important to ensure a proper Na content, since Na-doping improves the absorber quality in CZTS just as it does in CIGS [13]. The low deposition temperatures of PED and PLD impede the diffusion on Na from the SLG substrate so that it must be intentionally incorporated in the growing films by growing a NaF layer as done in PED of CIGSe [3].

4 Conclusions

We have compared the deposition of CZTS by Pulsed Electron Deposition and Pulsed Laser Deposition. Both PLD and PED result in crystalline CZTS at 300 $^{\circ}$C. However, secondary phases appear in the films by both methods: likely ZnS near the bottom and $Cu_{2-x}S$ at the surface in the PED films made at 250-325 $^{\circ}$C and Cu_2SnS_3 and Sn_2S_3 near the surface in the PLD films. PED films made at room temperature showed preferential ablation of SnS and/or S, as did low-fluence PLD. Changing the discharge voltage and pressure in PED and the fluence in PLD makes it possible to alter the film composition from Cu-poor to Cu-rich, while the open question remains the control of the S and Sn content.

References

[1] M.D. Strikovski, J. Kim, S.H. Kolagani, Plasma Energetics in Pulsed Laser and Pulsed Electron Deposition, in: G. Dhanaray, B. Kullaiah, V. Prasad, M. Dudley (Eds.), Springer Handb. Cryst. Growth, Part E Ep. Growth Thin Film., Springer-Verlag Berlin Heidelberg, Heidelberg, 2010: pp. 1193–1211.

[2] T. Witke, A. Lenk, B. Schultrich, C. Schultheiss, Investigation of plasma produced by laser and electron pulse ablation, Surf. Coatings Technol. 74–75 (1995) 580–585. doi:10.1016/0257-8972(95)08308-1.

[3] S. Rampino, N. Armani, F. Bissoli, M. Bronzoni, D. Calestani, M. Calicchio, N. Delmonte, E. Gilioli, E. Gombia, R. Mosca, L. Nasi, F. Pattini, A. Zappettini, M. Mazzer, 15% efficient Cu(In,Ga)Se2 solar cells obtained by low-temperature pulsed electron deposition, Appl. Phys. Lett. 101 (2012) 132107. doi:10.1063/1.4755772.

[4] T. Venkatesan, X.D. Wu, A. Inam, J.B. Wachtman, Observation of two distinct components during pulsed laser deposition of high Tc superconducting films, Appl. Phys. Lett. 52 (1988) 1193–1195. doi:10.1063/1.99673.

[5] H. Du, F. Yan, M. Young, B. To, C.S. Jiang, P. Dippo, D. Kuciauskas, Z. Chi, E.A. Lund, C. Hancock, W.M. Hlaing Oo, M.A. Scarpulla, G. Teeter, Investigation of combinatorial coevaporated thin film Cu2ZnSnS4. I. Temperature effect, crystalline phases, morphology, and photoluminescence, J. Appl. Phys. 115 (2014) 173502. doi:10.1063/1.4871664.

[6] M. Mazzer, S. Rampino, E. Gombia, M. Bronzoni, F. Bissoli, F. Pattini, M. Calicchio, A. Kingma, F. Annoni, D. Calestani, N. Cavallari, V. Thottapurath Vijayan, M. Lomascolo, A. Cretì, E. Gilioli, Progress on Low-Temperature Pulsed Electron Deposition of CuInGaSe2 Solar Cells, Energies. 9 (2016) 207. doi:10.3390/en9030207.

[7] S. Rampino, F. Annoni, M. Bronzoni, M. Calicchio, E. Gombia, M. Mazzer, F. Pattini, E. Gilioli, Joule heating-assisted growth of Cu(In,Ga)Se2 solar cells, J. Renew. Sustain. Energy. 7 (2015) 13112. doi:10.1063/1.4906979.

[8] A. Chirilă, P. Reinhard, F. Pianezzi, P. Bloesch, A.R. Uhl, C. Fella, L. Kranz, D. Keller, C. Gretener, H. Hagendorfer, D. Jaeger, R. Erni, S. Nishiwaki, S. Buecheler, A.N. Tiwari,

Potassium-induced surface modification of Cu(In,Ga)Se2 thin films for high-efficiency solar cells, Nat. Mater. 12 (2013) 1107–1111. doi:10.1038/nmat3789.

[9] P. Jackson, R. Wuerz, D. Hariskos, E. Lotter, W. Witte, M. Powalla, Effects of heavy alkali elements in Cu(In,Ga)Se2 solar cells with efficiencies up to 22.6%, Phys. Status Solidi - Rapid Res. Lett. 10 (2016) 583–586. doi:10.1002/pssr.201600199.

[10] S. Tajima, M. Umehara, M. Hasegawa, T. Mise, T. Itoh, Cu2ZnSnS4 photovoltaic cell with improved efficiency fabricated by high-temperature annealing after CdS buffer-layer deposition, Prog. Photovoltaics Res. Appl. 15 (2016) 659–676. doi:10.1002/pip.2837.

[11] W. Wang, M.T. Winkler, O. Gunawan, T. Gokmen, T.K. Todorov, Y. Zhu, D.B. Mitzi, Device Characteristics of CZTSSe Thin-Film Solar Cells with 12.6% Efficiency, Adv. Energy Mater. 4 (2014) 1–5. doi:10.1002/aenm.201301465.

[12] A. Cazzaniga, A. Crovetto, C. Yan, K. Sun, X. Hao, J. Ramis Estelrich, S. Canulescu, E. Stamate, N. Pryds, O. Hansen, J. Schou, Ultra-thin Cu2ZnSnS4 solar cell prepared by pulsed laser deposition, Submitted. (2016).

[13] T. Mise, S. Tajima, T. Fukano, K. Higuchi, T. Washio, K. Jimbo, H. Katagiri, Improving the photovoltaic performance of co-evaporated Cu2ZnSnS4 thin-film solar cells by incorporation of sodium from NaF layers, Prog. Photovoltaics Res. Appl. 24 (2016) 1009–1015. doi:10.1002/pip.2745.

[14] A. Kramida, Y. Ralchenko, N. Reader, J., NIST ASD Team, NIST Atomic Spectra Database (ver. 5.3), Natl. Inst. Stand. Technol. Gaithersburg, MD. (2015). http://physics.nist.gov/asd (accessed March 31, 2016).

[15] M. Nistor, N.B. Mandache, J. Perrière, Pulsed electron beam deposition of oxides thin films, J. Phys. D. Appl. Phys. 41 (2008) 165205. doi:10.1088/0022-3727/41/16/165205.

[16] K. Moriya, K. Tanaka, H. Uchiki, Cu2ZnSnS 4 Thin Films Annealed in H 2 S Atmosphere for Solar Cell Absorber Prepared by Pulsed Laser Deposition, Jpn. J. Appl. Phys. 47 (2008) 602–604. doi:10.1143/JJAP.47.602.

[17] R.B. Ettlinger, A. Crovetto, S. Canulescu, A. Cazzaniga, L. Ravnkilde, T. Youngman, O. Hansen, N. Pryds, J. Schou, Formation of copper tin sulfide films by pulsed laser deposition at 248 and 355 nm, Appl. Phys. A. 122 (2016) 466. doi:10.1007/s00339-016-9939-4.

[18] S. Delbos, Kesterite thin films for photovoltaics: a review, EPJ Photovoltaics. 3 (2012) 35004.

doi:10.1051/epjpv/2012008.

[19] J. Chen, Y. Lv, M. Döbeli, Y. Li, X. Shi, L. Chen, Composition control of pulsed laser deposited copper (I) chalcogenide thin films via plasma/Ar interactions, Sci. China Mater. 58 (2015) 263–268. doi:10.1007/s40843-015-0039-0.

[20] K. Moriya, K. Tanaka, H. Uchiki, Fabrication of Cu 2 ZnSnS 4 Thin-Film Solar Cell Prepared by Pulsed Laser Deposition, Jpn. J. Appl. Phys. 46 (2007) 5780–5781. doi:10.1143/JJAP.46.5780.

[21] P.A. Fernandes, P.M.P. Salomé, A.F. da Cunha, Study of polycrystalline Cu2ZnSnS4 films by Raman scattering, J. Alloys Compd. 509 (2011) 7600–7606. doi:10.1016/j.jallcom.2011.04.097.

[22] L. Price, I. Parkin, A. Hardy, R. Clark, Atmospheric pressure chemical vapor deposition of tin sulfides (SnS, Sn2S3, and SnS2) on glass, Chem. Mater. (1999) 1792–1799. doi:10.1021/cm990005z.

[23] D.M. Berg, M. Arasimowicz, R. Djemour, L. Gütay, S. Siebentritt, S. Schorr, X. Fontané, V. Izquierdo-Roca, A. Pérez-Rodriguez, P.J. Dale, Discrimination and detection limits of secondary phases in Cu2ZnSnS4 using X-ray diffraction and Raman spectroscopy, Thin Solid Films. 569 (2014) 113–123. doi:10.1016/j.tsf.2014.08.028.

[24] L. Sun, J. He, H. Kong, F. Yue, P. Yang, J. Chu, Structure, composition and optical properties of Cu2ZnSnS4 thin films deposited by Pulsed Laser Deposition method, Sol. Energy Mater. Sol. Cells. 95 (2011) 2907–2913. doi:10.1016/j.solmat.2011.06.026.

[25] B. Shin, O. Gunawan, Y. Zhu, N.A. Bojarczuk, S.J. Chey, S. Guha, Thin film solar cell with 8.4 % power conversion efficiency using an earth-abundant Cu2ZnSnS4 absorber, Prog. Photovoltaics Res. Appl. 21 (2013) 72–76. doi:10.1002/pip.1174.

[26] S. Chen, J.H. Yang, X.G. Gong, A. Walsh, S.H. Wei, Intrinsic point defects and complexes in the quaternary kesterite semiconductor Cu2ZnSnS4, Phys. Rev. B - Condens. Matter Mater. Phys. 81 (2010) 35–37. doi:10.1103/PhysRevB.81.245204.

[27] A. Weber, R. Mainz, H.W. Schock, On the Sn loss from thin films of the material system Cu-Zn-Sn-S in high vacuum, J. Appl. Phys. 107 (2010) 1–6. doi:10.1063/1.3273495.

[28] A. Redinger, D.M. Berg, P.J. Dale, S. Siebentritt, The consequences of kesterite equilibria for efficient solar cells., J. Am. Chem. Soc. 133 (2011) 3320–3. doi:10.1021/ja111713g.

[29] K. Sekiguchi, K. Tanaka, K. Moriya, H. Uchiki, Epitaxial growth of Cu2ZnSnS4 thin films by

pulsed laser deposition, Phys. Status Solidi. 3 (2006) 2618–2621. doi:10.1002/pssc.200669603.

[30] M.R. Byeon, E.H. Chung, J.P. Kim, T.E. Hong, J.S. Jin, E.D. Jeong, J.S. Bae, Y.D. Kim, S. Park, W.T. Oh, Y.S. Huh, S.J. Chang, S.B. Lee, I.H. Jung, J. Hwang, The effects for the deposition temperature onto the structural, compositional and optical properties of pulsed laser ablated Cu2ZnSnS4 thin films grown on soda lime glass substrates, Thin Solid Films. 546 (2013) 387–392. doi:10.1016/j.tsf.2013.05.032.

[31] F. Pattini, M. Bronzoni, F. Mezzadri, F. Bissoli, E. Gilioli, S. Rampino, Dynamics of evaporation from CuGaSe 2 targets in pulsed electron deposition technique, J. Phys. D. Appl. Phys. 46 (2013) 245101. doi:10.1088/0022-3727/46/24/245101.

[32] S. Rampino, F. Bissoli, E. Gilioli, F. Pattini, Growth of Cu(In,Ga)Se2 thin films by a novel single-stage route based on pulsed electron deposition, Prog. Photovoltaics Res. Appl. 21 (2013) 588–594. doi:10.1002/pip.1234.

[33] D.H. Lowndes, Growth and Doping of Compound Semiconductor Films by Pulsed Laser Ablation, in: J.C. Miller, R.F. Haglund (Eds.), Laser Ablation and Desorption, Exp. Methods Phys. Sci., Academic Press, 1997: pp. 475–571.

[34] M. Dimitrievska, A. Fairbrother, X. Fontané, T. Jawhari, V. Izquierdo-Roca, E. Saucedo, A. Pérez-Rodríguez, Multiwavelength excitation Raman scattering study of polycrystalline kesterite Cu2ZnSnS4 thin films, Appl. Phys. Lett. 104 (2014) 21901. doi:10.1063/1.4861593.

[35] D.M. Berg, R. Djemour, L. Gütay, S. Siebentritt, P.J. Dale, X. Fontane, V. Izquierdo-Roca, A. Pérez-Rodriguez, Raman analysis of monoclinic Cu2SnS3 thin films, Appl. Phys. Lett. 100 (2012) 192103. doi:10.1063/1.4712623.

Table 1: Deposition parameters for PED and PLD

	PED	PLD (248 nm)
Power (W/cm^2)	Max 1.2*10^8 †	5*10^7 @ 1 J/cm^2
Pulse length (ns)	100	20
Spot size (mm^2)	7	5
Target-substrate distance (cm)	8	4.5
Pressure (mbar)	~2*10^{-3} (Ar)	< 5*10^{-5}
Pulse rate (Hz)	7-10	15

† $CuGaSe_2$ deposition at 18 kV; note that the PED pulse is polyenergetic and has a tail of lower-energy electrons

Table 2: Deposition rates of CIGSe and CZTS by PED and PLD

Material	**Method**	**Specifications**	**nm/pulse**
CZTS	PED, 7 mm^2 spot	18-19 kV, room T	~0.04-0.1
		14-17 kV, room T	~0.02
		10 kV, room T	~0.001
CZTS	PLD (248 nm), 5 mm^2 spot	0.5 J/cm^2, room T	~0.03
	PLD (248 nm), 7 mm^2 spot	0.6 J/cm^2, room T	~0.05
CIGSe	PED, 7 mm^2 spot	16 kV, room T-500 °C	~0.08 [32]

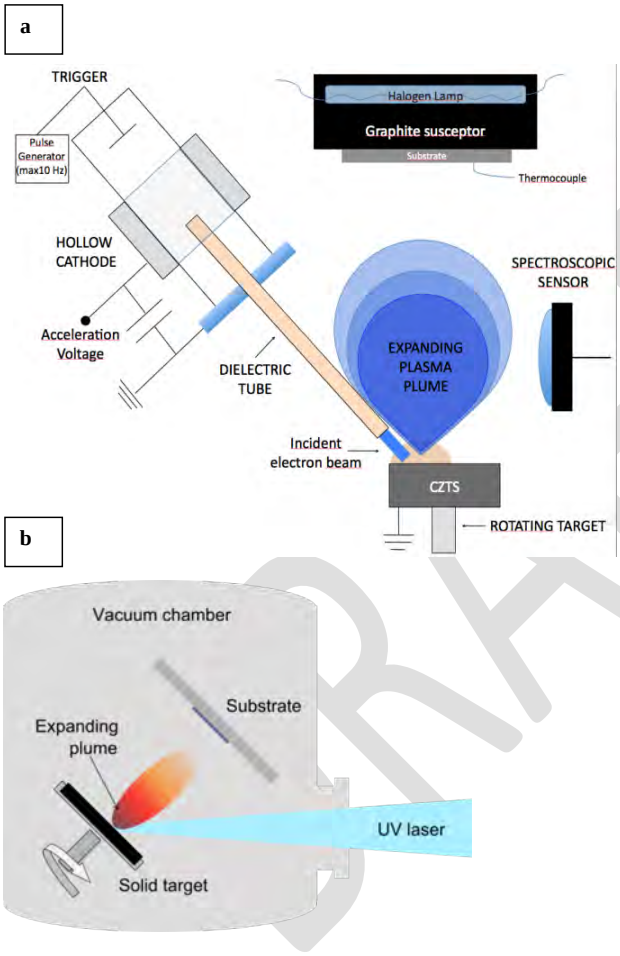

Figure 1: Setup for (a) pulsed electron deposition and (b) pulsed laser deposition.

Figure 2: SEM images of as-deposited films at room temperature by PED (18 kV discharge voltage, a-b) and PLD (0.5 J/cm2, c-d).

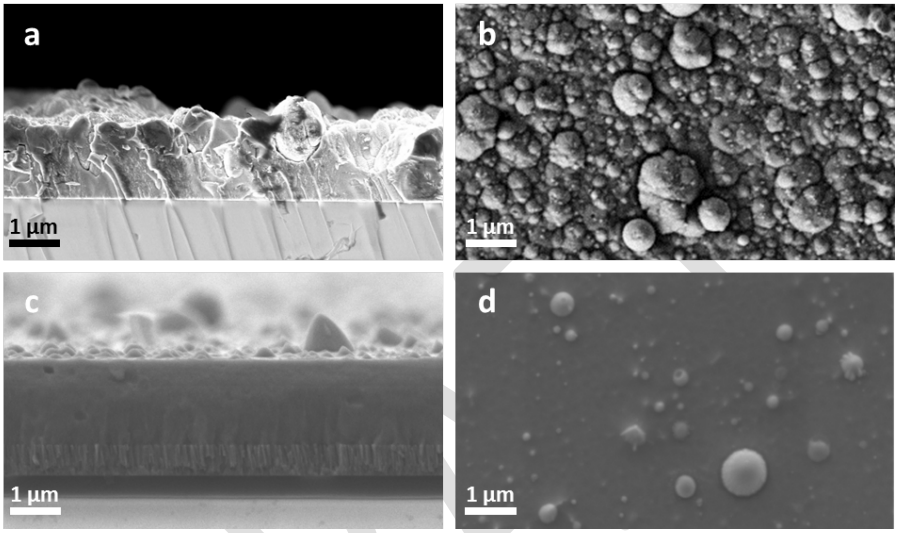

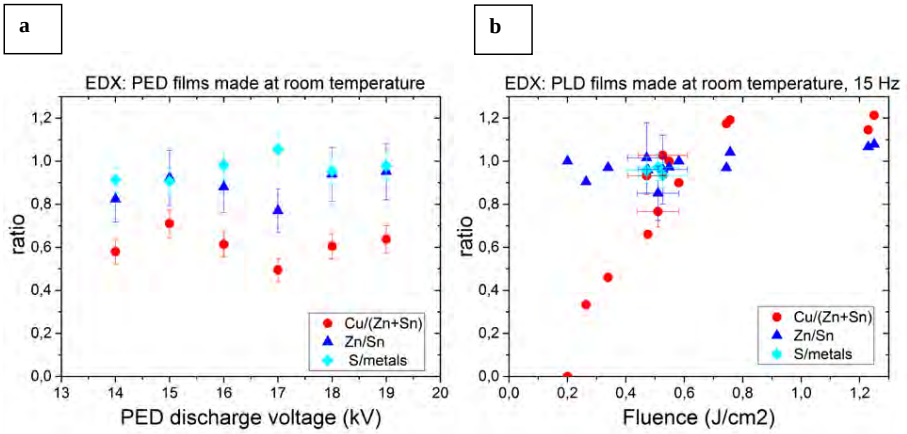

Figure 3: Composition measured by EDX of films made at room temperature by (a) PED and (b) PLD versus PED discharge voltage and fluence respectively. Most of the PLD data (b) is from [12]. Error bars represent 95 % confidence intervals for comparing measurements; the absolute error in instrument quantification may be larger.

Figure 4: PED films deposited with 18 kV bias at elevated temperature. Note different scale in (c) compared to (a) and (b) in cross section.

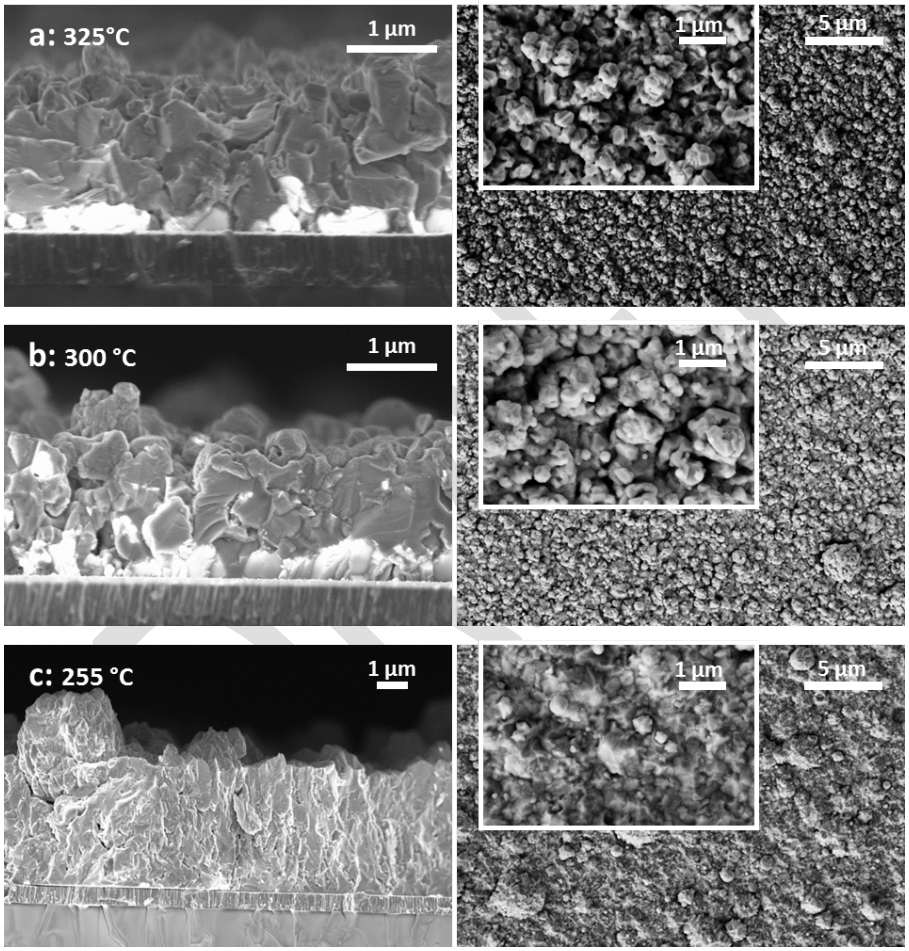

Figure 5: PLD films deposited at 300 °C at 0.5 J/cm^2. Other films deposited under similar conditions looked almost indistinguishable from the film shown here.

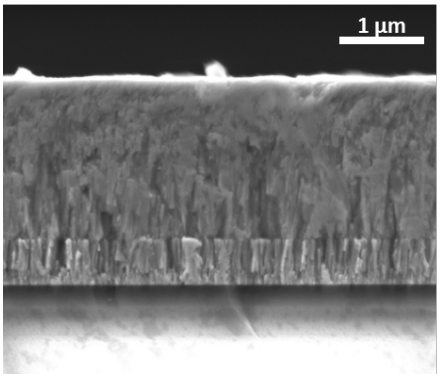

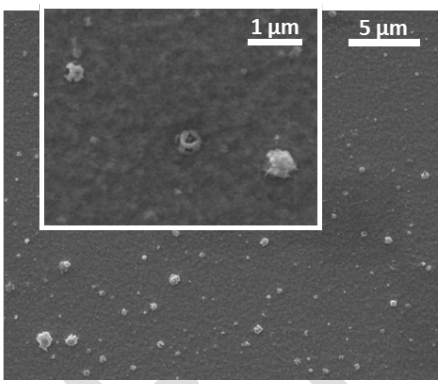

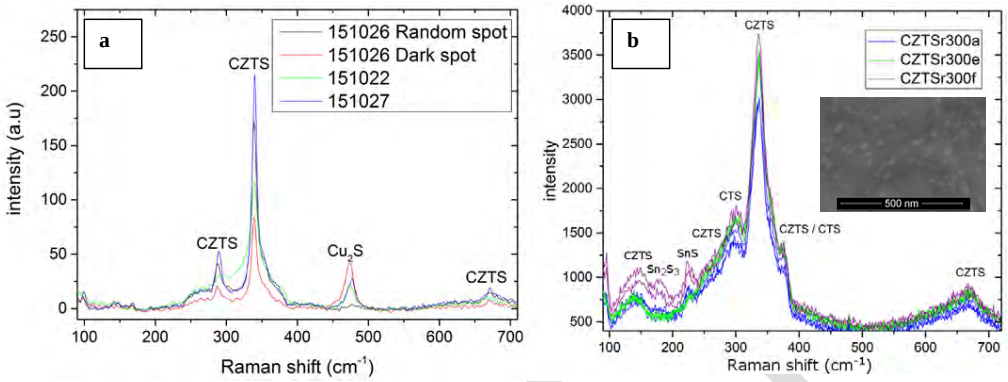

Figure 6: Raman spectra of CZTS films made by PED (a) and PLD (b) at ~300 °C. The "random spot" on one of the PED films corresponds to most of the surface as viewed through an optical microscope, while the "dark spot" is from an isolated spot that looked dark in the microscope. For the other two PED films and for the PLD films, the Raman spectra did not vary significantly from one spot to another. The inset in (b) shows the surface of a 300 °C PLD film at high magnification with small grains visible that may be SnS or Sn_2S_3; they were most easily visible on this film where the corresponding Raman peaks were brightest. Reference peak positions: CZTS [34], Cu_2S and tetragonal and cubic CTS [21], monoclinic CTS [35], SnS and Sn_2S_3 from [22].

Figure 7: X-ray diffractogram of the PED and PLD films as-deposited at 255-300 °C.
a: Diffractogram of PED film deposited at 255 °C (same film shown in fig. 4 c). Stars: ∑CZTS peaks (CZTS, cubic or tetragonal CTS, $Cu_3SnS_{3.6}$, and/or ZnS). Circled stars match only the tetragonal phases CZTS, tetragonal CTS or $Cu_3SnS_{3.6}$. Triangles: most likely orthorhombic Sn_2S_3. Inset: the 47.5° peak position compared to reference peaks. **b**: X-ray diffractogram of a sample films deposited by PLD at 300 °C. Legend and inset as in a.

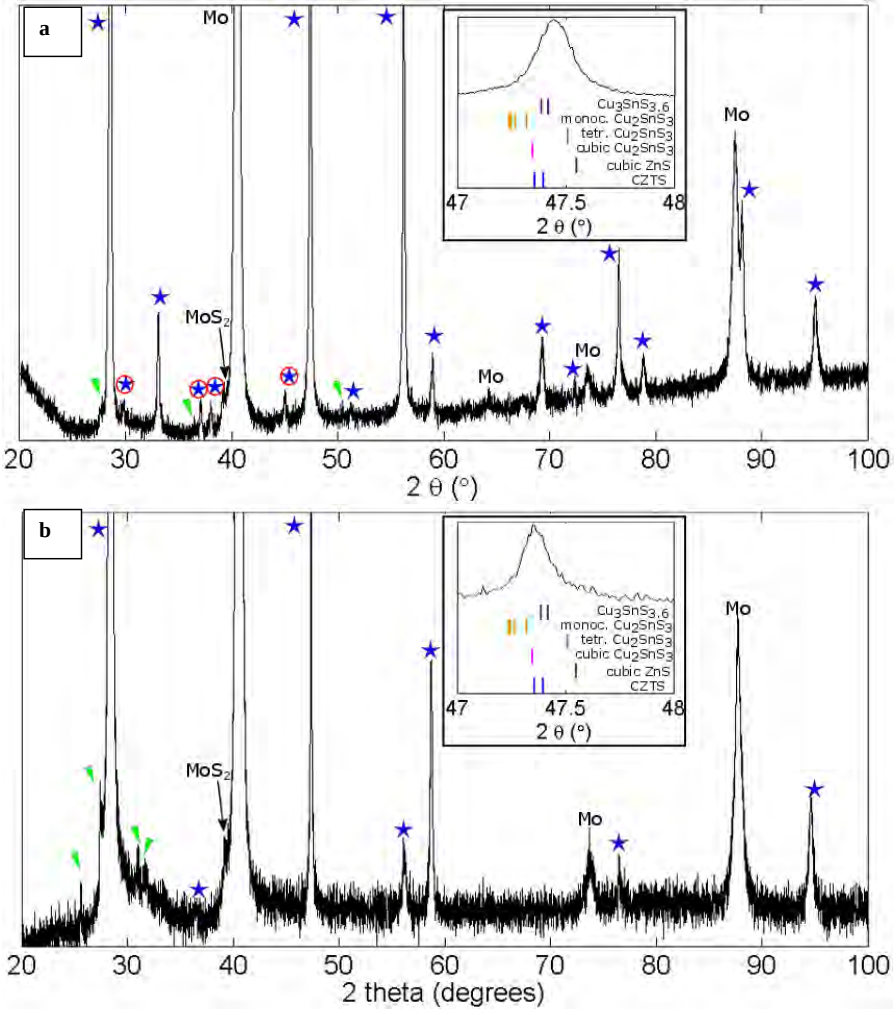

Supplementary information for

Pulsed Electron vs. Pulsed Laser deposition for the growth of CZTS films

Rebecca B. Ettlinger[(1)]*, Francesco Pattini[(2)], Stefano Rampino[(2)], Matteo Bronzoni[(2)], Filippo Annoni[(2)], Andrea Crovetto[(3)], Edoardo Bosco[(3)], Andrea C. Cazzaniga[(1)], Edmondo Gilioli[(2)], Ole Hansen[(3)] and Jørgen Schou[(1)]

[(1)] DTU Fotonik, Technical University of Denmark, DK-4000 Roskilde, Denmark

[(2)] IMEM-CNR, Institute of Materials for Electronic and Magnetism, 43124 Parma, Italy

[(3)] DTU Nanotech, Technical University of Denmark, DK-2800 Kgs. Lyngby, Denmark

* corresponding author: reet@fotonik.dtu.dk

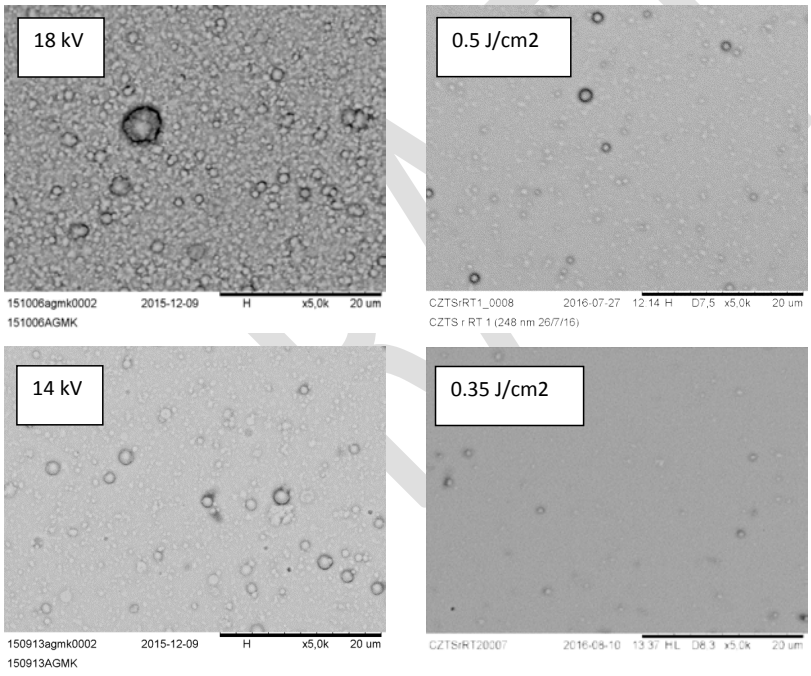

Figure S1: Reduction in droplets with reduction in voltage/fluence. Left: PED films made on soda lime glass at room temperature. Right: PLD films made on Mo-coated soda lime glass at room temperature. Images taken with 15 kV electrons using the TM3000 tabletop SEM.

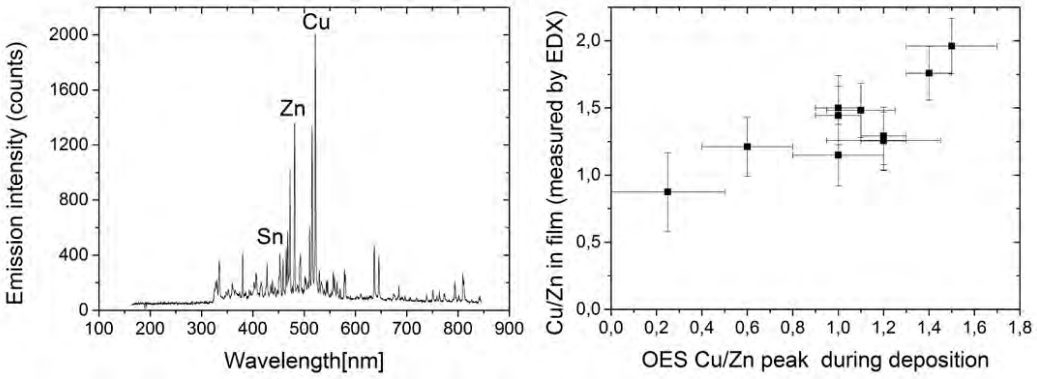

Figure S2: Optical Emission Spectroscopy (OES): **a** Typical optical emission spectrum with main Sn+, Zn+ and Cu+ atomic emission lines. **b** Cu/Zn ratio measured by EDX in the room temperature films versus estimated average ratio of the OES Cu+ to Zn+ emission line intensity in the ablation plume.

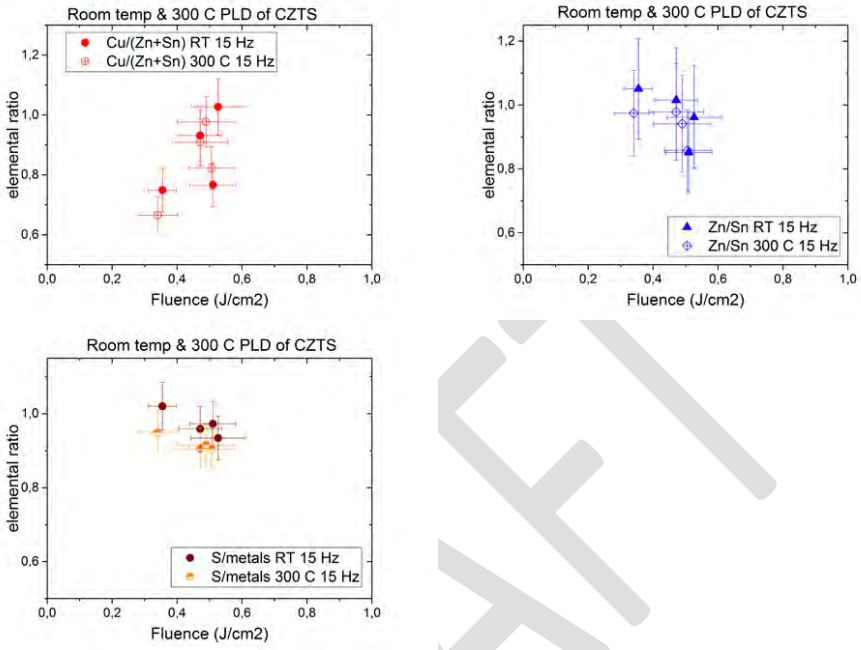

Figure S3: Composition of PLD films made at 300 °C vs. room temperature

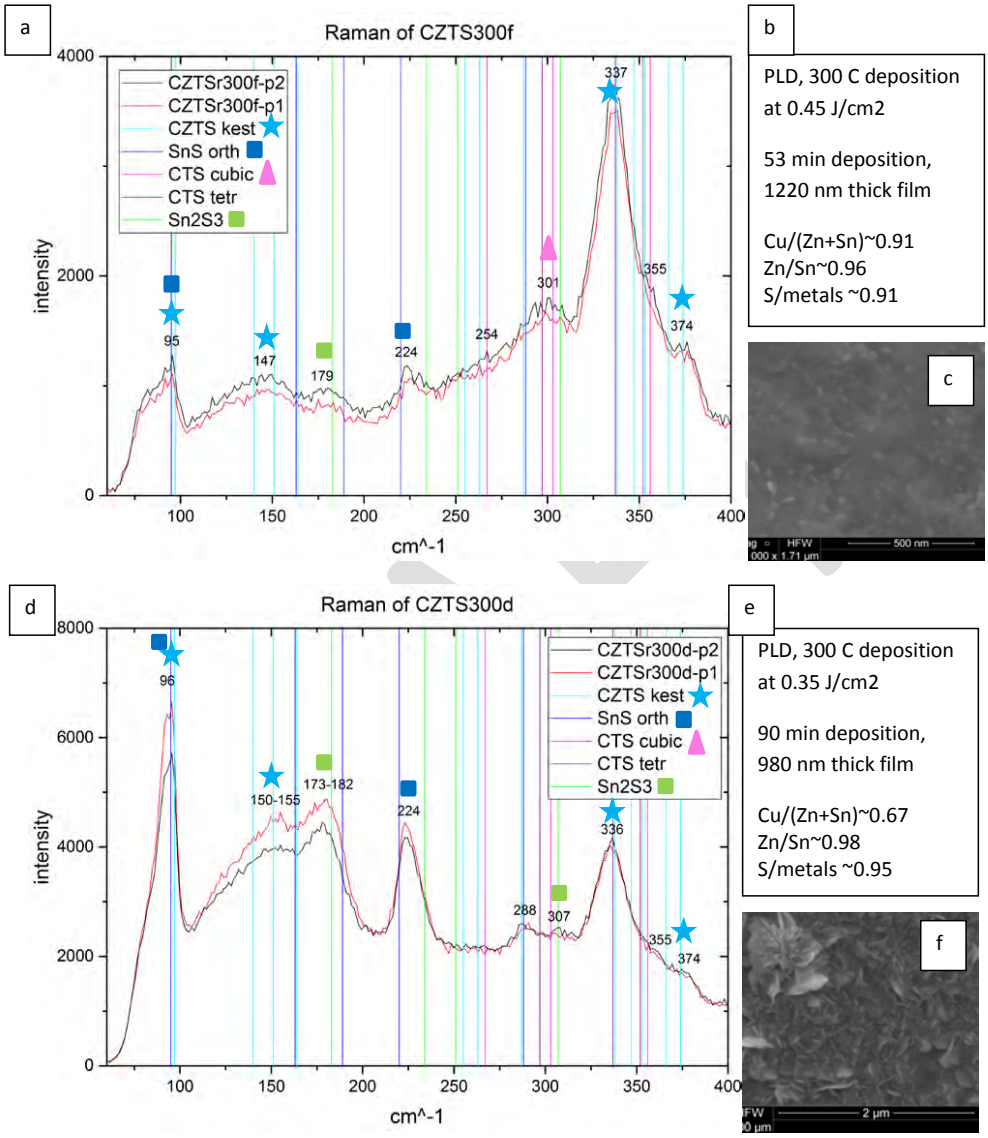

Figure S4: Secondary phases in PLD films deposited at 300 C: a) Raman spectrum of film made at 0.45 J/cm^2; this is one of the films shown in Figure 6 b in the main article. b) Deposition and composition information on the film in (a); c) SEM image of film surface. d) Raman spectrum of film made at 0.35 J/cm2 and nearly twice as long deposition time as the film in (a). e) Deposition and composition information on the film in (d); f) SEM image of film surface (note different magnification than (c)).

Discussion related to Figure S4:

The secondary phase peaks seen in Raman measurements at ~95 cm^{-1}, ~179 cm^{-1} and 225 cm^{-1} were strongest in one of the three films included in Fig 6b. The data for this film is reproduced in Fig. S4 a-c. Small crystallites are visible on the film (Fig. S4 c), perhaps corresponding to the phase giving rise to these secondary phase peaks. This idea is strengthened by comparison to a film made at lower fluence, which was more Cu-poor, and for which the deposition time at 300 °C was longer because the deposition rate is lower at low fluence (Fig. S4 d-f). The Raman spectrum of this film is completely dominated by the secondary phase peaks at ~95 cm^{-1}, ~179 cm^{-1} and 225 cm^{-1}. The film surface was covered in flaky crystallites (seen in the SEM image, Fig. S4 f). The peaks could correspond to SnS (peaks at ~96, ~163, ~189 (main), 220 cm^{-1} and 288 cm^{-1}) or Sn_2S_3 (peaks at 183, 234, 251 and 307 cm^{-1}) [1]. Chandrasekar et al. investigated the orientation dependent Raman peaks for SnS and found that the peak at ~95 cm^{-1}, 192 cm^{-1} and 218 cm^{-1} are especially strong along one axis, suggesting that the SnS crystals in our films may have a preferential growth orientation [2]. These authors used excitation wavelengths of 632 nm [1] and 647 nm [2] where we used 532 nm, which may help explain the differences in the relative peak intensities we measured.

Surprisingly, XRD of the low-fluence film showed only ∑CZTS peaks – very low intensity and broad compared to the other films even taking into account that this film was thinner than the other films deposited at 300 °C in this study. The absence of SnS_y or other secondary phase peaks might indicate that the secondary phase crystals mainly occurred on the surface and did not occupy a large fraction of the total volume, since they are not detected in XRD.

[1] L. Price, I. Parkin, A. Hardy, R. Clark, Atmospheric pressure chemical vapor deposition of tin sulfides (SnS, Sn2S3, and SnS2) on glass, Chem. Mater. (1999) 1792–1799. doi:10.1021/cm990005z.

[2] H.R. Chandrasekhar, R.G. Humphreys, U. Zwick, M. Cardona, Infrared and Raman spectra of the IV-VI compounds SnS and SnSe, Phys. Rev. B. 15 (1977) 2177–2183. doi:10.1103/PhysRevB.15.2177.

Appendix E

Reference matrix for PLD of CZTS

As part of the work in this thesis, I surveyed the litereature on PLD of CZTS, CTS and ZnS. While there were no publications on PLD of CTS when I started my project, there was a wealth of literature on ZnS and also a significant amount of work on CZTS. I found it easiest to keep track of the references using the tabular form shown in this appendix. The tables have been recently updated.

References on PLD of CZTS are shown here while references on PLD of ZnS are shown in Appendix F.

Table E.1: Literature on PLD of CZTS

Ref	PLD specs	Substrate	Fluence	Pressure	Composition	Main results/notes
UV PLD of CZTS						
[168]	266 nm NdYAG 10 ns	500 °C SLG substrate 5 hour deposition	0.5-0.8 J/cm2 2 mm2 spot	vacuum	Cu-rich, Zn-poor at lower fluence, Cu-rich, S-poor at highest fluence (EMPA, error reported, films 0.5-0.6 µm thick). Polycrystalline CZTS-phase target, Cu-poor, Zn-rich, S-rich	Describe making target in detail; made up of CZTS polycrystals, not binaries. Conclude that transfer is non-stoichiometric. Very low deposition rate.
[159]	248 nm KrF 30 ns	300-450 °C Mo/SLG	200 mJ laser energy (no mention of spot size or window transmission)	vacuum	EDX of 1.2 um films: Cu-rich, Zn-poor, S-poor (no error bars). Attribute to light Cu mass, volatile Zn and S	Describe making target. Strain: CZTS lattice parameters in as-deposited film smaller than bulk. (112) orientation of as-deposited films. Less (112) orientation at higher temp.
[160]	248 nm KrF 10 ns	room temperature Mo/SLG	1.5 J/cm2	Vacuum 2*10-4 mbar	EMPA: Cu-poor, Sn + S rich compared to target as-deposited. Target Cu-rich, S-poor. Post-annealed film 1 micron thick.	Describe making target. Anneal in N2 300-500 °C, results in higher Sn content [or maybe SnS migrates to surface?]. Droplets on surface of Cu-Sn-S. Surface resistivity > volume resistivity. Make 1.74 % efficient solar cell.
[158]	As above 30 Hz	As above	0.7, 1.5 J/cm2	As above	Composition of as-deposited films not shown. Target Cu-rich, S-poor	Fewer droplets at lower fluence in as-deposited films. Droplets are Cu-Sn-S. Very low crystallinity as-deposited (low, broad XRD peak). Anneal in N2 and H2S+N2, best stoichiometry with H2S. Make solar cell, worse than previous, maybe due to non-optimal composition.

Continued on Next Page...

Table E.1 – Continued

Ref	PLD specs	Substrate	Fluence	Pressure	Composition	Main results/notes
[139]	As above	n-type (100) GaP substrate 300, 350, 400 °C	0.85 J/cm2	Vacuum 2*10-4 mbar	EMPA: S-poor, metals almost stoichiometric. Least S-poor at 300 and 400 °C. Zn-rich/Sn poor at 400 °C. Films several µm thick	Epitaxial growth at 350 and 400 °C (narrowest/tallest XRD peaks at 400 °C)
[169]	248 nm KrF 25 ns 10 Hz	450 °C Si wafer substrates with 100 nm SiO2 coating	2 J/cm2	Vacuum (4*10-6)	Cu-rich, Sn-poor target. Films are 1µm thick. As-deposited Cu-poor, Zn-, Sn- and S-rich (esp Sn-rich) comp to target (EDX), Zn-poor compared to Sn-content. Acknowledge that there can be significant error in quantification- mainly use it for comparison.	Measure thermal conductivity. Anneal some films in N2+H2S at 500 °C for 5 hrs and find much higher thermal conductivity in these. As-deposited films are (112)-oriented. Small secondary phase peaks.
[161]	248 nm KrF 5 Hz	200-400 °C SLG	200 mJ laser energy (no spot size or window transmission)	vacuum	EDX of films 450-650 nm thick. Cu-rich, S-poor, esp. above 300 °C. Sn decrease at 350, 400 °C. SIMS: Cu-rich back, Zn + Na-rich surface. [Trust trends rather than absolute numbers due to thinness]	Higher temp: thinner films, larger grains
[162]	248 nm KrF 10 ns 5 Hz	300 °C ITO	130-180 mJ laser energy (no spot size or window transmission)	10^{-7} mbar	EDX of films 500 nm thick. Sn-rich and S-poor [but cannot fully trust absolute numbers due to thinness] Target composition not shown.	No trend in composition compared to different laser energy. 100's of nm grain size, smooth, densely packed.
[164]	355 nm, 4-7 ns	RT-300 °C. Corning glass, Si wafer	0.5-4	Vacuum 10^{-6} mbar	EDX on films only about 200 nm thick. No Zn at lowest fluence.	CZTS compound target (commercial). Show droplets and droplet composition (some Sn-rich, some Cu-rich)

Continued on Next Page...

Table E.1 – Continued

Ref	PLD specs	Substrate	Fluence	Pressure	Composition	Main results/notes
PLD at 248 nm of CZTO and CZT targets						
[170]	248 nm 25 ns	Room temp, Mo/SLG	?	Vacuum (5*10-6 mbar)	Composition variation in as-deposited CZTO films as a function of dist from sample center quite homogenous [Measure with EDX on 275-350 nm thick film so absolute quantification inaccurate]	PLD of CZTO followed by sulfurization/ selenization: CZTS/ CZTSSe/ CZTSe. Reach 4.94 % solar cell efficiency for CZTS. 500 nm thick sulfurized film. Anneal at 570 °C, 20 min, with S and Sn powder.
[167]	248 nm 4 Hz	RT-150 °C 5 cm target-substrate dist, 3.75 mm2 spot	2.8 J/cm2, 20000 pulses so 1 hr 20 min. Ablation threshold at 2 J/cm2	0.006-0.03 mbar (Ar?) (pump to 10-6 mbar first)	EDX of 90-300 nm films, so measured change in composition may be an effect of thickness. Apparently Zn-rich, higher pressure gives less Cu in films. Apparently Cu-rich droplets, [difficult to measure droplet composition accurately].	PLD of CZT followed by sulfurization at 550 °C in Ar/H2S flow 1 hr (optimized). Multiphase target; describe target making. Very low dep rate. Droplets partly absorbed in film after annealing.
PLD of CZTSe at 1064 nm						
[165]	1064 Nd:YAG, 25 ns, 10 Hz	Corning glass, RT to 500 °C	1.5 J/cm2	Vacuum	Se- and Sn-poor relative to target and to ideal composition.	Describes CZTSe target making. Droplets have same composition as target. Fewer droplets at higher deposition temperature.
PLD of metallic targets at 1064 nm in H2S						
[163]	1064 Nd:YAG 10 ns 20-30 Hz	Room temperature	Quartz Increase fluence from 2.5 to 7.5 J/cm^2 to prevent CuxS on the target.	H2S	RBS: From Zn-rich/ Sn-poor target get slightly Zn-rich, Sn-poor, S-stoichiometric films. Cannot resolve Cu/Zn RBS peak, so deposited Cu-free film to confirm. S stoichiometric at high fluence only with high (0.05 mbar) H2S pressure and low (20 Hz) rep rate.	Cu and Zn/Sn target. H2S gas sulfurizes Cu target unless high fluence is used. As-deposited films peel off in air. Anneal in N2 at 300-400 °C: relieve strain, better adhesion and also CZTS XRD & Raman peaks. Do not check ZnS with UV Raman

Appendix F

Reference matrix for PLD of ZnS

References on PLD of ZnS are shown below, while references on PLD CZTS were shown in Appendix E.

Table F.1: Literature on PLD of ZnS, ordered from most recent (2015) to oldest (1993)

Ref	PLD type	Fluence (J/cm2)	Pressure (mbar)	Substrate temp (°C)	Structure	Other
UV PLD of CZTS						
[201]	248 nm KrF, 20 ns	1-7.8	Ar 0.003	550	(111) oriented cubic and/or (001) oriented hex on (100)-oriented Si. For high Cr-content, some hex phase	Cr-doped ZnS (Cr 2-5 atomic %). Cr-content increases with fluence. XRD FWHM lowest for lowest Cr-content (and lowest fluence).
[12]	248 nm KrF	6	Vacuum 10^{-8}	100-250-350	Zinc blende (cubic) on porous Si,	Higher deposition temp -> better luminescence, larger grains. Luminescence (blue-green) ascribed to defect centers in the band gap
[260]	248 nm KrF	6	Vacuum 10^{-8}	200	Zinc blende (cubic) on porous Si after vacuum anneal at 300 C	Longer anneal at 300 C ->larger grains (smaller FWHM of XRD peak)
[200]	1064 nm Nd:YAG, 10 ns	<1	0.03	450 (whole chamber is heated)	Cubic/hex nanoparticle films	Aim to obtain bimetallic clusters of ZnCoS (where Co-substitutes Zn on some lattice sites). Use 2 % Co target; deposits were Co-enriched.
[195]	248 nm, 30 ns, 5-10 Hz	75-250 mJ	?	550	002-oriented α ZnS on Al2O3 (0001) substrates. Crystallinity poor at lower temperature.	Aim: p-type transparent conductive ZnS by Cu-doping. Targets ZnS mixed with 6-26 % Cu2S. S-rich films at 550 C and lower. S-loss above 550 C. Cu-incorporation increase at high fluence
[261]	248 nm , 25 ns, 10 MHz	400 mJ	$2*10^{-7}$	200, 300, 400	Si, fused silica substrates. Cubic phase as-deposited at 200 C (maybe with a bit of wurtzite mixed in? side peak), wurtzite phase at 300, 400 C	RBS evaluation of composition: 51 % Zn, 49 % S at 400 C.

Continued on Next Page...

Table F.1 – Continued

Ref	PLD type	Fluence (J/cm2)	Pressure (mbar)	Substrate temp (°C)	Structure	Other
[262]	266 and 532 nm Nd:YAG, 5 ns, 10 Hz	<1	?	25, 400	Si (100) substrates. Cubic ZnS at 450 C, 266 nm and 25 C, 532 nm. Cubic/amorphous mix at 25 C, 266 nm. 532 nm at 450 C: nanoparticles with mixed hex/cubic phase.	Film thickness increased when substrate temperature increased from 25 to 450 C. UV results in smooth films, 532 nm gives particulates up to hundreds of nm.
[197]	248 nm KrF	3-5	0_2: 10^{-8}	450-725	Hexagonal on sapphire. Higher dep temperature gives smaller FWHM of XRD peaks	Beam-target angle 30° Higher dep temperature gives higher surface roughness due to crystal growth, lower growth rate (re-evaporation) and higher band gap energy (from Tauc plot based on transmittance). No ZnO detected. (assume same laser as Chung et al. 2009, Ferroelectrics)
[84]	248 nm 25 ns	200 mJ	10^{-5}	20-600	Cubic (111)-oriented on quartz glass at ALL temps. Smaller FWHM of XRD peaks at higher temp.	Dense, smooth films, 30 nm grains. Increased band gap with increasing deposition temp. XRF shows somewhat S-rich films, decreasing S-content (from 52 % towards 50 %) with increasing deposition temperature
[199]	355 nm Nd:YAG, 5 ns pulses	0.3 J/cm2, 5*10-5 mbar		400	They claim cubic ZnS but there are unidentified peaks (not hex ZnS, not Zn)	330 nm thick film. Excitonic transitions below band gap

Continued on Next Page...

Table F.1 – Continued

Ref	PLD type	Fluence (J/cm2)	Pressure (mbar)	Substrate temp (°C)	Structure	Other
[198]	248 nm KrF, 20 ns pulses	2 J/cm2	H2S: Ar mix (25 % H2S) up to 0.1 mbar	500	Epitaxial cubic ZnS on (111) YSZ at 0.1 mbar Mix cubic/hex epitaxial ZnS on (111) YSZ at lower pressure Non-epitaxial growth (?polycrystalline?) of cubic and maybe hex ZnS on (001) YSZ	Substrate chosen because it is transparent though the lattice mismatch with ZnS is 5 %. Attribute absorption in monocrystalline sample to exciton A in zinc-blende at approx 3.8 eV. Mix cubic/hex sample has broad photoluminescence peak from sulfur vacancy or stacking faults
[263]	193 nm ArF	2 J/cm2	Ar: 0.7	150, 250, 350, 450	On (001) Si and ITO coated glass substrates: cubic at 150 C, mix hex/cubic at higher temperatures. Mostly hex at 450 C. Film orientation different on the two substrates.	ZnS:Mn. Focus on ellipsometry and photoluminescence changes at different temperatures. Increasing band gap with increasing temperature.
[76]	XeCl 308 nm laser 10 Hz	123 mJ	10^{-5}	150-250	Si. Orientation of ZnS to match Si substrate (1 0 0). Thick films also have (1 1 1) peak matching target	ZnS:Ag,Cl Without background gas, the plume partially erodes the new layers resulting in slow growth and smooth appearance
[264]	248 nm KrF 10 Hz	5	10^{-6}	200-700	Cubic on Si (001): (111) oriented at 600 C, (100) oriented at 700 C	ZnS+ species are present along with Zn+ and S+ in plume (most Zn+ and S+). Decreasing growth rate with increasing T (re-evaporation of Zn+ and S+ species?)
[81]	248 nm KrF 10 Hz	20 J/cm2	?	RT-700	Hex on Si and sapphire Amorphous at RT (but they have an XRD peak, only a wide one?)	Growth rate drops with T (especially above 550 C) Band gap E increases with T Film close to stoichiometric (indistinguishable from standard +/- 1 % by EDS measurement)

Continued on Next Page...

Table F.1 – Continued

Ref	PLD type	Fluence (J/cm2)	Pressure (mbar)	Substrate temp (°C)	Structure	Other
[106]	XeCl 308 nm	0.02-2	0.8-10 bar	RT	NA	Study the ablation threshold of ZnS thin films under high pressure. Harder to ablate thinner films (200 vs 600 nm vs bulk) due to heat transport by Si-substrate, harder to ablate under pressure.
[79]	248 nm KrF laser 1.5x3 mm spot size, 50 Hz	2.5 J/cm2,	Ar 10^{-3}	350	SnO2 and ITO coated glass. High background pressure gives better crystallinity and higher cathode luminescence	ZnS:Mn target Anneal at 450 deg C for 2 hrs in Ar at 10^{-3} mbar. Stoichiometry best at short target-substrate distance, Zn proportion increases at long distances
[137]	193 nm ArF 10 Hz 15 ns pulse Spot 2 mm2	1.2-1.5 J/cm2	5x10^{-8} Ar gas added at varied pressure	100-400 deg C (?)	(111) and (100) InP, GaAs substrate 300 C best crystallinity. Above 400 C, bad surface morphology, loss of S/Se (100) substrate: (100)-oriented cubic crystal. (111) substrate: cubic ZnS as well. Glass: random in-plane orientation, still cubic	Collective investigation of ZnS, ZnSe, CdS, CdSe, CdTe Sustrate-target dist varied, optimized for ZnS at 10 cm with 1.2 J/cm2 High dep rate (high laser repetition rate) gives defects b/c atoms need time to migrate (10 Hz is low enough to avoid this)
[78]	248 nm 50-100 Hz 20 ns pulse	2.5 ? 20 J/cm2	N2 10^{-3}	250 deg dep, 500 dec C anneal	Borosilicate glass. Mix of hex and cubic ZnS - ? or not clear? Mostly hex after anneal ? or at least more crystalline	Mg-doped ZnS target Stoichiometry: More Zn at high fluence, more S at low fluence
[196]	248 nm KrF 1 Hz 35 ns pulse	0.2-1.5 J/cm2	2*10^{-5}	Substrate T from 150 to 450 °C	GaAs	Epitaxial growth. Films faulted near interface with GaAs. Optimum T 325 °C judged from XRD rocking curve minimum. Films 275 nm thick (± 25 nm)

Appendix G

Material constants

Table G.1: Thermal properties of S, Zn, Sn, Cu, Ag, ZnS, cubic Cu_2SnS_3 and CZTS [265, 266, 105, 267]. T_m: melting point (1 atm); T_b: boiling point (1 atm); C_p: Specific heat at 273-300 K ; E_{atom}: cohesive energy. Numbers for S refer to the monoclinic form. Below 95 °C, S is in rhombohedral form, 2.2 g/cm^3.

	density (ρ) g/cm^3	T_m K	T_b K	C_p J/(g K)	$\Delta\ H_{fus}$ kJ/mol	$\Delta\ H_{vap}$ kJ/mol	E_{atom} eV/atom
S	2.0	115	445	0.71	1.24	45	2.85
Zn	7.14	693	1180	0.39	7.3	124	1.35
Sn	7.30	505	2705	0.23	7.1	296	3.14
Cu	8.94	1357	2840	0.39	13.3	301	2.95
Ag	10.5	1234	2483	0.24	12.0	258	3.49
α-ZnS	4.1	1293	1973				na
β-ZnS	4.1	(1020) ‡	1973	0.47	30	206	na
CTS (cubic)	5.0	1110-1120		0.4			na
CZTS	4.56	1259	1973	0.05			na

‡ phase transition from β-ZnS to α-ZnS

Table G.2: Thermal diffusivity and thermal diffusion length assuming a power pulse of 5 ns for S, Cu, Zn, Sn, Ag, ZnS, cubic Cu_2SnS_3 and CZTS as well as the band gap E_g for the semiconductors [105, 265, 266, 268]. Numbers for S refer to the monoclinic form. Below 95 °C, S is in rhombohedral form, 2.2 g/cm^3.

	Thermal diffusivity, κ_{th} W/(cm K)			Thermal diffusion length, l_{th} µm			E_g eV
	@300K	@1000 K	@3000 K	@300K	@1000 K	@3000 K	@300K
S	0.0003			0.063			na
Zn	1.2	0.67		0.9	0.7		na
Sn	0.67	0.41		0.9	0.7		na
Cu	4.0	3.56	1.8	1.5	1.4	1.0	na
Ag	4.3	3.75	1.9	1.8	1.7	1.2	na
αZnS	0.46	-	-				3.67
βZnS	0.25	-	-	0.5			3.49
CTS cubic	0.03	-	-	0.02			≈ 1
CZTS	0.05	-	-	0.6			≈ 1.5

Bibliography

[1] F. Cardarelli, *Materials Handbook*. London: Springer Verlag, 2008.

[2] Kaneka Corporation, "World's Highest Conversion Efficiency of 26.33% Achieved in a Crystalline Silicon Solar Cell - A World First in a Practical Cell Size," 2016.

[3] M. A. Green, K. Emery, Y. Hishikawa, W. Warta, and E. D. Dunlop, "Solar cell efficiency tables (version 48)," *Prog. Photovoltaics Res. Appl.*, vol. 24, pp. 905–913, jul 2016.

[4] I. Clover, "Third phase of Dubai's DEWA solar project attracts record low bid of US 2.99 cents/kWh: pv-magazine," 2016.

[5] S. Delbos, "Kesterite thin films for photovoltaics: a review," *EPJ Photovoltaics*, vol. 3, p. 35004, aug 2012.

[6] R. Jaffe, J. Price, M. Hitzman, and F. Slakey, "Energy Critical Elements," *APS News*, 2011.

[7] P. Harrisson, "Global Sulphur Market Outlook," tech. rep., 2013.

[8] G. Haxel, J. Hedrick, and G. Orris, "Rare Earth Elements — Critical Resources for High Technology," tech. rep., 2002.

[9] U.S. Geological Survey, "Metal Prices in the United States Through 2010," tech. rep., 2013.

[10] S. Tajima, M. Umehara, M. Hasegawa, T. Mise, and T. Itoh, "Cu2ZnSnS4 photovoltaic cell with improved efficiency fabricated by high-temperature annealing after CdS buffer-layer deposition," *Prog. Photovoltaics Res. Appl.*, vol. 25, pp. 14–22, jan 2017.

[11] S. Tajima, T. Itoh, H. Hazama, K. Ohishi, and R. Asahi, "Improvement of the open-circuit voltage of Cu 2 ZnSnS 4 solar cells using a two-layer structure," *Appl. Phys. Express*, vol. 8, p. 082302, aug 2015.

[12] C.-f. Wang, B. Hu, W.-b. Li, and H.-h. Yi, "Luminescence properties of ZnS/porous Si composites," *Opt. - Int. J. Light Electron Opt.*, vol. 125, pp. 554–556, jan 2014.

[13] B. Shin, O. Gunawan, Y. Zhu, N. A. Bojarczuk, S. J. Chey, and S. Guha, "Thin film solar cell with 8.4 % power conversion efficiency using an earth-abundant Cu2ZnSnS4 absorber," *Prog. Photovoltaics Res. Appl.*, vol. 21, pp. 72–76, 2013.

[14] K. Wang, O. Gunawan, T. Todorov, B. Shin, S. J. Chey, N. A. Bojarczuk, D. Mitzi, and S. Guha, "Thermally evaporated Cu2ZnSnS4 solar cells," *Appl. Phys. Lett.*, vol. 97, no. 14, p. 143508, 2010.

[15] M. Nakashima, T. Yamaguchi, H. Itani, J. Sasano, and M. Izaki, "Cu2SnS3 thin film solar cells prepared by thermal crystallization of evaporated Cu/Sn precursors in sulfur and tin atmosphere," *Phys. Status Solidi*, vol. 12, pp. 761–764, jun 2015.

[16] A. Kanai, K. Toyonaga, K. Chino, H. Katagiri, and H. Araki, "Fabrication of Cu2SnS3 thin-film solar cells with power conversion efficiency of over 4%," *Jpn. J. Appl. Phys.*, vol. 54, p. 08KC06, aug 2015.

[17] N. Aihara, H. Araki, A. Takeuchi, K. Jimbo, and H. Katagiri, "Fabrication of Cu 2 SnS 3 thin films by sulfurization of evaporated Cu-Sn precursors for solar cells," *Phys. status solidi*, vol. 10, pp. 1086–1092, aug 2013.

[18] M. Umehara, Y. Takeda, T. Motohiro, T. Sakai, H. Awano, and R. Maekawa, "Cu2Sn(1-x)Ge(x)S3 (x = 0.17) Thin-Film Solar Cells with High Conversion Efficiency of 6.0%," *Appl. Phys. Express*, vol. 6, p. 045501, apr 2013.

[19] H. Katagiri, "Survey of Development of CZTS-based Thin Film Solar Cells," in *3rd Int. Conf. Photonics 2012*, (Penang), 2012.

[20] T. Mise, S. Tajima, T. Fukano, K. Higuchi, T. Washio, K. Jimbo, and H. Katagiri, "Improving the photovoltaic performance of co-evaporated Cu2ZnSnS4 thin-film solar cells by incorporation of sodium from NaF layers," *Prog. Photovoltaics Res. Appl.*, vol. 24, pp. 1009–1015, jul 2016.

[21] A. Crovetto, *Cu2ZnSnS4 solar cells: Physics and technology by alternative tracks*. Phd thesis, Technical University of Denmark, 2016.

[22] D. A. R. Barkhouse, R. Haight, N. Sakai, H. Hiroi, H. Sugimoto, and D. B. Mitzi, "Cd-free buffer layer materials on Cu 2ZnSn(S xSe 1-x) 4: Band alignments with ZnO, ZnS, and In 2S 3," *Appl. Phys. Lett.*, vol. 100, no. 19, pp. 4–9, 2012.

[23] International Energy Agency IEA, "Key Renewables Trends: Excerpt from Renewables Information (2016 edition)," tech. rep., 2016.

[24] B. Burger, K. Kiefer, C. Kost, S. Nold, S. Philipps, R. Preu, J. Rentsch, T. Schlegl, G. Stryi-Hipp, G. Willeke, H. Wirth, I. Brucker, A. Häberle, and W. Warmuth, "Photovoltaics Report," tech. rep., Fraunhofer Institute for Solar Energy Systems, 2016.

[25] V. Fthenakis, "Sustainability of photovoltaics: The case for thin-film solar cells," *Renew. Sustain. Energy Rev.*, vol. 13, pp. 2746–2750, dec 2009.

[26] V. Fthenakis and H. C. Kim, "Land use and electricity generation: A life-cycle analysis," *Renew. Sustain. Energy Rev.*, vol. 13, no. 6-7, pp. 1465–1474, 2009.

[27] A. Anctil and V. Fthenakis, "Critical metals in strategic photovoltaic technologies: abundance versus recyclability," *Prog. Photovoltaics Res. Appl.*, vol. 21, pp. 1253–1259, sep 2013.

[28] J. Collier, S. Wu, and D. Apul, "Life cycle environmental impacts from CZTS (copper zinc tin sulfide) and Zn3P2 (zinc phosphide) thin film PV (photovoltaic) cells," *Energy*, vol. 74, pp. 314–321, 2014.

[29] C. R. Chitambar, "Medical applications and toxicities of gallium compounds," *Int. J. Environ. Res. Public Health*, vol. 7, no. 5, pp. 2337–2361, 2010.

[30] M. Stage, "Landbruget om svinefoder: Alternativer til zink og kobber er dyre," 2015.

[31] M. A. Green, *Solar Cells - Operating Principles, Technology and System Applications*. The University of New South Wales, 1998.

[32] C. Honsberg and S. Bowden, "PVEducation," 2014.

[33] S. Siebentritt, "Why are kesterite solar cells not 20% efficient?," *Thin Solid Films*, vol. 535, pp. 1–4, may 2013.

[34] S. Schorr, "Part II The Physics and Chemistry of Quaternary Chalcogenide Semiconductors," in *Copp. Zinc Tin Sulfide-Based Thin-Film Sol. Cells* (K. Ito, ed.), ch. 3, pp. 55–72, John Wiley & Sons, Ltd, 1 ed., 2015.

[35] A. Lafond, L. Choubrac, C. Guillot-Deudon, P. Fertey, M. Evain, and S. Jobic, "X-ray resonant single-crystal diffraction technique, a powerful tool to investigate the kesterite structure of the photovoltaic Cu2ZnSnS4 compound," *Acta Crystallogr. Sect. B Struct. Sci. Cryst. Eng. Mater.*, vol. 70, no. 2, pp. 390–394, 2014.

[36] J. J. S. Scragg, L. Choubrac, A. Lafond, T. Ericson, and C. Platzer-Björkman, "A low-temperature order-disorder transition in Cu2ZnSnS4 thin films," *Appl. Phys. Lett.*, vol. 104, p. 041911, jan 2014.

[37] X. Liu, Y. Feng, H. Cui, F. Liu, X. Hao, G. Conibeer, D. B. Mitzi, and M. Green, "The current status and future prospects of kesterite solar cells: a brief review," *Prog. Photovoltaics Res. Appl.*, vol. 24, pp. 879–898, jun 2016.

[38] H. Du, F. Yan, M. Young, B. To, C. S. Jiang, P. Dippo, D. Kuciauskas, Z. Chi, E. A. Lund, C. Hancock, W. M. Hlaing Oo, M. A. Scarpulla, and G. Teeter, "Investigation of combinatorial coevaporated thin film Cu2ZnSnS4. I. Temperature effect, crystalline phases, morphology, and photoluminescence," *J. Appl. Phys.*, vol. 115, p. 173502, may 2014.

[39] D. M. Berg, M. Arasimowicz, R. Djemour, L. Gütay, S. Siebentritt, S. Schorr, X. Fontané, V. Izquierdo-Roca, A. Pérez-Rodriguez, and P. J. Dale, "Discrimination and detection limits of secondary phases in Cu2ZnSnS4 using X-ray diffraction and Raman spectroscopy," *Thin Solid Films*, vol. 569, no. 0, pp. 113–123, 2014.

[40] I. Olekseyuk, I. Dudchak, and L. Piskach, "Phase equilibria in the Cu2S–ZnS–SnS2 system," *J. Alloys Compd.*, vol. 368, pp. 135–143, apr 2004.

[41] J. J. Scragg, *Copper Zinc Tin Sulfide Thin Films for Photovoltaics - Synthesis and Characterisation by Electrochemical Methods*. Phd thesis, The University of Bath, 2011.

[42] M. Dimitrievska, A. Fairbrother, E. Saucedo, A. Pérez-Rodríguez, and V. Izquierdo-Roca, "Influence of compositionally induced defects on the vibrational properties of device grade Cu2ZnSnSe4 absorbers for kesterite based solar cells," *Appl. Phys. Lett.*, vol. 106, no. 7, p. 073903, 2015.

[43] J. Just, C. M. Sutter-Fella, D. Lützenkirchen-Hecht, R. Frahm, S. Schorr, and T. Unold, "Secondary phases and their influence on the composition of the kesterite phase in CZTS and CZTSe thin films," *Phys. Chem. Chem. Phys.*, vol. 18, no. 23, pp. 15988–15994, 2016.

[44] L. E. Valle Rios, K. Neldner, G. Gurieva, and S. Schorr, "Existence of off-stoichiometric single phase kesterite," *J. Alloys Compd.*, vol. 657, pp. 408–413, 2016.

[45] S. Chen, A. Walsh, X. G. Gong, and S. H. Wei, "Classification of lattice defects in the kesterite Cu2ZnSnS4 and Cu2ZnSnSe4 earth-abundant solar cell absorbers," *Adv. Mater.*, vol. 25, no. 11, pp. 1522–1539, 2013.

[46] L. Choubrac, A. Lafond, C. Guillot-Deudon, Y. Moëlo, and S. Jobic, "Structure flexibility of the Cu2ZnSnS4 absorber in low-cost photovoltaic cells: from the stoichiometric to the copper-poor compounds.," *Inorg. Chem.*, vol. 51, pp. 3346–8, mar 2012.

[47] D. B. Mitzi, O. Gunawan, T. K. Todorov, and D. A. R. Barkhouse, "Prospects and performance limitations for Cu-Zn-Sn-S-Se photovoltaic technology," *Phil. Trans. R. Soc. A*, vol. 371, no. July, p. 20110432, 2013.

[48] M. Jiang and X. Yan, "Cu2ZnSnS4 Thin Film Solar Cells: Present Status and Future Prospects," in *Sol. Cells - Res. Appl. Perspect.*, ch. 5, InTech, mar 2013.

[49] C. Platzer-Björkman, T. Ericson, J. Scragg, and T. Kubart, "Reactive Sputtering of CZTS," in *Copp. Zinc Tin Sulfide-Based Thin-Film Sol. Cells* (K. Ito, ed.), pp. 203–219, John Wiley & Sons, Ltd., 2015.

[50] M. Grossberg, J. Krustok, and O. Volobujeva, "Growth of CZTS-Based Monograins and Their Application to Membrane Solar Cells," in *CZTS-based Thin Film Sol. Cells* (K. Ito, ed.), pp. 289–310, John Wiley & Sons, Ltd., 2015.

[51] B.-A. Schubert, B. Marsen, S. Cinque, T. Unold, R. Klenk, S. Schorr, and H.-W. Schock, "Cu2ZnSnS4 thin film solar cells by fast coevaporation," *Prog. Photovoltaics Res. Appl.*, vol. 19, pp. 93–96, jan 2011.

[52] I. Repins, C. Beall, N. Vora, C. DeHart, D. Kuciauskas, P. Dippo, B. To, J. Mann, W.-C. Hsu, A. Goodrich, and R. Noufi, "Co-evaporated Cu2ZnSnSe4 films and devices," *Sol. Energy Mater. Sol. Cells*, vol. 101, pp. 154–159, jun 2012.

[53] B. Shin, Y. Zhu, T. Gershon, N. A. Bojarczuk, and S. Guha, "Epitaxial growth of kesterite Cu2ZnSnS4 on a Si(001) substrate by thermal co-evaporation," *Thin Solid Films*, vol. 556, pp. 9–12, 2014.

[54] A. Redinger and S. Siebentritt, "Coevaporation of Cu2ZnSnSe4 thin films," *Appl. Phys. Lett.*, vol. 97, no. 9, p. 092111, 2010.

[55] A. Weber, R. Mainz, and H. W. Schock, "On the Sn loss from thin films of the material system Cu-Zn-Sn-S in high vacuum," *J. Appl. Phys.*, vol. 107, no. 1, pp. 1–6, 2010.

[56] A. Redinger, D. M. Berg, P. J. Dale, and S. Siebentritt, "The consequences of kesterite equilibria for efficient solar cells.," *J. Am. Chem. Soc.*, vol. 133, pp. 3320–3, mar 2011.

[57] J. J. Scragg, T. Ericson, T. Kubart, M. Edoff, and C. Platzer-Björkman, "Chemical Insights into the Instability of Cu2ZnSnS4 Films during Annealing," *Chem. Mater.*, vol. 23, pp. 4625–4633, oct 2011.

[58] J. J. Scragg, P. J. Dale, D. Colombara, and L. M. Peter, "Thermodynamic Aspects of the Synthesis of Thin-Film Materials for Solar Cells," *ChemPhysChem*, vol. 13, pp. 3035–3046, aug 2012.

[59] X. Wu, F. Lai, Y. Lin, Z. Huang, and R. Chen, "Effects of substrate temperature and annealing on the structure and optical properties of ZnS film," *Proc. SPIE Vol.*, vol. 6722, p. 67222L, dec 2007.

[60] Y.-T. T. Zhai, S. Chen, J.-H. H. Yang, H.-J. J. Xiang, X.-G. G. Gong, A. Walsh, J. Kang, and S.-H. H. Wei, "Structural diversity and electronic properties of Cu2SnX3 (X=S, Se): A first-principles investigation," *Phys. Rev. B*, vol. 84, pp. 1–6, aug 2011.

[61] P. A. Fernandes, P. M. P. Salomé, and A. F. Da Cunha, "CuxSnSx+1 (x = 2, 3) thin films grown by sulfurization of metallic precursors deposited by dc magnetron sputtering," *Phys. Status Solidi Curr. Top. Solid State Phys.*, vol. 7, no. 3-4, pp. 901–904, 2010.

[62] D. Avellaneda, M. T. S. Nair, and P. K. Nair, "Cu2SnS3 and Cu4SnS4 Thin Films via Chemical Deposition for Photovoltaic Application," *J. Electrochem. Soc.*, vol. 157, no. 6, p. D346, 2010.

[63] D. M. Berg, R. Djemour, L. Gütay, S. Siebentritt, P. J. Dale, X. Fontane, V. Izquierdo-Roca, and A. Pérez-Rodriguez, "Raman analysis of monoclinic Cu2SnS3 thin films," *Appl. Phys. Lett.*, vol. 100, no. 19, p. 192103, 2012.

[64] X.-a. Chen, H. Wada, A. Sato, and M. Mieno, "Synthesis, Electrical Conductivity, and Crystal Structure of Cu4Sn7S16 and Structure Refinement of Cu2SnS3," *J. Solid State Chem.*, vol. 151, no. 139, pp. 144–151, 1998.

[65] P. Zawadzki, A. Zakutayev, and S. Lany, "Entropy-Driven Clustering in Tetrahedrally Bonded Multinary Materials," *Phys. Rev. Appl.*, vol. 3, p. 034007, 2015.

[66] D. Tiwari, T. K. Chaudhuri, T. Shripathi, U. Deshpande, and R. Rawat, "Non-toxic, earth-abundant 2% efficient Cu2SnS3 solar cell based on tetragonal films direct-coated from single metal-organic precursor solution," *Sol. Energy Mater. Sol. Cells*, vol. 113, pp. 165–170, jun 2013.

[67] P. Zawadzki, L. L. Baranowski, H. Peng, E. S. Toberer, D. S. Ginley, W. Tumas, A. Zakutayev, and S. Lany, "Evaluation of photovoltaic materials within the Cu-Sn-S family," *Appl. Phys. Lett.*, vol. 103, no. 25, p. 253902, 2013.

[68] M. Nakashima, J. Fujimoto, T. Yamaguchi, and M. Izaki, "Cu2SnS3 thin-film solar cells fabricated by sulfurization from NaF/Cu/Sn stacked precursor," *Appl. Phys. Express*, vol. 8, p. 042303, apr 2015.

[69] T. A. Kuku and O. A. Fakolujo, "Photovoltaic characteristics of thin films of Cu2SnS3," *Sol. Energy Mater.*, vol. 16, no. 1-3, pp. 199–204, 1987.

[70] L. L. Baranowski, P. Zawadzki, S. Christensen, D. Nordlund, S. Lany, A. C. Tamboli, L. Gedvilas, D. S. Ginley, W. Tumas, E. S. Toberer, and A. Zakutayev, "Control of Doping in Cu2SnS3 through Defects and Alloying," *Chem. Mater.*, vol. 26, pp. 4951–4959, sep 2014.

[71] S. Fiechter, M. Martinez, G. Schmidt, W. Henrion, and Y. Tomm, "Phase relations and optical properties of semiconducting ternary sulfides in the system Cu–Sn–S," *J. Phys. Chem. Solids*, vol. 64, pp. 1859–1862, sep 2003.

[72] M. E. Fleet, "Structural transformations in natural ZnS," *Am. Mineral.*, vol. 62, pp. 540–546, 1977.

[73] A. S. Barnard, C. A. Feigl, and S. P. Russo, "Morphological and phase stability of zinc blende, amorphous and mixed core-shell ZnS nanoparticles - Supplementary Information," *Nanoscale*, vol. 2, pp. 2294–2301, 2010.

[74] J. T. Cox, J. E. Waylonis, and W. R. Hunter, "Optical Properties of Zinc Sulfide in the Vacuum Ultraviolet," *J. Opt. Soc. Am.*, vol. 49, no. 8, pp. 807–810, 1959.

[75] J. McCloy and R. Tustison, "Technical Issues in Processing," in *Chem. Vap. Depos. Zinc Sulfide*, ch. 2, pp. 31–51, Society of Photo-Optical Instrumentation Engineers, 2013.

[76] K. T. Hillie, C. Curren, and H. C. Swart, "ZnS thin films grown on Si (100) by XeCl pulsed laser ablation," *Appl. Surf. Sci.*, vol. 177, pp. 73–77, 2001.

[77] R. P. Rao, "Recent Developments in Display Phosphors," in *Proc ASID*, (New Delhi), pp. 7–8, 2006.

[78] M. McLaughlin, H. F. Sakeek, P. Maguire, W. G. Graham, J. Molloy, T. Morrow, S. Laverty, and J. Anderson, "Properties of ZnS thin films prepared by 248-nm pulsed laser deposition," *Appl. Phys. Lett.*, vol. 63, no. 14, p. 1865, 1993.

[79] C. Karner, P. Maguire, M. McLaughlin, S. Laverty, W. G. Graham, T. Morrow, and R. M. Bowman, "Pulsed-laser deposition of ZnS and SrS for ACTFEL and field-emission displays," in *Second Int. Conf. Sci. Technol. Disp. Phosphors*, 1996.

[80] T. Kryshtab, V. S. Khomchenko, J. A. Andraca-Adame, V. E. Rodionov, V. B. Khachatryan, and Y. A. Tzyrkunov, "The influence of doping element on structural and luminescent characteristics of ZnS thin films," *Superlattices Microstruct.*, vol. 40, no. 4-6 SPEC. ISS., pp. 651–656, 2006.

[81] Z.-J. Xin, R. J. Peaty, H. N. Rutt, and R. W. Eason, "Epitaxial growth of high-quality ZnS films on sapphire and silicon by pulsed laser deposition," *Semicond. Sci. Technol.*, vol. 14, pp. 695–698, aug 1999.

[82] Y. C. Cheng, C. Q. Jin, F. Gao, X. L. Wu, W. Zhong, S. H. Li, and P. K. Chu, "Raman scattering study of zinc blende and wurtzite ZnS," *J. Appl. Phys.*, vol. 106, no. 12, 2009.

[83] S. Zanettini, F. Bissoli, L. Nasi, P. Ranzieri, and E. Gilioli, "Low temperature pulsed electron deposition and characterization of ZnS films for application in solar cells," *Cryst. Res. Technol.*, vol. 46, pp. 881–884, aug 2011.

[84] P.-f. Luo, G.-s. Jiang, and C.-f. Zhu, "Pulsed Laser Deposition ZnS Buffer Layers for CIGS Solar Cells," *Chinese J. Chem. Phys.*, vol. 22, pp. 97–101, feb 2009.

[85] T. Kato, H. Hiroi, N. Sakai, S. Muraoka, and H. Sugimoto, "Characterization of Front and Back Interfaces on Cu2ZnSnS4 Thin-Film Solar Cells," in *27th Eur. Photovolt. Sol. Energy Conf. Exhib.*, pp. 2236–2239, 2012.

[86] M. Nguyen, K. Ernits, K. F. Tai, C. F. Ng, S. S. Pramana, W. A. Sasangka, S. K. Batabyal, T. Holopainen, D. Meissner, A. Neisser, and L. H.Wong, "ZnS buffer layer for Cu2ZnSn(SSe)4 monograin layer solar cell," *Sol. Energy*, vol. 111, pp. 344–349, 2015.

[87] D. A. R. Barkhouse, O. Gunawan, T. Gokmen, T. K. Todorov, and D. B. Mitzi, "Device characteristics of a 10.1% hydrazine-processed Cu2ZnSn(Se,S)4 solar cell," *Prog. Photovoltaics Res. Appl.*, vol. 20, pp. 6–11, jan 2012.

[88] T. Unold and H. Schock, "Nonconventional (Non-Silicon-Based) Photovoltaic Materials," *Annu. Rev. Mater. Res.*, vol. 41, pp. 297–321, aug 2011.

[89] C. N. R. Rao and K. P. R. Pisharody, "Transition metal sulfides," *Prog. Solid State Chem.*, vol. 10, pp. 207–270, 1974.

[90] P. Sinsermsuksakul, L. Sun, S. W. Lee, H. H. Park, S. B. Kim, C. Yang, and R. G. Gordon, "Overcoming Efficiency Limitations of SnS-Based Solar Cells," *Adv. Energy Mater.*, vol. 4, no. 15, pp. 1–7, 2014.

[91] L. A. Burton and A. Walsh, "Phase Stability of the Earth-Abundant Tin Sulfides SnS, SnS2, and Sn2S3," *J. Phys. Chem. C*, vol. 116, pp. 24262–24267, nov 2012.

[92] T. Venkatesan, K. S. Harshavardhan, M. Strikovski, and J. Kim, "Recent Advances in the Deposition of Multi-Component Oxide Films by Pulsed Energy Deposition," in *Thin Film. Heterostruct. Oxide Electron.* (S. B. Ogale, ed.), ch. 13, pp. 385–413, New York: Springer Science+Business Media, Inc, 2005.

[93] M. N. R. Ashfold, F. Claeyssens, G. M. Fuge, and S. J. Henley, "Pulsed laser ablation and deposition of thin films," *Chem. Soc. Rev.*, vol. 33, pp. 23–31, jan 2004.

[94] J. Schou, "Physical aspects of the pulsed laser deposition technique: The stoichiometric transfer of material from target to film," *Appl. Surf. Sci.*, vol. 255, pp. 5191–5198, mar 2009.

[95] R. Eason, ed., *Pulsed Laser Deposition of Thin Films.* Hoboken, NJ, USA: John Wiley & Sons, Inc., nov 2006.

[96] D. H. Lowndes, "Growth and Doping of Compound Semiconductor Films by Pulsed Laser Ablation," in *Laser Ablation Desorption, Exp. Methods Phys. Sci.* (J. C. Miller and R. F. Haglund, eds.), vol. 30, pp. 475–571, Academic Press, 1997.

[97] D. B. Geohegan, "Diagnostics and characteristics of pulsed laser deposition laser plasmas," in *Pulsed Laser Depos. Thin Film.* (D. B. Chrisey and G. K. Hubler, eds.), ch. 5, New York: John Wiley & Sons, Inc., 1994.

[98] P. R. Willmott and J. R. Huber, "Pulsed laser vaporization and deposition," *Rev. Mod. Phys.*, vol. 72, no. 1, pp. 315–328, 2000.

[99] J. Schou, "Laser Beam-Solid Interactions: Fundamental Aspects," in *Mater. Surf. Process. by Dir. Energy Tech.* (Y. Pauleau, ed.), ch. 2, pp. 35–66, Elsevier Ltd, 1 ed., 2006.

[100] K. S. Harshavardhan and M. Strikovski, "Pulsed Electron-Beam Deposition of High Temperature Superconducting Films for Coated Conductor Applications," in *Second. HTS Conduct.* (A. Goyal, ed.), ch. 8, pp. 109–133, Boston: Kluwer Academic Publishers, 2005.

[101] M. D. Strikovski, J. Kim, and S. H. Kolagani, "Plasma Energetics in Pulsed Laser and Pulsed Electron Deposition," in *Springer Handb. Cryst. Growth, Part E Ep. Growth Thin Film.* (G. Dhanaray, B. Kullaiah, V. Prasad, and M. Dudley, eds.), ch. 35, pp. 1193–1211, Heidelberg: Springer-Verlag Berlin Heidelberg, 2010.

[102] A. Piel, *Plasma Physics.* Berlin, Heidelberg: Springer-Verlag, 2010.

[103] N. L. LaHaye, S. S. Harilal, P. K. Diwakar, and A. Hassanein, "The effect of laser pulse duration on ICP-MS signal intensity, elemental fractionation, and detection limits in fs-LA-ICP-MS," *J. Anal. At. Spectrom.*, vol. 28, no. 11, p. 1781, 2013.

[104] P. Balling and J. Schou, "Femtosecond-laser ablation dynamics of dielectrics: basics and applications for thin films," *Reports Prog. Phys.*, vol. 76, p. 036502, mar 2013.

[105] D. Bäuerle, *Laser Processing and Chemistry*. Berlin, Heidelberg: Springer Berlin Heidelberg, 2011.

[106] W. M. Cranton, P. H. Key, D. Sands, C. B. Thomas, and F. X. Wagner, "XeCl laser ablation of thin film ZnS," *Appl. Surf. Sci.*, vol. 96-98, pp. 501–504, 1996.

[107] S. Fähler and H.-U. Krebs, "Calculations and experiments of material removal and kinetic energy during pulsed laser ablation of metals," *Appl. Surf. Sci.*, vol. 96-98, no. 95, pp. 61–65, 1996.

[108] W. Svendsen, O. Ellegaard, and J. Schou, "Laser ablation deposition measurements from silver and nickel," *Appl. Phys. A*, vol. 255, pp. 247–255, 1996.

[109] R. Kelly and R. W. Dreyfus, "On the effect of Knudsen-layer formation on studies of vaporization, sputtering, and desorption," *Surf. Sci.*, vol. 198, no. 1-2, pp. 263–276, 1988.

[110] S. I. Anisimov, D. Bäuerle, and B. Luk'yanchuk, "Gas dynamics and film profiles in pulsed-laser deposition of materials," *Phys. Rev. B*, vol. 48, no. 16, 1993.

[111] A. Ojeda-G-P, C. W. Schneider, M. Döbeli, T. Lippert, and A. Wokaun, "The flip-over effect in pulsed laser deposition: Is it relevant at high background gas pressures?," *Appl. Surf. Sci.*, vol. 357, pp. 2055–2062, 2015.

[112] T. N. Hansen, J. Schou, and J. G. Lunney, "Angle-resolved energy distributions of laser ablated silver ions in vacuum," *Appl. Phys. Lett.*, vol. 72, no. 15, p. 1829, 1998.

[113] D. B. Geohegan, "Fast intensified-CCD photography of YBa2Cu3O 7-x laser ablation in vacuum and ambient oxygen," *Appl. Phys. Lett.*, vol. 60, no. 22, pp. 2732–2734, 1992.

[114] J. Chen, Y. Lv, M. Döbeli, Y. Li, X. Shi, and L. Chen, "Composition control of pulsed laser deposited copper (I) chalcogenide thin films via plasma/Ar interactions," *Sci. China Mater.*, vol. 58, no. 4, pp. 263–268, 2015.

[115] D. P. Norton, "Pulsed Laser Deposition of Complex Materials: Progress Toward Applications," in *Pulsed Laser Depos. Thin Film.* (R. W. Eason, ed.), pp. 3–31, Hoboken, NJ, USA: John Wiley & Sons, Inc., mar 2006.

[116] H.-U. Krebs, "Pulsed Laser Deposition of Metals," in *Pulsed Laser Depos. Thin Film.* (R. W. Eason, ed.), ch. 16, pp. 363–382, Hoboken, NJ, USA: John Wiley & Sons, Inc., 2006.

[117] Z. Zhu, X. J. Zheng, and W. Li, "Multilayer growth of BaTiO3 thin films via pulsed laser deposition: An energy-dependent kinetic Monte Carlo simulation," *Appl. Surf. Sci.*, vol. 256, no. 20, pp. 5876–5881, 2010.

[118] T. Venkatesan, X. D. Wu, A. Inam, and J. B. Wachtman, "Observation of two distinct components during pulsed laser deposition of high Tc superconducting films," *Appl. Phys. Lett.*, vol. 52, no. 14, pp. 1193–1195, 1988.

[119] H.-U. Krebs, S. Fiihler, and O. Bremert, "Laser deposition of metallic alloys and multilayers," *Appl. Surf. Sci.*, vol. 86, pp. 86–89, 1995.

[120] A. Ojeda-G-P, C. W. Schneider, M. Döbeli, T. Lippert, and A. Wokaun, "The importance of pressure and mass ratios when depositing multi-element oxide thin films by pulsed laser deposition," *Appl. Surf. Sci.*, vol. 389, pp. 126–134, 2016.

[121] T. Ohnishi, M. Lippmaa, T. Yamamoto, S. Meguro, and H. Koinuma, "Improved stoichiometry and misfit control in perovskite thin film formation at a critical fluence by pulsed laser deposition," *Appl. Phys. Lett.*, vol. 87, no. 24, pp. 1–3, 2005.

[122] B. Dam, J. H. Rector, J. Johansson, J. Huijbregtse, and D. G. De Groot, "Mechanism of incongruent ablation of SrTiO[sub 3]," *J. Appl. Phys.*, vol. 83, no. 6, p. 3386, 1998.

[123] H. Uchiki, O. Machida, A. Tanaka, and H. Hirasawa, "Preparation of AgGaS2 Films by Excimer Laser Deposition," *Jpn. J. Appl. Phys.*, vol. 32, pp. 764–766, 1993.

[124] R. F. Haglund, "Mechanisms of Laser Induced Desorption and Ablation," in *Laser Ablation Desorption, Exp. Methods Phys. Sci.* (J. C. Miller and R. F. Haglund, eds.), ch. 2, pp. 15–138, Academic Press, 1997.

[125] M. Frumar, B. Frumarova, P. Nemec, T. Wagner, J. Jedelsky, and M. Hrdlicka, "Thin chalcogenide films prepared by pulsed laser deposition – new amorphous materials applicable in optoelectronics and chemical sensors," *J. Non. Cryst. Solids*, vol. 352, pp. 544–561, may 2006.

[126] H. M. Christen and G. Eres, "Recent advances in pulsed-laser deposition of complex oxides.," *J. Phys. Condens. Mat.*, vol. 20, no. 26, p. 264005, 2008.

[127] J. Lanèok, M. Jelí, L. Jastrabí, L. Soukup, J. Oswald, K. Jurek, and F. Flory, "Laser deposition of waveguiding Ti : sapphire and chalcogenide glass AsS films," *Superf. y Vacio*, vol. 9, pp. 316–319, 1999.

[128] A. Zakery, "Low loss waveguides in pulsed laser deposited arsenic sulfide chalcogenide films," *J. Phys. D. Appl. Phys.*, vol. 35, no. 22, pp. 2909–2913, 2002.

[129] S. Fähler, M. Störmer, and H.-U. Krebs, "Origin and avoidance of droplets during laser ablation of metals," *Appl. Surf. Sci.*, vol. 109-110, pp. 433–436, 1997.

[130] R. Timm, P. R. Willmott, and J. R. Huber, "Ablation and blow-off characteristics at 248 nm of Al, Sn and Ti targets used for thin film pulsed laser deposition," *J. Appl. Phys.*, vol. 80, no. 3, p. 1794, 1996.

[131] T. Ohnishi, H. Koinuma, and M. Lippmaa, "Pulsed laser deposition of oxide thin films," *Appl. Surf. Sci.*, vol. 252, no. 7, pp. 2466–2471, 2006.

[132] S. Rampino, F. Pattini, C. Malagù, L. Pozzetti, M. Stefancich, and M. Bronzoni, "Application of a substrate bias to control the droplet density on Cu(In,Ga)Se2 thin films grown by Pulsed Electron Deposition," *Thin Solid Films*, vol. 562, pp. 307–313, jul 2014.

[133] W. Kautek, B. Roas, and L. Schultz, "Formation of Y-Ba-Cu-oxide thin films by Pulsed Laser Deposition: A comparative study in the UV, visible and IR range," *Thin Solid Films*, vol. 191, no. Preparation and characterization, pp. 317–2334, 1990.

[134] G. Koren, A. Gupta, R. J. Baseman, M. I. Lutwyche, and R. B. Laibowitz, "Laser wavelength dependent properties of YBa2Cu3O7δ thin films deposited by laser ablation," *Appl. Phys. Lett.*, vol. 55, no. 23, p. 2450, 1989.

[135] A. C. Cazzaniga, *Fabrication of thin film CZTS solar cells with Pulsed Laser Deposition. PhD thesis.* Phd thesis, Technical University of Denmark, 2016.

[136] K. Ujimoto, T. Yoshimura, A. Ashida, and N. Fujimura, "Effect of Target Surface Microstructure on Morphological and Electrical Properties of Pulsed- Laser-Deposited BiFeO3 Epitaxial Thin Films," *Jpn. J. Appl. Phys.*, vol. 52, p. 045803, 2013.

[137] W. P. Shen and H. S. Kwok, "Crystalline phases of II-VI compound semiconductors grown by pulsed laser deposition," *Appl. Phys. Lett.*, vol. 65, no. 17, p. 2162, 1994.

[138] S. Amoruso, R. Bruzzese, N. Spinelli, R. Velotta, M. Vitiello, and X. Wang, "Dynamics of laser-ablated MgB2 plasma expanding in argon probed by optical emission spectroscopy," *Phys. Rev. B*, vol. 67, p. 224503, jun 2003.

[139] K. Sekiguchi, K. Tanaka, K. Moriya, and H. Uchiki, "Epitaxial growth of Cu2ZnSnS4 thin films by pulsed laser deposition," *Phys. Status Solidi*, vol. 3, pp. 2618–2621, sep 2006.

[140] J. J. Dubowski, D. F. Williams, P. B. Sewell, and P. Norman, "Epitaxial growth of (100) CdTe on (100) GaAs induced by pulsed laser evaporation," *Appl. Phys. Lett.*, vol. 46, no. 11, pp. 1081–1083, 1985.

[141] J. Levoska, S. Leppävouri, F. Wang, O. Kusmartseva, A. E. Hill, E. Ahmed, R. D. Tomlinson, and R. D. Pilkington, "Pulsed laser ablation deposition of CuInSe2 and CuIn(1-x)Ga(x)Se2 thin films," *Phys. Scr.*, vol. T54, pp. 244–247, 1994.

[142] L. W. Martin, Y. H. Chu, and R. Ramesh, "Advances in the growth and characterization of magnetic, ferroelectric, and multiferroic oxide thin films," *Mater. Sci. Eng. R Reports*, vol. 68, no. 4-6, pp. 89–133, 2010.

[143] J. Christiansen and C. Schultheiss, "Production of High Current Particle Beams by Low Pressure Spark Discharges," *Zeitschrift für Phys. A*, vol. 290, pp. 35–41, 1979.

[144] Q. D. Jiang, F. C. Matacotta, G. Masciarelli, F. Fuso, E. Arimondo, M. C. Konijnenberg, G. Müller, C. Schultheiss, and G. Sandrin, "Characterization and in situ fluorescence diagnostic of the deposition of YBa2Cu3O(7-x) thin films by pseudo-spark electron beam ablation," *Supercond. Sci. Technol.*, vol. 6, no. 8, pp. 567–572, 1993.

[145] Q. D. Jiang, F. C. Matacotta, M. C. Konijnenberg, G. Müller, and C. Schultheiss, "Deposition of YBa2Cu307_x thin films by channel-spark pulsed electron beam ablation," *Thin Solid Films*, vol. 241, pp. 2896–2902, 1994.

[146] M. Nistor, N. B. Mandache, and J. Perrière, "Pulsed electron beam deposition of oxides thin films," *J. Phys. D. Appl. Phys.*, vol. 41, p. 165205, aug 2008.

[147] M. Höbel, J. Geerk, G. Linker, and C. Schultheiss, "Deposition of superconducting YBaCuO thin films by pseudospark ablation," *Appl. Phys. Lett.*, vol. 56, no. 10, pp. 973–975, 1990.

[148] S. Rampino, N. Armani, F. Bissoli, M. Bronzoni, D. Calestani, M. Calicchio, N. Delmonte, E. Gilioli, E. Gombia, R. Mosca, L. Nasi, F. Pattini, a. Zappettini, and M. Mazzer, "15% efficient Cu(In,Ga)Se2 solar cells obtained by low-temperature pulsed electron deposition," *Appl. Phys. Lett.*, vol. 101, no. 13, p. 132107, 2012.

[149] S. Tricot, N. Semmar, L. Lebbah, and C. Boulmer-Leborgne, "ZnO sublimation using a polyenergetic pulsed electron beam source: numerical simulation and validation," *J. Phys. D. Appl. Phys.*, vol. 43, no. 6, p. 65301, 2010.

[150] S. Tricot, C. Boulmer-Leborgne, M. Nistor, E. Millon, and J. Perrière, "Dynamics of a pulsed-electron beam induced plasma: application to the growth of zinc oxide thin films," *J. Phys. D. Appl. Phys.*, vol. 41, no. 17, p. 175205, 2008.

[151] M. Strikovski and K. S. Harshavardhan, "Parameters that control pulsed electron beam ablation of materials and film deposition processes," *Appl. Phys. Lett.*, vol. 82, no. 6, pp. 853–855, 2003.

[152] M. Nistor and N. B. Mandache, "Electron energy distribution function of a pulsed intense electron beam," *J. Optoelectron. Adv. Mater.*, vol. 7, no. 3, pp. 1619–1622, 2005.

[153] F. Pattini, M. Bronzoni, F. Mezzadri, F. Bissoli, E. Gilioli, and S. Rampino, "Dynamics of evaporation from CuGaSe2 targets in pulsed electron deposition technique," *J. Phys. D. Appl. Phys.*, vol. 46, p. 245101, jun 2013.

[154] J. Li, H. Du, J. Yarbrough, A. Norman, K. Jones, G. Teeter, F. L. Terry, and D. Levi, "Spectral optical properties of Cu2ZnSnS4 thin film between 0.73 and 6.5 eV," *Opt. Express*, vol. 20, p. A327, mar 2012.

[155] D. Drouin, A. R. Couture, D. Joly, X. Tastet, V. Aimez, and R. Gauvin, "CASINO V2.42—A Fast and Easy-to-use Modeling Tool for Scanning Electron Microscopy and Microanalysis Users," *Scanning*, vol. 29, pp. 92–101, may 2007.

[156] S. Adachi, "Physical Properties: Compiled Experimental Data," in *Copp. Zinc Tin Sulfide-Based Thin-Film Sol. Cells* (K. Ito, ed.), ch. 7, pp. 149–178, Wiley, 1 ed., 2015.

[157] A. Cazzaniga, A. Crovetto, C. Yan, K. Sun, X. Hao, J. Ramis Estelrich, S. Canulescu, E. Stamate, N. Pryds, O. Hansen, and J. Schou, "Ultra-thin Cu2ZnSnS4 solar cell prepared by pulsed laser deposition," *submitted*, 2016.

[158] K. Moriya, K. Tanaka, and H. Uchiki, "Cu2ZnSnS4 Thin Films Annealed in H 2 S Atmosphere for Solar Cell Absorber Prepared by Pulsed Laser Deposition," *Jpn. J. Appl. Phys.*, vol. 47, pp. 602–604, jan 2008.

[159] L. Sun, J. He, H. Kong, F. Yue, P. Yang, and J. Chu, "Structure, composition and optical properties of Cu2ZnSnS4 thin films deposited by Pulsed Laser Deposition method," *Sol. Energy Mater. Sol. Cells*, vol. 95, pp. 2907–2913, oct 2011.

[160] K. Moriya, K. Tanaka, and H. Uchiki, "Fabrication of Cu 2 ZnSnS 4 Thin-Film Solar Cell Prepared by Pulsed Laser Deposition," *Jpn. J. Appl. Phys.*, vol. 46, pp. 5780–5781, sep 2007.

[161] M. Byeon, E. Chung, J. Kim, T. Hong, J. Jin, E. Jeong, J. Bae, Y. Kim, S. Park, W. Oh, Y. Huh, S. Chang, S. Lee, I. Jung, and J. Hwang, "The effects for the deposition temperature onto the structural, compositional and optical properties of pulsed laser ablated Cu2ZnSnS4 thin films grown on soda lime glass substrates," *Thin Solid Films*, vol. 546, pp. 387–392, nov 2013.

[162] H. He, M. Xiao, Q. Zhong, Y. Fu, X. Shen, and J. Zeng, "Influence of laser pulse energy on the microstructure and optical properties of Cu2ZnSnS4 films by one-step pulsed laser deposition," *Ceram. Int.*, vol. 40, pp. 13263–13267, 2014.

[163] G. Surgina, a.V. Zenkevich, I. Sipaylo, V. Nevolin, W. Drube, P. Teterin, and M. Minnekaev, "Reactive pulsed laser deposition of Cu2ZnSnS4 thin films in H2S," *Thin Solid Films*, vol. 535, pp. 44–47, may 2013.

[164] N. S. Che Sulaiman, C. H. Nee, S. L. Yap, Y. S. Lee, T. Y. Tou, and S. S. Yap, "The growth of nanostructured Cu2ZnSnS4 films by pulsed laser deposition," *Appl. Surf. Sci.*, vol. 354, pp. 42–47, nov 2015.

[165] R. A. Wibowo, E. S. Lee, B. Munir, and K. H. Kim, "Pulsed laser deposition of quaternary Cu 2ZnSnSe 4 thin films," *Phys. Status Solidi Appl. Mater. Sci.*, vol. 204, no. 10, pp. 3373–3379, 2007.

[166] J. He, L. Sun, Y. Chen, J. Jiang, P. Yang, and J. Chu, "Influence of sulfurization pressure on Cu2ZnSnS4 thin films and solar cells prepared by sulfurization of metallic precursors," *J. Power Sources*, vol. 273, pp. 600–607, 2015.

[167] S. Kala, H. Kaur, A. Rastogi, V. N. Singh, and T. D. Senguttuvan, "Structural and opto-electronic features of pulsed laser ablation grown Cu2ZnSnS4 films for photovoltaic applications," *J. Alloys Compd.*, vol. 658, pp. 324–330, 2016.

[168] Y. Watanabe, H. Miura, Y.-G. Shim, and K. Wakita, "Cu2ZnSnS4 thin film deposited by pulse laser deposition," *Phys. Status Solidi*, vol. 12, no. 6, pp. 733–736, 2015.

[169] W. D. Thompson, A. Nandur, and B. E. White, "Thermal transport in Cu2ZnSnS4 thin films," *J. Appl. Phys.*, vol. 119, no. 9, p. 095108, 2016.

[170] X. Jin, C. Yuan, L. Zhang, G. Jiang, W. Liu, and C. Zhu, "Pulsed laser deposition of Cu2ZnSn(SxSe1 - x)4 thin film solar cells using quaternary oxide target prepared by combustion method," *Sol. Energy Mater. Sol. Cells*, vol. 155, pp. 216–225, oct 2016.

[171] A. D. Compaan, "Laser processing for thin-film photovoltaics," in *Proc. SPIE, Laser-Induced Thin Film Process.* (J. J. Dubowski, ed.), vol. 2403, p. 224, apr 1995.

[172] H. Dittrich, M. Klose, M. Brieger, R. Schäffler, and H.-W. Schock, "CuInSe2 Thin Film Solar Cells by Pulsed Laser Deposition," in *Photovolt. Spec. Conf. 1993, Conf. Rec. Twenty Third IEEE*, pp. 617–620, 1993.

[173] M. Klose, R. Schäffler, G. Irmer, M. Brieger, D. Schmid, and H. W. Schock, "Raman scattering investigations of CuInSe2 films deposited by co-evaporation and laser ablation," *Proc. SPIE Laser-Induced Thin Film Process.*, vol. 2403, pp. 240–250, 1995.

[174] V. F. Gremenok, E. P. Zaretskaya, I. V. Bodnar, and I. A. Victorov, "Chalcopyrite CuGa(x)In(1-x)Se2 Thin Films Produced by Laser-Assisted Evaporation," in *Jpn. J. Appl. Phys.*, vol. 32, pp. 90–91, 1993.

[175] A. S. Kindyak, V. Kindyak, and V. Gremenok, "Energy-gap variations in thin laser-deposited Cu(In,Ga)Se2 films," *Mater. Lett.*, vol. 28, pp. 273–275, 1996.

[176] A. Yoshida, N. Tanahashi, T. Tanaka, Y. Demizu, Y. Yamamoto, and T. Yamaguchi, "Preparation of CuInSe2 thin films with large grain by excimer laser ablation," *Sol. Energy Mater. Sol. Cells*, vol. 50, no. 1-4, pp. 7–12, 1998.

[177] A. Tverjanovich, E. N. Borisov, E. S. Vasilieva, O. V. Tolochko, I. E. Vahhi, S. Bereznev, and Y. S. Tveryanovich, "CuInSe2 thin films deposited by UV laser ablation," *Sol. Energy Mater. Sol. Cells*, vol. 90, no. 20, pp. 3624–3632, 2006.

[178] S. Leppavuori, J. Levoska, A. E. Hill, R. D. Tomlinson, J. Frantti, O. Kusmartseva, H. Moilanen, and R. D. Pilkington, "Laser ablation deposition as a preparation method for sensor materials," *Sensors Actuators A. Phys.*, vol. 41, no. 1-3, pp. 145–149, 1994.

[179] Y. H. Jo, B. C. Mohanty, and Y. S. Cho, "Enhanced electrical properties of pulsed laser-deposited CuIn0.7Ga0.3Se2 thin films via processing control," *Sol. Energy*, vol. 84, no. 12, pp. 2213–2218, 2010.

[180] S.-c. Chen, D.-H. Hsieh, H. Jiang, Y.-K. Liao, F.-i. Lai, C.-H. Chen, C. W. Luo, J.-Y. Juang, Y.-l. Chueh, K.-H. Wu, and H.-C. Kuo, "Growth and characterization of Cu(In,Ga)Se2 thin films by nanosecond and femtosecond pulsed laser deposition," *Nanoscale Res. Lett.*, vol. 9, pp. 1–7, jan 2014.

[181] C.-C. Chen, X. Qi, W.-C. Chang, M.-G. Tsai, I.-G. Chen, C.-Y. Lin, P.-H. Wu, and K.-P. Chang, "The effects of pulse repetition rate on the structural, optical, and electrical properties of CIGS films grown by pulsed laser deposition," *Appl. Surf. Sci.*, vol. 351, pp. 772–778, 2015.

[182] M. G. Tsai, H. T. Tung, I. G. Chen, C. C. Chen, Y. F. Wu, X. D. Qi, Y. Hwu, C. Y. Lin, P. H. Wu, and C. W. Cheng, "Annealing Effect on the Properties of Cu(In0.7Ga0.3)Se-2 Thin Films Grown by Femtosecond Pulsed Laser Deposition," *J. Am. Ceram. Soc.*, vol. 96, no. 32252, pp. 2419–2423, 2013.

[183] S. H. Lee, C. K. Kim, J. H. In, D. S. Kim, H. J. Ham, and S. H. Jeong, "Nd:YAG laser ablation characteristics of thin CIGS solar cell films," *Appl. Phys. B*, vol. 113, no. 3, pp. 403–409, 2013.

[184] A. D. Compaan, M. M. Pearce, P. M. Voyles, D. Spry, Z. Feng, A. Fischer, M. Shao, and R. G. Bohn, "Pulsed laser deposition for CdTe-based photovoltaics," in *Proc. SPIE, Laser-Induced Thin Film Process.* (J. J. Dubowski, ed.), vol. 2403, p. 232, apr 1995.

[185] P. Bhattacharya and D. N. Bose, "Pulsed laser deposition of CdTe thin films for heterojunctions on silicon," *Semicond. Sci. Technol.*, vol. 6, pp. 384–387, may 1991.

[186] R. A. Ismail, K. I. Hassan, O. A. Abdulrazaq, and W. H. Abode, "Optoelectronic properties of CdTe/Si heterojunction prepared by pulsed Nd:YAG-laser deposition technique," *Mater. Sci. Semicond. Process.*, vol. 10, no. 1, pp. 19–23, 2007.

[187] X. Yang, Z. Bao, R. Luo, B. Liu, P. Tang, B. Li, J. Zhang, W. Li, L. Wu, and L. Feng, "Preparation and characterization of pulsed laser deposited CdS/CdSe bi-layer films for CdTe solar cell application," *Mater. Sci. Semicond. Process.*, vol. 48, pp. 27–32, 2016.

[188] A. Kadhim, P. Harrison, J. Meeth, A. Al-Mebir, G. Zeng, and J. Wu, "Development of Combinatorial Pulsed Laser Deposition for Expedited Device Optimization in CdTe/CdS Thin-Film Solar Cells," *Int. J. Opt.*, vol. 2016, pp. 1–7, 2016.

[189] B. Li, J. Liu, G. Xu, R. Lu, L. Feng, and J. Wu, "Development of pulsed laser deposition for CdS/CdTe thin film solar cells," *Appl. Phys. Lett.*, vol. 101, no. 15, 2012.

[190] A. Bylica, P. Sagan, I. Virt, G. Wisz, M. Bester, I. Stefaniuk, and M. Kuzma, "Layers of CdTe and CdS obtained by PLD on ITO substrates," *Thin Solid Films*, vol. 511-512, pp. 439–442, 2006.

[191] B. Ghosh, S. Hussain, D. Ghosh, R. Bhar, and A. K. Pal, "Studies on CdTe films deposited by pulsed laser deposition technique," *Phys. B Condens. Matter*, vol. 407, no. 21, pp. 4214–4220, 2012.

[192] S. K. Pandey, U. Tiwari, R. Raman, C. Prakash, V. Krishna, V. Dutta, and K. Zimik, "Growth of cubic and hexagonal CdTe thin films by pulsed laser deposition," *Thin Solid Films*, vol. 473, no. 1, pp. 54–57, 2005.

[193] Y. Tairov and V. Tsvetkov, "Growth of Polytypic Crystals," in *Cryst. Growth Prop. Appl. Vol. 10, Growth Defect Struct.* (H. C. Freyhardt, ed.), p. 24, Springer Verlag, 1984.

[194] N. R. Paudel, K. A. Wieland, and A. D. Compaan, "Ultrathin CdS/CdTe solar cells by sputtering," *Sol. Energy Mater. Sol. Cells*, vol. 105, pp. 109–112, 2012.

[195] A. M. Diamond, L. Corbellini, K. R. Balasubramaniam, S. Chen, S. Wang, T. S. Matthews, L. W. Wang, R. Ramesh, and J. W. Ager, "Copper-alloyed ZnS as a p-type transparent conducting material," *Phys. Status Solidi Appl. Mater. Sci.*, vol. 209, no. 11, pp. 2101–2107, 2012.

[196] J. W. McCamy, D. H. Lowndes, J. D. Budai, R. A. Zuhr, and X. Zhang, "Epitaxial ZnS films grown on GaAs (001) and (111) by pulsed-laser ablation," *J. Appl. Phys.*, vol. 73, no. 11, pp. 7818–7822, 1993.

[197] J.-K. Chung, W.-J. Kim, S. S. Kim, T. K. Song, S.-Y. Park, T. K. Lee, and C. J. Kim, "The epitaxial growth and optical properties of ZnS thin films, deposited by pulsed laser deposition," *Phys. Scr.*, vol. T139, p. 014018, may 2010.

[198] H. Hiramatsu, H. Ohta, M. Hirano, and H. Hosono, "Heteroepitaxial growth of single-phase zinc blende ZnS films on transparent substrates by pulsed laser deposition under H2S atmosphere," *Solid State Commun.*, vol. 124, pp. 411–415, dec 2002.

[199] S. Yano, R. Schroeder, B. Ullrich, and H. Sakai, "Absorption and photocurrent properties of thin ZnS films formed by pulsed-laser deposition on quartz," *Thin Solid Films*, vol. 423, pp. 273–276, jan 2003.

[200] M. Jadraque, A. B. Evtushenko, D. Ávila-Brande, M. López-Arias, V. Loriot, Y. G. Shukhov, L. S. Kibis, A. V. Bulgakov, and M. Martín, "Co-doped ZnS clusters and nanostructures produced by pulsed laser ablation," *J. Phys. Chem. C*, vol. 117, no. 10, pp. 5416–5423, 2013.

[201] M. Nematollahi, X. Yang, U. J. Gibson, and T. W. Reenaas, "Pulsed laser ablation and deposition of ZnS:Cr," *Thin Solid Films*, vol. 590, pp. 28–32, 2015.

[202] J. G. Kang, Y. D. Ko, K. J. Choi, J. G. Park, and D. W. Kim, "Fabrication of tin monosulfide nanosheet arrays using laser ablation," *Appl. Phys. A Mater. Sci. Process.*, vol. 103, no. 2, pp. 505–510, 2011.

[203] S. Y. Hong, R. Popovitz-Biro, Y. Prior, and R. Tenne, "Synthesis of SnS2/SnS fullerene-like nanoparticles: A superlattice with polyhedral shape," *J. Am. Chem. Soc.*, vol. 125, pp. 10470–10474, aug 2003.

[204] Y. Lv, J. Chen, R.-K. Zheng, J. Song, T. Zhang, X. Li, X. Shi, and L. Chen, "Photo-induced enhancement of the power factor of Cu2S thermoelectric films," *Sci. Rep.*, vol. 5, p. 16291, 2015.

[205] B. Yang, H. X. Guo, K. B. Yin, Y. D. Xia, L. Chen, J. Yin, and Z. G. Liu, "The <00l>-oriented growth of Cu2S films and its switching properties," *J. Electroceramics*, vol. 22, no. 1-3, pp. 87–90, 2009.

[206] M. Mahjouri-Samani, M.-w. Lin, K. Wang, A. R. Lupini, J. Lee, L. Basile, A. Boulesbaa, C. M. Rouleau, A. A. Puretzky, I. N. Ivanov, K. Xiao, M. Yoon, and D. B. Geohegan, "Patterned arrays of lateral heterojunctions within monolayer two-dimensional semiconductors," *Nat. Commun.*, vol. 6, p. 7749, jul 2015.

[207] P. Němec, V. Nazabal, M. Pavlišta, A. Moreac, M. Frumar, and M. Vlček, "Gallium-lanthanum-sulphide amorphous thin films prepared by pulsed laser deposition," *Mater. Chem. Phys.*, vol. 117, no. 1, pp. 23–25, 2009.

[208] J. Schubert, M. J. Schöning, C. Schmidt, M. Siegert, S. Mesters, W. Zander, P. Kordos, H. Lüth, A. Legin, Y. G. Mourzina, B. Seleznev, and Y. G. Vlasov, "Chalcogenide-based thin film sensors prepared by pulsed laser deposition technique," *Appl. Phys. A*, vol. 69, no. 7, pp. S803–S805, 1999.

[209] Y. G. Mourzina, M. J. Schöning, J. Schubert, W. Zander, A. V. Legin, Y. G. Vlasov, and H. Lüth, "Copper, cadmium and thallium thin film sensors based on chalcogenide glasses," *Anal. Chim. Acta*, vol. 433, no. 1, pp. 103–110, 2001.

[210] R. B. Ettlinger, A. Cazzaniga, S. Canulescu, N. Pryds, and J. Schou, "Pulsed laser deposition from ZnS and Cu2SnS3 multicomponent targets," *Appl. Surf. Sci.*, vol. 336, pp. 385–390, 2015.

[211] R. B. Ettlinger and M. A. Sørensen, "Force Spectroscopy of DNA and RNA: Structure and Kinetics from Single-Molecule Experiments," in *Nucleic Acid Nanotechnol.* (J. Kjems, E. Ferapontova, and K. V. Gothelf, eds.), vol. 29 of *Nucleic Acids and Molecular Biology*, ch. 2, pp. 23–52, Berlin, Heidelberg: Springer Berlin Heidelberg, 2014.

[212] A. Kramida, Y. Ralchenko, J. Reader, and NIST ASD Team, "NIST Atomic Spectra Database (ver. 5.3)," 2015.

[213] A. Crovetto, R. Chen, R. B. Ettlinger, A. C. Cazzaniga, J. Schou, C. Persson, and O. Hansen, "Dielectric function and double absorption onset of monoclinic Cu2SnS3: Origin of experimental features explained by first-principles calculations," *Sol. Energy Mater. Sol. Cells*, vol. 154, pp. 121–129, 2016.

[214] M. Fox, "Chapter 1-2, Appendix A," in *Opt. Prop. Solids*, pp. 1–48, 255–262, 2001.

[215] A. B. Murphy, "Band-gap determination from diffuse reflectance measurements of semiconductor films, and application to photoelectrochemical water-splitting," *Sol. Energy Mater. Sol. Cells*, vol. 91, no. 14, pp. 1326–1337, 2007.

[216] P. Kubelka, "New Contributions to the Optics of Intensely Light-Scattering Materials. Part I," *J. Opt. Soc. Am.*, vol. 38, no. 5, pp. 448–457, 1948.

[217] R. López and R. Gómez, "Band-gap energy estimation from diffuse reflectance measurements on sol-gel and commercial TiO 2: A comparative study," *J. Sol-Gel Sci. Technol.*, vol. 61, no. 1, pp. 1–7, 2012.

[218] R. B. Ettlinger, A. Crovetto, S. Canulescu, A. Cazzaniga, L. Ravnkilde, T. Youngman, O. Hansen, N. Pryds, and J. Schou, "Formation of copper tin sulfide films by pulsed laser deposition at 248 and 355nm," *Appl. Phys. A*, vol. 122, no. 4, p. 466, 2016.

[219] B. Hafner, "Energy Dispersive Spectroscopy on the SEM: A Primer," tech. rep., 2006.

[220] D. E. Newbury and N. W. M. Ritchie, "Faults and foibles of quantitative scanning electron microscopy/energy dispersive x-ray spectrometry (SEM/EDS)," in *Proc. SPIE* (M. T. Postek, D. E. Newbury, S. F. Platek, and T. K. Maugel, eds.), vol. 8378, p. 837803, may 2012.

[221] N. Kourkoumelis, "PowDLL, a reusable .NET component for interconverting powder diffraction data: Recent developments," in *Powder Diffraction, ICDD Annu. Spring Meet.* (L. O'Neill, ed.), vol. 28, p. 142, JCPDS-ICDD, 2013.

[222] E. J. Mittemeijer, "Crystallography," in *Fundam. Mater. Sci.*, ch. 4, pp. 1–594, Berlin, Heidelberg: Springer Berlin Heidelberg, 2010.

[223] D. M. Berg and P. J. Dale, "Kesterites: Equilibria and Secondary Phase Identification," in *Copp. Zinc Tin Sulfide-Based Thin-Film Sol. Cells* (K. Ito, ed.), ch. 5, p. 114, Newark, Delaware: John Wiley & Sons, Ltd, 1st ed., 2015.

[224] M. Dimitrievska, A. Fairbrother, X. Fontané, T. Jawhari, V. Izquierdo-Roca, E. Saucedo, and A. Pérez-Rodríguez, "Multiwavelength excitation Raman scattering study of polycrystalline kesterite Cu2ZnSnS4 thin films," *Appl. Phys. Lett.*, vol. 104, p. 021901, jan 2014.

[225] P. A. Fernandes, P. M. P. Salomé, and A. F. da Cunha, "Study of polycrystalline Cu2ZnSnS4 films by Raman scattering," *J. Alloys Compd.*, vol. 509, pp. 7600–7606, jul 2011.

[226] L. Price, I. Parkin, A. Hardy, and R. Clark, "Atmospheric pressure chemical vapor deposition of tin sulfides (SnS, Sn2S3, and SnS2) on glass," *Chem. Mater.*, no. 12, pp. 1792–1799, 1999.

[227] A. Cazzaniga, R. B. Ettlinger, S. Canulescu, J. Schou, and N. Pryds, "Nanosecond laser ablation and deposition of silver, copper, zinc and tin," *Appl. Phys. A*, pp. 2–5, jan 2014.

[228] K. Ito, "An Overview of CZTS-Based Thin-Film Solar Cells," in *Copp. Zinc Tin Sulfide-Based Thin-Film Sol. Cells* (K. Ito, ed.), ch. 1, pp. 3–41, John Wiley & Sons, Ltd, 1 ed., 2014.

[229] A. A. Voevodin, J. S. Zabinski, and J. G. Jones, "Pulsed Laser Deposition of Tribological Coatings," *Pulsed Laser Depos. Thin Film. Appl. Growth Funct. Mater.*, pp. 585–609, 2006.

[230] S. Fähler, K. Sturm, and H.-U. Krebs, "Resputtering during the growth of pulsed-laser-deposited metallic films in vacuum and in an ambient gas," *Appl. Phys. Lett.*, vol. 75, no. 24, p. 3766, 1999.

[231] B. Thestrup, B. Toftmann, J. Schou, B. Doggett, and J. G. Lunney, "Ion dynamics in laser ablation plumes from selected metals at 355 nm," *Appl. Surf. Sci.*, vol. 197-198, pp. 175–180, sep 2002.

[232] S. Amoruso, R. Bruzzese, N. Spinelli, and R. Velotta, "Characterization of laser-ablation plasmas," *J. Phys. B At. Mol. Opt. Phys.*, vol. 32, no. 14, pp. 130–172, 1999.

[233] A. Cazzaniga, R. B. Ettlinger, S. Canulescu, J. Schou, and N. Pryds, "Nanosecond laser ablation and deposition of silver, copper, zinc and tin," *Appl. Phys. A*, pp. 2–5, jan 2014.

[234] S. A. Vanalakar, G. L. Agawane, A. S. Kamble, C. W. Hong, P. S. Patil, and J. H. Kim, "Fabrication of Cu2SnS3 thin film solar cells using pulsed laser deposition technique," *Sol. Energy Mater. Sol. Cells*, vol. 138, pp. 1–8, 2015.

[235] A. Redinger, D. M. Berg, P. J. Dale, and S. Siebentritt, "The consequences of kesterite equilibria for efficient solar cells," *J. Am. Chem. Soc.*, vol. 133, no. 10, pp. 3320–3323, 2011.

[236] P. A. Fernandes, P. M. P. Salomé, and A. F. da Cunha, "A study of ternary Cu2SnS 3 and Cu3SnS4 thin films prepared by sulfurizing stacked metal precursors," *J. Phys. D. Appl. Phys.*, vol. 43, p. 215403, jun 2010.

[237] A.-J. Cheng, M. Manno, A. Khare, C. Leighton, S. A. Campbell, and E. S. Aydil, "Imaging and phase identification of Cu2ZnSnS4 thin films using confocal Raman spectroscopy," *J. Vac. Sci. Technol. A Vacuum, Surfaces, Film.*, vol. 29, no. 5, p. 051203, 2011.

[238] J. de Wild, E. V. Robert, B. E. Adib, D. Abou-Ras, and P. J. Dale, "Secondary phase formation during monoclinic Cu2SnS3 growth for solar cell application," *Sol. Energy Mater. Sol. Cells*, vol. 157, pp. 259–265, 2016.

[239] T. P. Mernagh and A. G. Trudu, "A laser Raman microprobe study of some geologically important sulphide minerals," *Chem. Geol.*, vol. 103, no. 1-4, pp. 113–127, 1993.

[240] N. Aihara, Y. Matsumoto, and K. Tanaka, "Exciton luminescence from Cu2SnS3 bulk crystals," *Appl. Phys. Lett.*, vol. 108, no. 9, 2016.

[241] M. Umehara, Y. Takeda, S. Tajima, T. Motohiro, T. Sakai, and R. Maekawa, "Improvement of red light response of Cu2Sn1-xGexS3 solar cells by optimization of CdS buffer layers," *J. Appl. Phys.*, vol. 118, no. 15, 2015.

[242] M. Mazzer, S. Rampino, E. Gombia, M. Bronzoni, F. Bissoli, F. Pattini, M. Calicchio, A. Kingma, F. Annoni, D. Calestani, N. Cavallari, V. Thottapurath Vijayan, M. Lomascolo, A. Cretì, and E. Gilioli, "Progress on Low-Temperature Pulsed Electron Deposition of CuInGaSe2 Solar Cells," *Energies*, vol. 9, no. 3, p. 207, 2016.

[243] S. Rampino, F. Bissoli, E. Gilioli, and F. Pattini, "Growth of Cu(In,Ga)Se2 thin films by a novel single-stage route based on pulsed electron deposition," *Prog. Photovoltaics Res. Appl.*, vol. 21, pp. 588–594, nov 2013.

[244] R. B. Ettlinger, F. Pattini, S. Rampino, M. Bronzoni, F. Annoni, A. Crovetto, E. Bosco, A. C. Cazzaniga, E. Gilioli, O. Hansen, and J. Schou, "Pulsed electron vs. pulsed laser deposition for the growth of CZTS films," *in prep.*, no. 1, pp. 1–24, 2016.

[245] M. Nistor, F. Gherendi, and N. B. Mandache, "Angular distribution of species in pulsed energy beam deposition of oxide films," *Appl. Surf. Sci.*, vol. 258, no. 23, pp. 9274–9277, 2012.

[246] G. Monaco, M. Gastaldi, P. Nicolosi, M. G. Pelizzo, E. Gilioli, S. Rampino, F. Bissoli, F. Pattini, S. Agnoli, G. Granozzi, and N. Manuzzato, "Silicon carbide thin films for EUV and soft X-ray applications," *Eur. Phys. J. Spec. Top.*, vol. 169, no. 1, pp. 159–165, 2009.

[247] J. E. Mathis and H. M. Christen, "Factors that influence particle formation during pulsed electron deposition of YBCO precursors," *Phys. C Supercond. its Appl.*, vol. 459, no. 1-2, pp. 47–51, 2007.

[248] F. Sava, M. Popescu, G. Socol, E. Axente, I. N. Mihailescu, and M. Nistor, "Amorphous SnSe 2 films," *J. Optoelectron. Adv. Mater.*, vol. 8, no. 4, pp. 1367 – 1371, 2006.

[249] M. Bronzoni, M. Stefancich, and S. Rampino, "Role of substrate temperature on the structural, morphological and optical properties of CuGaSe 2 thin films grown by Pulsed Electron Deposition technique," *Thin Solid Films*, vol. 520, pp. 7054–7061, oct 2012.

[250] J. K. Larsen, S.-Y. Li, J. J. S. Scragg, Y. Ren, C. Hägglund, M. D. Heinemann, S. Kretzschmar, T. Unold, and C. Platzer-Björkman, "Interference effects in photoluminescence spectra of Cu2ZnSnS4 and Cu(In,Ga)Se2 thin films," *J. Appl. Phys.*, vol. 118, no. 3, 2015.

[251] A. Kanai, H. Araki, A. Takeuchi, and H. Katagiri, "Annealing temperature dependence of photovoltaic properties of solar cells containing Cu2SnS 3 thin films produced by co-evaporation," *Phys. Status Solidi*, vol. 252, no. 6, pp. 1239–1243, 2015.

[252] N. Song, M. Young, F. Liu, P. Erslev, S. Wilson, S. P. Harvey, G. Teeter, Y. Huang, X. Hao, and M. A. Green, "Epitaxial Cu2ZnSnS4 thin film on Si (111) 4° substrate," *Appl. Phys. Lett.*, vol. 106, no. 25, p. 252102, 2015.

[253] M. A. Green, "Commercial progress and challenges for photovoltaics," *Nat. Energy*, vol. 1, no. January, pp. 1–4, 2016.

[254] K. Oishi, G. Saito, K. Ebina, M. Nagahashi, K. Jimbo, W. S. Maw, H. Katagiri, M. Yamazaki, H. Araki, and A. Takeuchi, "Growth of Cu2ZnSnS4 thin films on Si (100) substrates by multisource evaporation," *Thin Solid Films*, vol. 517, pp. 1449–1452, dec 2008.

[255] T. Todorov, T. Gershon, O. Gunawan, C. Sturdevant, and S. Guha, "Perovskite-kesterite monolithic tandem solar cells with high open-circuit voltage," *Appl. Phys. Lett.*, vol. 105, p. 173902, oct 2014.

[256] T. P. White, N. N. Lal, and K. R. Catchpole, "Tandem solar cells based on high-efficiency c-Si bottom cells: Top cell requirements for >30% efficiency," *IEEE J. Photovoltaics*, vol. 4, no. 1, pp. 208–214, 2014.

[257] T. Arai, S. Tajima, S. Sato, K. Uemura, T. Morikawa, and T. Kajino, "Selective CO2 conversion to formate in water using a CZTS photocathode modified with a ruthenium complex polymer," *Chem. Commun.*, vol. 47, p. 12664, 2011.

[258] X. Xin, M. He, W. Han, J. Jung, and Z. Lin, "Low-cost copper zinc tin sulfide counter electrodes for high-efficiency dye-sensitized solar cells," *Angew. Chemie - Int. Ed.*, vol. 50, pp. 11739–11742, dec 2011.

[259] C. Bourgès, P. Lemoine, O. I. Lebedev, R. Daou, V. Hardy, B. Malaman, and E. Guilmeau, "Low thermal conductivity in ternary Cu4Sn7S16 compound," *Acta Mater.*, vol. 97, pp. 180–190, 2015.

[260] C.-f. Wang, B. Hu, H.-h. Yi, and W.-b. Li, "Structure and photoluminescence properties of ZnS films grown on porous Si substrates," *Opt. Laser Technol.*, vol. 43, pp. 1453–1457, nov 2011.

[261] S. P. Patel, A. Chawla, R. Chandra, J. Prakash, P. Kulriya, J. Pivin, D. Kanjilal, and L. Kumar, "Structural phase transformation in ZnS nanocrystalline thin films by swift heavy ion irradiation," *Solid State Commun.*, vol. 150, pp. 1158–1161, jul 2010.

[262] M. Sanz, M. López-Arias, E. Rebollar, R. De Nalda, and M. Castillejo, "Laser ablation and deposition of wide bandgap semiconductors: Plasma and nanostructure of deposits diagnosis," *J. Nanoparticle Res.*, vol. 13, no. 12, pp. 6621–6631, 2011.

[263] K. M. Yeung, W. S. Tsang, C. L. Mak, and K. H. Wong, "Optical studies of ZnS:Mn films grown by pulsed laser deposition," *J. Appl. Phys.*, vol. 92, no. 7, pp. 3636–3640, 2002.

[264] Y. Z. Yoo, Y. Osaka, T. Fukumura, Z. Jin, M. Kawasaki, H. Koinuma, T. Chikyow, P. Ahmet, A. Setoguchi, and S. F. Chichibu, "High temperature growth of ZnS films on bare Si and transformation of ZnS to ZnO by thermal oxidation," *Appl. Phys. Lett.*, vol. 78, no. 5, pp. 616–618, 2001.

[265] L. Berger, "Properties of Semiconductors," in *CRC Handb. Chem. Phys.* (W. M. Haynes, T. J. Bruno, and D. R. Lide, eds.), ch. 12, pp. 12–80 – 12–93, Boca Raton, FL: CRC Press, Taylor and Francis Group, LLT, 96 ed., 2015.

[266] S. Adachi, "Appendix A Summary: Physical Properties of CZTS and CZTSe," in *Earth-Abundant Mater. Sol. Cells*, ch. App A, pp. 363–367, Chichester, UK: John Wiley & Sons, Ltd, oct 2015.

[267] C. Kittel, *Introduction to Solid State Physics*. Wiley, 3 ed., 1966.

[268] "Properties of the Elements and Inorganic Compounds," in *CRC Handb. Chem. Phys.* (W. M. Haynes, T. J. Bruno, and D. R. Lide, eds.), ch. 4, pp. 4–43 – 4–101, Boca Raton, FL: CRC Press, 96 ed., 2015.